Simplified Finite-State Predictive Torque Control Strategies for Induction Motor Drives

By

Md. Habibullah

A thesis submitted in fulfillment of the requirements
for the degree of Doctor of Philosophy

Faculty of Engineering and Information Technologies
The University of Sydney
2016

CERTIFICATE OF ORIGINALITY

I hereby declare that this submission is my own work and, to the best of my knowledge and belief, contains no material previously published or written by another person, nor material which to a substantial extent has been accepted for the award of any other degree or diploma at The University of Sydney or any other educational institution, except where due acknowledgment is made in this thesis. Any contribution made to the research by others, with whom I have worked at The University of Sydney or elsewhere, is explicitly acknowledged in the thesis.

I also declare that the intellectual content of this thesis is the product of my own work, except to the extent that assistance from others in the projects design and conception or in style, presentation and linguistic expression is acknowledged.

Signature: .... Date: ....

Md. Habibullah

Dedicated To My Parents

Abstract

Fast and accurate torque control and low current harmonic distortion of electrical drives are mandatory requirements in most industrial applications. To fulfil these requirements, model predictive control (MPC) is expected to be an effective control strategy in the near future. The finite-state predictive torque control (FS-PTC) of motor drives is an MPC strategy. In FS-PTC, a finite number of possible control actions—voltage vectors in this study—are evaluated against control objectives (torque, flux and other system constraints) in an iterative prediction loop. After this, an optimum voltage vector is selected by minimising a predefined cost function and applied to the motor terminals via an inverter. The cost function includes prediction errors of control objectives with weighting factors and other system constraints. Using the weighting factors, various control objectives of different magnitudes, as well as units, are combined in the same cost function. However, designing a cost function with appropriate weighting factors is a complex task. In addition, a conventional FS-PTC is computationally expensive, as it uses all voltage vectors available from the inverter for the predictions of control objectives. The computational burden is increased rapidly with the number of admissible voltage vectors and objectives to be controlled, resulting in a low sampling frequency and consequent degraded control performance. Complex calculations in the prediction loop also increase the computational burden. This thesis develops a simplified FS-PTC algorithm based on selected prediction vectors (SPVs). This reduces the number of voltage vectors required to be predicted and the objectives to be controlled. The sign of torque or stator flux deviation and the position of stator flux are used to select the prediction vectors. The proposed SPVs strategy also assists reducing the average switching frequency for a two-level voltage source inverter fed induction motor (IM) drive. As a result, the cost function is simplified, as the frequency term is not required. To take advantage of multi-level inverter drives that offer the benefits of low harmonic distortion in stator currents as well as low torque ripple and switching frequency, this thesis proposes to integrate the FS-PTC with a three-level neutral-point clamped (3L-NPC) inverter driven IM drive. The neutral-point voltage variation problem inherited from the topology of 3L-NPC VSI is easily handled by considering the voltage variation as a variable to the cost function. Similarly, apart from the inverter topology itself, the average switching frequency is reduced further, and is maintained as almost constant for a particular speed at different load torques. Using the SPVs strategy reduces the computational burden for the proposed three-level inverter fed drive without affecting the system performance. However, an appropriate weighting factor is required for torque and flux errors in the cost function. This leads to the development of a second simplified FS-PTC which does not require complex torque calculations in the prediction loop and hence tuning effort on the weighting factor. A new reference stator flux vector calculator (RSFVC) with an inner proportional-integral torque regulator is employed to convert the torque and flux amplitude references into an equivalent stator flux reference vector. This stator flux reference is used in the cost function for the flux error calculation. The required processing power for the RSFVC-based FS-PTC is further reduced by combining it with the SPVs strategy. The proposed simplified FS-PTC strategies in terms of computational efficiency, cost function design, torque and flux responses, robustness and average switching frequency are validated through experimental results.

Finally, a speed-sensorless simplified FS-PTC of IM supplied from a 3L-NPC inverter is proposed. For sensorless operation, PTC requires an estimated speed and rotor/stator flux. In this study, the rotor speed and flux are estimated accurately using an extended Kalman filter (EKF). Due to the large number of available voltage vectors, the FS-PTC with EKF for a multi-level inverter-fed sensorless drive is computationally expensive. Consequently, the controller requires a long sampling time that yields worse torque, flux and speed responses, especially at low-speed. The proposed SPVs strategy is employed to overcome this problem. Experimental results illustrate that the proposed sensorless strategy can estimate speed accurately over a wide speed range, including the field-weakening region, while maintaining robustness and excellent torque and flux responses.

List of Publications

Journal papers

- M. Habibullah and D.D.-C. Lu, “A Speed-Sensorless FS-PTC of Induction Motors Using Extended Kalman Filters,” *IEEE Transactions on Industrial Electronics*, vol. 62, no. 11, pp. 6765–6778, Nov. 2015.
- M. Habibullah, D.D.-C. Lu, D. Xiao, and M. F. Rahman, “A Simplified Finite-State Predictive Direct Torque Control for Induction Motor Drive,” *IEEE Transactions on Industrial Electronics*, vol. 63, no. 6, pp. 3964–3975, June 2016.
- M. Habibullah, D.D.-C. Lu, D. Xiao, and M. F. Rahman, “Finite-State Predictive Torque Control of Induction Motor Supplied from a Three-Level NPC Voltage Source Inverter,” *IEEE Transactions on Power Electronics*, vol. 32, no. 1, pp. 479–489, January 2017.
- M. Habibullah, D.D.-C. Lu, D. Xiao, J. Fletcher, and M. F. Rahman, “Predictive Torque Control of Induction Motor Sensorless Drive Fed by a 3L-NPC Inverter,” *IEEE Transactions on Industrial Informatics*, early access, 2016.
- M. Habibullah, D.D.-C. Lu, D. Xiao, Ilham Osman, and M. F. Rahman, “Performance Investigation of Selected Prediction Vectors Based FS-PTC for 3L-NPC Inverter Fed Motor Drive,” *IEEE Transactions on Industry Applications* (under review).
- M. Habibullah, D.D.-C. Lu, D. Xiao, J. Fletcher, and M. F. Rahman, “Low Complexity Predictive Torque Control Strategies for a Three-level Inverter Driven Induction Motor,” *IET Electric Power Applications* (under review).

Conference papers

- M. Habibullah, D.D.-C. Lu, D. Xiao, and M. F. Rahman, "Performance Investigation of Selected Prediction Vectors Based FS-PTC for 3L-NPC Inverter Fed Motor Drive," *8th Annual IEEE Energy Conversion Congress & Exposition (ECCE 2016), accepted for publication.*
- M. Habibullah and D.D.-C. Lu, "An improved sensorless FS-PTC of induction motors using estimated stator currents," *IEEE 6th International Symposium on Sensorless Control for Electrical Drives (SLED)*, pp. 1-6, June 2015.
- M. Habibullah, D.D.-C. Lu, D. Xiao, and M. F. Rahman, "A computationally efficient FS-PTC for IM with minimum voltage vectors," *2015 IEEE 11th International Conference on Power Electronics and Drive Systems (PEDS)*, pp. 992–997, 9-12 June 2015.
- M. Habibullah and D.D.-C. Lu, "Encoderless FS-PTC for Induction Motor with Extended Kalman Filter" *Australasian Universities Power Engineering Conference (AUPEC)*, Perth WA, pp. 1-6, 28 Sept-1 Oct 2014.

Thesis authorship attribution statement

Chapter 3 of this thesis is partly published as [109], [110]. Chapter 4 of this thesis is partly published as [113]. Chapter 6 of this thesis is partly published as [94], [117–119].

All the results published in the above papers are the outcome of my research work. I proposed the idea, analysed the data and wrote the papers. I was the corresponding author for all the papers. The co-authors in the papers were my supervisor and co-supervisors. Their contributions are properly mentioned in the acknowledgments.

Acknowledgements

I would like to thank my PhD supervisor, Associate Prof. Dylan D.-C. Lu for his guidance, encouragement and continuous support throughout my PhD period. Not only been an academic guide he is also a good friend. He inspired me in all aspects, his sincerity, the way he supervises, the way he treats his students and how he organizes his works. I am thankful to him for his confidence in me and I really appreciated the freedom that he gave me during all periods of my study. I would also like to thank Dr. Swamidoss Sathiakumar for being my supervisor at the last stage of my study.

I am very much grateful to Prof. M. F. Rahman and Prof. John Fletcher for giving me the opportunity to work in the energy systems laboratory at the University of New South Wales (UNSW). I conducted experiment in this lab under their supervision. My sincere thank also goes to Dr. Dan Xiao at UNSW for his co-operation throughout my project. He helped me in experimental setup and control algorithm implementation.

It has been a great pleasure to work with the people of power group at The University of Sydney. I would like to thank them for the time we were discussing together about our research. They include Dr. Khairul Safuan Bin Muhammad, Dr. Le An, Dr. Mingfei Wu, Mr. Golosorkhi E. Mohammad Sadegh, Mr. Jian Qi, Mr. Juan Carlos Ostos Giraldo, Mr. Yue Yao, Mr. Sushan Reza, Mr. John Long Soon, Mr. Parvez Akter, Mr. Jim Munro, Mr. Anand Fernando, Ms. Tian Cheng, Ms. Yuezhu Lu, Mr. Mehdi Garmroodi, Mr. Hesamuddin, Mr. Ahmadyar Syabir and Mr. Chanaka Keerthisinghe. I would also like to acknowledge Elite Editing proofreading service for grammar checking of my thesis.

I would like to say thanks to my parents because of whom I am at this stage of my study. Special thanks to my elder brother Md. Saifullah for his nice caring to all of my family matters during this study.

Contents

Abbreviations

AC	Alternating current
CCS-MPC	Continuous control set model predictive control
DB	Deadbeat
DC	Direct current
DSP	Digital signal processor
DTC	Direct torque control
EKF	Extended Kalman filter
EMF	Electromotive force
EMI	Electro-magnetic interference
FCS-MPC	Finite control set model predictive control
FOSMO	Full-order sliding mode observer
FOC	Field orientation control
FS-PTC	Finite state predictive torque control
IM	Induction motor
LO	Luenberger observer
MPC	Model predictive control
MRAS	Model reference adaptive system
PCC	Predictive current control
PI	Proportional-integral
PMSM	Permanent magnet synchronous machine
PPR	Pulse per revolution
PTC	Predictive torque control
PV	Photovoltaic
PWM	pulse width modulation

RSFVC	Reference stator flux vector calculator
SM	Synchronous motor
SMO	Sliding mode observer
SPVs	Selected prediction vectors
SVM	Space vector modulation
THD	Total harmonic distortion
VSI	Voltage source inverter
2L-VSI	Two-level voltage source inverter
3L-ANPC	Three-level active neutral-point clamped
3L-NPC	Three-level neutral-point clamped

List of Figures

List of Tables

Chapter 1

Introduction

1.1 Background

The electric motor is an energy conversion medium that converts electrical energy into mechanical energy through mechanical rotation. An electromagnetic interaction (i.e., force) taking place inside the motor produces the rotation. By controlling the rotational force effectively, the number of revolutions of the motor shaft per unit time (i.e., the motor's speed) can be controlled efficiently. An electric motor with proper control arrangements is known as a variable or adjustable speed drive, and is used for many automated industries, such as metal rolling, paper, plastic and steel, fibre processing and textile mills, rail vehicle and robotics. The modern industrial economy depends largely on electric motors [1]. Many other applications of electric motors exist, such as elevators, household appliances, pumps and compressors, disc drives, machine tools and industrial fans. Recent developments include electric vehicles, which are becoming another promising application of electric motors [2].

1.1.1 DC and AC motors

Based on the type of required power source, electric motors can be divided into two categories: direct current (DC) and alternating current (AC) [3]. DC motors consist mainly of two independent parts: armature (rotor) and field (stator). These elements are powered separately from two constant or DC sources; thus, the stator and rotor magnetic fields are independent. Current flows in the armature winding is time varying, even though the supplied terminal current is DC. A brush-commutator (a mechanical switch) arrangement in the DC motor turns the DC into AC, and ensures the time varying current in the armature winding. An interaction between this time varying electric field and the constant magnetic field from the field circuit creates a rotational force that accelerates the rotational part ‘armature’ of the motor. The time varying current in the armature winding produces a time varying magnetic field. As the two magnetic fields are independent, designing a controller for the DC motor is an easy task. However, the commutator and associated brushes make the DC motor bulky, and require frequent maintenance. The cost of the motor is also high due to the brush-commutator arrangement. In contrast, an AC motor is powered from an AC source, as mentioned earlier; the brush and commutator are not required. This is why an AC motor is simpler in construction and less expensive than a DC motor. Prior to the 1960s, DC motors were used traditionally as variable speed drives, whereas AC motors were used as constant speed drives for different industrial applications [4]. Later on, the advent of semiconductor devices and their continuous progression put AC motor in situations where DC motors dominated. Various types of converter topologies and different pulse width modulation (PWM) strategies have made it possible to use AC motors as variable speed drives by changing the supplied constant voltage and frequency into variable voltage and frequency.

AC motors are classified into two categories: synchronous and asynchronous. The rotor of a synchronous motor (SM) rotates at the same speed as the frequency of the stator current; thus, it is called ‘synchronous’. For an asynchronous motor, the rotor runs at lower speeds than the synchronous speed. All induction motors (IMs) are asynchronous. They have been used widely in different industrial applications. An IM consists mainly of a stator (stationary part) and a rotor (rotational part). Based on the rotor structure, IMs are further classified into two groups: squirrel-cage and wound. In the cage type, the rotor circuit is shorted itself; in the wound type, the rotor terminals are available outside. The squirrel-cage type IM with a voltage source converter has received universal acceptance by industry [5]. Unlike DC motors, rotor and stator variables in an IM are dependent on each other. Because AC supply is applied only to the stator terminals, which creates a rotating magnetic field (stator flux) in the stator core. An electromotive-force (EMF) is induced in the rotor circuit through induction, so called IM. Subsequently, the induced EMF causes rotor current and the rotor magnetic field (rotor flux), as the rotor circuit is shorted. The magnitude of the induced rotor voltage is dependent on the relative velocity (i.e., slip) between the stator flux and the rotor conductors. An electromagnetic interaction between the magnetic field from the stator and the electric field from the rotor creates a rotational force (the torque) that accelerates the rotor. As the stator and rotor variables are coupled, designing controllers for IM is a relatively complex task. The complexity is further increased if high performance control is required. The controllers are designed in such a way that the stator and rotor fields can be controlled independently. Consequently, torque and flux can be controlled separately. This decoupled control of IM ensures a similar performance to that of the separately excited DC motors.

1.1.2 Existing classical control strategies: FOC and DTC

High performance control—the fast and accurate torque control, low current total harmonic distortion (THD)—of electrical drives is a mandatory requirement for many industrial applications [6]. Two well established high performance control strategies exist for AC drives: field orientation control (FOC) [7] and direct torque control (DTC) [8]. FOC was first introduced in the 1970s and brought a revolution in AC motor control [9]. DTC was introduced in the 1980s and offered a simpler control structure than FOC [8]. Both controllers have been accepted widely in different industrial applications, pushing traditional DC motors towards obsolescence. In the FOC, the stator currents are decomposed into two components: d-axis component for flux and q-axis component for torque, to realize the behaviour of a separately excited DC machine. Both currents are regulated by two linear proportional-integral (PI) controllers in the synchronously rotating reference frame. A decoupled control of torque and flux is achieved by aligning the d-axis with the rotor flux position. Finally, the gate pulses of a particular inverter are generated using space vector modulation (SVM) to produce the desired voltage vector. The FOC strategy provides good dynamic torque and flux responses with constant switching frequency [10]. However, the control structure is complex because of two PI regulators, SVM blocks and axis transformation which requires a high resolution shaft-mounted speed sensor. Moreover, the robustness of the controller has significant parameter dependency. In contrast, the DTC structure [8] is simpler as it does not have any axis transformation (between the synchronous and stationary frames) and modulation blocks. This control strategy has emerged as an alternative to the FOC strategy [11]. It uses a predefined switching table based on the stator flux position and error signs of torque and flux to select the most appropriate voltage vector for the inverter. The controller provides quick dynamic response. However, the DTC structure includes two hysteresis blocks for controlling torque and flux, which produces more ripple in the torque and flux and variable switching frequency [12]. Moreover, varying the switching frequency over a wide range yields more ripple in torque. Research continues on the DTC strategy to negate these drawbacks and to ensure energy efficient operation of motor drives [13]. This thesis focuses on another promising control strategy named predictive torque control (PTC). This controller has neither modulation nor hysteresis blocks, and is thus a simpler structure compared with the FOC and DTC. The PTC concept is based on model predictive control (MPC), as discussed below.

1.1.3 Background, principle and basic structure of MPC

MPC was first introduced in 1960s and received industrial acceptance in the late 1970s [14]. Since then, MPC has become popular for different industrial applications [15–17], especially in the chemical industry, where desired control objectives do not change frequently. This means that the time constant in chemical processes is long enough to undertake the required calculations online and to update the control actions. At that time, MPC was not suitable for dynamic adaptive systems, such as power electronics applications, where the desired control objectives change frequently and hence require a shorter time constant. It is because the speed of available digital signal processors (DSPs) was not high enough to accomplish the necessary calculations within the short control duration. Nevertheless, MPC applications to power electronics started from 1980s. Initially, the controller was applied to high-power and low-switching frequency applications [18]. Later, due to the continuous development of DSPs, MPC has been spread out in different branches of power electronics [19].

MPC is not a single control idea, but rather a family of control strategies. However, all control strategies (to a greater or lesser degree) are based on the following principle (see also Fig. 1.1):

1) The future or predicted outputs of the controller $\hat{y}(t+k)$, $k = 0 \cdots N$ are predicted over a predefined control horizon N, called the prediction horizon, using the available information until time t. The available information includes a model of the system, the measured system states $y(t)$ and the control input $u(t)$ applied to the system. If any particular state is not available for measurement, it has to be obtained using the mathematical model of the system.

2) The sequence of future optimal control actions $u(t+k)$, where $k = 0 \cdots N-1$, is calculated by minimising a cost function. The cost function includes prediction errors and other system constraints. The optimal control actions try to maintain the predicted outputs $\hat{y}(t+k)$ as close as possible to the reference $y^*(t+k)$.

3) Among N optimal control actions in a sequence within the prediction horizon, only the first element of the sequence is applied as the optimal control action to the system. It is a repetitive procedure from step 1) for every prediction horizon.

The basic structure of MPC is shown in Fig. 1.2. It consists mainly of two parts: prediction/plant model and optimiser. The plant model—mostly a state-space model for power electronics applications—predicts the control outputs using past inputs, present plant outputs and future optimal control inputs. The past inputs are already known, and the present plant outputs are obtained by measurements or estimations. Another fundamental part, the optimiser, outputs the proposed control inputs, which are used in the prediction model. The optimiser works based on the cost function, prediction/future errors and system constraints. Generally, all control objectives that depend on the type of application are set in the cost function in terms of prediction errors with appropriate weighting factors. The errors are obtained simply using absolute or quadratic values. A quadratic function is better than an absolute value for good tracking accuracy [20]. The weighting factors in the cost function are selected based on the importance of a particular

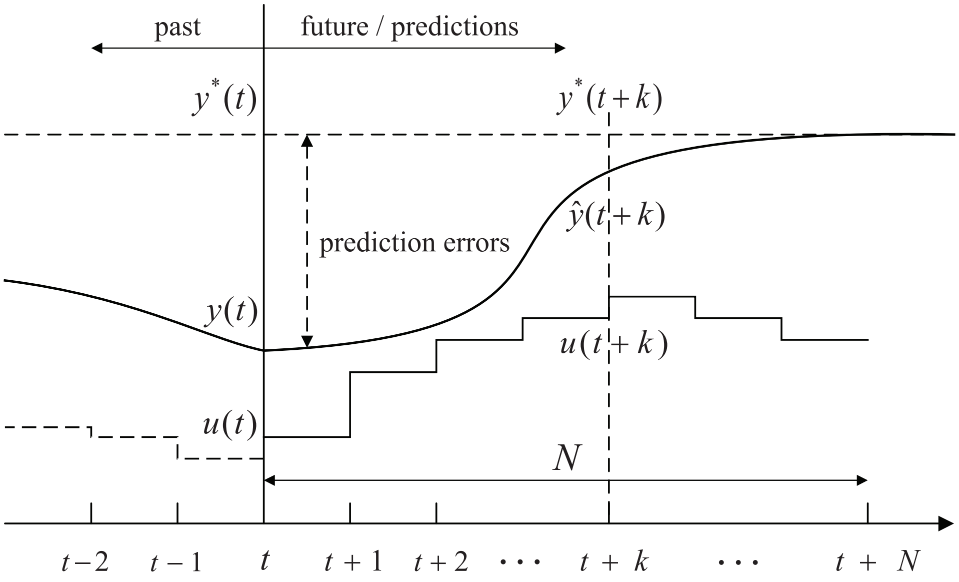

Figure 1.1: Working principle of MPC.

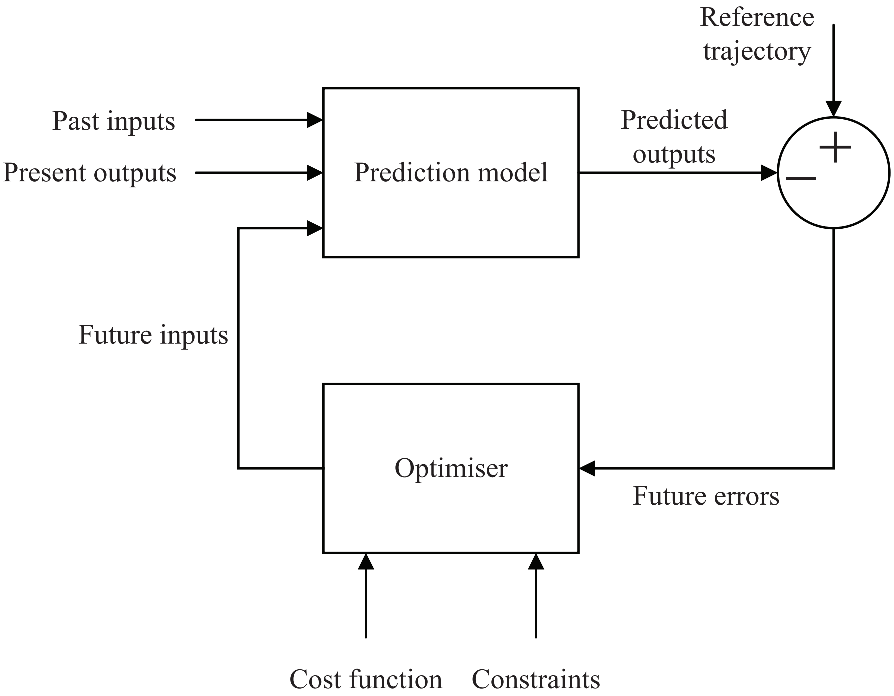

Figure 1.2: Fundamental structure of MPC [16].

control objective in relation to the other control objectives. Selecting an appropriate weighting factor is not an easy task, and it is a new direction of research for MPC. Another variable of the optimiser, the system constraint, is considered using a logic function. If the predicted value of the desired variable is within a predefined limit, it gives a zero value, or otherwise infinity—a very high value—to the optimiser. The whole MPC procedure is implemented through a micro-controller embedded in the system. The performance of the system is dependent on the speed of the micro-controller and the required number of calculations. For a specific micro-controller, a large number of calculations demands long control duration, which degrades the control performance. The computational load of the MPC algorithm is determined mainly by the prediction model's complexity, the type of cost function and constraints, the prediction horizon length and the number of control objectives.

Based on prediction horizons, there are two types of MPC: one-step (short) and longer prediction horizons. With long prediction horizons, the performance of MPC is expected to be better. However, the calculation effort will increase exponentially, and the model errors lead to a worsening of the control variables. Moreover, designing a cost function would be complex, especially for motor drive applications. These (computational burden, model errors and cost function design) are the main obstacles in implementing the longer prediction horizons based MPC. On the other hand, short prediction horizon has been successfully applied to various power electronics applications [20]. The modelling of a system and designing the cost function are very simple and intuitive. Hence, in this thesis, short prediction horizon based MPC has been considered.

1.2 Literature review

1.2.1 Predictive torque control (PTC)

MPC for motor drives has drawn much attention from the research community in the last few years, due to its simple concept, intuitive features, easy inclusion of nonlinearities, multivariable optimisation and ease of practical implementation [19–31]. Moreover, MPC meets the requirements of modern control systems, such as using plant model and digital control platforms, and allows consideration of system constraints and restrictions [28]. The recent advent of new powerful processors and their successful applications in power electronics have also increased the interest in MPCs [32–38]. There are two types of MPC [23, 26]: continuous control set MPC (CCS-MPC) and finite control set MPC (FCS-MPC). In CCS-MPC, the controller generates a continuous output for a modulator, and the modulator generates the switching states for the inverter to generate the required voltage. Due to the presence of the modulator, the controller yields a constant switching frequency. Conversely, in FCS-MPC, the finite number of control actions available in the system—inverter switching states for motor drives—are evaluated against the desired control objectives. The outputs of the controller are discrete, and are directly used to switch the power switches *on/off* in the inverter. The controller yields a variable switching frequency due to the absence of a modulator. The FS-PTC of motor drives is an FCS-MPC strategy [29, 39–43]. In FS-PTC, torque and stator flux are predicted for the finite number of admissible switching states of a voltage source inverter (VSI). The switching state that minimises torque and flux ripple most is chosen as the optimal switching state, and is obtained by actuating a predefined cost function. Several targets, variables and constraints with appropriate weighting factors can be included in the cost function and controlled simultaneously. The selected optimum switching state is applied directly to the inverter to produce the voltage vector to be applied to the motor terminals in the next sampling instant, without requiring an intermediate modulation stage [29]. Another important advantage of PTC is that it has no inner current control loop. As a result, the controller yields fast dynamic response. However, for speed control, the PTC structure has a cascaded linear PI controller based on the outer speed-loop. The speed can also be controlled directly by introducing a speed error function to the cost function [44]. In that case, the speed state should be predicted using a motor model in discrete time steps. Nevertheless, the PTC structure is simpler compared with the classical control strategies of FOC and DTC [7, 8, 45]. A comprehensive study comparing PTC and existing classical control strategies is detailed in [45, 46]. According to this research, the PTC can achieve a similar or even better (under some conditions) performance when compared with the DTC and FOC strategies. A detailed comparison between the classical control and PTC is presented in Table 1.1 to better illustrate the existing methods and the necessity to develop new algorithms. It can be seen that, in most cases, PTC can compete with the FOC and DTC. However, it has some inherent limitations, such as the variable switching frequency, higher computational cost, weighting factor tuning and higher current distortion [46]. Researchers are currently trying to overcome these problems [47, 48].

Table 1.1: Comparison among FOC, DTC and PTC

Index	FOC	DTC	PTC
Structural complexity	higher	lower	lower
Axis transformation	yes	no	no
Modulator	yes	no	no
Parameter sensitivity	higher	lower	higher
Position sensor	yes	no	no
Switching frequency	fixed	variable	variable
Inclusion of system nonlinearity	hard	hard	easy
Dynamic response	slower	faster	faster
Torque and flux ripple	lower	higher	lower
Current THD	lower	higher	higher
Computational complexity	lower	lower	higher
Weighting factor	no	no	yes

1.2.2 Two- and three-level inverters for PTC

Generally, several types of power converters are employed to produce the voltage vectors applied to motor terminals. These include two-level VSI (2L-VSI), neutral-point clamped VSI, cascaded H-bridge inverter, flying-capacitor inverter and matrix converters [29]. Among these, the 2L-VSI is used extensively in industry applications [20]. For medium- and high-power applications, multilevel converters—most prominently three-level inverters—are preferred over 2L-VSI. However, in a three-level inverter, the number of admissible switching states is 27; all switching states should be evaluated through the cost function in FS-PTC, which is inevitably time consuming. The computational burden grows rapidly with the number of admissible switching states of an inverter resulting in a low sampling frequency of the control algorithm. In fact, considering even all eight admissible switching states of 2L-VSI becomes computationally expensive to achieve complete benefits of FS-PTC (such as torque and flux ripple reduction) through multiobjective optimisation and/or a long prediction horizon $N \geq 2$ [49].

A 2L-VSI has some inherent limitations. The maximum voltage rating of the semiconductor switches in the inverter limits the maximum dc-link voltage. The inverter requires a higher switching frequency and produces more harmonic content in the output voltage and current due to the limited number of voltage levels. Additionally, for the DTC and PTC strategies with 2L-VSI, the switching frequency varies over a wide frequency range. As a result, the controllers suffer from a significant torque and flux ripple. Moreover, a 2L-VSI produces high dV/dt at the output voltage, which leads to machine windings insulation and bearing failure [50]. It is also the cause of some conducted electromagnetic interference (EMI) during the drive system operation. In contrast, multilevel inverter topologies—the most commonly used is the three-level neutral-point clamped (3L-NPC) VSI—can reduce many of these limitations considerably [51].

The 3L-NPC VSI has many advantages over the 2L-VSI such as lower ripple, switching frequency, stress on semiconductor switches and harmonic content in the output voltage and current [51]. However, the inverter has some drawbacks, such as neutral-point voltage variation (caused by capacitor voltage unbalance) [52], higher common mode voltage [53] and unequal loss distribution among semiconductor devices [54]. Among these drawbacks, the neutral-point voltage variation has serious effects on control performance [55]. It increases the torque and flux ripple as well as the distortion in stator currents. The inverter requires higher value capacitors due to unequal voltage sharing. Moreover, it imposes higher voltage stress on the semiconductor switches, which can outweigh the aforementioned advantages of a 3L-NPC VSI. Fortunately, the opposite effect of redundant vectors (small vectors) on the dc-link capacitors charge can be employed to ensure the capacitor voltages balance [52].

Research has already been conducted on three-level inverter DTC motor drives, some of which consider the aforementioned drawbacks [12, 50, 52]. In most cases, high performance control is achieved by sacrificing the simplicity of the basic DTC [52]. On the other hand, it is proved that the MPC can control the neutral-point voltage variation effectively in a very intuitive way without sacrificing the simplicity of the control structure [56]. However, the MPC control strategy has been applied successfully to particular multilevel power converter applications [29, 56–62]. These applications are mostly in current and power control, where the objective function is relatively easy to design. In contrast, motor drive control is more complex; thus, more research is required in this area to test the effectiveness of the FS-PTC with multi-level inverters. References [63, 64] have reported on the three-level inverter fed PTC IM drive. In [64], analysis has been conducted for high-speed operation, in which the improved torque response is achieved by using a specially fabricated microprocessor [65], which is not available commercially for electrical drive applications. Additionally, the range of average switching frequency variations in FS-PTC has not been addressed in [63, 64].

1.2.3 Sensorless PTC

Before achieving wide industrial acceptance, PTC must fulfil some requirements. One of the main requirements is speed encoderless (simply called sensorless) control. A speed sensor requires additional space, software and electronic circuits to install into the system, which increases the system cost. In particular, sensorless operation is important for the IM, since the machine often requires to operate in a hostile environment.

For sensorless PTC operation, the rotor speed must be estimated accurately using a proper observer. The estimated speed, together with the measured stator current and dc-link voltage, is fed back to the predictive controller for stator current prediction, and consequently the torque. Accurate estimation is particularly important for PTC as estimation error leads to incorrect predictions, which subsequently yield a sub-optimal selection of the voltage vectors.

Different sensorless strategies for the classical controllers have already been published in the technical literature, based on different observers, such as the sliding mode observer (SMO) [66], extended Kalman filter (EKF) [67–70], model reference adaptive system (MRAS) [71] and the Luenberger observer (LO) [72]. The performance of these observers should now be tested extensively in relation to the PTC. The aim here is to determine an optimum observer. Currently, sensorless predictive control is usually designed based on stator current control—the predictive current control (PCC) [73–75]—or both the stator flux and torque control (the PTC [76–78]). Attention concentrates on the proper design of observers for the estimations of stator/rotor flux and rotor speed. Two different kinds of observers—stator voltage model for stator flux and full-order sliding mode observer (FOSMO) for speed—are proposed in [76]. These observers are combined with a prediction model developed by using sliding mode feedback for stable operation of the machine over a wide speed range. The controller produces high current THD at low speeds. In [77], an encoderless FS-PTC is proposed with a compensated MRAS observer. An online stator resistance estimator confirms the robustness of the controller against parameter uncertainty. However, the stator current THD is still very high at lower speeds, and the control performance is affected significantly by the noisy estimated speed. To improve the low-speed performance, a speed independent observer and prediction models are proposed in [78], using a revised prediction model and a FOSMO. The controller produces a satisfactory speed response, even though the estimated speed is still noisy. In addition, the observer is influenced considerably by the stator resistance variations, producing oscillations in the torque and flux responses. In the aforementioned studies [76–78], low-speed drive performance has not been analysed under full-load torque. Analyses have been conducted only for the 2L-VSI. Moreover, all possible voltage vectors produced by the inverter have been evaluated for prediction and actuation in the FS-PTC, requiring additional computation.

Based on the aforementioned literature review, integration of the FS-PTC with the 3L-NPC VSI driven IM drives without speed-sensor will be an interesting research topic and would present a practical application. Unfortunately, to date, the performance of a sensorless FS-PTC has not been explored for a 3L-NPC inverter. The main reason for this is the required computational burden of the control algorithm, which limits the sampling frequency and degrades the control performance.

1.2.4 Implementation challenges of PTC

As mentioned earlier, computational burden is an implementation challenge of the FS-PTC algorithm; this topic is open for research. The computational burden depends on the number of prediction vectors and the complexity of calculations—mainly stator current and torque—in the iterative prediction loop. The prediction vectors are defined as the voltage vectors required for prediction and actuation in the prediction loop to determine the optimum voltage vector. In recent years, research has been conducted to reduce the number of calculations required [47,79–91]. In [47], a computationally efficient predictive DTC for medium voltage drives is proposed. By adopting branch and bound algorithm and by discarding some optimal sequences, the number of switching sequences is reduced. The performance is further improved with a modified sphere decoding algorithm [79]. The number of possible switching sequences is also reduced in [80] to reduce the torque ripple by using a long prediction horizon, even though the number of calculations is still high. Recently, a fast MPC strategy with a sub-module voltage sorting balanced method has been presented in [81] for modular multilevel converter for medium/high-voltage motor drive systems. The MPC algorithm is simplified by reducing the number of calculations required in the variable prediction process and the finite control set from possible switching states to selected output voltage levels. Other published techniques to reduce the number of calculations and thus simplify MPC design include the single prediction methods [82, 83], the sector distribution method [82, 84], choosing a subset of adjacent vectors [85], a modified switching algorithm [86], the double-vector-based approach [87], graphical algorithm [88], an efficient FPGA implementation [89], a deadbeat (DB) concept [90] and the Lyapunov function based approach [91]. The former techniques [82–91] have been applied to power converters only for current, voltage and/or power control, where the objective function is relatively easy to design. The control algorithms may not work for motor drives, as the control aspects are complex and completely different to those considered in [82–91]. Recently, a DB solution has been proposed in [92] to reduce the computational burden of the original FS-PTC. The controller seems effective for a multilevel converter or for a long predictive horizon ($N > 1$). However, complex calculations to determine the DB voltage vector outweigh the the controller's advantage for a short prediction horizon ($N = 1$). A computationally viable simulation study on MPC-based variable speed drive is presented in [93], where a modified sphere decoding algorithm is employed to solve the optimisation problem. For speed sensorless motor drives [94], reducing the computational burden is important as the execution time of a speed observer is significant compared to the control duration. In this case, the controller itself should be computationally efficient.

Another key issue in FS-PTC implementation is selecting the weighting factors used in the cost function [29]. Because different control objectives in the cost function have different magnitudes and units. The weighting factors bring the control variables in a relation to combine them in the same cost function. They are also used to tune the importance or cost of a particular objective in relation to the other control objectives. Different strategies using online and offline search procedures are proposed in [95–97]; these depend greatly on system parameters and require a comprehensive mathematical analysis. When the desired control objectives are more than two, trial and error methods are used running computer simulations, which are extremely time consuming [98–100]. To avoid this, a multiobjective ranking-based strategy is proposed in [49] for PTC. However, the computational burden is greatly increased, even for the 2L-VSI, due to the use of all admissible inverter switching states. Moreover, the aforementioned algorithm is only applied for two control objectives; in general (including switching frequency with torque and flux errors), three control objectives are required for PTC [42]. A two-vector-based PTC without weighting factor is proposed in [101, 102]. The weighting factor is avoided by converting the torque and flux magnitude references into an equivalent stator flux reference vector. The torque reference conversion is performed based on the position of the rotor flux and the angle between the stator and rotor flux. Thus, the conversion technique is rotor flux oriented and dependent on the machine parameters. The computational burden of the control algorithm has not been addressed in the analysis. In addition, the method proposed in [101] considers a pulse generation technique similar to a modulation stage to fix the switching frequency. Some other solutions are proposed, such as the fuzzy decision-making strategy [103, 104], sorting-based strategy [105] and look-up table based weighting factor [106]. In [104], fuzzy PTC is presented for the 3L-NPC VSI fed IM drive, with no need to tune the weighting factors. However, the tuning effort for the priority coefficients of each membership function is still required. This means that the proposed method does not truly solve the weighting factor problem. Its practical value should also be evaluated. Because the fuzzy-decision-making strategy is not as easy as conventional PTC. Besides, only the simulation results are illustrated, and it is observed that the dc-link capacitor voltages fluctuate over a large range. Hence, the weighting factor tuning issue is still an open question in relation to the PTC.

1.3 Thesis objectives

The objectives of this thesis are as follows:

1) Development of a simplified FS-PTC based on selected prediction vectors (SPVs) to reduce the number of prediction vectors and hence the computational burden.

2) Integration of the FS-PTC with a 3L-NPC inverter driven IM drive to take the advantages of low harmonic distortion in the stator currents, small torque ripple and low average switching frequency. In addition, application of the SPVs approach in the FS-PTC to reduce the computational burden of the control strategy without affecting system performance.

3) Development of a second simplified FS-PTC of the 3L-NPC inverter fed IM drive based on the reference stator flux vector calculator (RSFVC), which does not require complex torque calculations in the prediction loop and hence tuning the weighting factor between torque and flux errors in the cost function.

4) Development of a speed-sensorless FS-PTC for the 3L-NPC VSI driven IM drive, and application of the SPVs approach in the FS-PTC to reduce the computational burden of the control algorithm.

1.4 Thesis structure

This thesis is organised as follows. Chapter 2 presents the modelling of the IM and power converters. The state-space model of the IM in a stationary reference frame is presented. The principle and mathematical models of both 2L-VSI and 3L-NPC VSI used in this study are described.

Chapter 3 presents a simplified FS-PTC, based on SPVs, to reduce the number of prediction vectors and hence the computational burden for a 2L-VSI fed IM drive. The structure of a conventional FS-PTC and its limitations are discussed. The chapter also shows how the proposed strategy yields a simpler design of cost function compared with the conventional FS-PTC strategy. The effectiveness of the proposed strategy is verified by experiment.

Chapter 4 proposes the integration of the FS-PTC with a 3L-NPC inverter driven IM drive. The proposed strategy is discussed step-by-step. To reduce the computational burden of the algorithm, the SPVs approach is applied. The experimental outcomes are discussed. The performance is compared with the performance achieved through the existing classical FOC and DTC strategies. Finally, another performance comparison between the proposed 3L-NPC VSI and the 2L-VSI fed IM drives is presented.

Chapter 5 gives a second simplified FS-PTC strategy based on RSFVC, which does not require complex torque calculations in the prediction loop; thus, there is no weighting factor for torque and flux errors in the cost function. The chapter reveals that the proposed strategy requires less calculation effort, which is further reduced by including the SPVs strategy with the RSFVC. Experimental verification is illustrated and compared with the FS-PTC proposed in Chapter 4.

Chapter 6 presents a speed-sensorless FS-PTC strategy for IM drive supplied from a 3L-NPC VSI. An EKF is introduced for rotor speed, rotor flux and stator current estimation; thus, the speed-sensor is avoided. The SPVs strategy is applied to the FS-PTC to reduce the calculation effort. A comparison between the SPVs- and RSFVC-based simplified FS-PTC strategies is presented, and selecting SPVs approach (between two proposed simplified approaches) for sensorless operation is justified. The experimental outcomes are illustrated and discussed to verify the effectiveness.

Finally, Chapter 7 gives the key achievements presented in the thesis and concludes with some future prospects.

Chapter 2

Modelling of the Induction Motor and Converters

2.1 Introduction

MPC requires an accurate mathematical model of the system. In addition, the model should be expressed in discrete form for digital implementation. This chapter describes the system's mathematical model. In this thesis, the system is comprised mainly of a three-phase IM with a speed encoder mounted on the rotor shaft, three-phase power converters and a DSP. In the PTC, the discrete mathematical model of the system is used to predict the desired control objectives.

This chapter is organised as follows. Section 2.2 gives the state-space representation of a three-phase system. Section 2.3 presents the mathematical model of the IM. The converter models are described in Section 2.4.

2.2 State-space representation of three-phase systems

State-space representation makes an AC circuit simple to represent and easy to understand and analyse. As mentioned earlier, this study considers a three-phase squirrel-cage IM. The IM is supplied from a three-phase AC source. It is well known that the three phases $(a-b-c)$ are located 120° apart in space, as shown in Fig. 2.1. They are linearly dependent on each other, which complicates the system model. To simplify the notation of three-phase electrical variables, such as voltage, current and flux, the variables can be modeled adequately using a two-axis reference frame. The two-axis representation of the three-phase system is called 'state-space representation'. This two-axis reference frame may be stationary ($\alpha-\beta$) or synchronous ($d-q$), as shown in Fig. 2.1. For the state-space representation, the components of a particular variable along $a-b-c$ coordinates are projected on $\alpha-\beta$ or $d-q$ coordinates. The two coordinates in each reference frame are mutually perpendicular to each other, and linearly independent. This independence makes it possible to control both the flux and torque of an AC machine independently, similar to a separately excited DC machine.

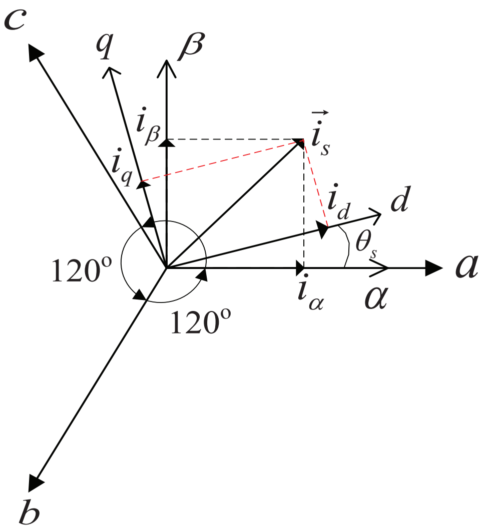

Figure 2.1: State-space two-axis representation of three-phase ($a-b-c$) systems showing the relationship between the stationary ($\alpha-\beta$) and synchronous ($d-q$) reference frames.

Using the current as an example, the transformation of the $a-b-c$ frame to an $\alpha-\beta$ frame—which is known as Clarke transformation—is expressed in matrix form as

$$\begin{bmatrix} i_\alpha \\ i_\beta \end{bmatrix} = \begin{bmatrix} \frac{2}{3} & \frac{-1}{3} & \frac{-1}{3} \\ 0 & \frac{\sqrt{3}}{3} & \frac{-\sqrt{3}}{3} \end{bmatrix} \begin{bmatrix} i_a \\ i_b \\ i_c \end{bmatrix}.$$

Sometimes it is necessary to transform the $\alpha-\beta$ frame into a $d-q$ frame, especially in vector control (i.e., FOC) design for motor drives. The transformation is called as Park transformation and can be expressed as

$$\begin{bmatrix} i_d \\ i_q \end{bmatrix} = \begin{bmatrix} cos(\theta_s) & sin(\theta_s) \\ -sin(\theta_s) & cos(\theta_s) \end{bmatrix} \begin{bmatrix} i_\alpha \\ i_\beta \end{bmatrix}$$

where θ_s is the angle between the $\alpha - \beta$ and $d - q$ reference frames, as shown in Fig. 2.1. Direct transformation from the $a - b - c$ frame to the $d - q$ frame (or vice versa) is also used for dynamic modelling of a three-phase system [107].

The current components of i_α and i_β are sinusoidal, as the current vector $\boldsymbol{i}_s$ rotates at a constant speed with respect to the $\alpha - \beta$ frame. In contrast, the i_d and i_q components are normally constant or piece-wise constant, and are thus linearised. The aforementioned two transformations are equally applicable for voltage and flux, and the transformations are reversible.

The state-space representation of the IM variables in both the $\alpha-\beta$ and $d-q$ reference frames is

stator voltage: $\boldsymbol{v}_s = v_{s\alpha} + jv_{s\beta}$, $\boldsymbol{v}_s = v_{sd} + jv_{sq}$;
rotor voltage: $\boldsymbol{v}_r = v_{r\alpha} + jv_{r\beta}$, $\boldsymbol{v}_r = v_{rd} + jv_{rq}$;
stator current: $\boldsymbol{i}_s = i_{s\alpha} + ji_{s\beta}$, $\boldsymbol{i}_s = i_{sd} + ji_{sq}$;
rotor current: $\boldsymbol{i}_r = i_{r\alpha} + ji_{r\beta}$, $\boldsymbol{i}_r = i_{rd} + ji_{rq}$;
stator flux: $\boldsymbol{\psi}_s = \psi_{s\alpha} + j\psi_{s\beta}$, $\boldsymbol{\psi}_s = \psi_{sd} + j\psi_{sq}$;
rotor flux: $\boldsymbol{\psi}_r = \psi_{r\alpha} + j\psi_{r\beta}$, $\boldsymbol{\psi}_r = \psi_{rd} + j\psi_{rq}$.

2.3 State-space model of the IM

The state-space model of a squirrel-cage IM in the $\alpha-\beta$ reference frame can be described by Eqs. (2.1)–(2.6):

$$\text{stator voltage equation: } \boldsymbol{v}_s = R_s\boldsymbol{i}_s + \frac{d\boldsymbol{\psi}_s}{dt} \tag{2.1}$$

$$\text{rotor voltage equation: } 0 = R_r\boldsymbol{i}_r + \frac{d\boldsymbol{\psi}_r}{dt} - j\omega_e\boldsymbol{\psi}_r \tag{2.2}$$

$$\text{stator flux equation: } \boldsymbol{\psi}_s = L_s\boldsymbol{i}_s + L_m\boldsymbol{i}_r \tag{2.3}$$

$$\text{rotor flux equation: } \boldsymbol{\psi}_r = L_m \boldsymbol{i}_s + L_r \boldsymbol{i}_r \tag{2.4}$$

$$\text{electromagnetic torque equation: } T_e = 1.5p\Im m\left\{\boldsymbol{\psi}_s^* \cdot \boldsymbol{i}_s\right\} \tag{2.5}$$

$$\text{torque balance equation: } J\frac{d\omega_m}{dt} = T_e - T_l \tag{2.6}$$

where $\boldsymbol{v}_s$ is the stator voltage vector, $\boldsymbol{i}_s$ is the stator current vector, $\boldsymbol{i}_r$ is the rotor current vector, $\boldsymbol{\psi}_s$ is the stator flux vector, $\boldsymbol{\psi}_r$ is the rotor flux vector, T_e is the electromagnetic torque, T_l is the load torque, ω_m is the rotor angular speed, ω_e is the rotor angular frequency, p is the number of pole pairs and the remaining parameters are the machine parameters.

The rotor angular frequency ω_e is related directly to the rotor angular speed ω_m by the number of pole pairs p as

$$\omega_e = p\omega_m. \tag{2.7}$$

The stator voltage Eq. (2.1) shows the relationship among the supplied voltage, stator ohmic drop and stator inductance drop. The inductance drop has two components: stator leakage-inductance drop and back EMF. At steady-state, the ohmic drop is negligible compared with the back EMF; thus, the stator flux is directly proportional to the supplied voltage. This assumption is generally used in the DTC strategy [8]. As the rotor of a squirrel-cage type is short circuited itself, the applied voltage at the rotor side is zero, as shown in Eq. (2.2). We can see that the induced rotor voltage is proportional to the slip (relative velocity between stator flux and rotor speed). Thus, in normal operations under a certain frequency, the induced rotor voltage is maximum at zero-speed (slip is equal to 1) and minimum at around synchronous speed (slip is close to 0). By replacing the variable $\boldsymbol{i}_r$ from Eq. (2.2) with the variables $\boldsymbol{\psi}_r$ and $\boldsymbol{i}_s$, the modified rotor voltage equation becomes

$$\frac{d\boldsymbol{\psi}_r}{dt} = R_r\frac{L_m}{L_r}\boldsymbol{i}_s - \left(\frac{R_r}{L_r} - j\omega_e\right)\boldsymbol{\psi}_r. \tag{2.8}$$

Equation (2.8) is called the rotor current model of the IM, in which $\boldsymbol{i}_s$ and $\boldsymbol{\psi}_r$ are considered as state variables. For a speed sensorless controller, ω_e is also treated as a state variable. Generally, the rotor current model is used to estimate the rotor flux. Using

Eqs. (2.3) and (2.4), a relationship is established between the stator and the rotor fluxes as

$$\hat{\boldsymbol{\psi}}_s = \frac{L_m}{L_r}\hat{\boldsymbol{\psi}}_r + \sigma L_s \boldsymbol{i}_s \tag{2.9}$$

where $\sigma = 1 - \frac{L_m^2}{L_s L_r}$ is the total leakage factor. Equation (2.9) is used to estimate the stator flux.

Some other parameters—not physical—are used frequently in machine modelling for compact expression. These are given in the following.

Rotor coupling factor: $k_r = \frac{L_m}{L_r}$

Equivalent resistance referred to stator: $R_\sigma = R_s + k_r^2 R_r$

Transient stator time constant: $\tau_\sigma = \frac{L_\sigma}{R_\sigma}$

Leakage inductance: $L_\sigma = \sigma L_s$

Rotor time constant: $\tau_r = \frac{L_r}{R_r}$

The electromagnetic torque developed by the motor is estimated using Eq. (2.5). The estimated torque quality is dependent directly on the stator current and stator flux and, thus on the measurement and estimation, respectively. In PTC, predictions of both the stator flux and stator current are required to predict the torque. Equation (2.1) is employed for stator flux prediction. The stator current is predicted using the equivalent equation of the stator and rotor dynamics of a cage type IM [108]; the expression in compact form is

$$\frac{d\boldsymbol{i}_s}{dt} = -\frac{1}{\tau_\sigma}\boldsymbol{i}_s + \frac{1}{\tau_\sigma R_\sigma}\left\{\left(\frac{k_r}{\tau_r} - jk_r\omega_e\right)\boldsymbol{\psi}_r + \boldsymbol{v}_s\right\}. \tag{2.10}$$

The torque balance in Eq. (2.6) is useful for designing a speed controller for motor drives. If the load torque T_l connected with the motor changes, the controller should compensate for any effects on speed. The motor will then spin at the command speed.

In this study, the continuous motor model, as shown in Eqs. (2.1)–(2.6) and (2.8)–(2.10), is discretised using forward-Euler or backward-Euler approximation, whichever is useful for a particular condition. The approximations are

$$\text{forward-Euler approximation: } \frac{dx}{dt} \approx \frac{x(k+1) - x(k)}{T_s} \tag{2.11}$$

$$\text{backward-Euler approximation: } \frac{dx}{dt} \approx \frac{x(k) - x(k-1)}{T_s} \tag{2.12}$$

where x is the state variable that needs to be discretized and T_s is the sampling time.

2.4 Converters models

In this work, two types of converters are considered to produce the necessary voltage vectors: 1) two-level (2L) and 2) 3L-NPC VSI.

2.4.1 Two-level inverter

The circuit topology of a 2L-VSI is shown in Fig. 2.2. The inverter produces two different levels of voltage, $+V_{dc}$ or $-V_{dc}$, at the output terminals, so called 2L-VSI. The required switching state variables S_x for each phase $x = \{a, b, c\}$ are either logic '1' or '0'. The two switching signals in each phase are complementary. Hence, only one switching signal is generated by the controller. Another switching signal is generated by using logic inversion and dead-time generator circuits. However, because of simplicity, dead-time compensation is not considered in this study. All possible switching states s are shown in Table 2.1. The switching states, in terms of vector for three phases, can be expressed as

$$\boldsymbol{S} = \frac{2}{3}(S_a + \boldsymbol{a}S_b + \boldsymbol{a}^2 S_c) \tag{2.13}$$

where $\boldsymbol{a} = e^{j\frac{2\pi}{3}}$.

A 2L-VSI produces eight voltage vectors corresponding to eight different state vectors at the output terminals, as shown in Fig 2.3. The voltage vectors generated by the inverter can be defined by

$$\boldsymbol{v} = \frac{2}{3}(v_a + \boldsymbol{a}v_b + \boldsymbol{a}^2 v_c) \tag{2.14}$$

where v_a, v_b and v_c are phase voltages.

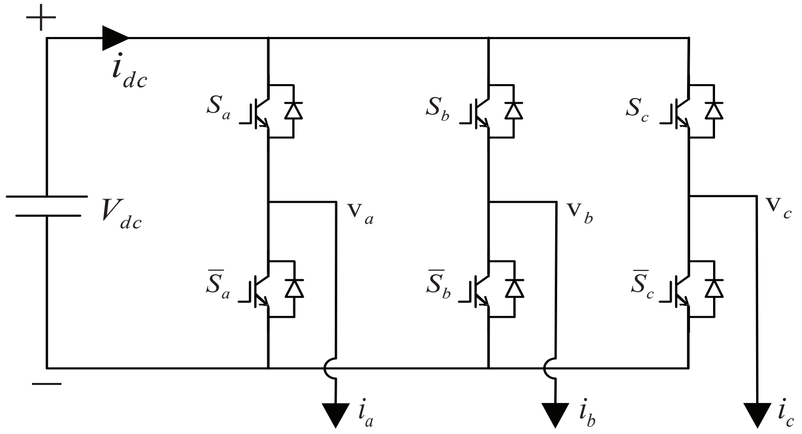

Figure 2.2: Circuit topology of a 2L-VSI showing positive convention for voltages and currents.

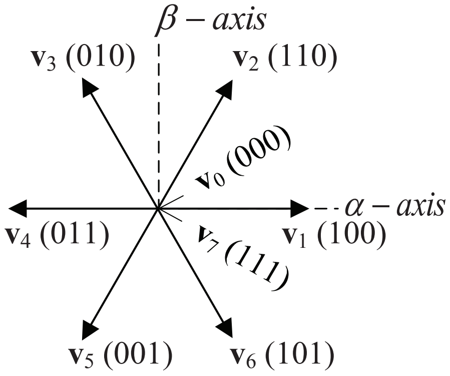

Figure 2.3: Space distribution of all admissible voltage vectors of the 2L-VSI.

The voltage vectors can also be expressed in terms of state vectors and the dc-link voltage as

$$\boldsymbol{v} = \boldsymbol{S}V_{dc}. \tag{2.15}$$

In this work, the inverter is considered as a nonlinear discrete system. The discrete nonlinear voltage vectors, as shown in Table 2.1, are the only control actions to drive the motor.

Table 2.1: Voltage vectors of the 2L-VSI

$\boldsymbol{v}_n$	$s = [s_a s_b s_c]$	$\boldsymbol{v} = v_\alpha + jv_\beta$
$\boldsymbol{v}_0$	0 0 0	0
$\boldsymbol{v}_1$	1 0 0	$2/3V_{dc}$
$\boldsymbol{v}_2$	1 1 0	$1/3V_{dc} + j\sqrt{3}/3V_{dc}$
$\boldsymbol{v}_3$	0 1 0	$-1/3V_{dc} + j\sqrt{3}/3V_{dc}$
$\boldsymbol{v}_4$	0 1 1	$-2/3V_{dc}$
$\boldsymbol{v}_5$	0 0 1	$-1/3V_{dc} - j\sqrt{3}/3V_{dc}$
$\boldsymbol{v}_6$	1 0 1	$1/3V_{dc} - j\sqrt{3}/3V_{dc}$
$\boldsymbol{v}_7$	1 1 1	0

2.4.2 3L-NPC inverter

The circuit topology of a 3L-NPC VSI is shown in Fig. 2.4. The inverter produces three different levels of voltage—$V_{dc}/2$, 0 and $-V_{dc}/2$—at the output terminals. These are based on the proper selection of switching signals applied to each semiconductor switches in phase $x = \{a, b, c\}$. For this reason, the inverter is called 3L-NPC VSI. The switching state variables $\{S_{x1}, S_{x2}\}$ with phase x may be either logic '0' or '1'. The lower two switching signals in each phase are complementary with the upper two switching signals. Thus, in practice, only the upper two switching signals for each phase are generated by the controller. Afterward, the other two switching signals in each phase are generated using logic inversion and deadtime generator circuits. The possible combinations of switching signals for each phase x are shown in Table 2.2. In each phase of the inverter, the output pole is connected to '+', '−' or '0', by turning on simultaneously the upper two switches, the lower two switches or the middle two switches, respectively. By connecting the output pole to '+', '−' or '0', the inverter generates $V_{dc}/2$, $-V_{dc}/2$ or 0, respectively, at the output terminals of the inverter phase. Including 19 different voltage vectors, the inverter can produce 27 voltage vectors, as shown in Fig. 2.5. Each of the voltage vectors is shown with the required levels of dc-link voltage, enclosed in a rectangular box, for the three phases. Based on their amplitudes, the voltage vectors are classified into four groups: zero vectors $\{\boldsymbol{v}_0 \cdots \boldsymbol{v}_2\}$, small vectors $\{\boldsymbol{v}_3 \cdots \boldsymbol{v}_{14}\}$, medium vectors $\{\boldsymbol{v}_{15} \cdots \boldsymbol{v}_{20}\}$ and large

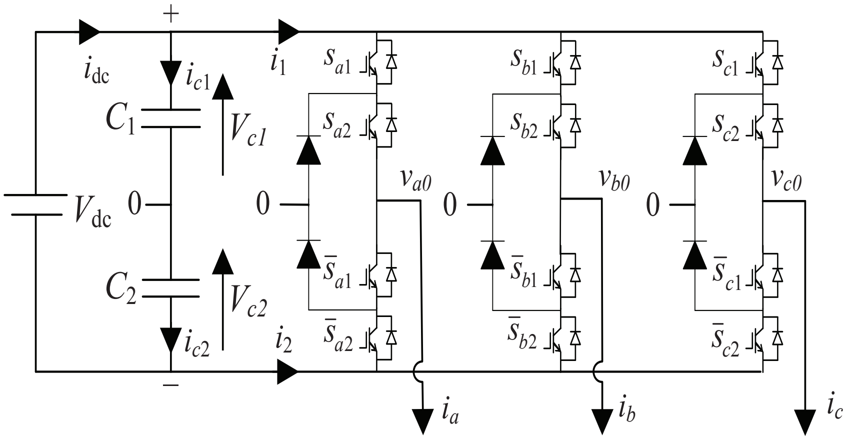

Figure 2.4: Schematic diagram of a 3L-NPC VSI showing positive convention for voltages and currents.

vectors $\{\boldsymbol{v}_{21} \cdots \boldsymbol{v}_{26}\}$. Complex representation of all possible voltage vectors with v_α and v_β components and the corresponding top two switching states of each phase are shown in Table 2.3. A nonlinear discrete model of the inverter [28] is used to produce these voltage vectors. The switching states with a similar colour and a similar phase position in the $\alpha - \beta$ plane in Fig. 2.5 produce similar voltage vectors in magnitude. However, they (the small vectors) have an opposite effect on the dc-link capacitor charge, which facilitates balancing the capacitor voltages.

Table 2.2: Possible switching combinations of each phase $x = \{a, b, c\}$

Switching states				Output
S_{x1}	S_{x2}	$\bar{S}_{x1}$	$\bar{S}_{x2}$	v_{x0}
1	1	0	0	$+V_{dc}/2$
0	1	1	0	0
0	0	1	1	$-V_{dc}/2$

Capacitor voltage unbalance in a 3L-NPC VSI occurs at the neutral-point '0', which is called as neutral-point voltage variation. As the neutral-point voltage variation is the difference between two capacitor voltages, it is simply known as the 'neutral-point voltage'. For motor drive applications, the neutral-point voltage increases torque and flux ripple, and distortion in the output stator current. Moreover, it imposes additional volt-

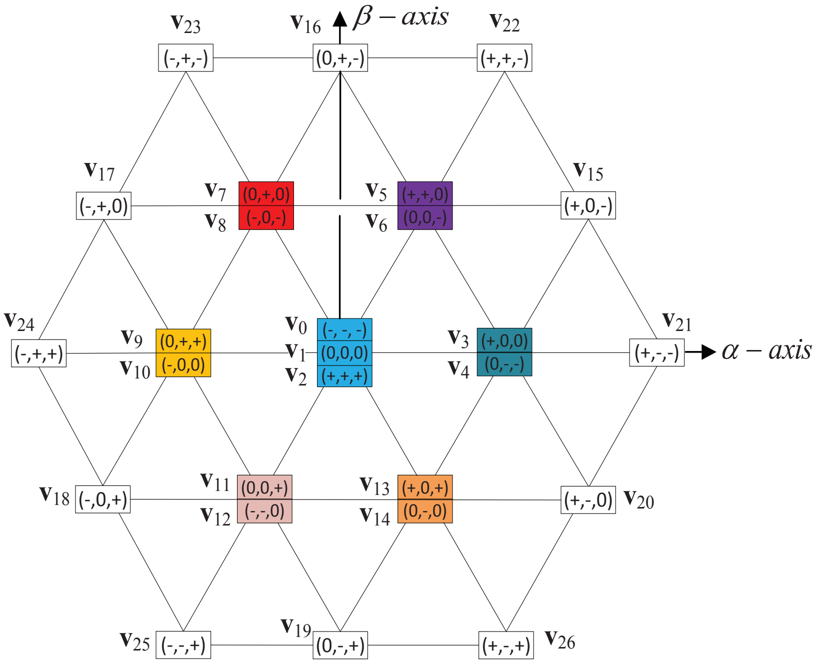

Figure 2.5: Admissible 27 voltage vectors of the 3L-NPC VSI showing the small vectors of equal magnitude (but an opposite effect on the dc-link capacitor charge) with a similar colour.

age stress on the semiconductor switches. Hence, the neutral-point voltage is controlled online using dynamic model of the capacitor. The discrete dynamic equations of two capacitor voltages are expressed as

$$V_{c1}(k+1) = V_{c1}(k) + \frac{1}{C} i_{c1}(k) T_s \tag{2.16}$$

$$V_{c2}(k+1) = V_{c2}(k) + \frac{1}{C} i_{c2}(k) T_s \tag{2.17}$$

where $V_{c1}(k)$ and $V_{c2}(k)$ are the two measured capacitor voltages, C is the capacitance of each capacitor, $i_{c1}(k)$ and $i_{c2}(k)$ are the currents flowing through the capacitors and T_s is the sampling time. The currents $i_{c1}(k)$ and $i_{c2}(k)$ are calculated based on only the upper two switching states $\{S_{x1}, S_{x2}\}$ in each phase $x = \{a, b, c\}$ of the inverter. The calculations are as follows:

$$i_{c1}(k) = i_{dc} - S_{a1}(k) i_a(k) - S_{b1}(k) i_b(k) - S_{c1}(k) i_c(k) \tag{2.18}$$

$$i_{c2}(k) = i_{dc} + \Bigg(1 - S_{a2}(k)\Bigg) i_a(k) + \Bigg(1 - S_{b2}(k)\Bigg) i_b(k) + \Bigg(1 - S_{c2}(k)\Bigg) i_c(k) \qquad (2.19)$$

where i_{dc} is the dc-link current supplied by the dc source.

Equations (2.16)–(2.19) show that the capacitor voltages—$V_{c1}(k+1)$ and $V_{c2}(k+1)$—and thus the neutral-point voltage at instant $k+1$ can be calculated using the present measured load currents, measured capacitor voltages and applied switching state. In this study, we have not needed to calculate dc-link current i_{dc}. This is because we only need the difference between two capacitor voltages. Since, i_{dc} is the common term in Eqs. (2.18) and (2.19), it will be cancelled automatically.

Table 2.3: Complex representation of all possible voltage vectors of the 3L-NPC VSI showing corresponding the upper two switching states s of each phase

$\boldsymbol{v}_n$	$s = [s_{a1}s_{a2}s_{b1}s_{b2}s_{c1}s_{c2}]$	$\boldsymbol{v} = v_\alpha + jv_\beta$
$\boldsymbol{v}_0$	0 0 0 0 0 0	0
$\boldsymbol{v}_1$	0 1 0 1 0 1	0
$\boldsymbol{v}_2$	1 1 1 1 1 1	0
$\boldsymbol{v}_3$	1 1 0 1 0 1	$1/3V_{dc}$
$\boldsymbol{v}_4$	0 1 0 0 0 0	$1/3V_{dc}$
$\boldsymbol{v}_5$	1 1 1 1 0 1	$1/6V_{dc} + j\sqrt{3}/6V_{dc}$
$\boldsymbol{v}_6$	0 1 0 1 0 0	$1/6V_{dc} + j\sqrt{3}/6V_{dc}$
$\boldsymbol{v}_7$	0 1 1 1 0 1	$-1/6V_{dc} + j\sqrt{3}/6V_{dc}$
$\boldsymbol{v}_8$	0 0 0 1 0 0	$-1/6V_{dc} + j\sqrt{3}/6V_{dc}$
$\boldsymbol{v}_9$	0 1 1 1 1 1	$-1/3V_{dc}$
$\boldsymbol{v}_{10}$	0 0 0 1 0 1	$-1/3V_{dc}$
$\boldsymbol{v}_{11}$	0 1 0 1 1 1	$-1/6V_{dc} - j\sqrt{3}/6V_{dc}$
$\boldsymbol{v}_{12}$	0 0 0 0 0 1	$-1/6V_{dc} - j\sqrt{3}/6V_{dc}$
$\boldsymbol{v}_{13}$	1 1 0 1 1 1	$1/6V_{dc} - j\sqrt{3}/6V_{dc}$
$\boldsymbol{v}_{14}$	0 1 0 0 0 1	$1/6V_{dc} - j\sqrt{3}/6V_{dc}$
$\boldsymbol{v}_{15}$	1 1 0 1 0 0	$1/2V_{dc} + j\sqrt{3}/6V_{dc}$
$\boldsymbol{v}_{16}$	0 1 1 1 0 0	$j1/\sqrt{3}V_{dc}$
$\boldsymbol{v}_{17}$	0 0 1 1 0 1	$-1/2V_{dc} + j\sqrt{3}/6V_{dc}$
$\boldsymbol{v}_{18}$	0 0 0 1 1 1	$-1/2V_{dc} - j\sqrt{3}/6V_{dc}$
$\boldsymbol{v}_{19}$	0 1 0 0 1 1	$-j1/\sqrt{3}V_{dc}$
$\boldsymbol{v}_{20}$	1 1 0 0 0 1	$1/2V_{dc} - j\sqrt{3}/6V_{dc}$
$\boldsymbol{v}_{21}$	1 1 0 0 0 0	$2/3V_{dc}$
$\boldsymbol{v}_{22}$	1 1 1 1 0 0	$1/3V_{dc} + j\sqrt{3}/3V_{dc}$
$\boldsymbol{v}_{23}$	0 0 1 1 0 0	$-1/3V_{dc} + j\sqrt{3}/3V_{dc}$
$\boldsymbol{v}_{24}$	0 0 1 1 1 1	$-2/3V_{dc}$
$\boldsymbol{v}_{25}$	0 0 0 0 1 1	$-1/3V_{dc} - j\sqrt{3}/3V_{dc}$
$\boldsymbol{v}_{26}$	1 1 0 0 1 1	$1/3V_{dc} - j\sqrt{3}/3V_{dc}$

2.5 Summary

This chapter has presented a state-space dynamic model of the IM in the stationary reference frame and the discrete mathematical models of both the 2L-VSI and 3L-NPC VSI. The chapter has discussed the relationships among different variables in the IM. It has also explained how the IM model and the nonlinear discrete inverter models may be considered in the predictive controller. Finally, a mathematical model is presented to control the neutral-point voltage inherited from the 3L-NPC topology.

Chapter 3

A Simplified FS-PTC for Two-Level Inverter Fed IM Drive

3.1 Introduction

This chapter presents a simplified FS-PTC based on SPVs to reduce the number of prediction vectors and hence the computational burden. The prediction vectors are defined as the number of voltage vectors required for predictions of the desired control objectives, such as torque and flux. The position of stator flux and the sign of torque-error have been considered to lessen the number of prediction vectors. Two adjacent forward/backward voltage vectors with an appropriate zero vector are always selected as the prediction vectors; thus, the average switching frequency of the power converter is reduced when compared to a conventional FS-PTC strategy. Including the frequency term in the cost function is not required; this would yield a simpler design of the cost function compared to conventional FS-PTC. To make a comparison with the existing all voltage vectors based FS-PTC scheme, a 2L-VSI is employed to produce the necessary voltage vectors.

This chapter addresses the first objective of the thesis, and part of the contribution is published in [109, 110]. The chapter is organised as follows. Section 3.2 describes the conventional FS-PTC step-by-step, and highlights some of its limitations. The proposed SPVs-based simplified FS-PTC is described in Section 3.3. The computational efficiency improvement in the proposed strategy is discussed in Section 3.4. Section 3.5 illustrates the experimental outcomes.

3.2 Conventional FS-PTC and its limitations

A conventional FS-PTC model comprises two steps: prediction and cost function optimisation, as shown in Fig. 3.1. However, the prediction requires a preliminary estimation step. Some variables unavailable for measurement are estimated in the estimation step. The performance and required computational burden of the model are analysed for a 2L-VSI.

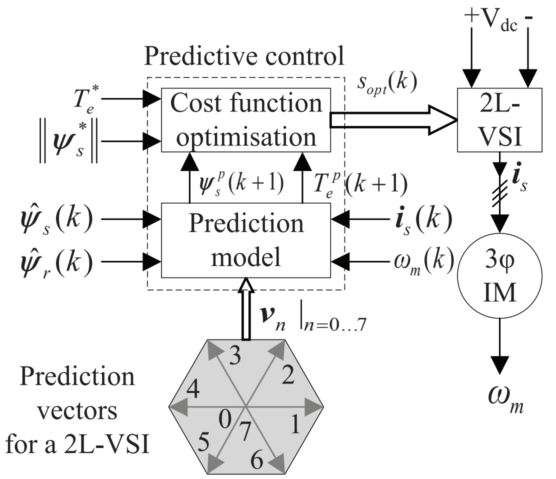

Figure 3.1: Conventional FS-PTC scheme for the 2L-VSI fed IM drive, where all possible voltage vectors are used as prediction vectors.

3.2.1 Estimation

In an FS-PTC system, estimations of stator flux $\hat{\boldsymbol{\psi}}_s$ and rotor flux $\hat{\boldsymbol{\psi}}_r$ are required based on the present measurements of stator current $\boldsymbol{i}_s$ and rotor speed ω_m. Conventionally, the rotor current model of the IM shown in Eq. (2.8) is employed to estimate the rotor flux. Then, the simple relationship between the stator and rotor flux is used to estimate the stator flux. The execution frequency of the estimator is the same as that of the controller. Using the standard backward-Euler approximation, the estimations of rotor and stator flux in discrete form can be expressed as

$$\hat{\boldsymbol{\psi}}_r(k) = \hat{\boldsymbol{\psi}}_r(k-1) + T_s\left[R_r\frac{L_m}{L_r}\boldsymbol{i}_s(k) - \left(\frac{R_r}{L_r} - j\omega_e(k)\right)\hat{\boldsymbol{\psi}}_r(k-1)\right] \tag{3.1}$$

$$\hat{\boldsymbol{\psi}}_s(k) = \frac{L_m}{L_r}\hat{\boldsymbol{\psi}}_r(k) + \sigma L_s\boldsymbol{i}_s(k). \tag{3.2}$$

The estimated electromagnetic torque can then be obtained as

$$\hat{T}_e(k) = 1.5p\Im m\left\{\hat{\boldsymbol{\psi}}_s(k)^* \cdot \boldsymbol{i}_s(k)\right\}. \tag{3.3}$$

3.2.2 Prediction

The first step of predictive control is performed by predicting the stator flux and torque. The selection of variables to be predicted is dependent on the desired objectives. More numbers of variables mean that the controller requires more calculations. Conventionally, all possible voltage vectors $\{\boldsymbol{v}_0 \cdots \boldsymbol{v}_7\}$ are evaluated to predict the desired objectives. The stator voltage model of the IM is generally used for stator flux prediction. Using the forward-Euler approximation, the voltage model in discrete time steps can be expressed as

$$\boldsymbol{\psi}_s^p(k+1) = \hat{\boldsymbol{\psi}}_s(k) + T_s\boldsymbol{v}_s(k) - T_sR_s\boldsymbol{i}_s(k). \tag{3.4}$$

In order to predict the electromagnetic torque, the stator current is also predicted. Hence, the predictions of the stator current discretising Eq. (2.10) and then the torque can be expressed as

$$\boldsymbol{i}_s^p(k+1) = \left(1 - \frac{T_s}{\tau_\sigma}\right)\boldsymbol{i}_s(k) + \frac{T_s}{(\tau_\sigma + T_s)}\left\{\frac{1}{R_\sigma}\left[\left(\frac{k_r}{\tau_r} - jk_r\omega_e(k)\right)\hat{\boldsymbol{\psi}}_r(k) + \boldsymbol{v}_s(k)\right]\right\} \tag{3.5}$$

$$T_e^p(k+1) = 1.5p\Im m\left\{\boldsymbol{\psi}_s^p(k+1)^* \cdot \boldsymbol{i}_s^p(k+1)\right\} \tag{3.6}$$

3.2.3 Cost function optimisation

The predicted variables are evaluated by a predefined cost function. Generally in FS-PTC, the cost function includes absolute values of torque-error ($T_e^* - T_e^p$) and flux-error

$(|\boldsymbol{\psi}_s^*| - |\boldsymbol{\psi}_s^p|)$. Hence, the cost function can be defined as

$$g = \left| T_e^*(k+1) - T_e^p(k+1) \right| + \lambda_f \left| |\boldsymbol{\psi}_s^*| - |\boldsymbol{\psi}_s^p(k+1)| \right| \tag{3.7}$$

where $T_e^*(k+1)$ is the reference torque and $T_e^p(k+1)$ is the predicted torque, $\boldsymbol{\psi}_s^*$ is the reference stator flux (which is always kept constant if field-weakening is not considered) and $\boldsymbol{\psi}_s^p(k+1)$ is the predicted stator flux; k and $k+1$ are the present and next sampling instant. In this study, the weighting factor λ_f sets the relative importance of the stator flux compared with the torque. Since the sampling time is very small, it is a common practice to assume $T_e^*(k)$ as $T_e^*(k+1)$ [46].

For average switching frequency reduction, a switching transition term n_{sw} is included in the cost function and can be defined as [28]

$$n_{sw}(k+1) = \sum_{x=\{a,b,c\}} |s_x(k+1)_i - s_x(k)| \tag{3.8}$$

where $s_x(k+1)$ is the probable switching state for the next time instant $k+1$, $s_x(k)$ is the applied switching state to the inverter at the time instant k and i is the index of possible voltage vectors $\{\boldsymbol{v}_0 \cdots \boldsymbol{v}_7\}$. Using the total number of switching transitions $n_{sw}(T)$ over the duration T, the average switching frequency $\bar{f}_{sw}$ per semiconductor switch is calculated by $\bar{f}_{sw} = n_{sw}(T)/12/T$. In the later part of this chapter, the conventional FS-PTC with switching transition term in the cost function is defined as FS-PTC($\bar{f}_{sw}$).

In order to protect from over-current, the cost function g must include another term I_m which is designed based on the maximum current capacity of the stator winding. Therefore, the term I_m can be defined as

$$I_m = \begin{cases} \infty, & \text{if } |\boldsymbol{i}_s^p(k+1)| > I_{max} \\ 0, & \text{otherwise.} \end{cases} \tag{3.9}$$

Thus, the complete cost function g for the controller is

$$g = \left| T_e^*(k+1) - T_e^p(k+1) \right| + \lambda_f \left| |\boldsymbol{\psi}_s^*| - |\boldsymbol{\psi}_s^p(k+1)| \right| + \lambda_n n_{sw}(k+1) + I_m \tag{3.10}$$

where λ_n is the weighting factor of n_{sw}. The fourth term I_m does not need a weighting factor. Under normal operating condition, the value of I_m is 0 and thus it has no effect on

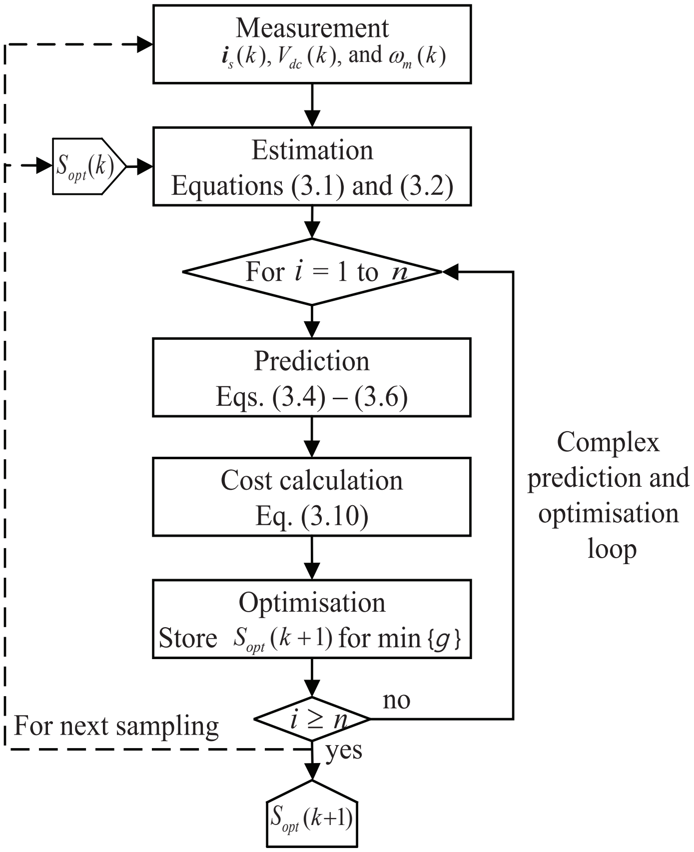

Figure 3.2: Conventional FS-PTC algorithm showing the complex prediction and optimisation loop.

g. During experiment, the value of I_{max} is set to 130% rated current. Hence, current ripple will not lead instability. Selecting proper weighting factors for the other three different objectives is a difficult task. The desired system performance may not be achieved due to improper selection of the weighting factors.

The switching state that yields minimum g in Eq. (3.10) is stored as an optimal switching state $S_{opt}(k+1)$, which is used as $S_{opt}(k)$ in the next sampling instant. The switching state $S_{opt}(k)$ produces voltage vector $\boldsymbol{v}_{opt}(k)$ which is applied to the motor terminals at instant k. The algorithm of the conventional FS-PTC is shown in Fig. 3.2. A complex loop of prediction and optimisation is apparent; this must be executed for all possible voltage vectors from a power converter.

3.2.4 Limitations of the conventional FS-PTC

The drawbacks of the conventional FS-PTC can be summarised as follows:

1) All voltage vectors are evaluated for prediction and optimisation, which is computationally expensive. The computational burden limits the sampling frequency and, thus, degrades control performance.

2) When a switching transition term is included in the cost function to reduce the average switching frequency, the computational burden is increased further. Moreover, selecting weighting factors for three different control objectives is difficult and, thus, designing a cost function is complex.

3.3 Proposed FS-PTC using SPVs

The structure of the proposed FS-PTC is similar to the conventional FS-PTC, as shown in Fig. 3.3. The main differences are the selection of prediction vectors $\boldsymbol{v}_j$ and the design of cost function, where j may be three values among $n = \{0 \cdots 7\}$. Conventionally, all voltage vectors of a 2L-VSI are employed for prediction and optimisation. In the proposed FS-PTC, only three—one zero and two active vectors—of the possible eight voltage vectors are evaluated. Thus, the computational burden is reduced.

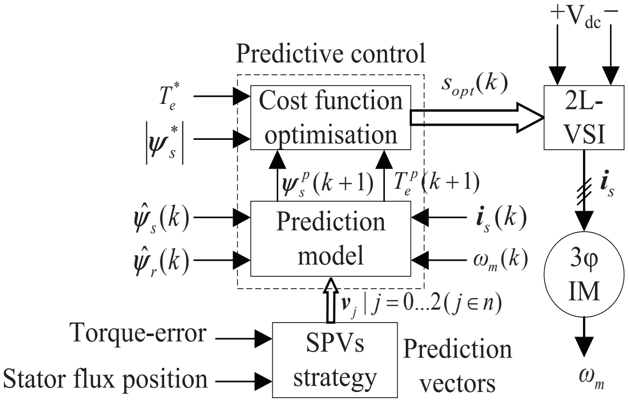

Figure 3.3: Proposed FS-PTC using SPVs strategy.

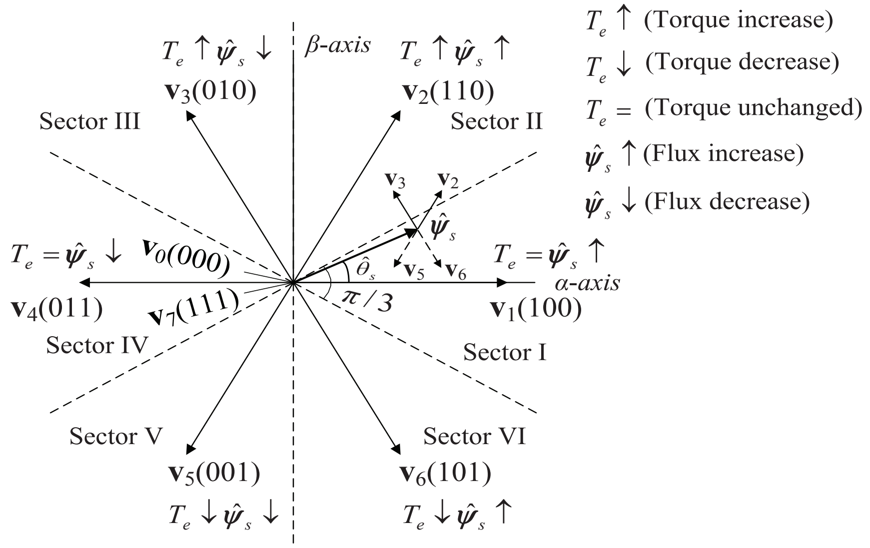

Figure 3.4: Space distribution of all admissible voltage vectors of a 2L-VSI showing the selection strategy of the prediction vectors.

3.3.1 Selecting prediction vectors

The selection process of prediction vectors is proposed based on the DTC strategy [8]. The prediction vectors are selected using the present position of the stator flux $\hat{\boldsymbol{\psi}}_s$ and the sign of torque-error $\delta T_e = (T_e^* - \hat{T}_e)$. The position of stator flux $\hat{\theta}_s$ is estimated as

$$\hat{\theta}_s = \arctan\left(\frac{\hat{\psi}_{\beta s}}{\hat{\psi}_{\alpha s}}\right). \tag{3.11}$$

We may recall that a 2L-VSI produces six active vectors $\{\boldsymbol{v}_1, \cdots, \boldsymbol{v}_6\}$ and two zero vectors $\{\boldsymbol{v}_0, \boldsymbol{v}_7\}$. In this study, only $\boldsymbol{v}_0$ is considered as the zero vector in the prediction and optimisation steps, to reduce the computational burden. This assumption is valid as no switching frequency term is included in the cost function, and the effects of $\boldsymbol{v}_0$ and $\boldsymbol{v}_7$ on torque and flux are similar. After optimisation, if the stored optimal voltage vector is a zero vector, then an appropriate zero vector (either $\boldsymbol{v}_0$ or $\boldsymbol{v}_7$) is selected so that one switching transition occurs. The number of switching transitions is calculated using the applied optimal switching state at time instant k. The space distribution of all voltage vectors in the $\alpha - \beta$ plane, showing the selection strategy of the prediction vectors, is shown in Fig. 3.4. Here, it is apparent that the active voltage vectors change periodically by an angle of $\pi/3$ rad steps. Accordingly, the $\alpha - \beta$ plane is divided into six sectors to identify the direction of rotation as

$$(2N-3)\,\pi/6 \leq \Theta\,(N) \leq (2N-1)\,\pi/6 \tag{3.12}$$

where $\Theta(N)$ is the sector with $N = 1, \cdots, 6$.

Let us consider that the stator flux $\hat{\boldsymbol{\psi}}_s$ is rotating in the counterclockwise direction. At a particular instant, different voltage vectors influence the torque and flux differently, and the possible conditions of torque deviation are $\delta T_e > 0$, $\delta T_e < 0$ and $\delta T_e = 0$, and flux deviation are $\delta\psi_s > 0$, $\delta\psi_s < 0$ and $\delta\psi_s = 0$, where $\delta\psi_s = \left(|\boldsymbol{\psi}_s^*| - \left|\hat{\boldsymbol{\psi}}_s\right|\right)$. In Fig. 3.4, the effects of all active vectors in terms of increase, decrease, or unchanged torque and flux are indicated by the symbols '↑', '↓' and '=', respectively, when the stator flux is located in sector I. These effects on torque and flux are analysed to determine the sign of torque- or flux-error. If $\hat{\boldsymbol{\psi}}_s$ is located in sector I and the torque-error $\delta T_e > 0$, then the voltage vectors that satisfy torque increase ($T_e \uparrow$) condition (as shown in Fig. 3.4) are selected as prediction vectors. Hence, the possible active prediction vectors are two adjacent forward vectors $\boldsymbol{v}_2(1\,1\,0)$ and $\boldsymbol{v}_3(0\,1\,0)$, which are represented by solid arrows on the tip of the stator flux $\hat{\boldsymbol{\psi}}_s$, as shown in Fig. 3.4. Selecting the two adjacent forward voltage vectors also ensures the possible condition of stator flux deviation $\delta\psi_s > 0$ or $\delta\psi_s < 0$. Similarly, for the same position of stator flux, if $\delta T_e < 0$, the possible active prediction vectors are two adjacent backward vectors $\boldsymbol{v}_6(1\,0\,1)$ and $\boldsymbol{v}_5(0\,0\,1)$. These are represented by dashed arrows on the tip of the stator flux $\hat{\boldsymbol{\psi}}_s$ in Fig. 3.4. Generally, the active vectors are always employed with a zero vector for the IM to reduce the torque and flux ripple effectively. Including a zero vector satisfies the possible conditions of $\delta T_e = 0$ and $\delta\psi_s = 0$. From Fig. 3.4, we can see that the active vectors $\boldsymbol{v}_1(1\,0\,0)$ or $\boldsymbol{v}_4(0\,1\,1)$ might also satisfy the condition $\delta T_e = 0$. However, applying a zero vector is more effective than the active vectors when $\delta T_e = 0$. This is because the stator flux speed should be controlled so it is as slow as possible. Hence, the total number of prediction vectors is three, whereas it is seven (considering one zero vector) in the conventional FS-PTC. A similar analysis is carried out when the stator flux is located in the other sectors. The selected active prediction vectors for all the sectors are shown in Table 3.1.

It is obvious that if $\hat{\theta}_s(k-1)$ and $\hat{\theta}_s(k)$ lie in the same sector and the signs of $\delta T_e(k-1)$ and $\delta T_e(k)$ are same, then maximum one switching transition is possible between two

Table 3.1: Stator flux position $\hat{\theta}_s(k)$ and torque-error δT_e dependent active prediction vectors

Θ δT_e	I	II	III	IV	V	VI
$\delta T_e > 0$	$\boldsymbol{v}_2$,$\boldsymbol{v}_3$	$\boldsymbol{v}_3$,$\boldsymbol{v}_4$	$\boldsymbol{v}_4$,$\boldsymbol{v}_5$	$\boldsymbol{v}_5$,$\boldsymbol{v}_6$	$\boldsymbol{v}_6$,$\boldsymbol{v}_1$	$\boldsymbol{v}_1$,$\boldsymbol{v}_2$
$\delta T_e < 0$	$\boldsymbol{v}_5$,$\boldsymbol{v}_6$	$\boldsymbol{v}_6$,$\boldsymbol{v}_1$	$\boldsymbol{v}_1$,$\boldsymbol{v}_2$	$\boldsymbol{v}_2$,$\boldsymbol{v}_3$	$\boldsymbol{v}_3$,$\boldsymbol{v}_4$	$\boldsymbol{v}_4$,$\boldsymbol{v}_5$

active vectors, due to the SPVs. Hence, the proposed SPVs strategy also reduces the average switching frequency of the power converter.

It is apparent from Fig. 3.4 that another switching table based on $\hat{\theta}_s$ (see Eq. 3.11) and flux-error $\delta\psi_s$ instead of torque-error δT_e can be developed. The possible active prediction vectors based on $\delta\psi_s$ for all sectors are shown in Table 3.2. However, a relatively lower priority on the stator flux in the cost function must be set compared with the δT_e-based prediction vectors to achieve satisfactory torque and flux performance. This is because the stator flux gets priority over the torque when $\delta\psi_s$-based prediction vectors (see Table 3.2) are considered. Performance in terms of computational burden, torque ripple and flux ripple will be almost similar. However, δT_e-based prediction vectors are considered in this case.

Table 3.2: Stator flux position $\hat{\theta}_s(k)$ and stator-flux-error $\delta\psi_s$ dependent active prediction vectors

Θ $\delta\psi_s$	I	II	III	IV	V	VI
$\delta\psi_s > 0$	$\boldsymbol{v}_6$,$\boldsymbol{v}_2$	$\boldsymbol{v}_1$,$\boldsymbol{v}_3$	$\boldsymbol{v}_2$,$\boldsymbol{v}_4$	$\boldsymbol{v}_3$,$\boldsymbol{v}_5$	$\boldsymbol{v}_4$,$\boldsymbol{v}_6$	$\boldsymbol{v}_1$,$\boldsymbol{v}_5$
$\delta\psi_s < 0$	$\boldsymbol{v}_3$,$\boldsymbol{v}_5$	$\boldsymbol{v}_4$,$\boldsymbol{v}_6$	$\boldsymbol{v}_1$,$\boldsymbol{v}_5$	$\boldsymbol{v}_6$,$\boldsymbol{v}_2$	$\boldsymbol{v}_1$,$\boldsymbol{v}_3$	$\boldsymbol{v}_2$,$\boldsymbol{v}_4$

3.3.2 Optimum voltage vector selection

Since two adjacent voltage vectors are selected for the prediction and optimisation, only one switching transition occurs at a particular time instant under a certain condition, as mentioned previously. Hence, the average switching frequency is reduced, and inclusion of the switching frequency term in the cost function is not required. This also reduces the computational burden of the proposed control strategy. The cost function used in the proposed simplified FS-PTC is as follows:

$$g = \Big| T_e^*(k+1) - T_e^p(k+1) \Big| + \lambda_f \Big| |\boldsymbol{\psi}_s^*| - |\boldsymbol{\psi}_s^p(k+1)| \Big| + I_m. \tag{3.13}$$

It is obvious that selecting the weighting factors in Eq. (3.13) is simpler compared to Eq. (3.10) used in the conventional FS-PTC.

In a real-time implementation, the control algorithm calculation time introduces one-step time delay that must be compensated [111]. This is done by two steps ahead prediction. The predicted stator flux $\boldsymbol{\psi}_s^p(k+1)$ and stator current $\boldsymbol{i}_s^p(k+1)$ are used as the initial states for predictions at time instant $k+2$. To predict $\boldsymbol{\psi}_s^p(k+1)$ and $\boldsymbol{i}_s^p(k+1)$, the optimum voltage vector $\boldsymbol{v}_{opt}(k)$ applied to the motor terminals at the instant k is employed in Eqs. (3.4) and (3.5), respectively. In this case, for selecting the prediction vectors, $\boldsymbol{\psi}_s^p(k+1)$ instead of $\hat{\boldsymbol{\psi}}_s(k)$ and $T_e^p(k+1)$ instead of $\hat{T}_e(k)$ are used to calculate $\hat{\theta}_s$ and δT_e, respectively. The predictions of the stator flux and torque at instant $k+2$ can be expressed as

$$\boldsymbol{\psi}_s^p(k+2) = \hat{\boldsymbol{\psi}}_s(k+1) + T_s \boldsymbol{v}_{opt}(k) - T_s R_s \boldsymbol{i}_s(k+1) \tag{3.14}$$

$$\begin{aligned} \boldsymbol{i}_s^p(k+2) = &\left(1 - \frac{T_s}{\tau_\sigma}\right) \boldsymbol{i}_s(k+1) + \frac{T_s}{(\tau_\sigma + T_s)} \times \\ &\left\{ \frac{1}{R_\sigma} \left[\left(\frac{k_r}{\tau_r} - jk_r\omega_e(k+1) \right) \hat{\boldsymbol{\psi}}_r(k+1) + \boldsymbol{v}_{opt}(k) \right] \right\} \end{aligned} \tag{3.15}$$

$$T_e^p(k+2) = 1.5p\Im m \left\{ \boldsymbol{\psi}_s^p(k+2)^* \cdot \boldsymbol{i}_s^p(k+2) \right\}. \tag{3.16}$$

As the rotor time constant τ_r is much greater than the sampling time T_s and the rotor flux changes slowly compared to the stator flux, it is a general practice to assume $\omega_e(k) = \omega_e(k+1)$ and $\hat{\boldsymbol{\psi}}_r(k) = \hat{\boldsymbol{\psi}}_r(k+1)$, respectively.

Hence, to implement the delay compensation scheme [111], the optimum voltage vector is selected by minimising the following cost function:

$$g = \Big| T_e^*(k+2) - T_e^p(k+2) \Big| + \lambda_f \Big| |\boldsymbol{\psi}_s^*| - |\boldsymbol{\psi}_s^p(k+2)| \Big| + I_m. \tag{3.17}$$

3.3.3 Average switching frequency reduction

The selection of only one zero vector, either $\boldsymbol{v}_0$ or $\boldsymbol{v}_7$, with two active vectors for the prediction and optimisation may increase the average switching frequency. For this reason, if $\boldsymbol{v}_0$ is selected as the optimum voltage vector, an appropriate zero vector, either $\boldsymbol{v}_0$ or $\boldsymbol{v}_7$, is selected in such a way that only one switching transition occurs at a particular time instant. For example, if the applied voltage vector at the time instant k is $\boldsymbol{v}_2(110)$ and the optimum voltage vector actuated for the next time instant $k+1$ is $\boldsymbol{v}_0$, then the switching state '111' is selected instead of '000' as the optimal switching state. Therefore, the state '000' is selected after '100', '010' and '001'; otherwise, '111' is selected as the zero vector.

3.3.4 Overall control structure

The complete schematic of the proposed simplified FS-PTC is shown in Fig. 3.5, which includes four parts: 1) rotor and stator flux estimation; 2) prediction vectors selection; 3) stator flux and torque prediction; and 4) cost function optimisation (optimum voltage vector selection). The rotor speed is measured using an encoder mounted on the motor shaft. A PI controller is employed to produce the reference torque, based on the speed error. The speed error is calculated by comparing the measured speed with the reference speed. The constant rated stator flux reference is commanded from outside the controller, as field-weakening is not considered in the present analysis. Both the aforementioned reference quantities (torque and flux) are used directly in the cost function to actuate the optimum switching state S_{opt} which produces optimum voltage vector.

3.3.5 Proposed control algorithm

The overall control procedure can be summarised by the following sequences.

Step 1) *Measurement*: Sampling $\boldsymbol{i}_s(k)$, $V_{dc}(k)$ and $\omega_m(k)$.

Step 2) *Apply*: Apply the optimum voltage vector $\boldsymbol{v}_{opt}(k)$ to the motor terminals.

Step 3) *Estimate*: Estimate the rotor flux $\hat{\boldsymbol{\psi}}_r(k)$ and the stator flux $\hat{\boldsymbol{\psi}}_s(k)$ using Eqs. (3.1) and (3.2), respectively.

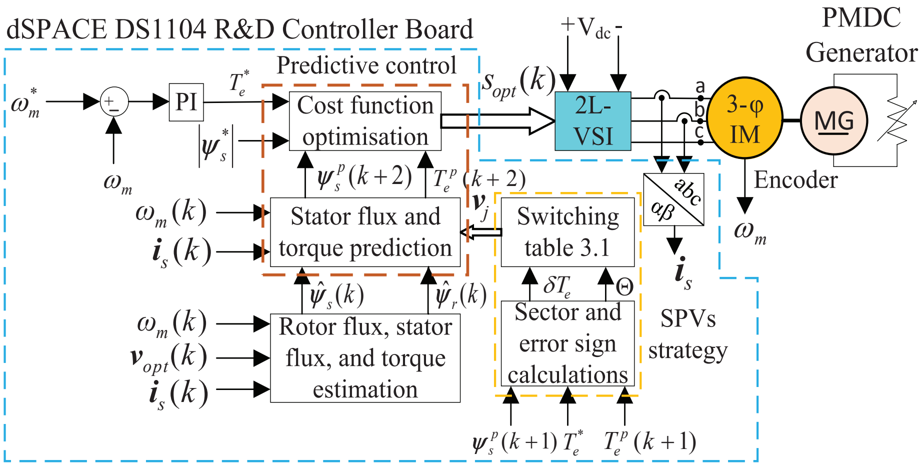

Figure 3.5: Proposed simplified FS-PTC system using torque-error-based SPVs.

Step 4) *Predict*: Predict the stator flux $\boldsymbol{\psi}_s^p(k+1)$, stator current $\boldsymbol{i}_s^p(k+1)$ and torque $T_e^p(k+1)$ using Eqs. (3.4)–(3.6).

Step 5) *Select prediction vectors*: Select the active prediction vectors using Table 3.1.

Step 6) *Predict and calculate cost*: Predict the stator flux $\boldsymbol{\psi}_s^p(k+2)$, stator current $\boldsymbol{i}_s^p(k+2)$ and torque $T_e^p(k+2)$ using Eqs. (3.14)–(3.16). Then, evaluate the predicted stator flux and torque by calculating the cost using the cost function (3.17). Execute these predictions and cost calculation loop for the selected two active vectors and one zero vector.

Step 7) *Optimise*: Select $\boldsymbol{v}_{opt}(k+2)$ which results minimum g in Eq. (3.17) and replace it with an appropriate zero vector if selected $\boldsymbol{v}_{opt}(k+2)$ is a zero vector. Return to step 1).

3.4 Computational efficiency improvement in the proposed FS-PTC algorithm

The proposed control algorithm is implemented using a dSPACE DS1104 R&D controller board with ControlDesk and MATLAB Simulink software packages. The execution time is measured with the dSPACE profiler [112]. The execution time of the proposed control

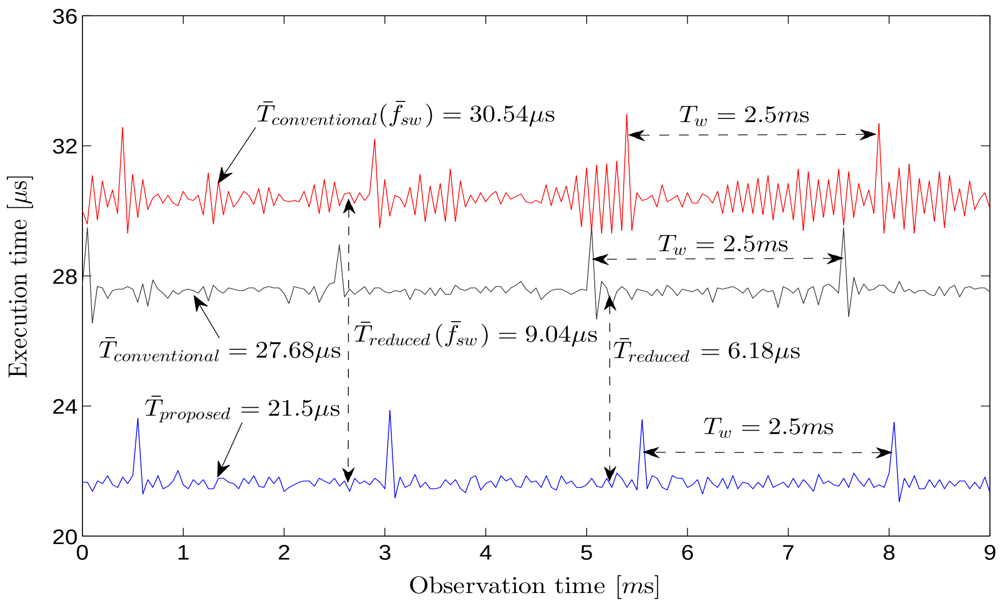

Figure 3.6: Execution times of the proposed and the conventional control algorithms.

algorithm is reduced, as the number of prediction vectors is less. The proposed algorithm requires additional calculations for the prediction vectors selection (calculations not used in the conventional PTC). However, the calculations are very simple. Therefore, the required extra execution time is much less—1.28 μs—than the reduced time in the prediction and optimisation steps.

The execution time of the proposed algorithm, compared to the conventional control algorithm, is illustrated in Fig. 3.6. Here, the average execution time of the conventional FS-PTC algorithm $\bar{T}_{conventional}$ without switching transition term in the cost function is 27.68 μs, which is further increased to 30.54 μs if the switching transition term is included in the cost function. The average execution time of the proposed simplified algorithm $\bar{T}_{proposed}$ is 21.5 μs. Hence, the reduced average execution times with and without switching transition term in the cost function are 30% and 22%, respectively. As the speed control loop is executed in every 2.5 ms, the execution time is increased in every 2.5 ms. Table 3.3 shows a comparison of overall execution times. Of course, the execution time is hardware- and (above all) programming-dependent. As the same hardware and programming techniques are used for all cases in this study, the comparison is fair.

Table 3.3: Overall execution times comparison between the proposed and conventional control algorithms

Index	Execution times (μs)		
	Conventional	Conventional ($\bar{f}_{sw}$)	Proposed
Measurement	6.63	6.67	6.64
Estimation	1.60	1.60	1.60
Prediction vectors selection	0.00	0.00	1.28
Prediction and optimisation	26.08	28.94	18.66
Total	38.30	42.20	31.76

3.5 Experimental results

The proposed controller is verified by experiment. The machines and controller parameters are given in Appendix A. The experimental setup is discussed and shown in Appendix B. The sampling time of the controller is set to 50 μs.

The performance of the proposed control system is measured mainly in terms of stator current THD, torque ripple, flux ripple and average switching frequency. A major effect of harmonic currents in rotating machinery is increased heating due to iron and copper losses at the harmonic frequencies. The harmonic components thus affect the machine efficiency, and can also affect the torque developed. Flux variations may produce higher current THD, and torque ripple causes acoustic noise in the system. The switching frequency affects the converter efficiency. Because the switching loss in the converter is directly proportional to the switching frequency.

The performance of the proposed simplified FS-PTC is compared with the two cases of conventional FS-PTC: 1) without and 2) with switching transition term in the cost function. All the voltage vectors $\{\boldsymbol{v}_0 \cdots \boldsymbol{v}_7\}$ are evaluated if switching transition term is considered in the cost function. Otherwise, seven different voltage vectors are evaluated and an appropriate zero voltage vector (either $\boldsymbol{v}_0$ or $\boldsymbol{v}_7$) is then selected, as explained in Section 3.3.3.

The following investigations are conducted to test the effectiveness of the proposed FS-PTC algorithm:

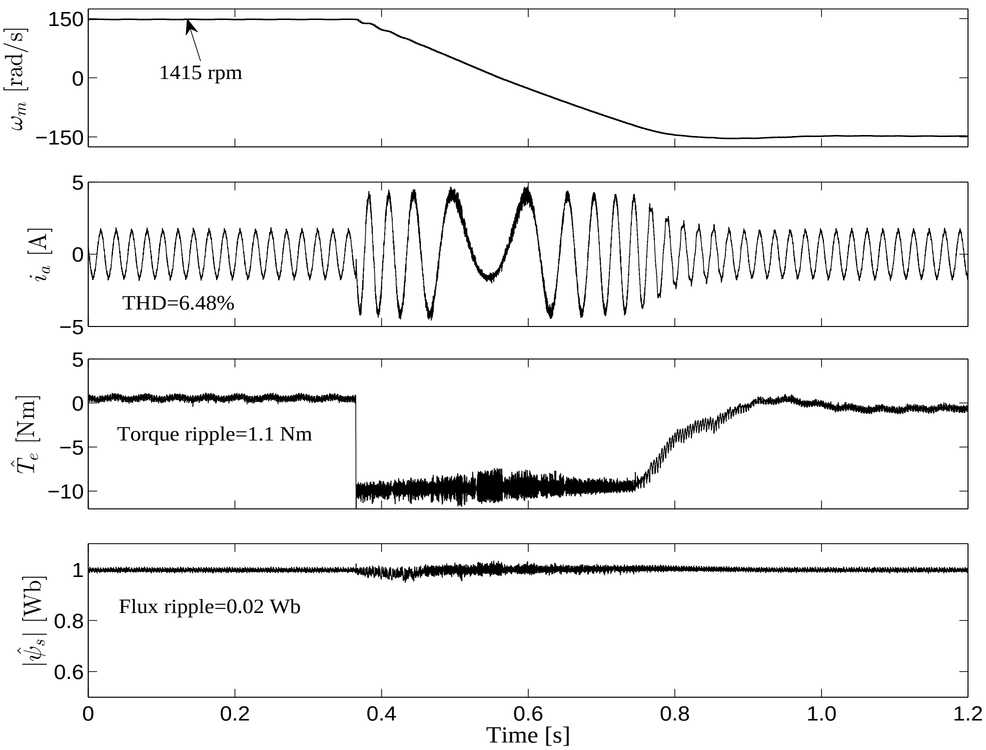

Figure 3.7: Experimental waveforms of speed, stator current, estimated torque and estimated stator flux at no-load torque under rated-speed (1415 r/min) reversal condition for the proposed SPVs-based FS-PTC.

a) transient capability of the FS-PTC under rated-speed reversal;

b) steady-state behaviour at medium- and low-speed operations;

c) investigation of average switching frequency;

d) robustness against external rated-load torque disturbance;

e) step rated-torque-transient characteristics;

f) step rated-speed-transient characteristics.

3.5.1 Investigation of transient capability under rated-speed reversal

First, a reverse speed operation of the proposed FS-PTC at rated-speed of 1415 r/min without load torque (although the dc machine is connected to the fed motor) is performed.

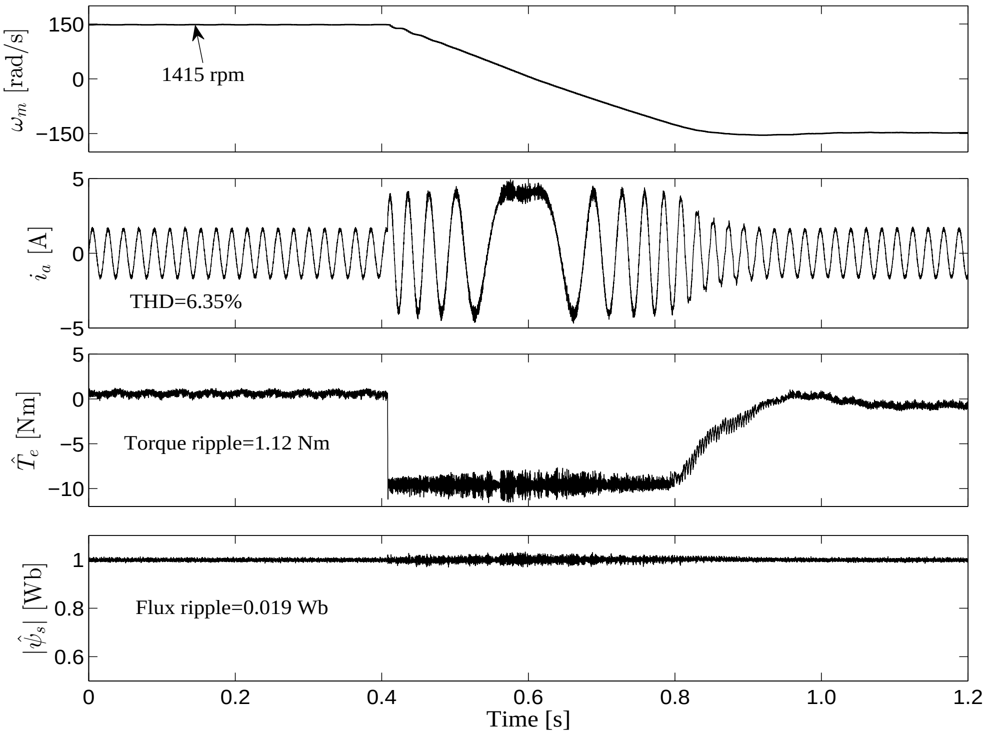

Figure 3.8: Experimental waveforms of speed, stator current, estimated torque and estimated stator flux at no-load torque under rated-speed (1415 r/min) reversal condition for the conventional FS-PTC.

Figure 3.7 shows the behaviour of the control system. From top to bottom, the curves are the speed, stator current, estimated torque and stator flux. The stator flux is constant at its rated value of 1.0 Wb. For comparison, same curves are plotted for the conventional all vectors based FS-PTC, where switching transition term is not included in the cost function, as shown in Fig. 3.8. It is seen that the performance in terms of torque and flux ripple is comparable. During speed reversal, the ripple is slightly increased for both the proposed and conventional control systems. This is because of high current flowing in the stator winding. The THD of the stator current i_a (calculated with 10 cycles up to 10 kHz) for the proposed FS-PTC is 6.48%, whereas it is 6.35% for the conventional FS-PTC. This slightly higher current THD for the proposed FS-PTC is due to the low average switching frequency. The average switching frequencies are 1.91 and 2.11 kHz for the proposed and conventional control systems, respectively. For THD calculation, the data is captured in ControlDesk and analysed in MATLAB.

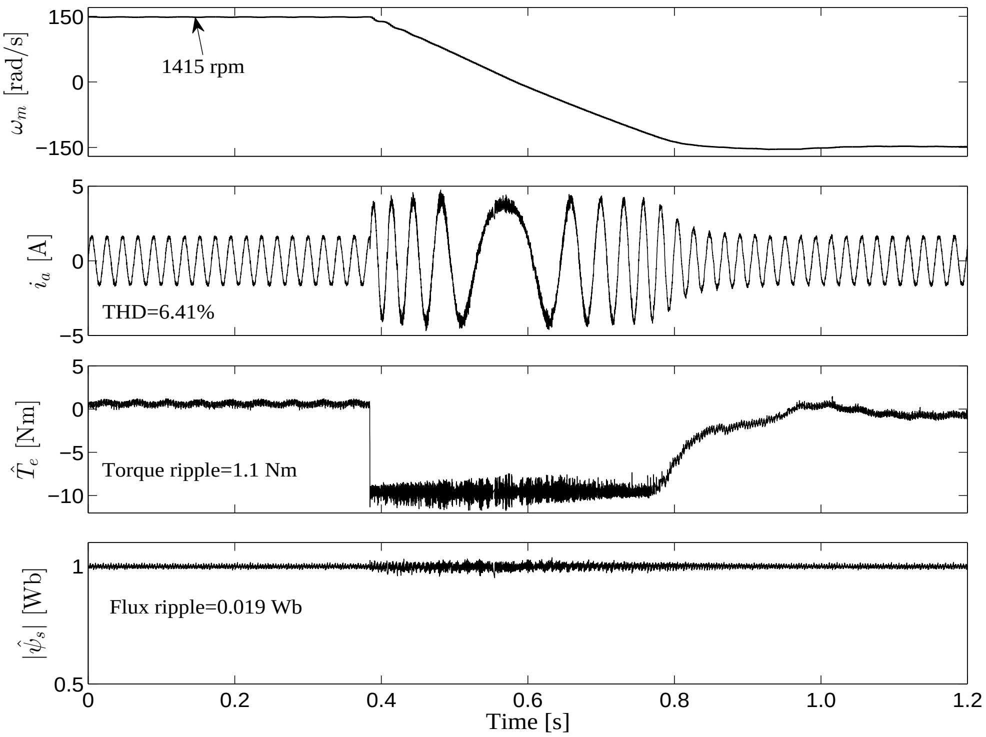

Figure 3.9: Experimental waveforms of speed, stator current, estimated torque and estimated stator flux at no-load torque under rated-speed (1415 r/min) reversal condition for the flux-error-based FS-PTC.

From Fig. 3.7, it can be noted that a very small dip is present in the stator flux response during speed reversal at time 0.4 s around. This is because the prediction vectors are selected based on the torque-error (see Table 3.1) regardless of the stator-flux-error. During the transient, at a particular position of the stator flux, the voltage vector that produces more torque is selected to reduce the torque-error and is applied to the motor terminals. Moreover, the vector producing more torque, in most cases, decreases stator flux and causes flux transient. One possible solution of this problem is to set a higher value of the weighting factor λ_f in the cost function, Eq. (3.17), during the transient than the steady-state condition. Another possible solution is to use the stator flux-error-based prediction vectors (see Table 3.2). In that case, a less priority should be set on the stator flux—small λ_f in the cost function—compared to the torque-error-based prediction vectors to achieve satisfactory torque and flux performance.

In order to justify the proposed solution mentioned earlier, the flux-error-based pre-

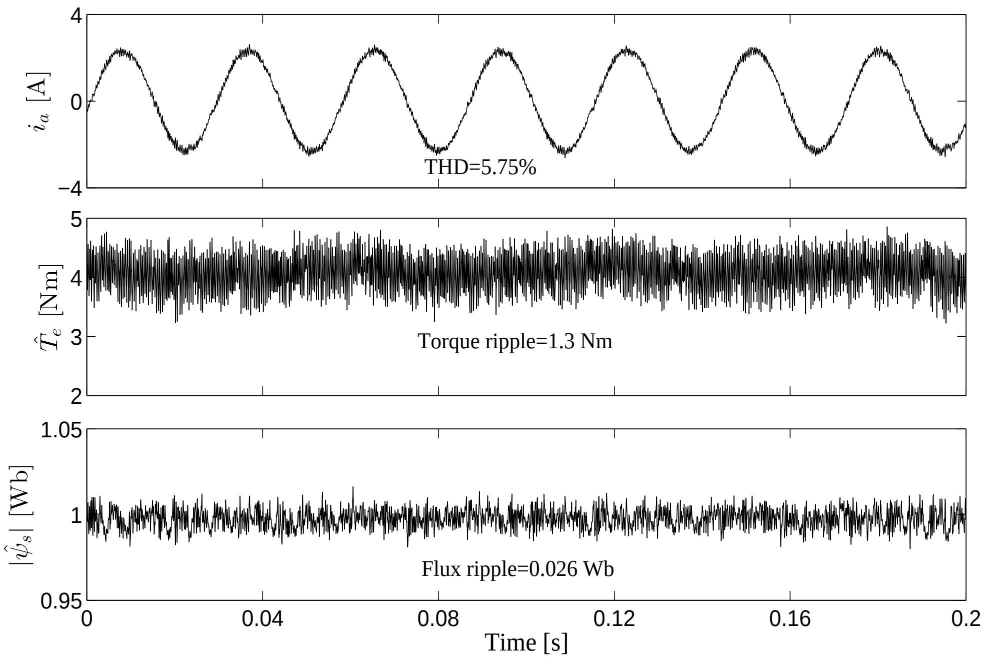

Figure 3.10: Experimental steady-state waveforms of stator current, estimated torque and estimated stator flux at 1000 r/min with 4.0 Nm load torque for the proposed SPVs-based FS-PTC.

diction vectors are considered. A reverse rated-speed of 1415 r/min operation without load torque is performed, and the behaviour of the control system is illustrated in Fig. 3.9. It can be seen that there is no dip in the stator flux response during speed reversal at time 0.4 s around, while the system performance—stator current THD, torque ripple and stator flux ripple—is comparable with the torque-error-based prediction vectors (see Fig. 3.7). Hence, the problem can be solved using flux-error-based prediction vectors.

3.5.2 Steady-state behaviour at medium- and low-speed operations

Figures. 3.10 and 3.11 show the steady-state characteristics of the proposed and conventional control systems, respectively, at a speed of 1000 r/min with 4.0 Nm load torque. It is observed that the torque and flux ripple is similar; the differences are 0.04 Nm and 0.002 Wb, respectively. However, the THD of the stator current for the proposed FS-PTC is marginally higher due to lower average switching frequency. The frequency spectra of

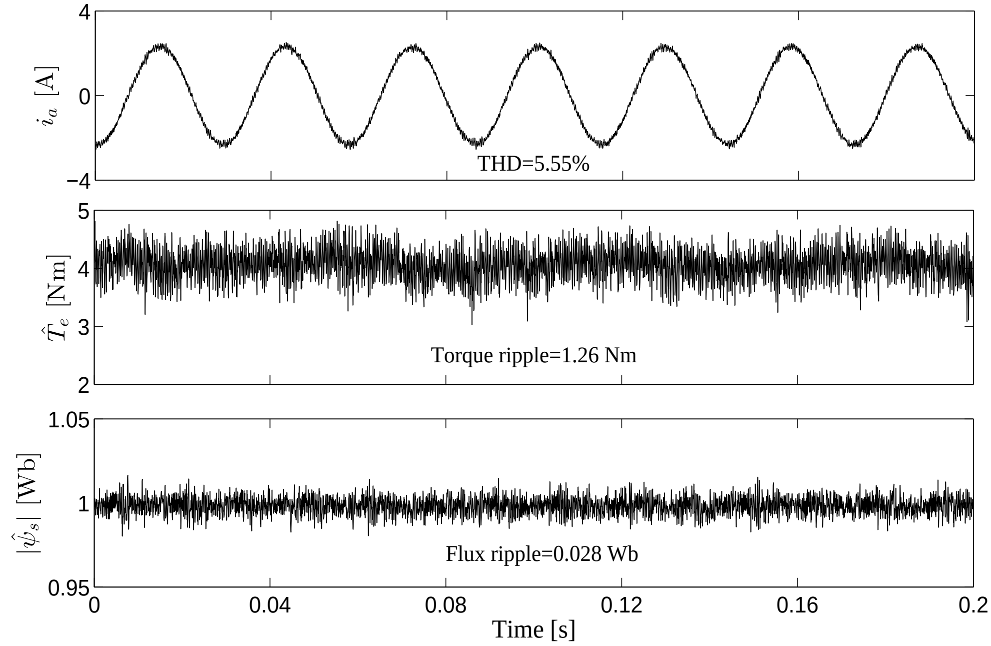

Figure 3.11: Experimental steady-state waveforms of stator current, estimated torque and estimated stator flux at 1000 r/min with 4.0 Nm load torque for the conventional FS-PTC.

the stator currents using the proposed and conventional control algorithms are presented in Figs. 3.13(a) and 3.13(b), respectively. The average switching frequency $\bar{f}_{sw}$ for the proposed control algorithm is lower by 16.62%. Moreover, the frequency spectrum is less distributed over a wide frequency range compared to the conventional control algorithm. This also confirms the reduction in the average switching frequency. To reduce the average switching frequency of the conventional FS-PTC, the switching transition term is included in the cost function. Then, a weighting factor is imposed on the frequency term, provided that the torque and flux ripple is almost similar. The responses of the system and the frequency spectrum of the stator current are presented in Figs. 3.12 and 3.13(c), respectively. The THD of the stator current is similar to the proposed control. However, the average switching frequency is still higher. If a greater weight is imposed on the switching transition term to reduce the average switching frequency further, the torque ripple increases (while keeping the weight of the stator-flux-error constant). Hence, selecting the weighting factors is a complex task. In this sense, the proposed FS-PTC is simpler compared to the conventional FS-PTC. Table 3.4 summarises the steady-state

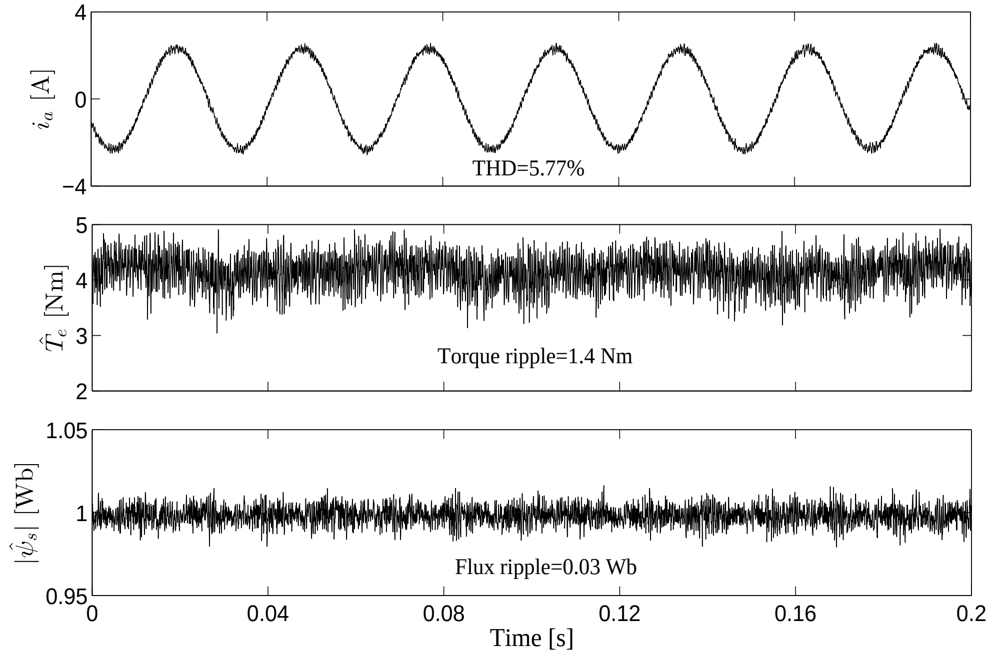

Figure 3.12: Experimental steady-state waveforms of stator current, estimated torque and estimated stator flux at 1000 r/min with 4.0 Nm load torque for the conventional FS-PTC with average switching frequency reduction.

performance of the proposed and conventional FS-PTC systems.

Table 3.4: Quantitative steady-state performance comparison between the conventional and the proposed control schemes with $\omega_m = 1000$ r/min, $T_l = 4$ Nm and $T_s = 50$ μs

Index	Conventional ($\bar{f}_{sw}$)	Conventional	Proposed
THD (for i_a) (%)	5.77	5.55	5.75
Torque ripple (Nm)	1.40	1.26	1.30
Flux ripple (Wb)	0.03	0.028	0.026
Average Switching frequency (kHz)	2.97	3.43	2.86

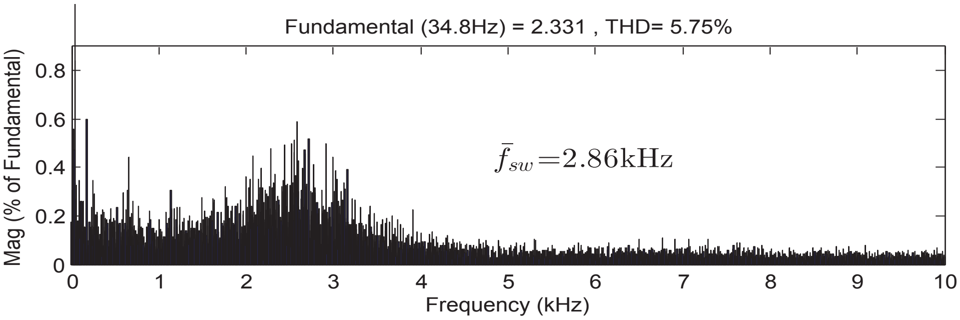

(a)

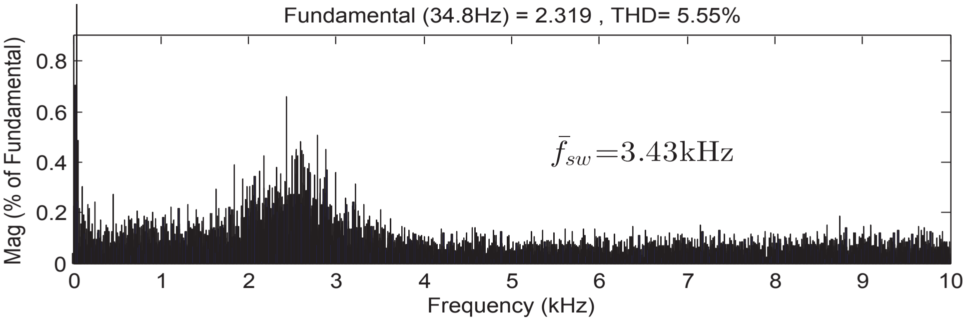

(b)

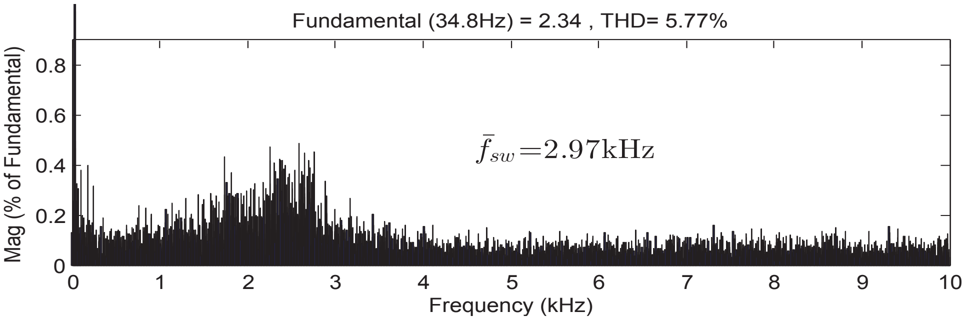

(c)

Figure 3.13: Experimental frequency spectra of stator current i_a at 1000 r/min using (a) proposed algorithm, (b) conventional algorithm and (c) conventional algorithm with average switching frequency reduction.

To test the low-speed performance, the machine is operated at 300 r/min at 50% rated-load torque. The waveforms corresponding to the proposed and conventional control algorithms are presented in Figs. 3.14 and 3.15, respectively. It is observed that the THD of the stator current, the torque ripple and the flux ripple are similar, provided that the switching frequency term is not included in the cost function. From the frequency spectra of the stator current, as shown in Figs. 3.17(a) and 3.17(b), it is seen that the

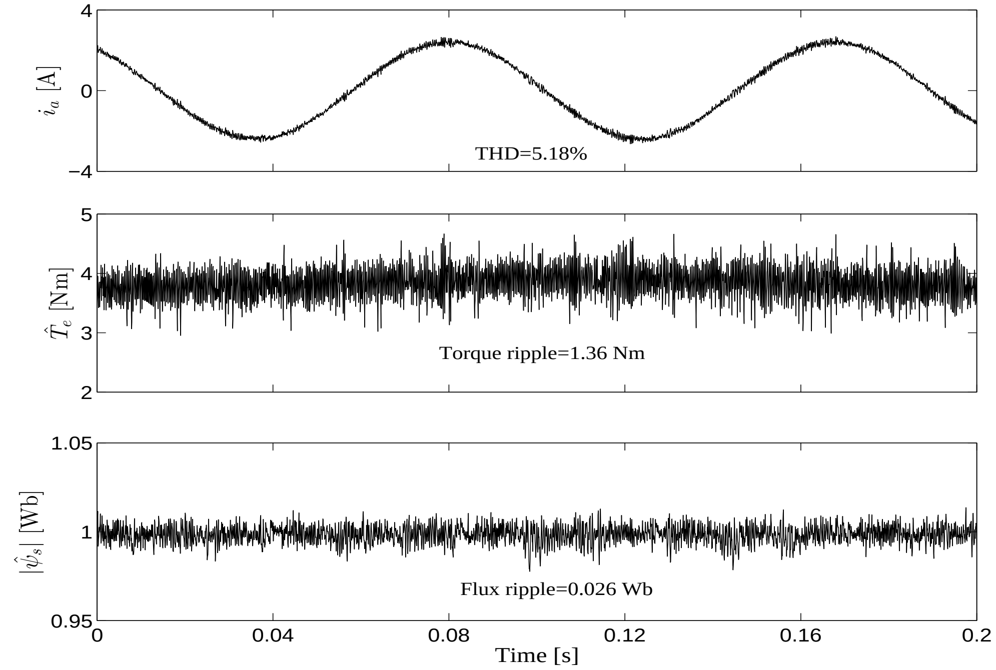

Figure 3.14: Experimental steady-state waveforms at 300 r/min with 50% rated-load torque for the proposed SPVs-based FS-PTC.

average switching frequency of the proposed FS-PTC is 4.90 kHz; In contrast, this is 4.83 kHz for the conventional FS-PTC. If the average switching frequency reduction is considered, the THD of the stator current is increased from 5.21% to 5.60%, as shown in Fig. 3.16, yielding slightly higher torque ripple by 0.05 Nm. However, the average switching frequency is reduced, as shown in Fig. 3.17(c), from 4.83 to 4.72 kHz. The improvement in average switching frequency is not significant at low speed, while keeping torque and flux ripple similar. It is noted that the frequency spectrum for the proposed FS-PTC algorithm is less distributed over a wide frequency range compared with both cases of the conventional FS-PTC algorithms.

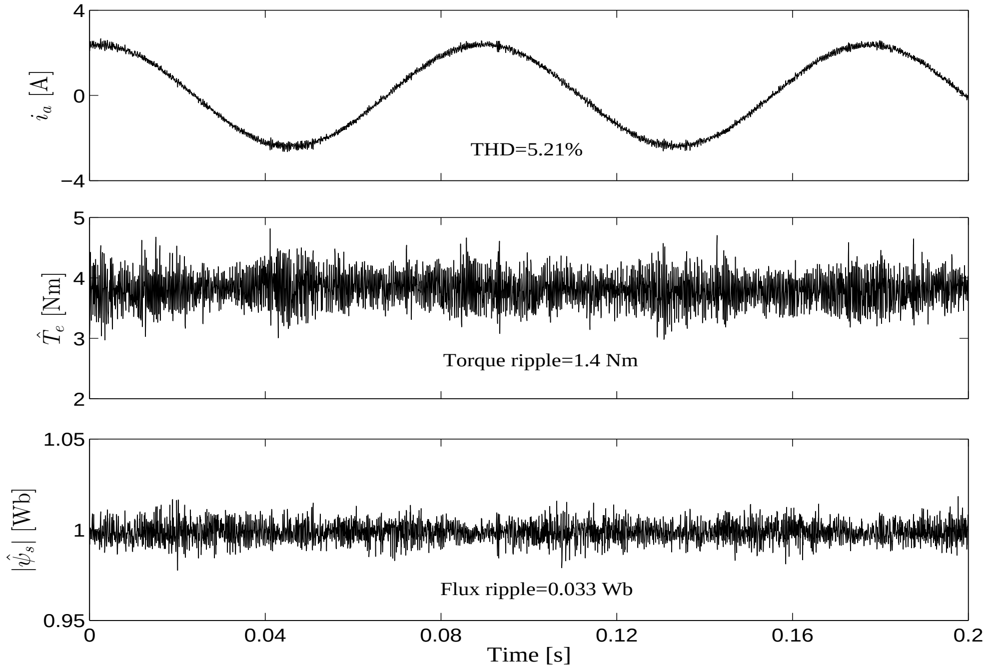

Figure 3.15: Experimental steady-state waveforms at 300 r/min at 50% rated-load torque for the conventional FS-PTC.

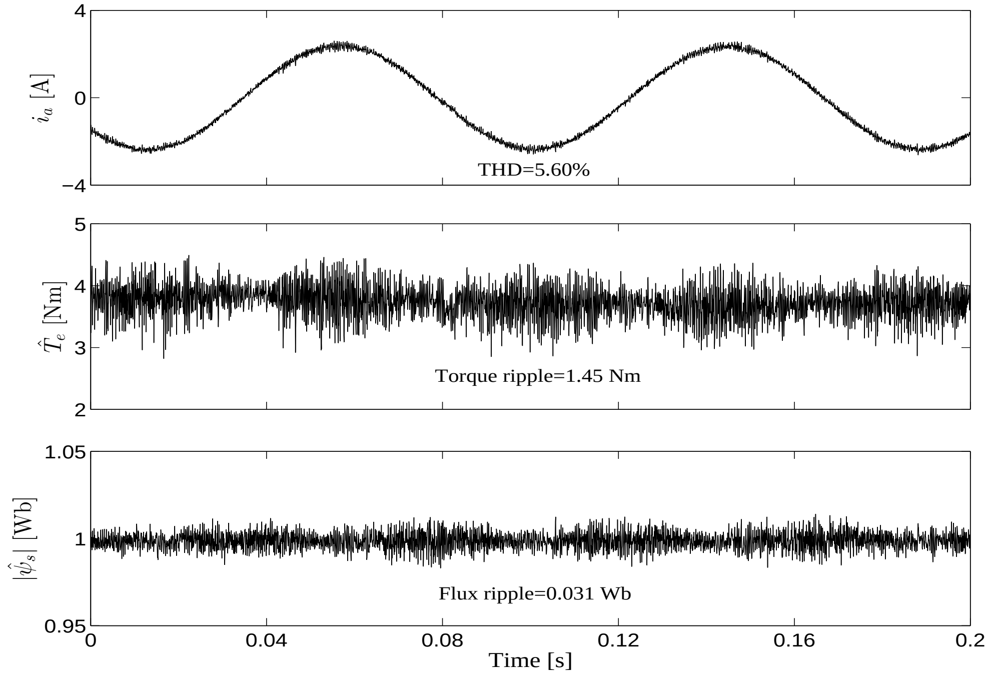

Figure 3.16: Experimental steady-state waveforms at 300 r/min at 50% rated-load torque for the conventional FS-PTC with average switching frequency reduction.

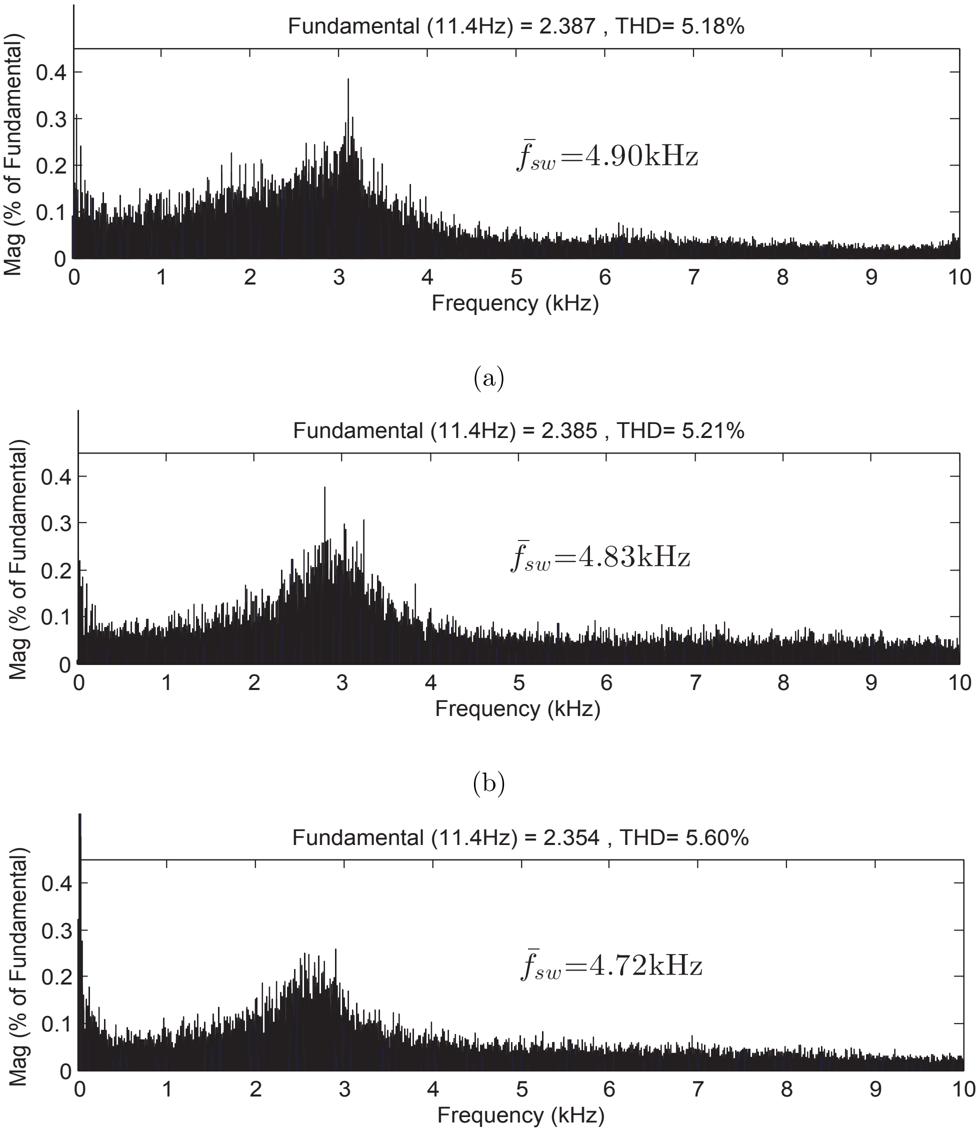

(a)

(b)

(c)

Figure 3.17: Experimental frequency spectra of the stator current i_a at 300 r/min using (a) proposed algorithm, (b) conventional algorithm and (c) conventional algorithm with average switching frequency reduction.

3.5.3 Investigation of average switching frequency

Figure 3.18(a) presents the average switching frequencies for the proposed and conventional control algorithms at different speeds and load torques. The average switching frequencies are comparable at low- and high-speeds with 50% or higher of the rated-load torque. The reduction in average switching frequencies for the proposed FS-PTC is significant—maximum 25% of average switching frequency—for the speed range of 400 to 1200 r/min, as can be seen in Fig. 3.18(b). The improvement in average switching frequency is also obvious from Fig. 3.18(c). However, in the whole operating range of the machine, the variation ranges of average switching frequencies for the conventional and proposed FS-PTC strategies are similar (1.58–5.58 kHz for both cases).

3.5.4 Investigation of robustness against rated-load torque disturbance

Figures 3.19 and 3.20 illustrate the responses to an external rated-load torque disturbance for the proposed and conventional control algorithms, respectively. The load torque, which is dependent on the rotor speed, is suddenly changed from 0 (no-load torque) to 7.4 Nm (full-load torque) at 1000 r/min. For both cases, it is observed that the stator current THD and the torque and flux ripple are similar before and after added load. During the load torque change, the stator flux remains constant at its rated value, which ensures decoupled control of the torque and flux. The motor speed returns to its original value within a short time (0.19 s), and the speed responses are identical during load disturbance. The average switching frequencies for the proposed FS-PTC algorithm before and after added load torque are 3.02 and 2.60 kHz, respectively; whereas the average switching frequencies before and after added load torque are 3.67 kHz and 3.09 kHz, respectively, for the conventional FS-PTC algorithm.

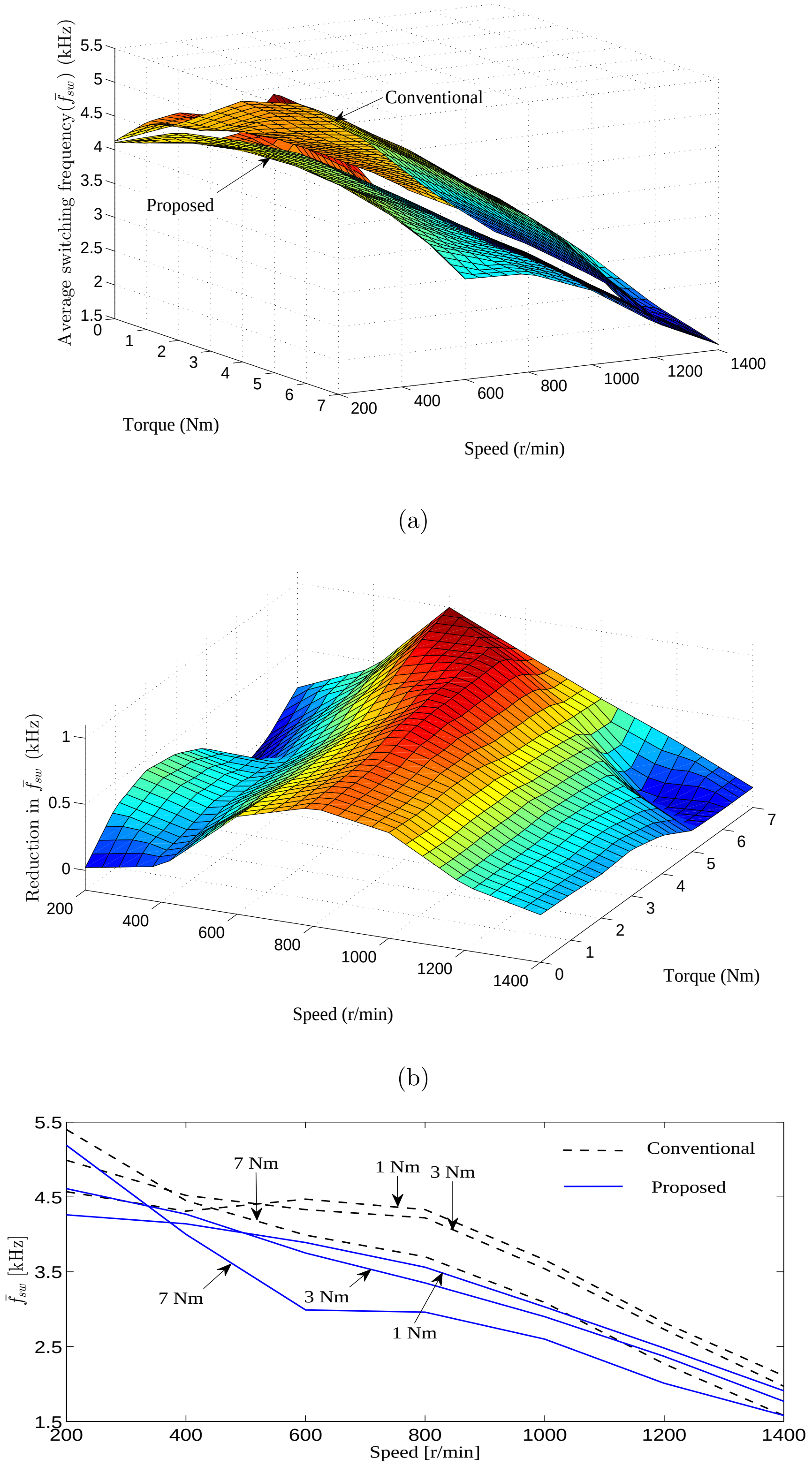

(a)

(b)

(c)

Figure 3.18: Experimental (a) average switching frequencies $\bar{f}_{sw}$ from 200 to 1400 r/min and 0 to 7 Nm, (b) reduction in $\bar{f}_{sw}$, and (c) $\bar{f}_{sw}$ vs. speed with torque as parameter.

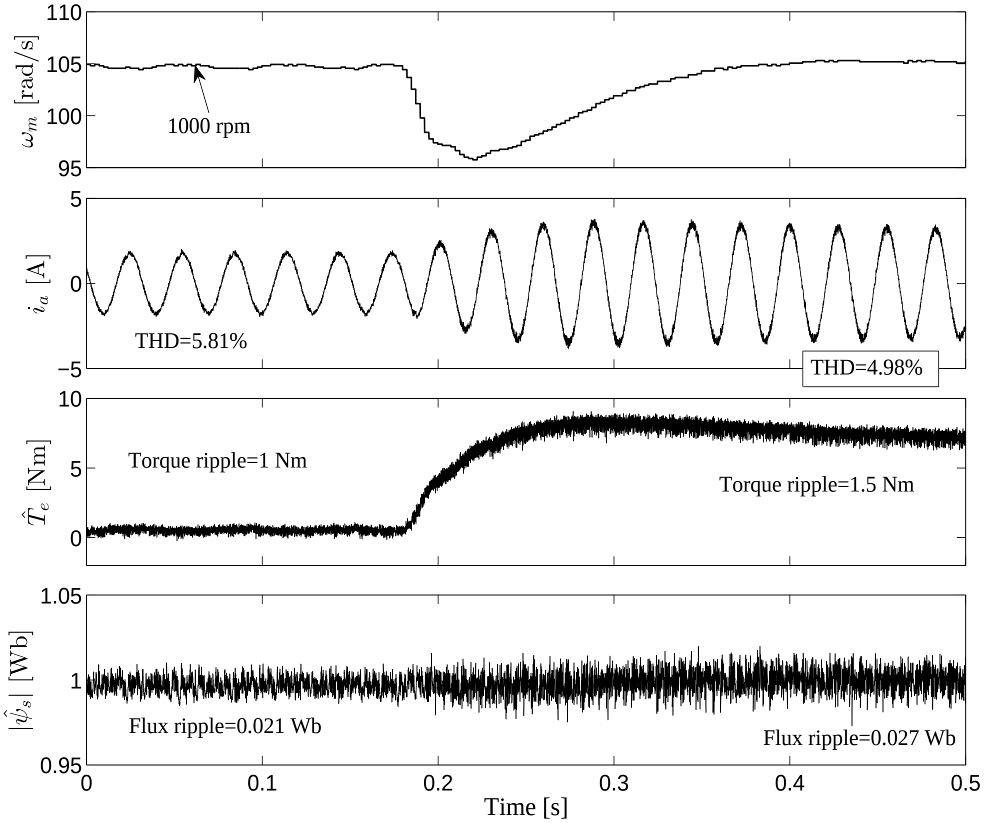

Figure 3.19: Experimental responses to an external rated-load torque disturbance at 1000 r/min for the proposed SPVs-based FS-PTC.

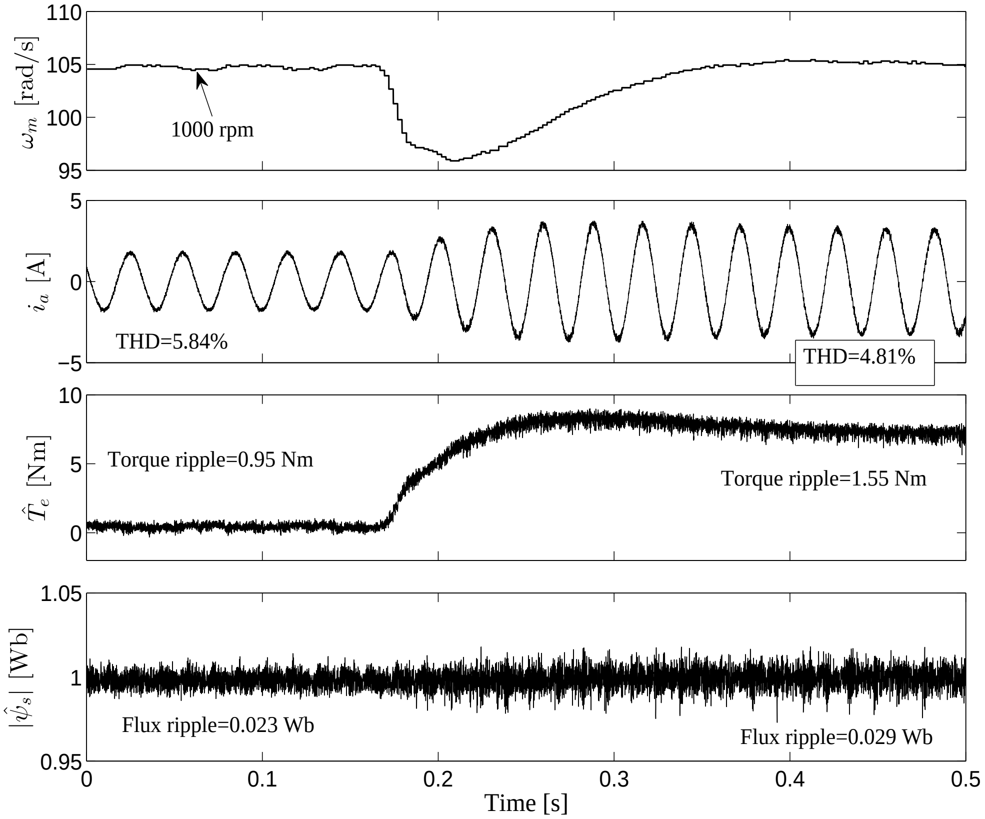

Figure 3.20: Experimental responses to an external rated-load torque disturbance at 1000 r/min for the conventional FS-PTC.

3.5.5 Step rated-torque-transient characteristics

Step rated-torque-transient characteristics of the proposed FS-PTC are tested, and illustrated in Fig. 3.21. A step rated-torque reference of 7.4 Nm is commanded. It is seen that the torque rise times for the proposed and the conventional control algorithms are very close with 0.5 ms versus 0.53 ms, respectively. Both control algorithms exhibit fast dynamic response, that indicate the equivalency of the proposed and the conventional control algorithms under rated-torque-transient condition.

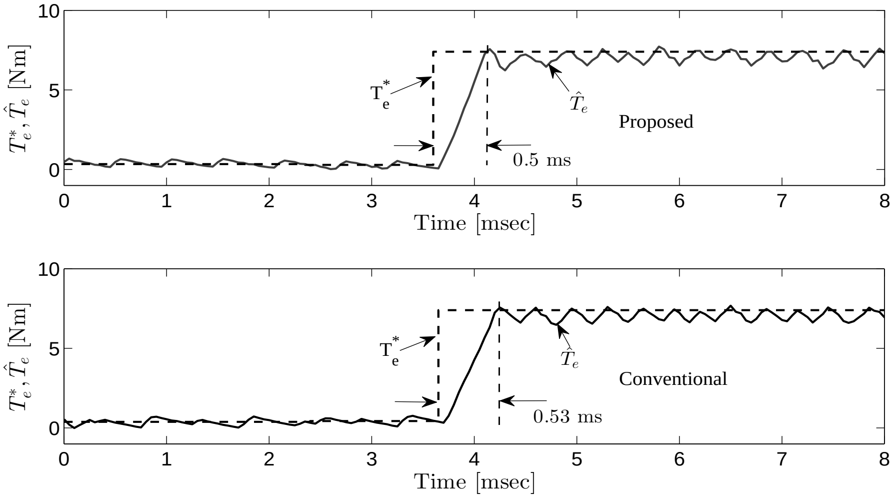

Figure 3.21: Experimental step rated-torque-transient of the proposed and conventional control algorithms at a step speed command from 0 to 1000 r/min.

3.5.6 Step rated-speed-transient characteristics

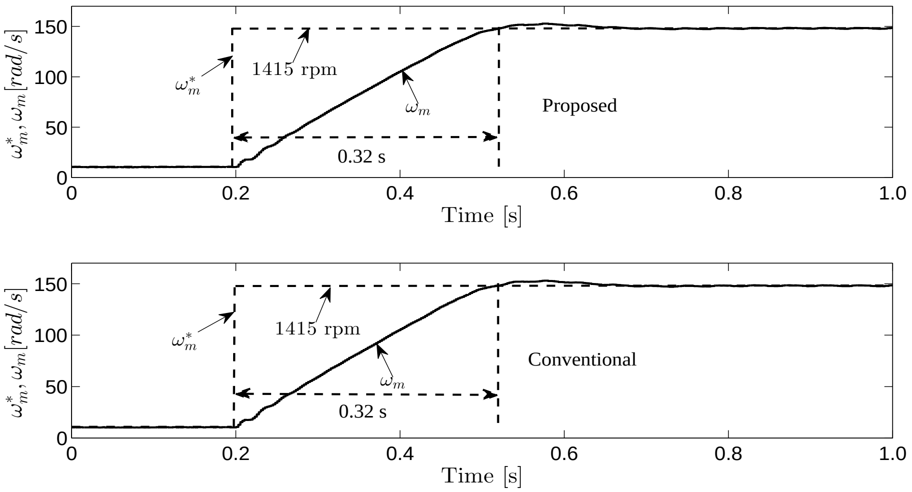

Figure 3.22: Experimental step rated-speed-transient of the proposed and conventional control algorithms.

Finally, rated-speed-transient behaviour of the proposed control algorithm is investigated and presented in Fig. 3.22. Initially, the machine is started with 100 r/min, and then a step rated-speed reference of 1415 r/min is commanded. Similar to the conventional control algorithm, the proposed FS-PTC can track the reference speed accurately without any significant overshoot, as can be seen in Fig. 3.22. Moreover, the speed rise times for both control algorithms are comparable.

3.6 Summary

This chapter has proposed a simplified FS-PTC algorithm that employs only three voltage vectors instead of the eight used in conventional FS-PTC for prediction and optimisation. The number of prediction vectors is reduced without any complex calculations. A reduction in the average switching frequency of each semiconductor switch is achieved by not including the switching transition term in the cost function, as is the case with conventional FS-PTC. The reduced number of control objectives in the cost function makes the selection of weighting factors simpler than in the conventional method. The proposed FS-PTC algorithm is verified by experiment. The maximum reduction in the average execution time and the average switching frequency of each semiconductor switch are 30% and 25% over the conventional FS-PTC, respectively. This is achieved without sacrificing the torque and flux performance achieved in the conventional method. Good performance in terms of stator current THD, robustness against load torque disturbance, step torque response and step speed response is also achieved using the proposed simplified SPVs-based FS-PTC.

Chapter 4

FS-PTC of a 3L-NPC Inverter Fed IM Drive

4.1 Introduction

The FS-PTC of a 2L-VSI fed drive suffers from high torque and flux ripple and average switching frequency, due to the limited number of available voltage vectors of the power converter. To take advantage of multi-level inverter drives that offer the benefits of lower harmonic current distortion, torque ripple and switching frequency over the 2L-VSI, this chapter proposes to integrate the FS-PTC with a 3L-NPC inverter driven IM drive. The drawback inherited from the topology of the 3L-NPC VSI, such as neutral-point voltage, is handled easily by treating it as a variable to the cost function. Similarly, apart from the inverter topology itself, the average switching frequency is reduced further. The variation range of average switching frequency is small, even almost constant at a particular speed at different load torques. The computational burden of the control algorithm is reduced by using the proposed SPVs strategy. This is achieved without affecting the system performance, including torque and flux ripple, torque dynamic, capacitor voltage balance and average switching frequency. The performance of the proposed controller is compared with that of the well established FOC and DTC strategies at a particular operating point. Another comparison between the two-level and the 3L-NPC inverter fed drives is presented to prove the logicality of selecting the multilevel instead of the two-level

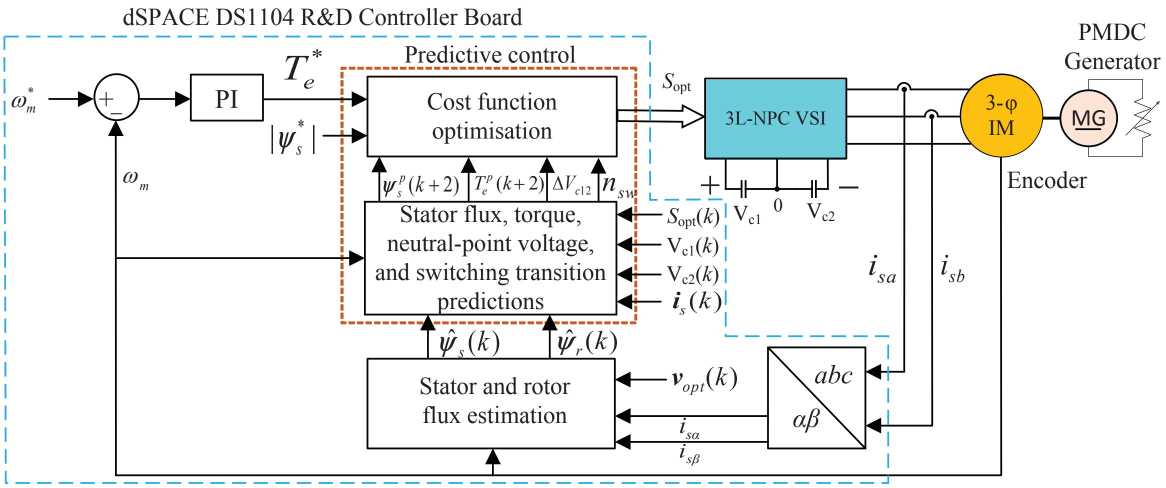

Figure 4.1: Proposed FS-PTC of a 3L-NPC inverter fed IM drive.

inverter.

This chapter addresses the second objective of the thesis, and part of the contribution is published in [113]. This chapter is organised as follows. The proposed control algorithm is discussed in Section 4.2. The computational capacity requirements and problem associated with the proposed FS-PTC are discussed in Sections 4.3 and 4.4, respectively. Section 4.5 presents the solution to the problem. Experimental results are presented in Section 4.6. The performance of the proposed FS-PTC is compared with the classical FOC and DTC strategies in Section 4.7. Another comparison between the two-level and the 3L-NPC inverter fed drives is presented is Section 4.8.

4.2 Proposed FS-PTC model

The basic structure of the proposed 3L-NPC VSI fed IM drive is similar to that of the 2L-VSI fed drive, as explained in Chapter 3. There are two structural differences: 1) replacing the 2L-VSI with the 3L-NPC VSI and 2) the number of required switching signals (12 for the 3L-NPC and 6 for the 2L-VSI). Due to the 3L-NPC inverter feature, the present analysis considers one additional control objective, the neutral-point voltage. The performance and required computational burden are analysed for the 3L-NPC VSI. The proposed FS-PTC model consists of three stages: estimation, prediction and cost function optimisation, as shown in Fig. 4.1. The voltage vector in the stationary reference frame $\boldsymbol{v}_{opt}$ shown in Fig. 4.1 is calculated using the measured dc-link voltages $\{V_{c1}, V_{c2}\}$ and applied switching state S_{opt}. The following subsections describe the main steps of the proposed FS-PTC.

4.2.1 Estimation of the rotor and stator flux

Similar to the 2L-VSI fed drive, the discrete rotor current model of the IM, as expressed by the Eq. (3.1), is used for the rotor flux estimation. The stator flux is then estimated based on the relationship between the rotor flux and the stator flux, as shown in Eq. (3.2).

4.2.2 Predictions of control objectives

After estimating the stator and rotor flux, all control objectives—such as the stator flux, electromagnetic torque, neutral-point voltage, average switching frequency and overcurrent—are predicted in the proposed FS-PTC. The stator flux and torque are predicted using the Eqs. (3.4)–(3.6); thus, these equations will not be repeated here.

As mentioned previously, it is necessary to control the capacitor voltage unbalance, also called the neutral-point voltage ΔV_{c12}. A large capacitor voltage unbalance may damage the semiconductor devices. It is also the cause of large torque and flux ripple. The neutral-point voltage is always attempted to maintain at zero value. Hence, it is necessary to investigate the effects of a given switching state on the capacitor voltages at instant $k+1$. Using Eqs. (2.16)–(2.19), the predicted neutral-point voltage at instant $k+1$, $\Delta V_{c12}(k+1)$ can be defined as

$$\Delta V_{c12}(k+1) = \Delta V_{c12}(k) - \frac{T_s}{C} \Delta i_{c12}(k+1) \tag{4.1}$$

where $\Delta V_{c12}(k) = V_{c1}(k) - V_{c2}(k)$, $\Delta i_{c12}(k+1) = i_{c1}(k+1) - i_{c2}(k+1)$. It is useful to mention that $\Delta i_{c12}(k+1)$ can be calculated from Eqs. (2.18) and (2.19) without calculating the dc-link current i_{dc}, as i_{dc} is a common variable in both equations.

For the average switching frequency reduction, the number of switching transitions n_{sw} is predicted at each time step. The calculation of n_{sw} is different from Eq. (3.8), as two switches are on at a particular time instant in each arm for the 3L-NPC inverter.

The calculations are as follows

$$n_{sw}(k+1) = \sum_{x=\{a,b,c\}} \left| S_{x1}(k+1)_i - S_{x1}(k) \right| + \left| S_{x2}(k+1)_i - S_{x2}(k) \right| \tag{4.2}$$

where $S_x(k+1)$ is the probable switching state for each phase $x = \{a, b, c\}$ for the next time instant $k+1$, $S_{x1}(k)$ and $S_{x2}(k)$ are the applied switching state $S_{opt}(k)$ to the inverter at the time instant k and i is the index of possible voltage vectors $\{\boldsymbol{v}_0 \cdots \boldsymbol{v}_{26}\}$ shown in Fig. 2.5.

4.2.3 Cost function optimisation

All the aforementioned predicted variables are evaluated using a predefined cost function to determine the optimum voltage vector $\boldsymbol{v}_{opt}$. The cost function includes the absolute values of torque-error $(T_e^* - T_e^p)$, flux-error $(|\boldsymbol{\psi}_s^*| - |\boldsymbol{\psi}_s^p|)$, neutral-point voltage ΔV_{c12} and number of switching transition n_{sw}. Hence, the cost function can be defined as

$$\begin{aligned} g = \left| T_e^*(k+1) - T_e^p(k+1) \right| + \lambda_f \left| |\boldsymbol{\psi}_s^*| - |\boldsymbol{\psi}_s^p(k+1)| \right| \\ + \lambda_{cv} \left| \Delta V_{c12}(k+1) \right| + \lambda_n n_{sw}(k+1) \end{aligned} \tag{4.3}$$

where λ_f, λ_{cv} and λ_n are the three weighting factors of flux error, neutral-point voltage and the number of switching transition, respectively. In this study, the weighting factor λ_f sets the relative importance of the stator flux over the torque.

Over-current protection is also implemented using Eq. (3.9). Thus, the complete cost function g for the controller is

$$\begin{aligned} g = \left| T_e^*(k+1) - T_e^p(k+1) \right| + \lambda_f \left| |\boldsymbol{\psi}_s^*| - |\boldsymbol{\psi}_s^p(k+1)| \right| \\ + \lambda_{cv} \left| \Delta V_{c12}(k+1) \right| + \lambda_n n_{sw}(k+1) + I_m. \end{aligned} \tag{4.4}$$

In Eq. (4.4), the term I_m does not need a weighting factor. Imposing proper weighting factors on the other three different objectives is very important. Otherwise, the desired system performance may not be achieved due to improper selection of the weighting factors.

In this study, λ_f is first tuned online, running the 3L-NPC inverter as a two-level inverter (by considering only large voltage vectors $\{\boldsymbol{v}_{21} \cdots \boldsymbol{v}_{26}\}$ produced by the 3L-NPC inverter). The stator flux requires more priority than the torque to achieve low torque and flux ripple. The neutral-point voltage ΔV_{c12} is then included in the cost function, and the inverter is run as desired 3L-NPC inverter. The weight λ_{cv} is tuned online until the two capacitor voltages are perfectly balanced, and, thus, the ΔV_{c12} is around zero. It is observed that the torque and flux ripple is less sensitive to the λ_{cv} variation, while increasing λ_{cv}. Even, the neutral-point voltage does not change after a certain value of λ_{cv}, while maintaining a similar torque and flux performance. Eventually, the number of switching transitions n_{sw} is included in the cost function. After a certain value of λ_n—while increasing—ΔV_{c12} is inversely related to the average switching frequency. Increasing the value of λ_n decreases the average switching frequency but increases ΔV_{c12}. Hence, λ_n is tuned online and is set to the certain value (as mentioned earlier); after that certain value, the ΔV_{c12} starts to increase.

The delay compensation scheme [111] is employed to overcome one step delay caused by digital implementation. All control objectives are predicted for the instant $k+2$. The stator flux, stator current and torque are predicted using Eqs. (3.14)–(3.16). The neutral-point voltage and the number of switching transitions are predicted simply by taking the predicted variables $\Delta V_{c12}(k+1)$ and $n_{sw}(k+1)$ one step forward using Eqs. (4.1) and (4.2), respectively, and the expressions are as follows:

$$\Delta V_{c12}(k+2) = \Delta V_{c12}(k+1) - \frac{T_s}{C}\Delta i_{c12}(k+2) \tag{4.5}$$

$$n_{sw}(k+2) = \sum_{x=\{a,b,c\}} \left| S_{x1}(k+2)_i - S_{x1}(k+1) \right| + \left| S_{x2}(k+2)_i - S_{x2}(k+1) \right| \tag{4.6}$$

where $\Delta V_{c12}(k+1)$ is assumed as $\Delta V_{c12}(k)$, since the variation is very small within two adjacent sampling instant. For the calculation of $\Delta i_{c12}(k+2)$, the measured phase currents $i_a(k)$, $i_b(k)$ and $i_c(k)$ are employed to avoid $\alpha-\beta$ to $a-b-c$ frame transformation. The switching states $S_{x1}(k+1)$ and $S_{x2}(k+1)$ are equal to the $S_{opt}(k)$.

All admissible voltage vectors should be evaluated for the predictions at instant $k+2$, and the final cost function becomes

$$\begin{aligned} g = \left| T_e^*(k+2) - T_e^p(k+2) \right| + \lambda_f \left| |\boldsymbol{\psi}_s^*| - |\boldsymbol{\psi}_s^p(k+2)| \right| \\ + \lambda_{cv} \left| \Delta V_{c12}(k+2) \right| + \lambda_n n_{sw}(k+2) + I_m. \end{aligned} \tag{4.7}$$

Among the 27 available voltage vectors from the 3L-NPC VSI, the voltage vector that yields minimum g is selected as voltage vector $\boldsymbol{v}_{opt}$, and is then applied to the motor terminals via the inverter in the next sampling instant.

4.2.4 Proposed control algorithm

The overall control procedure can be summarised by the following sequences.

Step 1) *Measurement*: Sampling $\boldsymbol{i}_s(k)$, $V_{c1}(k)$, $V_{c2}(k)$ and $\omega_m(k)$.

Step 2) *Apply*: Apply the optimum voltage vector $\boldsymbol{v}_{opt}(k)$.

Step 3) *Estimate*: Estimate the rotor flux $\hat{\boldsymbol{\psi}}_r(k)$ and the stator flux $\hat{\boldsymbol{\psi}}_s(k)$ using Eqs. (3.1) and (3.2), respectively.

Step 4) *Predict and evaluate*: Predict stator flux $\boldsymbol{\psi}_s^p(k+2)$, stator current $\boldsymbol{i}_s^p(k+2)$, torque $T_e^p(k+2)$, neutral-point voltage $\Delta V_{c12}(k+2)$ and number of switching transitions $n_{sw}(k+2)$ using Eqs. (3.14)–(3.16), (4.5) and (4.6), respectively. Also test the predicted current $\boldsymbol{i}_s^p(k+2)$ using Eq. (3.9) to avoid over-current in the stator winding. Then, evaluate the predicted variables by calculating the cost g using Eq. (4.7). Perform these predictions and evaluations for all the 27 voltage vectors.

Step 5) *Optimise*: Select $\boldsymbol{v}_{opt}(k+2)$ that results minimum g in Eq. (4.7). Return to step 1).

4.3 Computational capacity requirements for the proposed control algorithm

The proposed control algorithm is coded in C, and is implemented using a dSPACE DS1104 R&D controller board with ControlDesk. The required execution time is 59.15 μs, as shown in Table 4.1. The execution time is measured on a 250 MHz PowerPC in the DS1104 using the command 'RTLIB_TIC_START' and 'RTLIB_TIC_READ' in C. Most of the execution time is spent on the predictions—76.24% of the total execution time. Execution times for the predictions of torque and flux, neutral-point voltage, number of switching transitions and over-current are 17.4, 8.82, 9.15 and 8.54 μs, respectively. Hence, at the expense of a very small execution time, the neutral-point voltage and average switching frequency of the inverter can be controlled effectively using FS-PTC. It is apparent that execution times for other stages of the proposed controller are insignificant when compared with the predictions stage.

Table 4.1: Execution times of the proposed FS-PTC algorithm

Index	Execution time (μs)
Measurement	4.39
Switching	0.12
Voltage and current calculations	0.72
Estimation	1.60
Predictions	$\boxed{45.1}$
Optimisation	6.25
Switching frequency calculation	0.56
Total	59.15

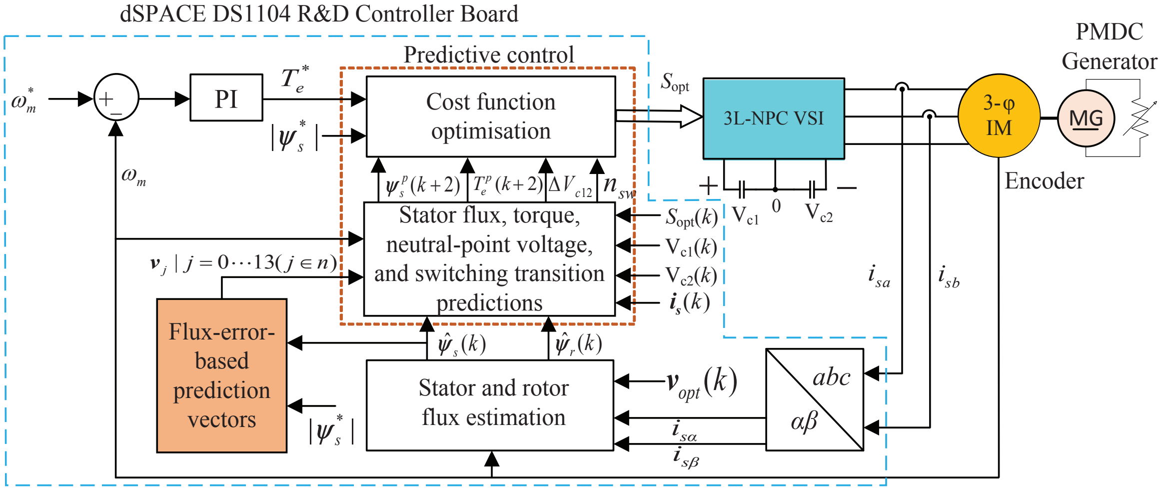

Figure 4.2: Simplified FS-PTC scheme for the proposed 3L-NPC inverter fed IM drive using the SPVs.

4.4 Problem of FS-PTC with the 3L-NPC VSI fed IM drive

Evaluating all the possible voltage vectors in the predictions stage requires a long execution time, as shown in the rectangular box in Table 4.1. The processing time of the predictions step is significant compared to other steps. The requirement for more computation limits the sampling frequency and thus degrades the control performance.

4.5 Proposed FS-PTC with the SPVs strategy

To avoid the aforementioned drawback, the SPVs strategy for the prediction and optimisation steps of the proposed FS-PTC is employed, as shown in Fig. 4.2. Except the prediction vectors block, the structure of the SPVs-based FS-PTC is similar to the all vectors based proposed FS-PTC, as can be seen in Fig. 4.2. The selected number of prediction vectors reduces the computational burden of the algorithm without affecting the system performance.

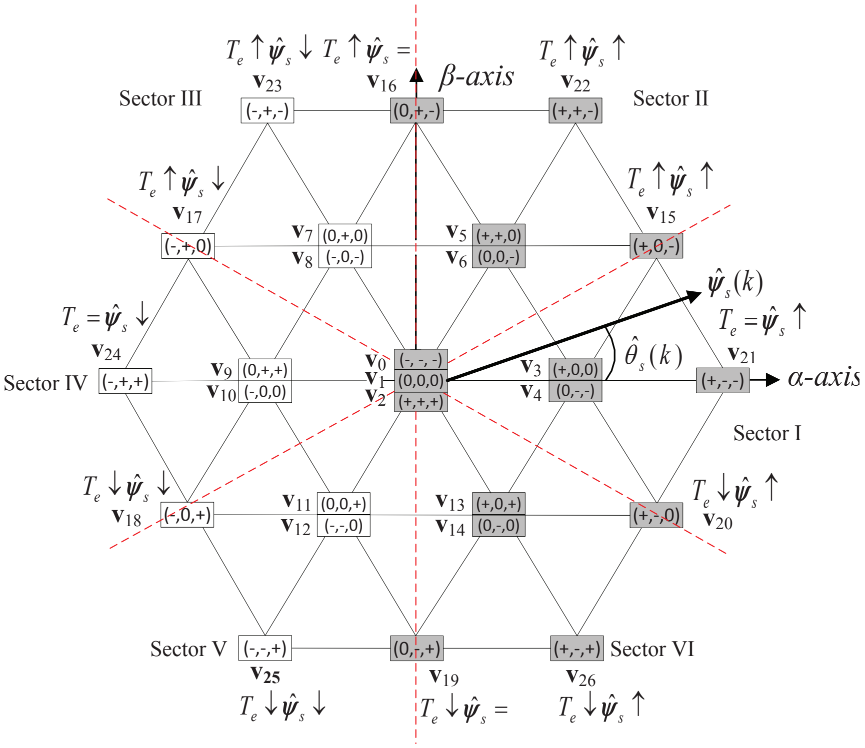

Figure 4.3: Stator-flux-error based selection of the possible prediction vectors. The rectangular boxes in grey indicate the prediction vectors when $\hat{\boldsymbol{\psi}}_s$ is located in sector I and $\delta\psi_s \geq 0$.

4.5.1 Selecting the prediction vectors

The prediction vectors selection strategy has already been explained in Section 3.3.1 for the 2L-VSI. There were two options for selecting the prediction vectors: 1) torque-error-based and 2) flux-error-based. For the 2L-VSI, the torque-error-based strategy was discussed in Section 3.3.1. The present analysis considers the flux-error-based selection strategy. This is more computationally efficient than the torque-error-based strategy. The reason for this computational efficiency is explained at the end of this sub-section. The following section discusses the flux-error-based SPVs strategy.

Consider that the stator flux $\hat{\boldsymbol{\psi}}_s$ is rotating in a counter-clockwise direction in the $\alpha - \beta$ plane divided into six sectors, as shown in Fig. 4.3. If $\hat{\boldsymbol{\psi}}_s$ is located in sector I and the flux-error $\delta\psi_s \geq 0$, then the voltage vectors that satisfy the flux increase '↑' condition, as shown in Fig. 4.3, are selected as prediction vectors. Accordingly, the possible active prediction vectors are the vectors that lie in the right-half of the α-β plane, as indicated in grey in Fig. 4.3. The SPVs also ensure all the possible conditions for torque-error. Similarly, for the same position of the stator flux, if $\delta\psi_s < 0$, the possible active prediction vectors are the voltage vectors lie in the left-half of the α-β plane. Generally, the active vectors are always employed with a zero vector for the IM to reduce the torque and flux ripple effectively. Including a zero vector also satisfies the possible conditions of $\delta T_e = 0$ and $\delta\psi_s = 0$. Hence, considering one zero vector, the total number of prediction vectors is fourteen, whereas this is 27 in conventional FS-PTC. Evaluation of only one zero vector in the prediction loop may increase the average switching frequency. However, use of all three zero vectors in the prediction loop is computationally expensive. For this reason, it would be useful to select an appropriate zero vector after the prediction loop. Hence, considering the computational complexity, one zero vector is used in the prediction loop. The possible prediction vectors for all the sectors for $\delta\psi_s \geq 0$ are shown in Table 4.2. The same table of prediction vectors can also be used for $\delta\psi_s < 0$; however, the sector in which the stator flux lies should be reversed. For example, if the stator flux is located in sector I and $\delta\psi_s < 0$, the sector IV should be selected for the possible prediction vectors.

Table 4.2: Possible prediction vectors for $\delta\psi_s \geq 0$ for the SPVs-based simplified FS-PTC strategy

Sector	Prediction vectors
I	$\boldsymbol{v}_1, \boldsymbol{v}_3, \boldsymbol{v}_4, \boldsymbol{v}_5, \boldsymbol{v}_6, \boldsymbol{v}_{13}, \boldsymbol{v}_{14}, \boldsymbol{v}_{15}, \boldsymbol{v}_{16}, \boldsymbol{v}_{19}, \boldsymbol{v}_{20}, \boldsymbol{v}_{21}, \boldsymbol{v}_{22}, \boldsymbol{v}_{26}$
II	$\boldsymbol{v}_1, \boldsymbol{v}_3, \boldsymbol{v}_4, \boldsymbol{v}_5, \boldsymbol{v}_6, \boldsymbol{v}_7, \boldsymbol{v}_8, \boldsymbol{v}_{15}, \boldsymbol{v}_{16}, \boldsymbol{v}_{17}, \boldsymbol{v}_{20}, \boldsymbol{v}_{21}, \boldsymbol{v}_{22}, \boldsymbol{v}_{23}$
III	$\boldsymbol{v}_1, \boldsymbol{v}_5, \boldsymbol{v}_6, \boldsymbol{v}_7, \boldsymbol{v}_8, \boldsymbol{v}_9, \boldsymbol{v}_{10}, \boldsymbol{v}_{15}, \boldsymbol{v}_{16}, \boldsymbol{v}_{17}, \boldsymbol{v}_{18}, \boldsymbol{v}_{22}, \boldsymbol{v}_{23}, \boldsymbol{v}_{24}$
IV	$\boldsymbol{v}_1, \boldsymbol{v}_7, \boldsymbol{v}_8, \boldsymbol{v}_9, \boldsymbol{v}_{10}, \boldsymbol{v}_{11}, \boldsymbol{v}_{12}, \boldsymbol{v}_{16}, \boldsymbol{v}_{17}, \boldsymbol{v}_{18}, \boldsymbol{v}_{19}, \boldsymbol{v}_{23}, \boldsymbol{v}_{24}, \boldsymbol{v}_{25}$
V	$\boldsymbol{v}_1, \boldsymbol{v}_9, \boldsymbol{v}_{10}, \boldsymbol{v}_{11}, \boldsymbol{v}_{12}, \boldsymbol{v}_{13}, \boldsymbol{v}_{14}, \boldsymbol{v}_{17}, \boldsymbol{v}_{18}, \boldsymbol{v}_{19}, \boldsymbol{v}_{20}, \boldsymbol{v}_{24}, \boldsymbol{v}_{25}, \boldsymbol{v}_{26}$
VI	$\boldsymbol{v}_1, \boldsymbol{v}_3, \boldsymbol{v}_4, \boldsymbol{v}_{11}, \boldsymbol{v}_{12}, \boldsymbol{v}_{13}, \boldsymbol{v}_{14}, \boldsymbol{v}_{15}, \boldsymbol{v}_{18}, \boldsymbol{v}_{19}, \boldsymbol{v}_{20}, \boldsymbol{v}_{21}, \boldsymbol{v}_{25}, \boldsymbol{v}_{26}$

If the torque-error-based selection strategy is followed, at a particular position of $\hat{\boldsymbol{\psi}}_s$, two additional small vectors will be included in the prediction vectors, as shown in Fig. 4.4. Eight small vectors instead of six participate in the pool of prediction vectors. This increases the number of prediction vectors. For example, if $\hat{\boldsymbol{\psi}}_s$ is located in sector I and $\delta T_e \geq 0$, all the voltage vectors along and above the $\alpha-$axis will be selected, as

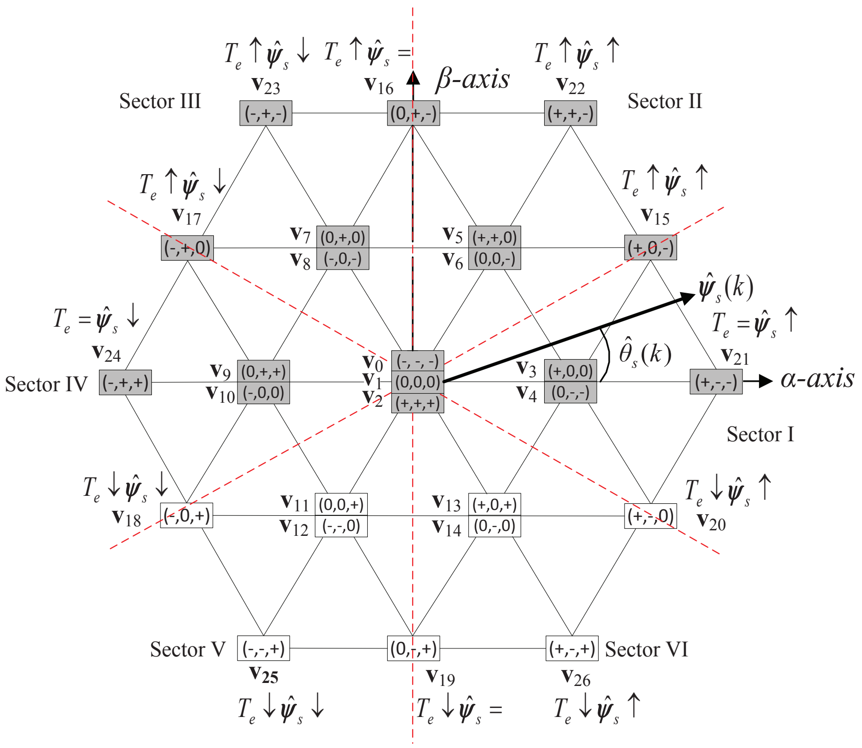

Figure 4.4: Torque-error-based selection of the possible prediction vectors. The rectangular boxes in grey indicate the prediction vectors when $\hat{\boldsymbol{\psi}}_s$ is located in sector I and $\delta T_e \geq 0$.

shown in grey in Fig. 4.4. The total number of prediction vectors will be 16, whereas this is 14 for the flux-error-based strategy. Thus, the flux-error based SPVs strategy is considered in this study.

4.5.2 Prediction and optimisation

For the predictions of control variables and optimisation of voltage vector, the same mathematical relations as those used in the all vectors based FS-PTC are employed. The only difference is that the value of the weighting factor λ_f in Eq. (4.7); λ_f is re-tuned. As explained in Chapter 3, a comparatively small value of λ_f is required for a similar performance with the proposed all voltage vectors based FS-PTC. It is noted that Eq. (4.7) contains the weighting factor λ_n for average switching frequency reduction. This was not necessary for the SPVs-based 2L-VSI fed FS-PTC drive. However, it is required for the 3L-NPC VSI, as all the SPVs are not adjacent and more than one switching transition may occur.

Table 4.3: Comparison between the execution times of the all vectors based FS-PTC and the SPVs-based FS-PTC algorithms

Index	Execution times (μs)	
	all vectors based FS-PTC	SPVs-based FS-PTC
Measurement	4.39	4.39
Switching	0.12	0.12
Voltage and current calculations	0.72	0.72
Estimation	1.60	1.60
Selection of prediction vectors	0.0	1.28
Predictions	$\boxed{45.1}$	$\boxed{24.36}$
Optimisation	6.25	3.4
Switching frequency calculations	0.56	0.56
Total	59.15	36.90

4.5.3 Improvement in computational efficiency

The execution time is measured on the same 250 MHz PowerPC in the DS1104. The required execution time is 36.9 μs, whereas the all voltage vectors based FS-PTC requires 59.15 μs, as shown in Table 4.3. Hence, the overall computational efficiency is improved by 38%. Particularly, in the prediction stage, the computational efficiency is improved by 46%—from 45.1 to 24.36 μs, as shown in the rectangular boxes in Table 4.3. Improvement is also obvious in the optimisation stage. The proposed control algorithm requires extra calculations for selectiing prediction vectors; however, this is insignificant (only 1.28 μs) compared to the total execution time.

4.6 Experimental Results

The control algorithm is coded in C and, thus, the cross compilation between MATLAB Simulink and C, as it is done in the chapter 3, is avoided. The controller parameters are given in Appendix A. The experimental setup is shown in Appendix B. The sampling period of the controller is set to 70 μs.

First, the effectiveness of the proposed all voltage vectors based FS-PTC of the 3L-NPC inverter fed drive in terms of torque and flux ripple, stator current THD, capacitor voltage balance and average switching frequency of the inverter is tested. The performance is compared to the SPVs-based FS-PTC strategy. A comparative analysis at a particular operating point is then conducted with the well established classical FOC and DTC strategies. Finally, another comparison between the 2L-VSI and 3L-NPC VSI fed IM drives is presented. The effectiveness of the proposed FS-PTC is investigated for the followings:

a) steady-state behaviour at medium- and low-speed operations;

b) transient capability of the FS-PTC under speed (rated) reversal;

c) weighting factor λ_{cv} sensitivity of the controller;

d) robustness against an external rated-load torque disturbance;

e) step rated-torque-transient characteristics;

f) average switching frequency.

4.6.1 Investigation of the steady-state behaviour at medium- and low-speed operations

Figure 4.5 shows the steady-state behaviour of the proposed FS-PTC system at a speed of 1000 r/min at full-load torque (7.4 Nm). From top to bottom, the curves are the stator current, estimated torque, stator flux and neutral-point voltage. The performance in terms of the torque and flux ripple is good (0.90 Nm and 0.02 Wb, respectively). The neutral-point voltage ΔV_{c12} is within 1.1 V(p–p)—0.19% of the used dc-link voltage—which is acceptable. The THD of the stator current i_a, calculated with 20 cycles up to maximum 5 kHz using MATLAB powergui, is 3.43%. Figure 4.6 shows the responses for the SPVs-based FS-PTC strategy. It can be seen that the THD of the stator current,

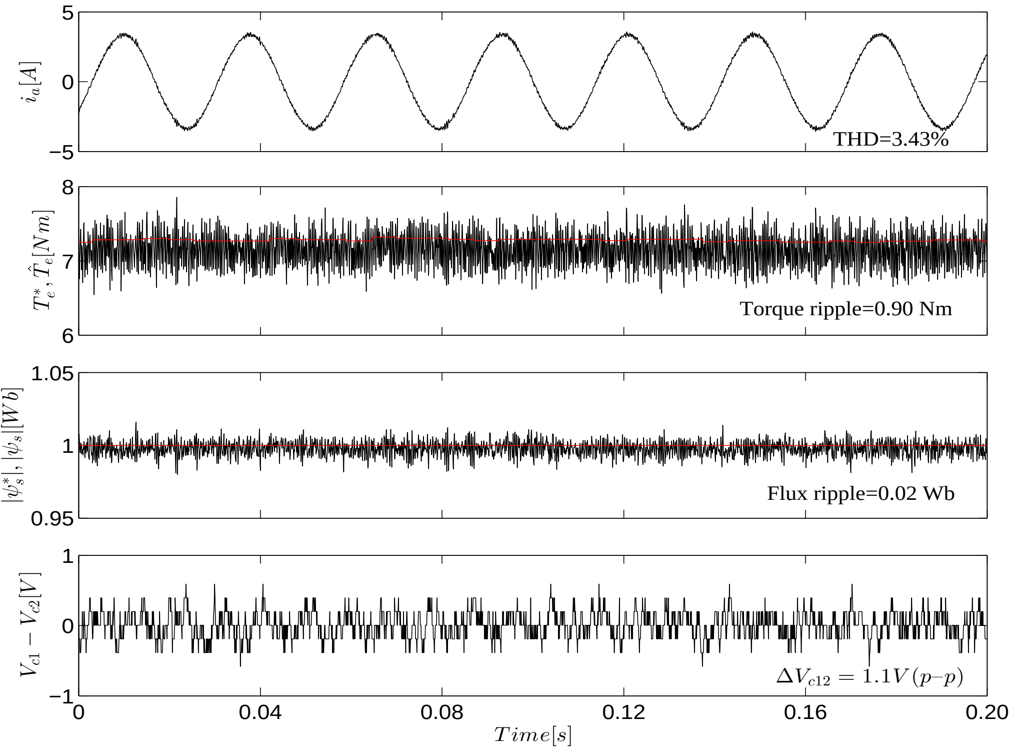

Figure 4.5: Experimental steady-state waveforms for the proposed all vectors based FS-PTC at 1000 r/min under rated-load torque. From top to bottom, stator current, torque, stator flux and neutral-point voltage.

torque and flux ripple, and neutral-point voltage are similar to the all voltage vectors based FS-PTC strategy.

Figure 4.7 illustrates the steady-state low-speed behaviour of the machine for the proposed FS-PTC at 200 r/min at 50% rated-load torque. The THD of the stator current, torque ripple and stator flux ripple are 4.14%, 0.83 Nm and 0.017 Wb, respectively. From Fig. 4.7, it is clear that two capacitor voltages are balanced, and the neutral-point voltage ΔV_{c12} is around 1 V(p–p). Hence, the overall low-speed performance of the proposed FS-PTC system is acceptable. The low-speed performance is also compared to that of the SPVs-based FS-PTC, as illustrated in Fig. 4.8. The low-speed performance of the SPVs-based FS-PTC strategy is similar to the all voltage vectors based FS-PTC strategy.

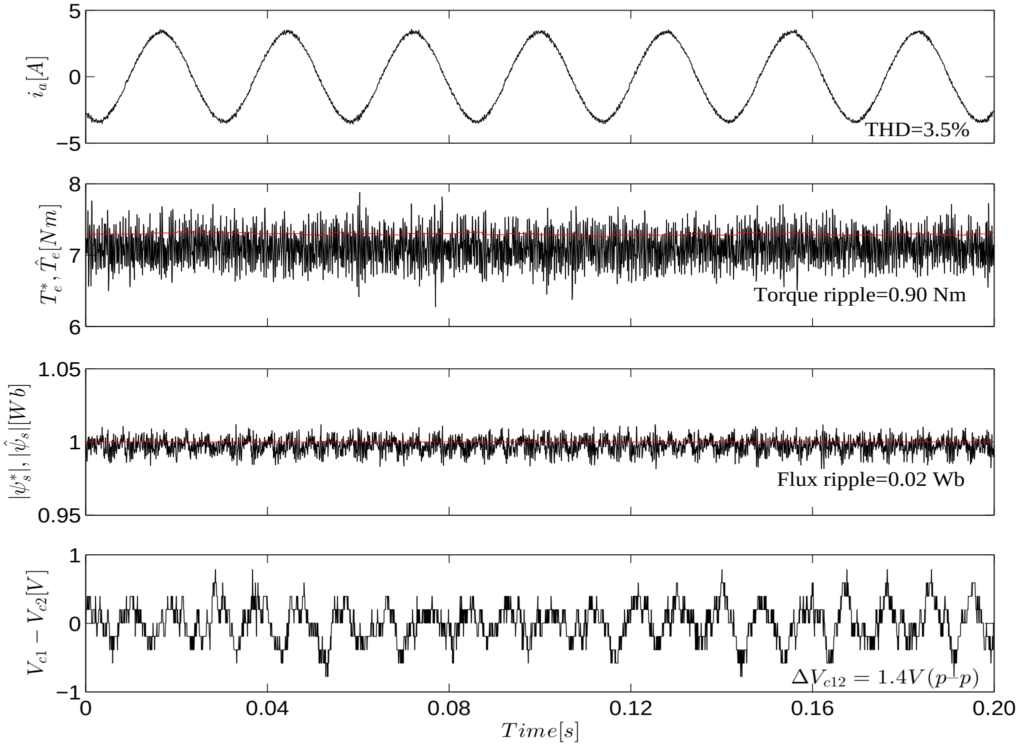

Figure 4.6: Experimental steady-state waveforms for the SPVs-based FS-PTC at 1000 r/min under rated-load torque. From top to bottom, stator current, torque, stator flux and neutral-point voltage.

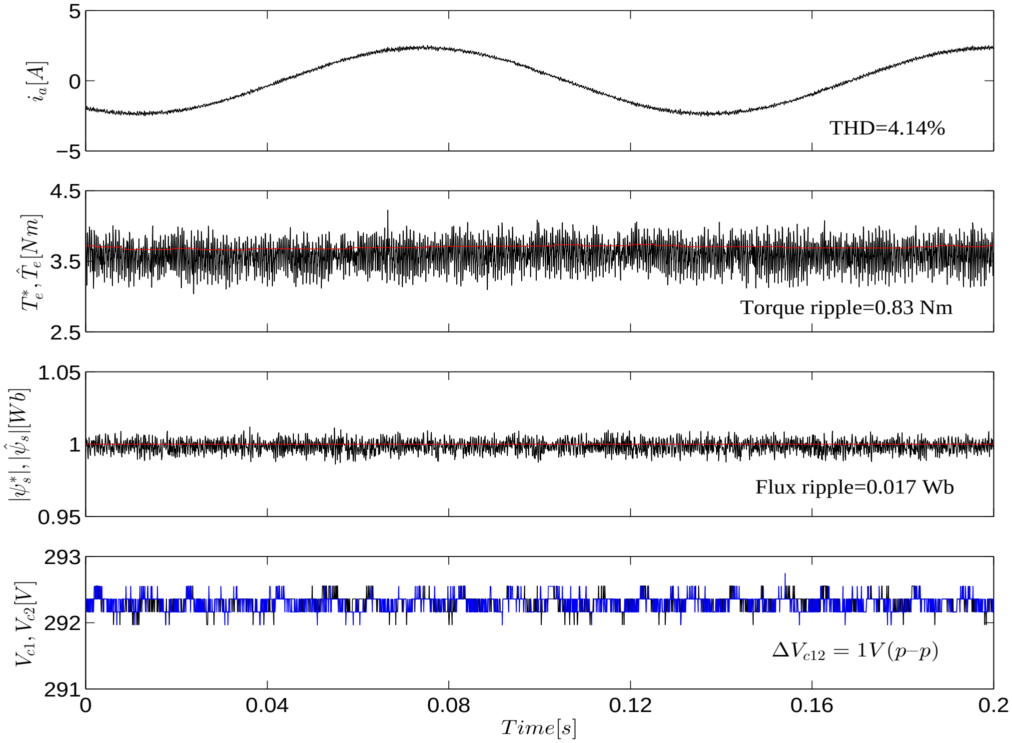

Figure 4.7: Experimental steady-state low-speed behaviour of the machine for the proposed FS-PTC at 200 r/min under 50% rated-load torque. From top to bottom, stator current, torque, stator flux and two dc-link voltages.

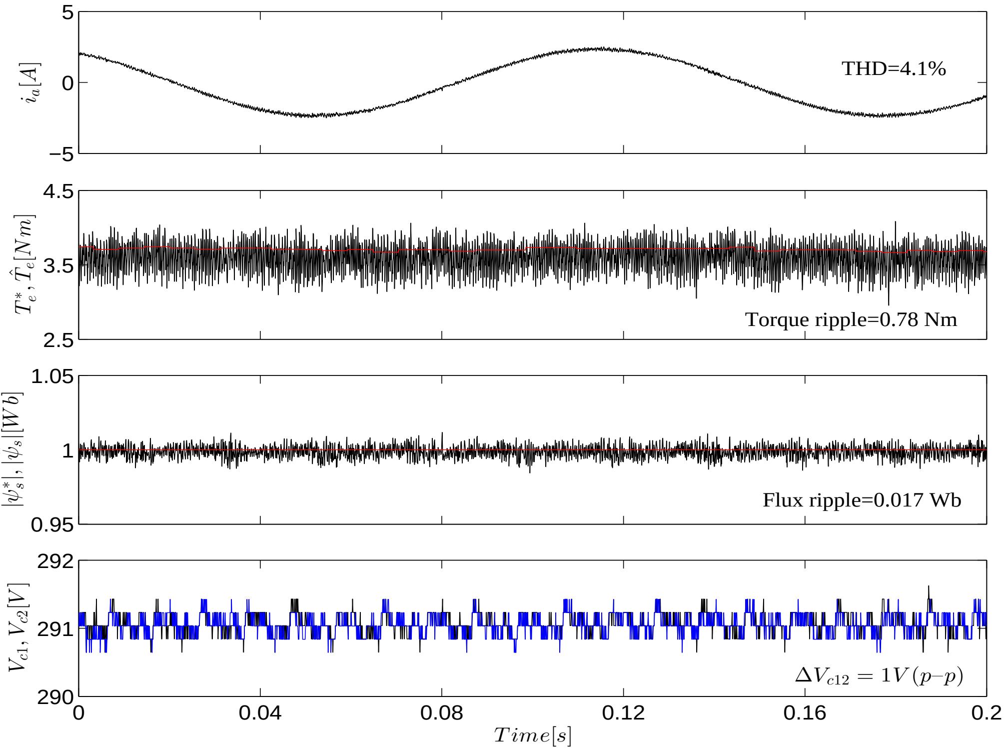

Figure 4.8: Experimental steady-state low-speed behaviour of the machine for the SPV-based FS-PTC at 200 r/min under 50% rated-load torque. From top to bottom, stator current, torque, stator flux and two dc-link voltages.

4.6.2 Investigation of the transient capability under rated-speed reversal

In order to test the transient capability of the proposed FS-PTC, the sudden reverse speed operation at the rated-speed of 1415 r/min without load torque is performed. However, the dc machine is connected to the fed motor. Figure 4.9 presents the behaviour of the control system. The stator flux is constant at its nominal value of 1.0 Wb. The performance in terms of torque and flux ripple is good; the torque ripple and the flux ripple are 0.8 Nm and 0.018 Wb, respectively. During the speed reversal, the ripple is slightly increased. This is because of the higher current flowing in the stator winding. The two capacitor voltages are also increased due to the regenerative process. The stator flux produces good sinusoidal stator current waveform; the THD of the stator current i_a is 4.42%. It is important to note that the capacitor voltages are balanced with very small fluctuations in both the transient and steady-state conditions; the maximum voltage fluctuation is 1.5 V during the transient. More importantly, the neutral-point voltage is always within 1V—0.17% of the used dc-link voltage—as shown in a small scale representation in Fig. 4.9. Hence, the neutral-point voltage has very negligible effect on the torque and flux ripple. Similar behaviour is investigated at the rated-speed-transient for the SPVs-based FS-PTC strategy, as illustrated in Fig. 4.10.

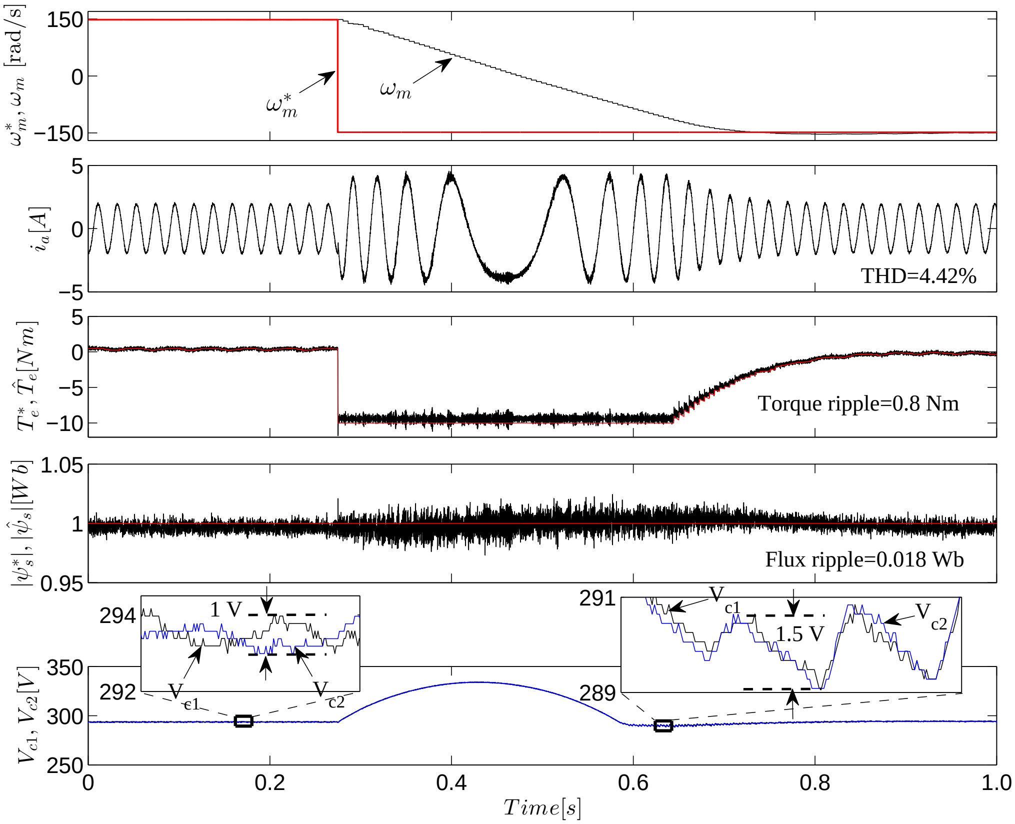

Figure 4.9: Experimental waveforms of speed, stator current, torque, stator flux and two capacitor voltages for the proposed FS-PTC at no-load at rated-speed (1415 r/min) reversal condition.

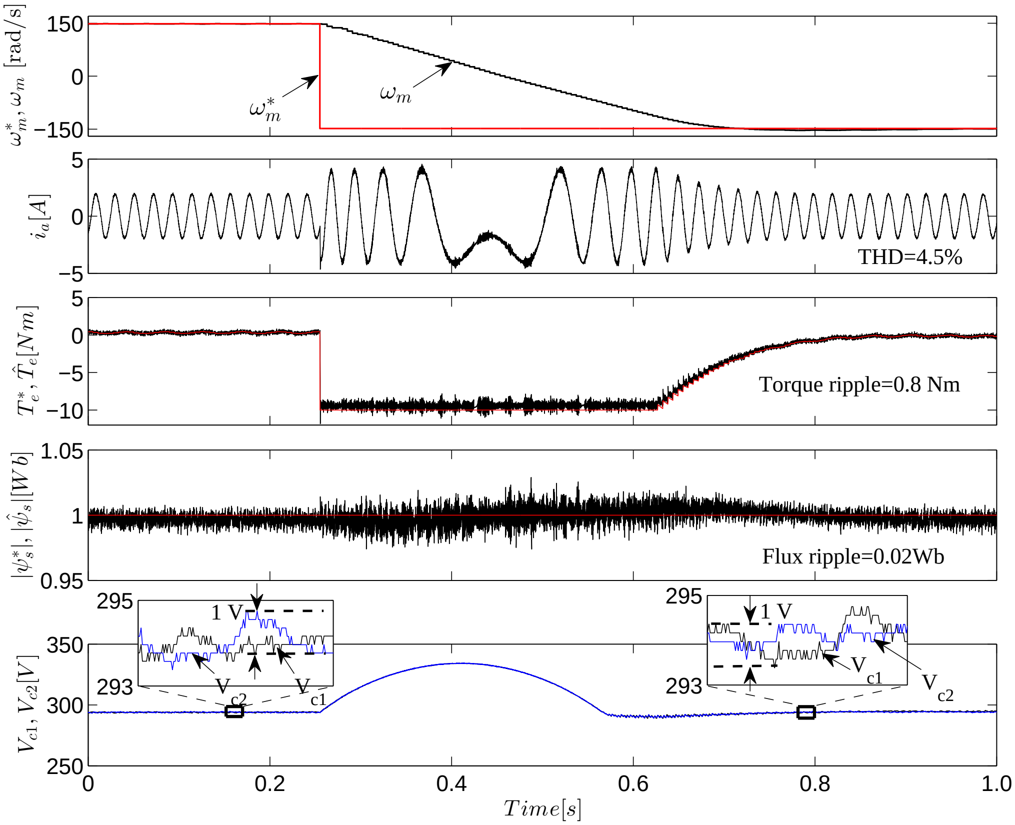

Figure 4.10: Experimental waveforms of speed, stator current, torque, stator flux and two capacitor voltages for the SPVs-based FS-PTC at no-load torque at rated-speed (1415 r/min) reversal condition.

4.6.3 Weighting factor λ_{cv} sensitivity of the controller

The weighting factors designing for the cost function of the proposed controller is not as complicated. This is because after a certain value of the weighting factor λ_{cv} of the neutral-point voltage ΔV_{c12}, the performance of the controller is almost unaffected with its change. To clarify these statements, another steady-state test is carried out at 700 r/min at no-load torque, and the weight λ_{cv} is increased from 0.00001 to 0.001 gradually within the time 0.0 to 0.5 s. The torque, stator flux and neutral-point voltage are unaffected with the change of λ_{cv}, as it can be seen from Fig. 4.11. Hence, λ_{cv} does not affect the controller performance after a certain value. This insensitivity of the controller facilitates the selection of a proper value of another weighting factor λ_n in the cost function.

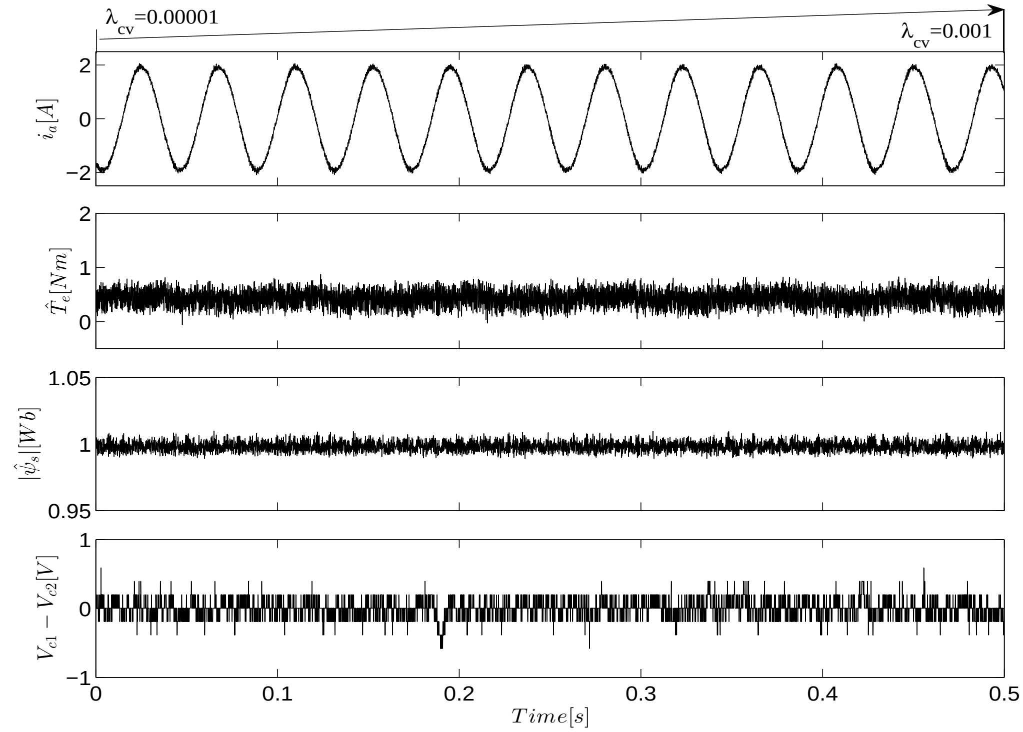

Figure 4.11: Experimental steady-state sensitivity analysis of the proposed controller with the change of weighting factor λ_{cv} of the neutral-point voltage ΔV_{c12} in the cost function at 700 r/min.

4.6.4 Investigation of the robustness against a rated-load torque disturbance

The robustness of the proposed control system against an external rated-load torque disturbance is tested, and is depicted in Fig. 4.12. There is a slight drop in the speed due to the load disturbance. The controller recovers the original speed within a short time (0.32 s). The load, which is dependent on rotor speed, is suddenly changed from no-load (0.8 Nm) to rated-load torque (7.4 Nm) as a disturbance on the machine. The torque ripple, flux ripple and fluctuations of dc-link voltages are slightly increased by 31.25%, 29.41% and 33.13%, respectively, after added load, as shown in Fig. 4.12. This is because the stator current magnitude is increased. However, the stator current THD is reduced by 22.95%. This improvement is due to the increase of the power component—load component—of the stator current. Although the two dc-link voltages are reduced by 4V around after added load and fluctuate within a range, they are almost balanced in all operating conditions, as can be seen in Fig. 4.12. Hence, the neutral-point voltage is very small and, thus, the control performance is unaffected by the neutral-point voltage. During load change, the stator flux remains as constant at its rated value, which ensures decoupled control of torque and flux. The robustness against a rated-load torque disturbance is also investigated for the SPVs-based FS-PTC strategy; the responses are shown in Fig. 4.13. It is seen that all the responses are similar to the all voltage vectors based FS-PTC strategy.

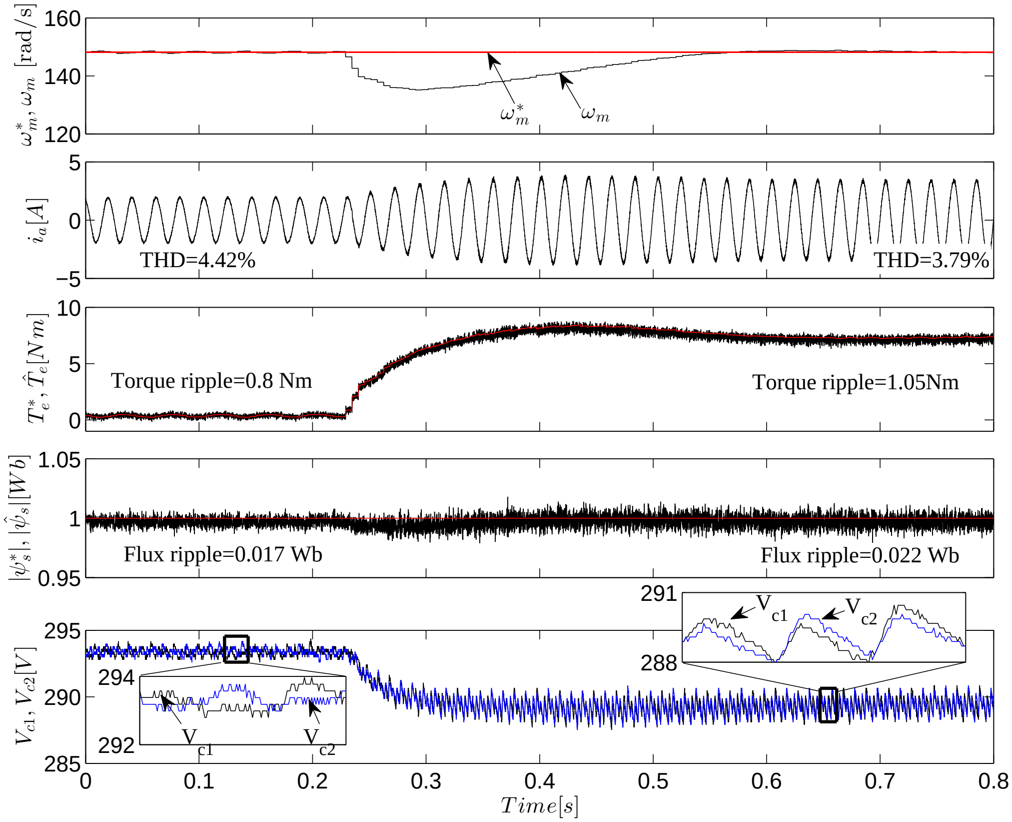

Figure 4.12: Experimental dynamic behaviour of the machine for the proposed FS-PTC at rated-speed under an external rated-load torque disturbance.

4.6.5 Step rated-torque response characteristics

Figure 4.14 illustrates the step rated-torque response characteristics. Initially, the machine is started with 100 r/min, and suddenly a step speed of 1000 r/min is then commanded to achieve a step torque command. The controller only selects large and medium voltage vectors—most prominently $\boldsymbol{v}_{22}$ or $\boldsymbol{v}_{16}$ in this case—during torque transient; this yields fast dynamic response, as shown in Fig. 4.14. The torque rise time of the proposed controller is 0.5 ms, which is excellent. From Fig. 4.14, it is clear that the dc-link voltages are balanced in both transient and steady-state conditions. Figure 4.15 shows the step rated-torque transient characteristics for the SPVs-based FS-PTC strategy. During the transient, the controller selects medium vectors (in this case $\boldsymbol{v}_{20}$) continuously. This yields fast dynamic response, similar to the proposed all voltage vectors based FS-PTC strategy.

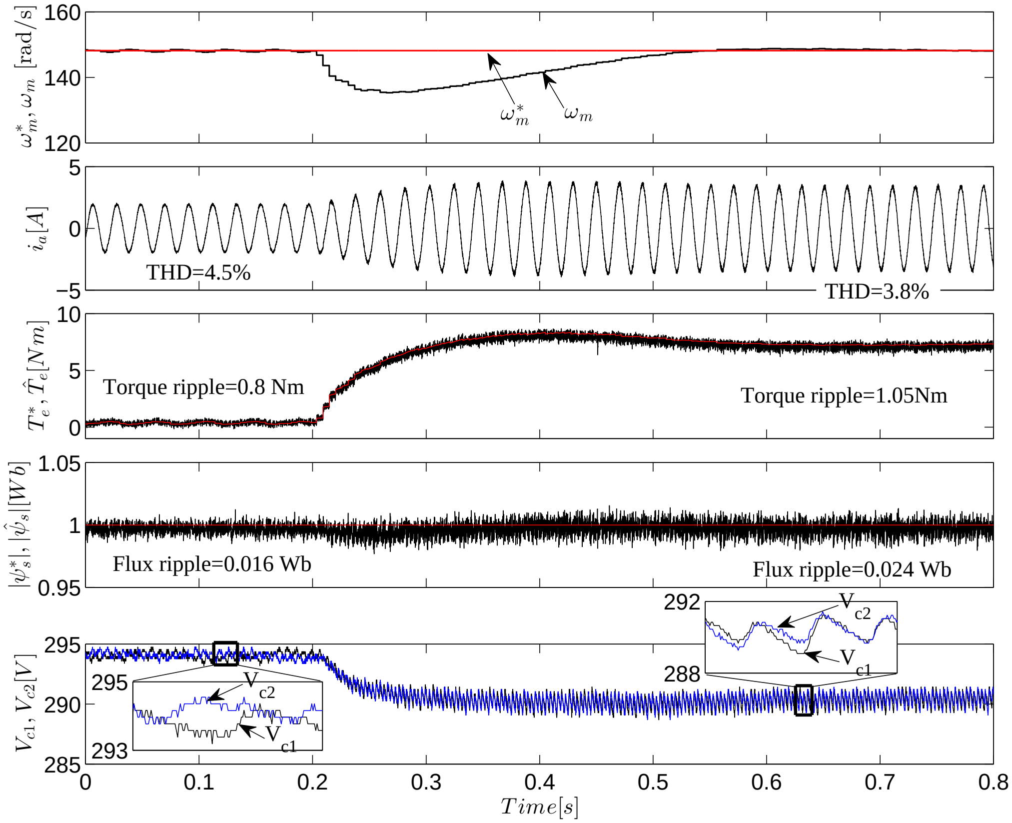

Figure 4.13: Experimental dynamic behaviour of the machine for the proposed SPVs-based FS-PTC at rated-speed under an external rated-load torque disturbance.

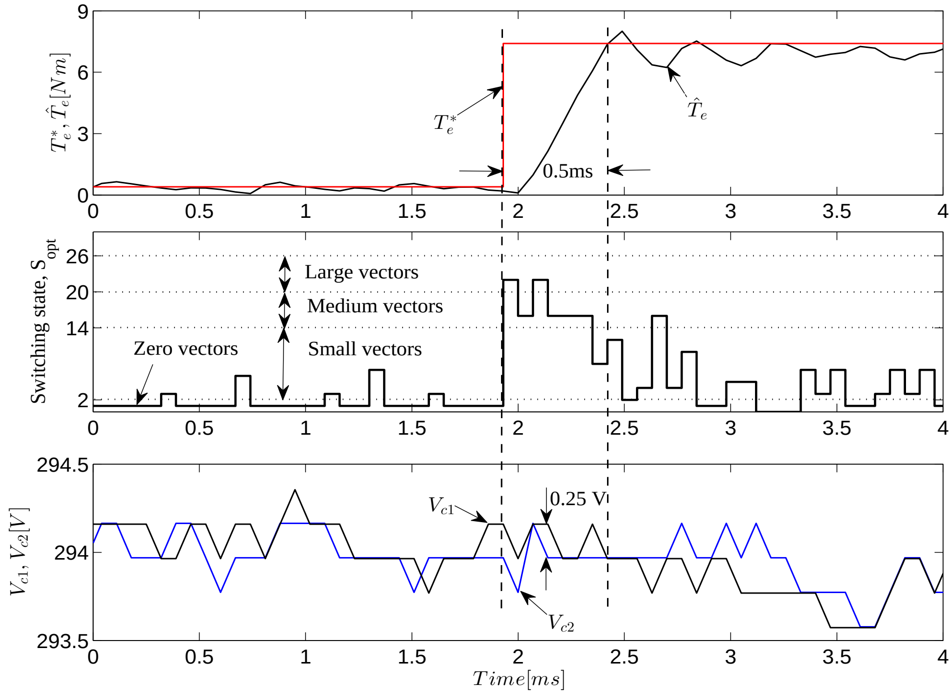

Figure 4.14: Experimental step rated-torque response of the proposed FS-PTC strategy showing selected inverter switching state and dc-link voltages.

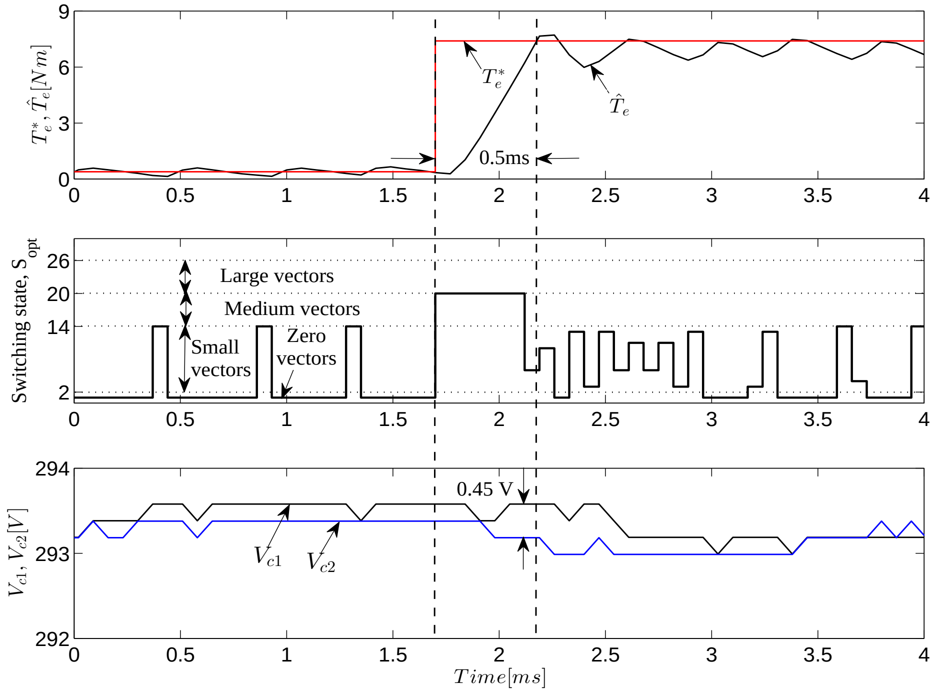

Figure 4.15: Experimental step rated-torque response of the SPVs-based FS-PTC strategy showing selected inverter switching state and dc-link voltages.

4.6.6 Investigation of the average switching frequency

Another investigation is conducted to observe the average switching frequency behaviour of the proposed FS-PTC strategy. We may recall that the switching transition term is included in the cost function to reduce the average switching frequency $\bar{f}_{sw}$ of the inverter and, thus, the switching losses. In the whole operating range of the machine, the average switching frequencies are reduced by up to 1.49 kHz (46%) with respect to the controller without switching transition term in the cost function, as shown in Fig. 4.16(a). For easy plotting, in Fig. 4.16(a), the average switching frequencies corresponding to the full-load torque (7.4 Nm) and rated-speed (1415 r/min) have been considered against the load torque of 7 Nm and the speed of 1400 r/min, respectively. The reduction in $\bar{f}_{sw}$ depends on the operating conditions of the motor—different speeds with different connected loads. Figure 4.16(b) shows that the average switching frequencies are reduced by significantly up to 1000 r/min with different connected loads. More importantly, the average switching frequencies are not varied over a wide frequency range in all operating conditions. For a particular speed, the maximum variation in average switching frequency is 9% of its maximum average value (1.78 kHz), which is almost constant, over a wide speed range of 200 to 1400 r/min at 0–7.4 Nm load torque. Figure 4.17(a) shows the average switching frequency and its variation at different speeds and loads for the SPVs-based FS-PTC and all vectors based FS-PTC. The average switching frequency under both control strategies is influenced by different speeds and loading conditions. Figure 4.17(b) gives clear information about the variation range of average switching frequency in all operating conditions; the variation ranges are 1.37–1.95 kHz and 1.28–1.78 kHz for the SPVs and all vectors based FS-PTC strategies, respectively. In case of the SPVs-based FS-PTC, the average switching frequency is slightly higher (maximum 380 Hz) than the all voltage vectors based FS-PTC at the speed range of 800 to 1100 r/min, as illustrated in Fig. 4.17(c). This is because a different weighting factor between torque and flux errors is employed in the cost function. Besides, including only one zero vector in the prediction loop somewhat increases the average switching frequency. However, at a particular speed, the maximum variation in average switching frequency is similar—within 11% of the maximum average value of 1.95 kHz—to the proposed all voltage vectors based FS-PTC. As the deviation is small, it is acceptable.

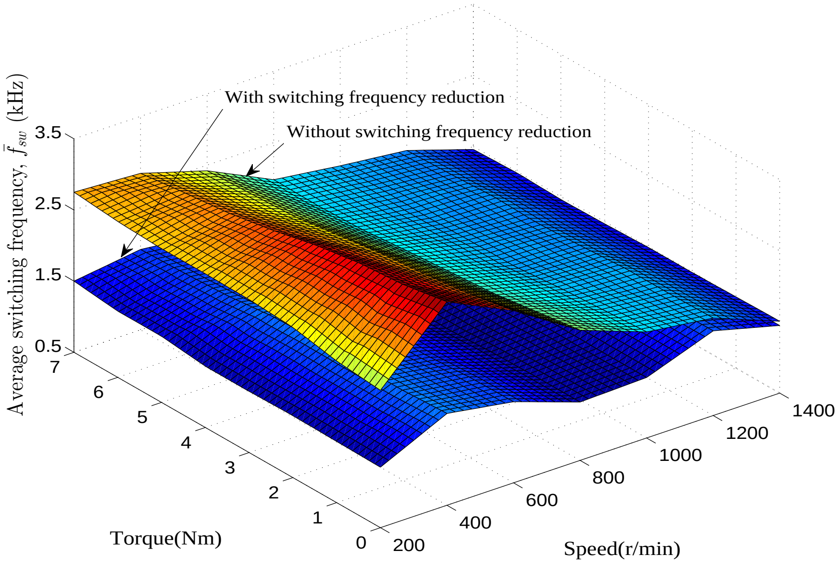

(a)

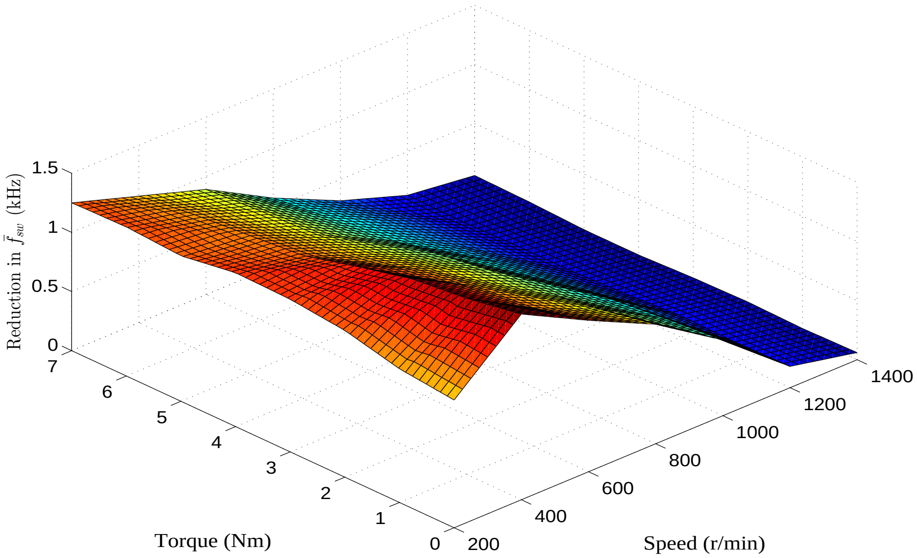

(b)

Figure 4.16: Experimental average switching frequencies $\bar{f}_{sw}$ for the proposed all vectors based FS-PTC from 200 to 1400 r/min and 0 to 7 Nm. (a) With and without the switching transition term included in the cost function, and (b) reduction in average switching frequencies.

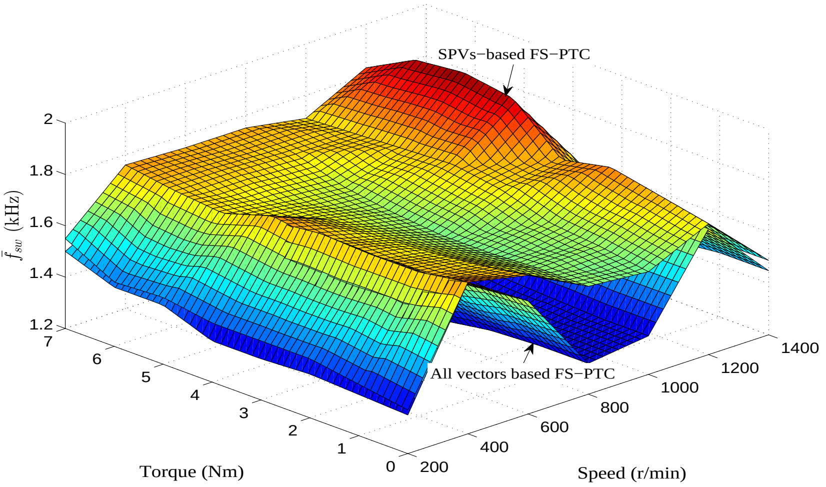

(a) Comparison with the all vectors based FS-PTC.

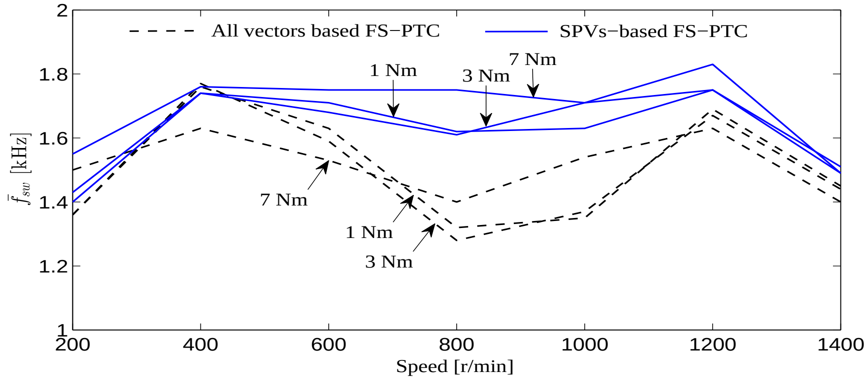

(b) $\bar{f}_{sw}$ vs. speed with torque as parameter.

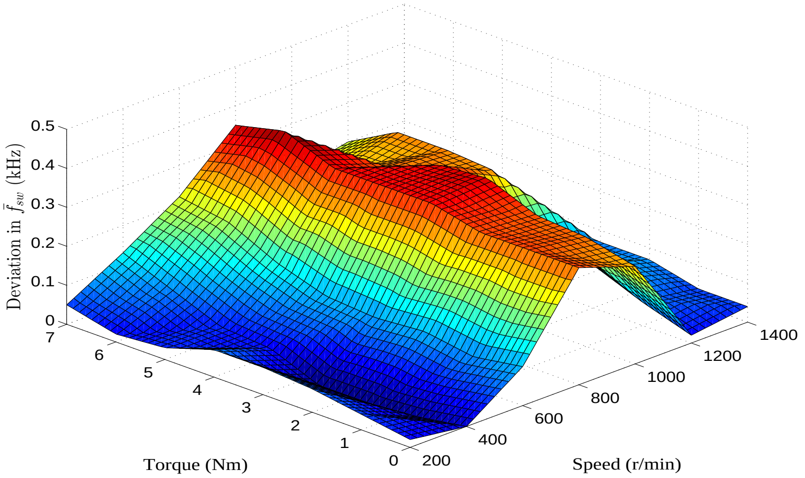

(c) Deviation in $\bar{f}_{sw}$ from 200 to 1400 r/min and 0 to 7 Nm.

Figure 4.17: Experimental average switching frequencies for the SPVs-based FS-PTC.

4.7 Performance comparison of FS-PTC with the FOC and DTC strategies

For the comparison purpose, other classical control methods (FOC and DTC) are also implemented with the same experimental setup, as shown in appendix B. As the FS-PTC is a variable switching frequency strategy, the average switching frequency at the specific operation point is considered as a reference for the implementation of the FOC and DTC strategies to achieve the fairest possible comparison. Hence, all the control strategies are implemented with an equivalent switching frequency. The operation point is set at 1000 r/min at rated-load torque (7.4 Nm) condition.

FOC is implemented as the guideline presented in [46]; the control structure is shown in appendix B (see Fig. B.6). The current is sampled at around 14.3 kHz (70 μs). The carrier frequency of the modulator in FOC is set to 1.78 kHz. This is because the maximum average switching frequency for the proposed FS-PTC at 1000 r/min under different load torques (0 to 7.4 Nm) is around 1.78 kHz. However, the average switching frequency for the FS-PTC at 1000 r/min at full-load torque is 1.51 kHz. The maximum average switching frequency is considered as the carrier frequency in FOC for the fairest possible comparison. The gain coefficients of the two PI current controllers are tuned in ControlDesk; the controller parameters are given in Appendix A (see Table A.5).

For the implementation of the DTC strategy, a two-level hysteresis flux regulator and a five-level hysteresis torque regulator are employed [114], and the control structure is shown in Appendix B (see Fig. B.7). The flux and torque hysteresis bands chosen are 0.01 Wb and 1.40 Nm, respectively. The two bands are tuned in such a way that the DTC strategy yields a similar average switching frequency to that of the proposed FS-PTC. The redundant states of the inverter are used to control the neutral-point voltage. As discussed in Chapter 2, each small vector has an alternative, and they (an small vector and the corresponding redundant) have the opposite effect on the dc-link capacitors charge. If a small vector is selected from the switching table and the difference between two capacitor voltages are out of permissible limit, then an appropriate small vector (between the selected small vector and its alternative redundant vector) is chosen. The

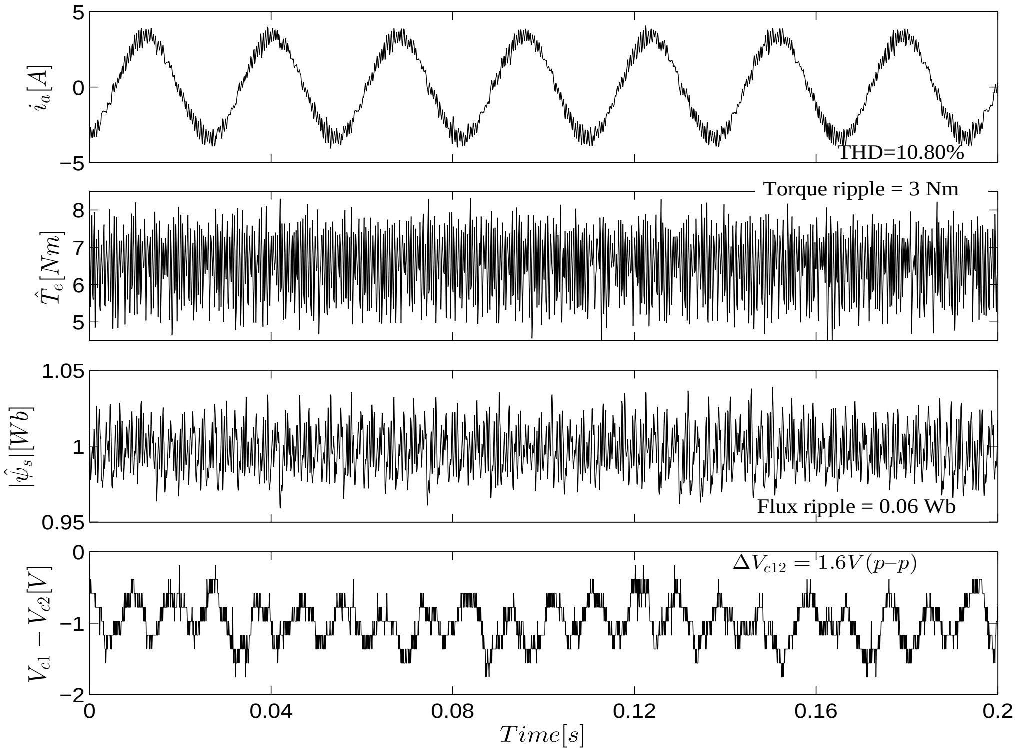

Figure 4.18: Experimental steady-state waveforms of stator current, estimated torque, estimated stator flux and neutral-point voltage for the DTC strategy at 1000 r/min under rated-load torque condition.

small vector is selected based on the sign of the capacitor voltage difference to control the capacitor voltages and, thus, the neutral-point voltage. The sampling time of the controller is set to 70 μs, which is the same as the proposed FS-PTC strategy.

Figures 4.18 and 4.19 show the responses of the system for the DTC and FOC strategies, respectively. From Fig. 4.18, it is clear that the classical DTC suffers not only from the large torque and flux ripple but also from the large current THD. By comparing between Figs. 4.5 and 4.19, it can be seen that the proposed FS-PTC strategy can compete with the FOC strategy at an equivalent switching frequency. To make a much clearer comparison, detailed quantitative results are presented in Table 4.4. The switching frequency for the FOC strategy is slightly higher. This is because, as mentioned previously, the maximum average switching frequency for the proposed FS-PTC at 1000 r/min and under different loading conditions is 1.78 kHz. During experiment, it is observed that FOC yields smaller steady-state torque and flux ripple, and current THD than the FS-

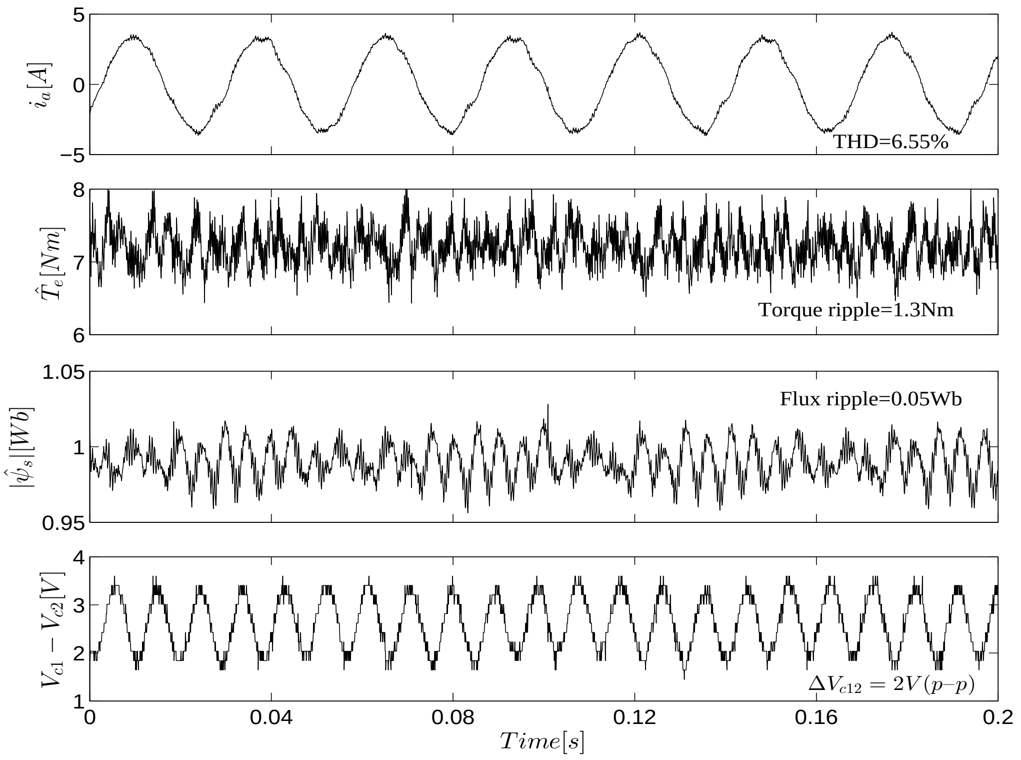

Figure 4.19: Experimental steady-state waveforms of stator current, estimated torque, estimated stator flux and neutral-point voltage for the FOC strategy at 1000 r/min under rated-load torque condition.

PTC at the switching frequency of 2 kHz. However, for the fairest possible comparison, those results have not been considered in the present analysis. In Table 4.4, the abbreviations f_{av} and f_{con} indicate the average and constant switching frequencies, respectively. It is important to note that the computational burden of the proposed FS-PTC is much higher compared to the both DTC and FOC strategies. However, the computational burden of the proposed FS-PTC is already reduced by 38% using the SPVs strategy.

Table 4.4: Quantitative comparison of the steady-state performance for different control strategies at 1000 r/min at full-load torque (7.4 Nm) with an equivalent switching frequency

Index	DTC	FOC	FS-PTC	FS-PTC (SPVs)
Torque ripple (Nm)	3.0	1.3	0.90	0.90
Flux ripple (Wb)	0.06	0.05	0.02	0.02
THD for i_a (%)	10.80	6.55	3.43	3.5
Neutral-point voltage (V_{p-p})	1.6	2.0	1.1	1.4
Switching frequency (kHz)	1.55 (f_{av})	1.78 (f_{con})	1.51 (f_{av})	1.71 (f_{av})
Calculation time (μs)	9.34	19.7	59.15	36.90

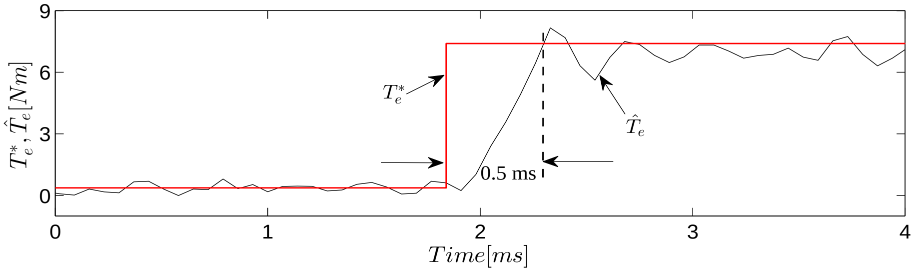

Figure 4.20: Experimental step rated-torque response of the DTC strategy.

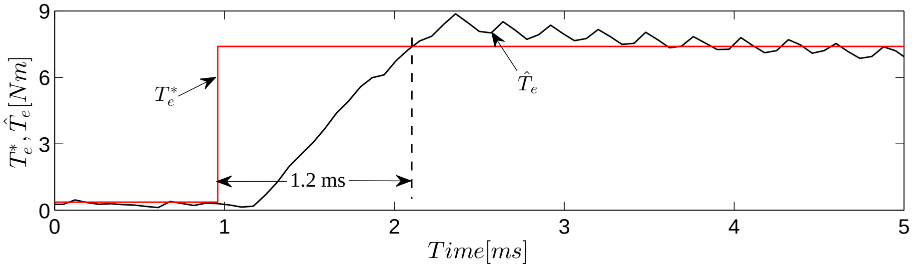

Figure 4.21: Experimental step rated-torque response of the FOC strategy.

Figs. 4.14, 4.20 and 4.21 also show that the torque dynamic of the proposed FS-PTC is faster than FOC strategy and is similar to the DTC strategy, as expected.

4.8 Performance comparison between the two- and three-level inverter fed IM drives

Finally, Table 4.5 presents another quantitative performance comparison between the 2L-VSI and 3L-NPC VSI fed IM drives. In both cases, all the available voltage vectors are evaluated in prediction and optimisation steps of the FS-PTC strategy. The computational capacity requirement for the algorithm of 3L-NPC VSI fed drive is higher than the 2L-VSI fed drive; thus, the algorithms are implemented with different sampling frequencies. It is shown that the THD of the stator current, torque ripple, flux ripple and average switching frequency for the 3L-NPC inverter are reduced by 28.7%, 41.9%, 31% and 51.3%, respectively, compared to the two-level inverter, as more number of voltage vectors are available in the 3L-NPC inverter. For this comparison, the steady-state performance at 1000 r/min at rated-load torque (7.4 Nm) is considered. The variation range of average switching frequency over a wide speed range is reduced significantly. However, the torque rise time is similar as 2L-VSI fed drive. This is because long and medium voltage vectors are selected during torque-transient.

Table 4.5: Quantitative dynamic performance comparison between the two- and three-level inverter fed IM drives

Index	2L-VSI	3L-NPC VSI
THD for i_a (%)	4.81	3.43
Torque ripple (Nm)	1.55	0.90
Flux ripple (Wb)	0.029	0.020
Average switching frequency (kHz)	3.10	1.51
Variation range of average switching frequency (kHz)	1.58–5.58	1.28–1.78
Torque rise time (ms)	0.53	0.50

4.9 Summary

This chapter has proposed an FS-PTC of IM drive, fed by a 3L-NPC VSI. The effectiveness of the proposed controller has been verified by extensive experimentation. The controller limits the neutral-point voltage within 0.2% of the dc-link voltage; thus, the drawback inherited from the converter topology is tackled effectively by including the voltage in the cost function. The average switching frequency is significantly reduced (apart from the inverter topology itself) by up to 46%. This is achieved by including the number of switching transitions in the cost function. The variation in average switching frequency for a particular speed at different load torques is within 9% of the maximum average switching frequency, which is almost constant. Good dynamic performance in terms of stator current THD, torque and flux ripple, robustness against load disturbance and step torque response is also achieved due to the increased number of voltage vectors available in the 3L-NPC VSI. The computational burden of the proposed FS-PTC is reduced by 38% using the SPVs strategy, without affecting the dynamic performance of the system. Experimental results also verify that the dynamic performance of the proposed FS-PTC is better than the classical DTC and FOC strategies at the specific operation point (equivalent switching frequency). Finally, another comparison between the 2L-VSI and 3L-NPC VSI fed drives is presented, showing the superiority of the 3L-NPC inverter over the two-level inverter in terms of current THD, torque and flux ripple, and average switching frequency and its variation range over a wide speed range.

Chapter 5

Simplified FS-PTC Using Reference Stator Flux Vector Calculator

5.1 Introduction

Apart from the number of available voltage vectors, complex torque calculations in the prediction loop of FS-PTC strategy increase the computational complexity. Thus, the FS-PTC algorithm demands more processing power, especially when phase number and inverter levels increase. Another problem is the selection of an appropriate weighting factor between torque and flux errors in the cost function. This chapter proposes a second simplified FS-PTC for the 3L-NPC VSI fed IM drive, which does not require torque calculations in the prediction loop and hence tuning effort on the weighting factor. The torque error is processed outside the prediction loop through a PI controller. A RSFVC is then employed to convert the torque and flux amplitude references into an equivalent stator flux reference vector. This flux reference is used in the cost function for stator flux error calculation. To reduce the computational complexity further, the proposed RSFVC is combined with the SPVs-based FS-PTC strategy, which is called a compound FS-PTC. Experimental results confirm that the proposed RSFVC-based FS-PTC reduces the computation time significantly and retains the advantages of conventional FS-PTC, such as fast dynamic response, robustness, low torque and flux ripple, and low stator current THD. It is useful to mention here that the all voltage vectors based FS-PTC

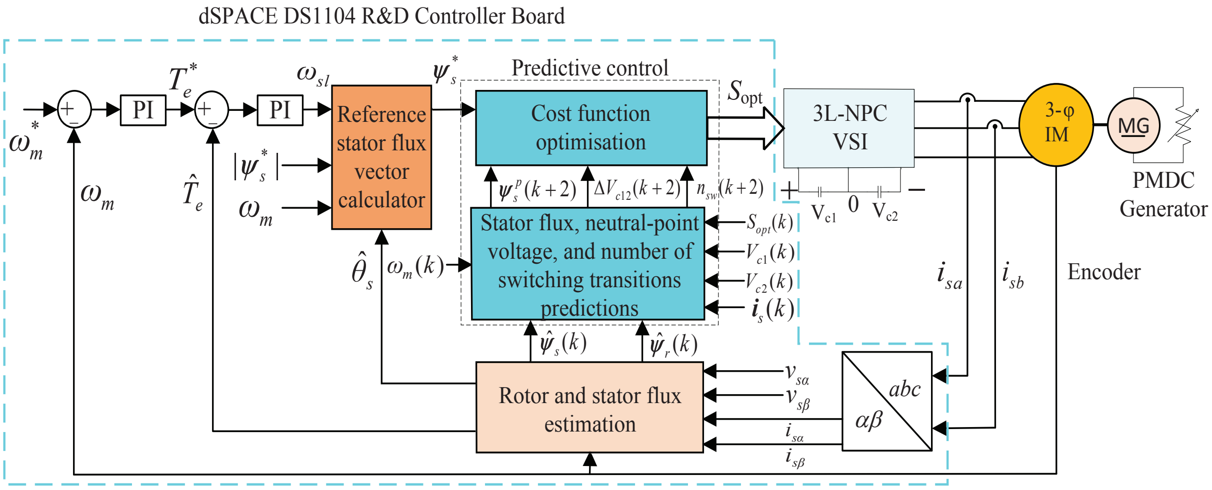

Figure 5.1: Proposed RSFVC-based simplified FS-PTC scheme.

proposed in chapter 4 is called a conventional FS-PTC in this chapter.

This chapter addresses the third objective of the thesis. The chapter is structured as follows. The proposed RSFVC is discussed in Section 5.2. The control algorithm is summarised in Section 5.3. Section 5.4 presents a compound FS-PTC strategy, which is a combination of both RSFVC and SPVs. The computational efficiency improvement is discussed in Section 5.5. Section 5.6 presents experimental results and discussion.

5.2 Proposed RSFVC-based FS-PTC

The proposed RSFVC-based simplified FS-PTC strategy comprises four steps: estimation, reference flux vector calculation, prediction and optimisation, as shown in Fig. 5.1. The prediction loop is simplified by removing the complex torque calculations from the prediction loop. However, the stator flux is predicted inside the loop. No tuning effort is required for the weighting factor between torque and flux errors. The steps of the proposed RSFVC-based FS-PTC are discussed below.

5.2.1 Estimation

The estimation process of the stator and rotor flux is same, as detailed in Chapters 3 and 4.

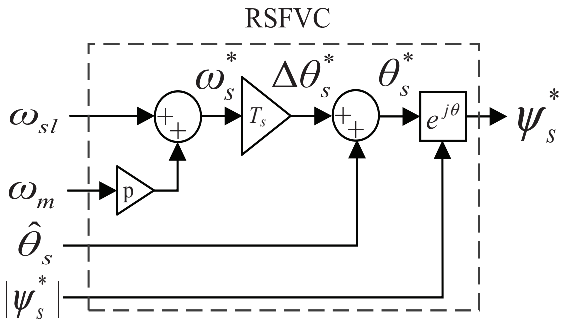

Figure 5.2: RSFVC based on both torque and stator flux amplitude references, measured rotor speed and calculated position of the stator flux.

5.2.2 Reference flux vector calculation

An equivalent stator flux reference vector $\boldsymbol{\psi}_s^*$ is produced using the RSFVC, and is applied to the controller for optimisation. Fig. 5.2 shows in detail the reference flux vector generated by the RSFVC. The angular slip frequency ω_{sl} (output of the torque regulator), measured rotor speed ω_m, position of the stator flux $\hat{\theta}_s$ at instant k and the amplitude of the stator flux $|\boldsymbol{\psi}_s^*|$ (which is assumed to be constant) are used as inputs to the RSFVC. In Fig. 5.2, the reference angular frequency of stator flux ω_s^* is produced by summing ω_{sl} and the rotor angular frequency ω_m. A PI controller is adopted to regulate the torque, as there is a nonlinear relationship exists between the torque dynamic and slip frequency under a constant $|\boldsymbol{\psi}_s|$ [8,115]. Reference [8], explains analytically that the rate of increasing of torque is almost proportional to the step difference of ω_{sl}. From [115], the expression of torque in terms of slip frequency is

$$T_e(t) = K\left(1 - e^{-\frac{t}{\tau}}\right)\omega_{sl} \tag{5.1}$$

where $K = \frac{3}{2}P\frac{L_m^2}{R_r L_s^2}\left|\boldsymbol{\psi}_s^*\right|^2$ and $\tau = \sigma\frac{L_r}{R_r}$.

The Laplace transform of Eq. (5.1) is

$$T_e(s) = K\left(\frac{1}{\tau s + 1}\right)\omega_{sl}(s) \Rightarrow \frac{T_e(s)}{\omega_{sl}(s)} = \frac{K}{\tau s + 1}. \tag{5.2}$$

Equation (5.2) shows that the relationship between the torque and slip frequency is equivalent to a first-order system. Hence, the PI controller is capable of tracking the reference torque. The equivalent system of the inner torque control loop with PI controller

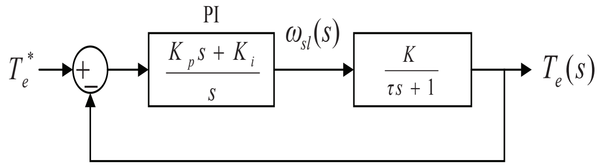

Figure 5.3: Inner torque control loop with PI compensation.

is shown in Fig. 5.3. Another PI controller for the outer speed-loop generates the reference torque. This reference torque is used to produce ω_{sl}. Hence, the new stator flux reference vector $\boldsymbol{\psi}_s^*$ is an optimal reference based on both torque and flux amplitude references.

The proposed RSFVC differs from the previous work published in [116], as the IM has a slip between the stator and rotor flux. In addition, the reference vector calculator in [116] was employed with a space vector modulation (SVM) based modified DTC strategy.

5.2.3 Prediction

The predictions of the stator flux, neutral-point voltage ΔV_{c12} and number of switching transitions n_{sw} are same, as detailed in Chapter 4.

5.2.4 Cost function optimisation

Considering only the torque and flux errors, the cost function g for the conventional FS-PTC is

$$g = \left| T_e^*(k+1) - T_e^p(k+1) \right| + \lambda_f \left| |\boldsymbol{\psi}_s^*| - |\boldsymbol{\psi}_s^p(k+1)| \right| \tag{5.3}$$

Using the calculated new reference stator flux vector $\boldsymbol{\psi}_s^*$, the cost function (5.3) can be expressed as

$$g = \left| \boldsymbol{\psi}_s^* - \boldsymbol{\psi}_s^p(k+1) \right|. \tag{5.4}$$

A weighting factor λ_f is avoided and hence the tuning effort.

Splitting into α and β components, Eq. (5.4) can be rewritten as

$$g = \left| \psi_{s\alpha}^* - \psi_{s\alpha}^p(k+1) \right| + \left| \psi_{s\beta}^* - \psi_{s\beta}^p(k+1) \right|. \tag{5.5}$$

Taking into account all the predicted variables, the complete cost function becomes

$$g = \left| \boldsymbol{\psi}_s^* - \boldsymbol{\psi}_s^p(k+1) \right| + \lambda_{cv} \left| \Delta V_{c12}(k+1) \right| + \lambda_n n_{sw}(k+1) \tag{5.6}$$

where λ_{cv} and λ_n are the two weighting factors of neutral-point voltage $\Delta V_{c12}(k+1)$ and number of switching transitions $n_{sw}(k+1)$, respectively.

Equation (5.6) shows that the cost function still contains two weighting factors (λ_{cv} and λ_n). However, the process of selecting these two weighting factors is well defined. First, λ_{cv} is tuned online until the ΔV_{c12} is around zero, while λ_n is set to zero. Then, the λ_n is tuned online until the ΔV_{c12} starts to increase. Details about the tuning procedures of λ_{cv} and λ_n have already been discussed in Chapter 4.

The delay compensation scheme [111] has been implemented to avoid one step delay caused by digital implementation. In this case, the cost function (5.6) is modified to

$$g = \left| \boldsymbol{\psi}_s^* - \boldsymbol{\psi}_s^p(k+2) \right| + \lambda_{cv} \left| \Delta V_{c12}(k+2) \right| + \lambda_n n_{sw}(k+2) \tag{5.7}$$

Among all the possible 27 switching states of the 3L-NPC VSI, the state that yields minimum g in Eq. (5.7) is selected as the optimal state S_{opt}, and applied to the motor terminals via the inverter.

5.3 Proposed control algorithm

The overall control procedure can be summarised by the following sequences.

Step 1) *Measurement*: Sampling $\boldsymbol{i}_s(k)$, $V_{c1}(k)$, $V_{c2}(k)$ and $\omega_m(k)$.

Step 2) *Apply*: Apply the optimum voltage vector $\boldsymbol{v}_{opt}(k)$.

Step 3) *Estimate*: Estimate the rotor flux $\hat{\boldsymbol{\psi}}_r(k)$ and the stator flux $\hat{\boldsymbol{\psi}}_s(k)$ using Eqs. (3.1) and (3.2), respectively.

Step 4) *Calculate*: Calculate the equivalent reference stator flux vector $\boldsymbol{\psi}_s^*$ using RS-FVC, as shown in Fig. 5.2.

Step 5) *Predict and evaluate*: Predict the stator flux $\boldsymbol{\psi}_s^p(k+2)$, neutral-point voltage $\Delta V_{c12}(k+2)$ and number of switching transitions $n_{sw}(k+2)$ using Eqs. (3.14), (4.5) and (4.6), respectively. Then, evaluate the predicted variables by calculating the cost g using Eq. (5.7). Perform these predictions and evaluations for all the 27 available voltage vectors.

Step 6) *Optimise*: Select $\boldsymbol{v}_{opt}(k+2)$ that results minimum g in Eq. (5.7). Return to step 1).

5.4 Compound FS-PTC: combination of the RSFVC and SPVs

The computational complexity of the proposed RSFVC-based FS-PTC is simplified further by reducing the number of iterations of the prediction loop. To do this, the SPVs strategy discussed in Chapter 4 is integrated with the proposed RSFVC-based FS-PTC, which is called compound FS-PTC; the control structure is shown in Fig. 5.4. The control strategy consists of estimation, reference flux vector calculation, selecting prediction vectors, predictions and cost function optimisation. As the SPVs strategy and RSFVC have already been discussed separately, here the compound FS-PTC will not be discussed again. However, it is useful to mention that the output of the RSFVC (i.e., $\boldsymbol{\psi}_s^*$) is used in the SPVs strategy for the flux-error calculation, and only 14 selected voltage vectors (instead of 27) are evaluated in the prediction loop. In addition, the gain coefficients of yhe PI speed and torque regulators are kept unchanged.

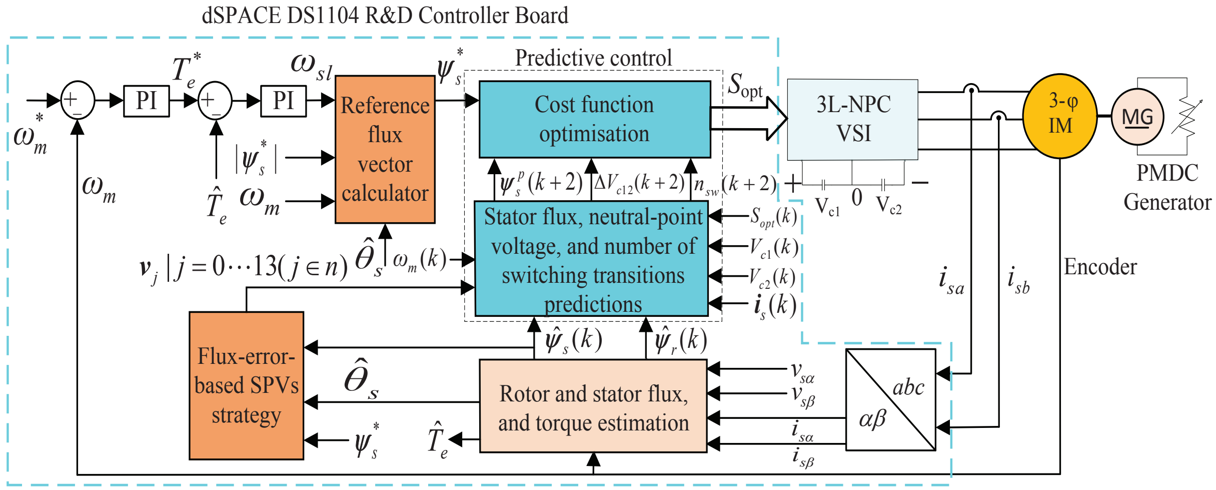

Figure 5.4: Compound FS-PTC scheme using both RSFVC and SPVs.

5.5 Computational efficiency improvement in the RSFVC-based FS-PTC algorithm

The control algorithm is coded in C environment. The required execution time of the proposed control algorithm is 36.82 μs, as shown in Table 5.1. This was 59.15 μs for the conventional FS-PTC algorithm. The computational efficiency of the prediction loop—comparing the values shown in the rectangular boxes—is improved by 56%. The overall computational efficiency of the control algorithm is improved by 38%. This is increased to 49% by including the SPVs strategy. The RSFVC takes only 4.40 μs. Hence, at the expense of a small execution time, the complex torque calculations are excluded from the prediction loop.

5.6 Experimental Results

The control algorithm is directly loaded to the dSPACE DS1104 R&D controller board through ControlDesk. The machines and the controller parameters are given in Appendix A. The experimental setup is shown in Appendix B. The sampling period of the controller is set to 70 μs.

Because of the inner torque control loop, the structure of the proposed RSFVC-based

Table 5.1: Execution times of the RSFVC-based FS-PTC, compound FS-PTC (RSFVC and SPVs) and conventional FS-PTC algorithms

Index	Execution time (μs)		
	RSFVC	Compound	Conventional
Measurement	4.39	4.39	4.39
Switching	0.12	0.12	0.12
Voltage and current calculations	0.72	0.72	0.72
Estimation	1.60	1.60	1.60
Reference flux vector calculation	4.40	4.40	0.0
Prediction vectors selection	0.0	1.28	0.0
Predictions	$\boxed{19.73}$	$\boxed{13.1}$	$\boxed{45.1}$
Optimisation	4.89	3.75	6.25
Switching frequency calculation	0.56	0.56	0.56
Total	36.82	30.33	59.15

FS-PTC is slightly different from the conventional FS-PTC structure. Hence, the stability of the proposed controller against parameters variation and dc-link voltage unbalance is tested at first. Then, the performance of the RSFVC-based FS-PTC in terms of torque and flux ripple, stator current THD, capacitor voltage balance and average switching frequency of the inverter is assessed by the following investigations:

a) stability against parameters variation and dc-link voltage unbalance;

b) steady-state behaviour;

c) speed-transient capability under rated-speed reversal;

d) robustness against rated-load torque disturbance;

e) torque-transient characteristics;

f) average switching frequency.

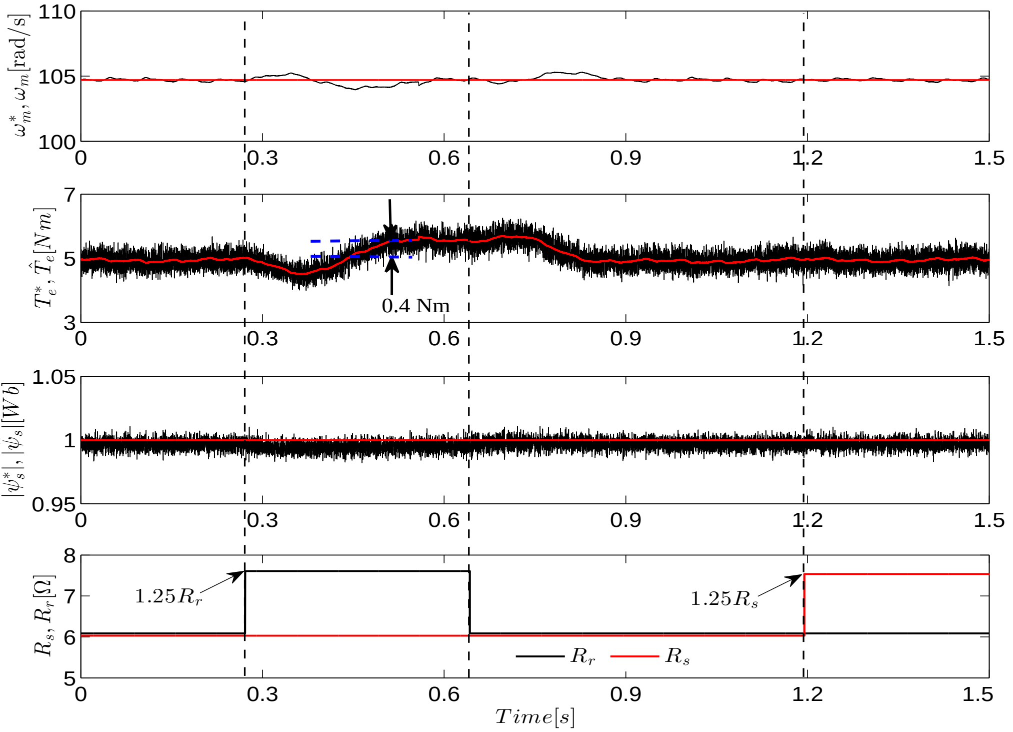

Figure 5.5: Experimental responses under step changes of R_r and R_s in the controller from 1 to 1.25 pu.

5.6.1 Stability test against parameters variation and dc-link voltage unbalance

The effects of R_r and R_s variation on the proposed control system are illustrated in Fig. 5.5, where controller parameters are step-changed by 0.25 pu. Since, the rotor current model is employed for the rotor flux estimation, the observer is influenced by the rotor resistance variation and insensitive to the stator resistance variation. Hence, the electromagnetic torque is increased by 8% (from 5 to 5.4 Nm) and the stator flux remains constant at 1.0 Wb. However, the oscillations in torque and flux are similar before and after changing the parameters in the controller. It can be seen that the rotor speed can follow the reference speed properly and the system is stable. The estimated torque and flux in Fig. 5.5 are based on the actual R_r and R_s, whereas the prediction model is based on the wrong R_r and R_s.

Fig. 5.6 shows the stability of the proposed control scheme with a 20% voltage un-

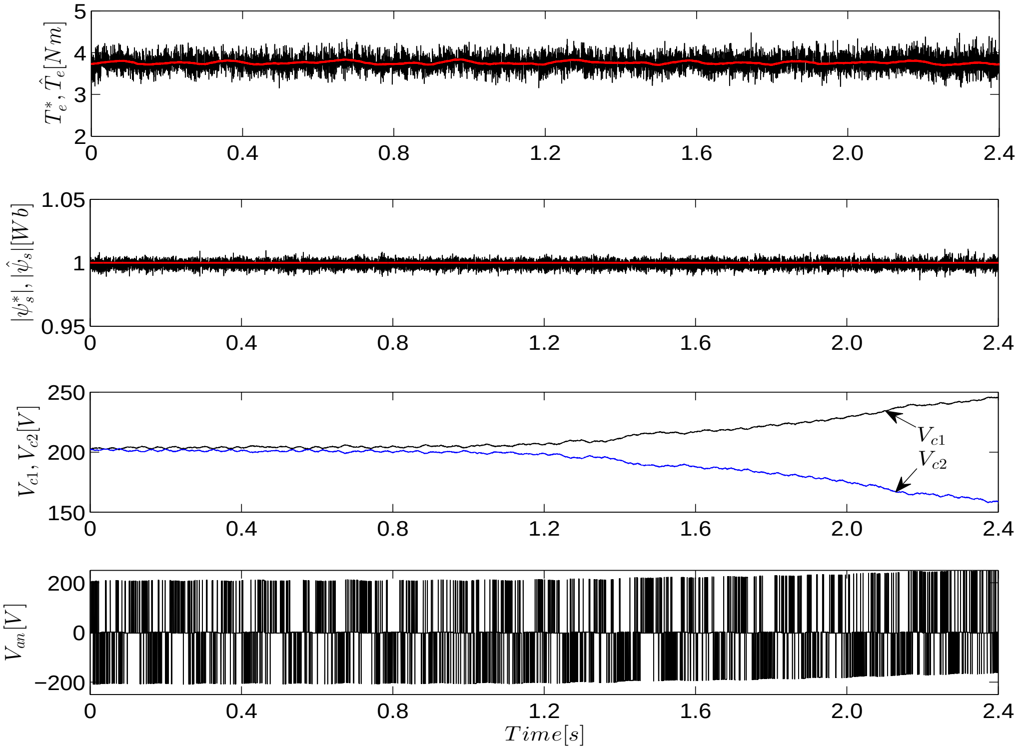

Figure 5.6: Experimental stability test at 200 r/min and 50% rated-load torque under the dc-link voltage unbalance by 20%.

balance. The machine is operated at 200 r/min with 50% rated-load torque. The torque and flux responses show that the system is stable under the dc-link voltage unbalance. However, the torque ripple is slightly increased due to the neutral-point voltage. The unbalance condition is produced online by setting $\lambda_{cv} = 0$ in the cost function (5.7). This investigation is carried out with a dc-link voltage 400 V to avoid capacitor over voltage.

5.6.2 Investigation of the steady-state behaviour

Figure 5.7(a) shows the steady-state behaviour of the proposed FS-PTC strategy at a speed of 1000 r/min at full-load torque (7.4 Nm). The performance in terms of torque and flux ripple is good; the torque ripple is 0.95 Nm and the flux ripple is 0.018 Wb. The two capacitor voltages are balanced, and the neutral-point voltage is thus around zero. The THD of the stator current i_a, calculated with 20 cycles up to maximum 5 kHz using MATLAB, is 3.5%. The current THD, torque and flux ripple, and neutral-point voltage are similar to the conventional FS-PTC, as illustrated in Fig. 5.7(b). Similar results have also been achieved for the compound FS-PTC, as shown in Fig. 5.8.

Steady-state low-speed behaviour is also tested at 200 r/min with 50% rated-load; the responses are illustrated in Fig. 5.9(a). The torque ripple, stator flux ripple and stator current THD are 0.86 Nm, 0.016 Wb and 4.3%, respectively. The low-speed performance is similar to the high-speed performance, as shown in Fig. 5.7(a) with different load torques. This confirms that the control system yields similar performance over a significant part of the operating range. From Figs. 5.9(a) and 5.9(b), it is seen that the low-speed performance of the RSFVC-based FS-PTC is similar to the conventional FS-PTC. The compound FS-PTC also yields similar low-speed performance to the conventional FS-PTC, as illustrated in Fig. 5.10.

Since the simplified FS-PTC strategies (RSFVC-based FS-PTC and compound FS-PTC) require less calculations, the controllers can be implemented with higher sampling frequency. The steady-state performance will then be improved. To test this steady-state improvement, the sampling time is set to 45 μs, and the responses for the RSFVC-based FS-PTC at 200 r/min at 3.7 Nm load torque are illustrated in Fig. 5.11. The current THD, torque ripple and flux ripple are reduced by 32.6%, 37.5% and 20.9%, respectively, as expected. As the sampling frequency is increased, the average switching frequency will be increased. There is an almost linear relationship between the sampling frequency and average switching frequency, as shown in Fig. 5.12. Hence, a trade-off must be maintained between the switching losses and the performance of the system (such as torque ripple, flux ripple and current THD).

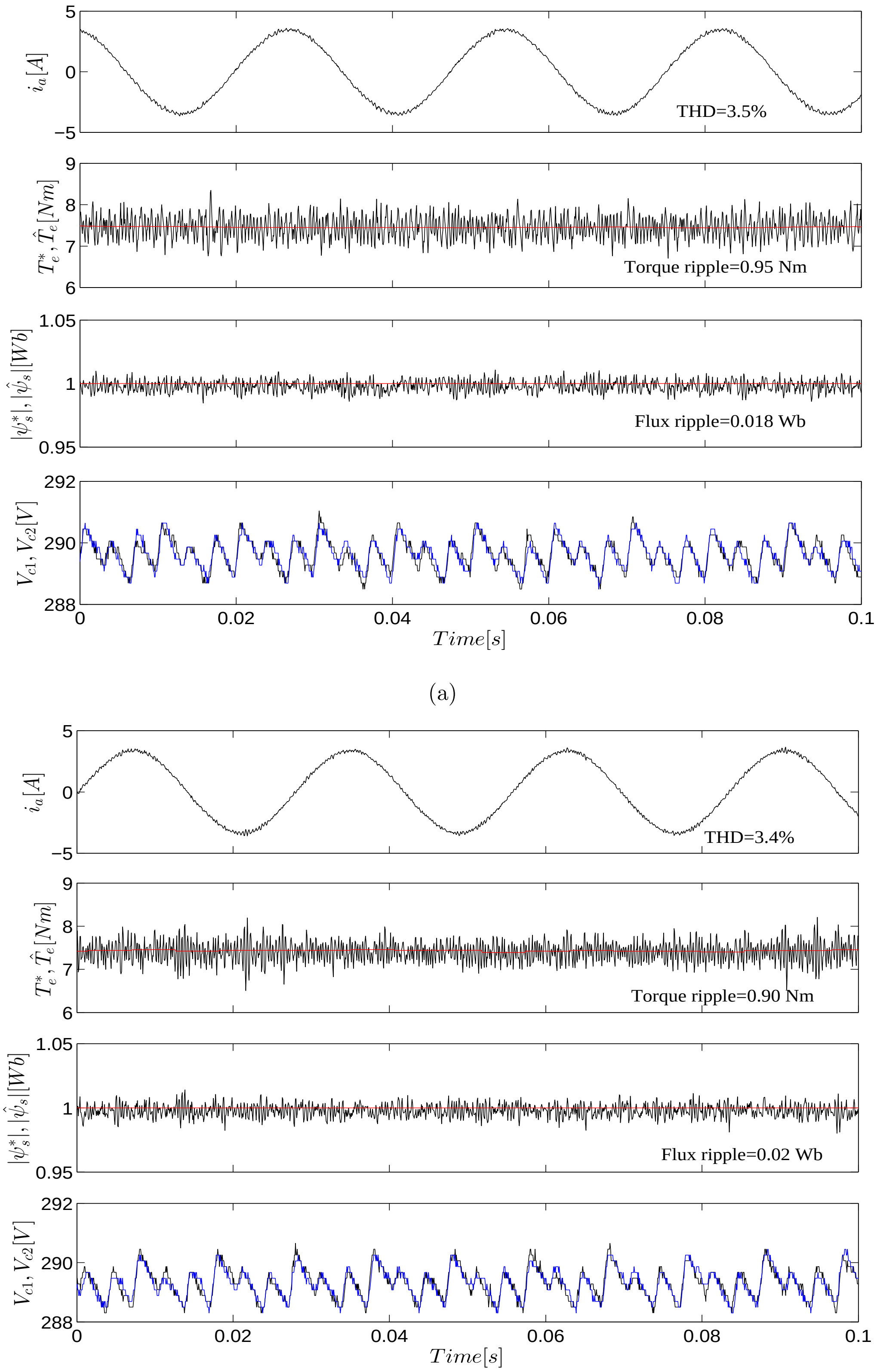

(a)

(b)

Figure 5.7: Experimental steady-state waveforms at 1000 r/min at rated-load torque. (a) RSFVC-based FS-PTC and (b) conventional FS-PTC.

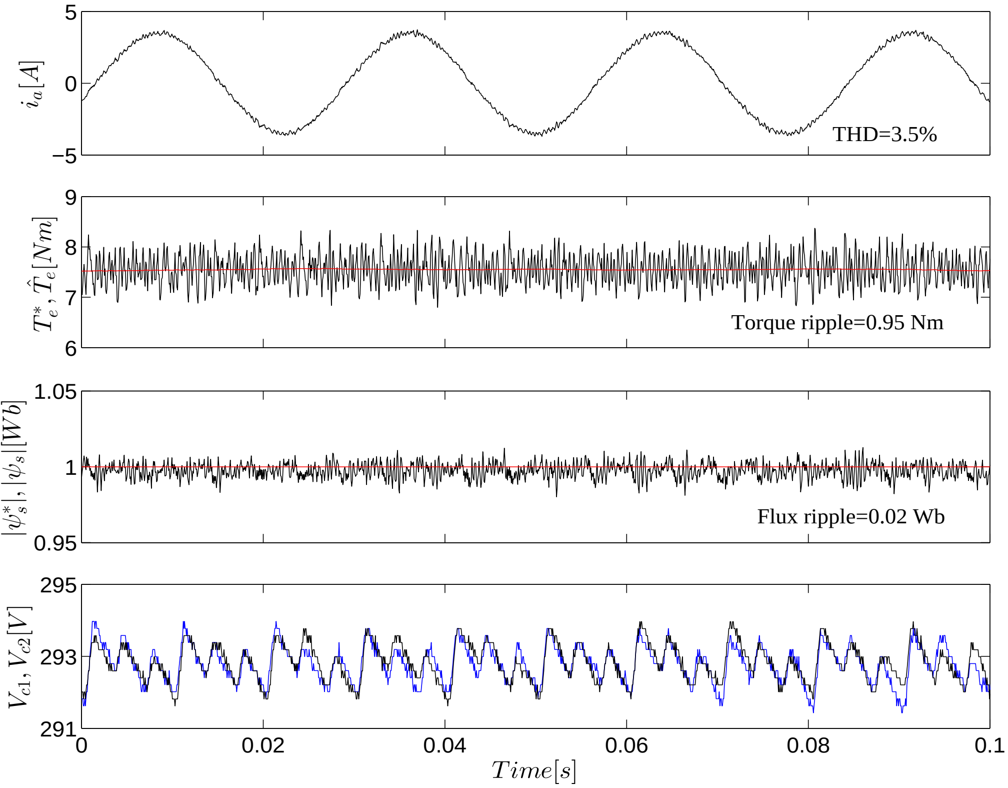

Figure 5.8: Experimental steady-state waveforms at 1000 r/min at rated-load torque for the compound FS-PTC.

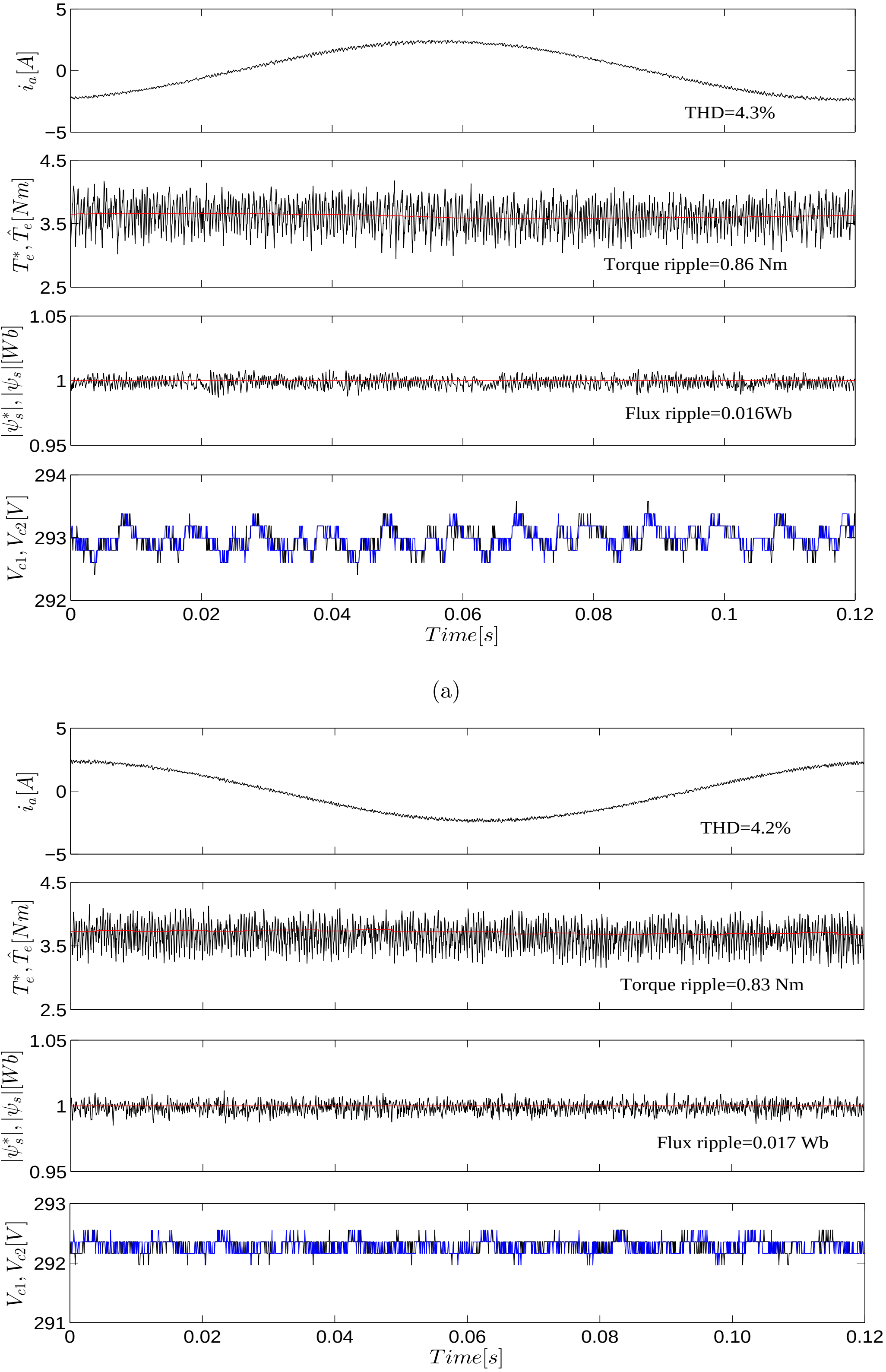

(a)

(b)

Figure 5.9: Experimental steady-state low-speed behaviour of the machine at 200 r/min at 50% rated-load torque. (a) RSFVC-based FS-PTC and (b) conventional FS-PTC.

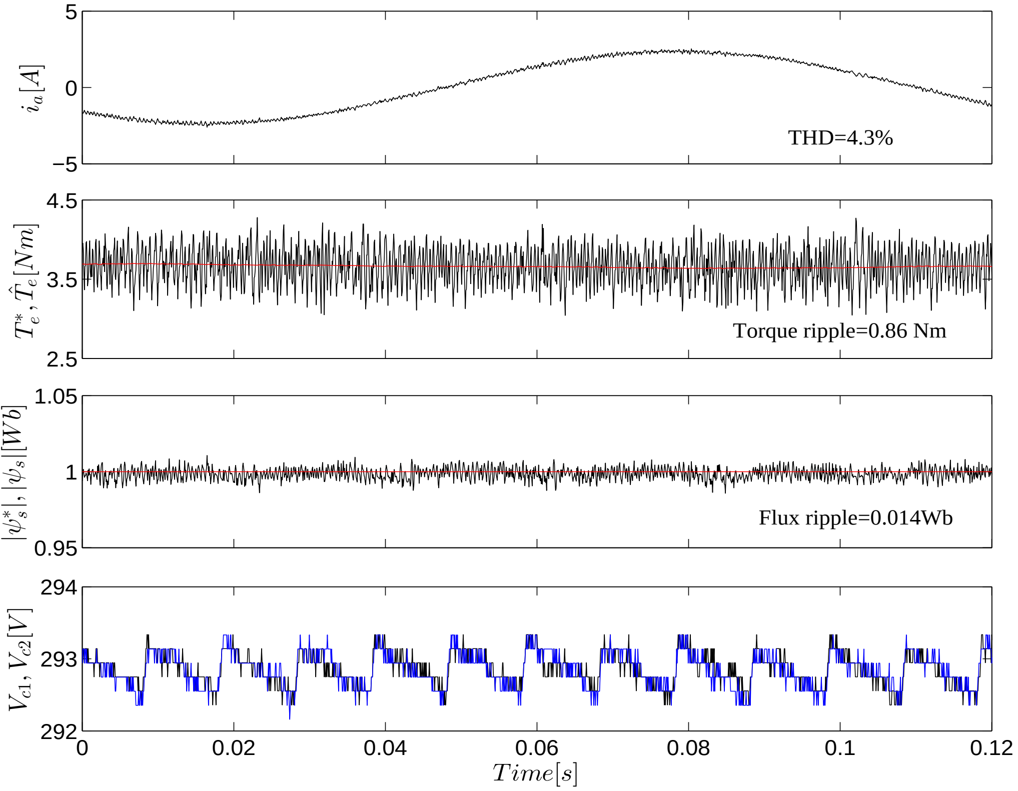

Figure 5.10: Experimental steady-state waveforms at 200 r/min at 50% rated-load torque for the compound FS-PTC.

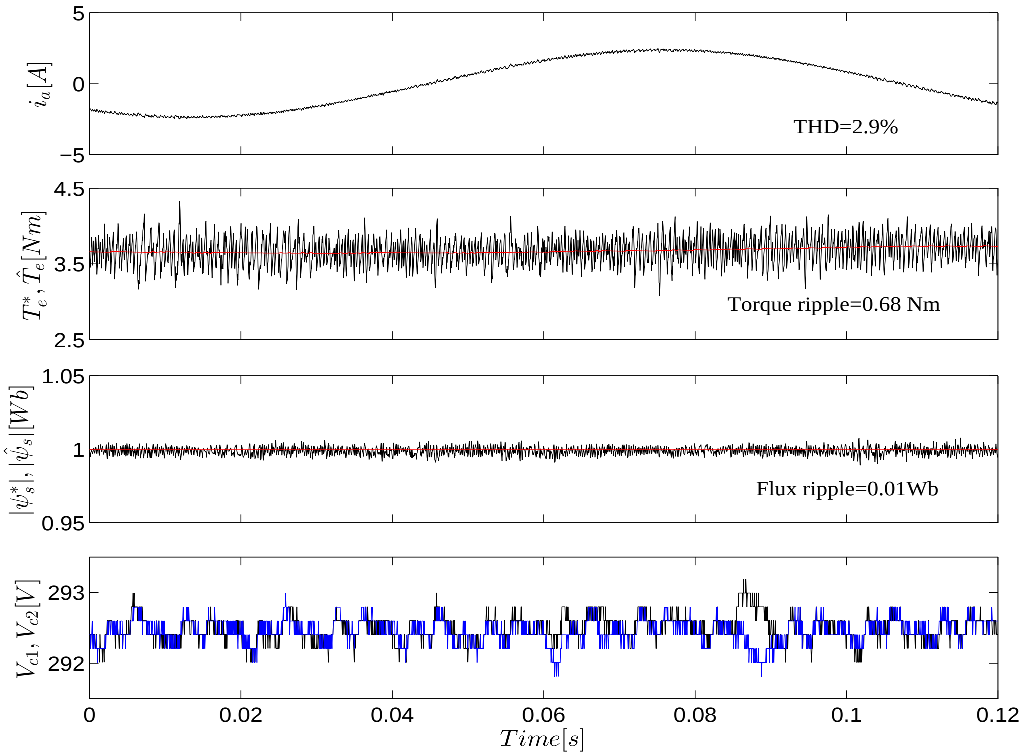

Figure 5.11: Experimental steady-state low-speed behaviour of the machine for the RSFVC-based FS-PTC at 200 r/min at 50% rated-load torque with the sampling time of 45 μs.

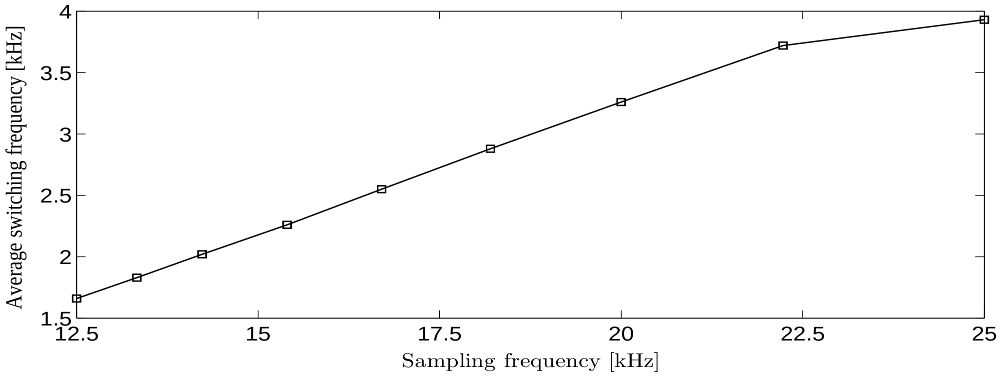

Figure 5.12: Relationship between the sampling frequency and average switching frequency.

5.6.3 Investigation of speed-transient capability under rated-speed reversal

Figure 5.13 demonstrates the speed-transient behaviour of the RSFVC-based FS-PTC strategy. The test is performed by reversing the motor speed from +1415 r/min (148 rad/s) to −1415 r/min (-148 rad/s) at no-load torque. The torque is limited to 10 Nm—135% rated torque. It can be seen that the stator flux is constant at its nominal value of 1.0 Wb. The performance in terms of torque and flux ripple is good; the ripple observed are 0.8 Nm and 0.016 Wb, respectively. During speed reversal, the ripple is slightly increased. This is because of higher current flowing in the stator winding. The THD of the stator current i_a is 4.5%. The two capacitor voltages are balanced and, thus, the neutral-point voltage has negligible effect on the torque and flux ripple. Similar behaviour is observed for the compound FS-PTC, as shown in Fig. 5.14.

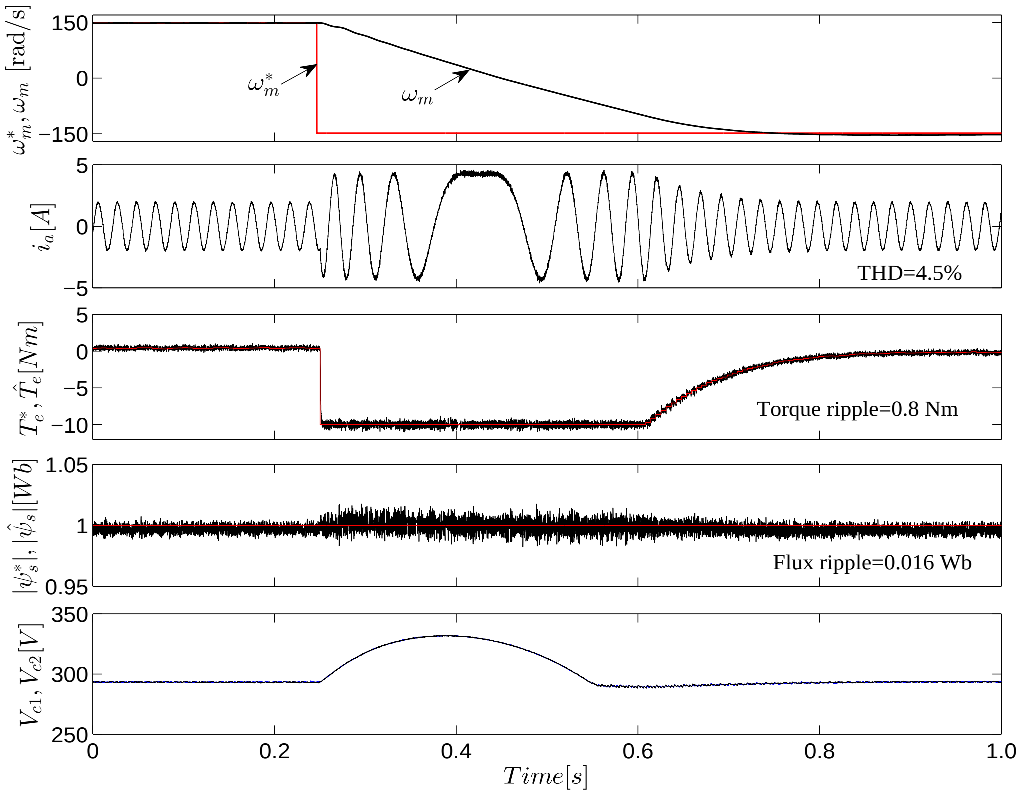

Figure 5.13: Experimental waveforms of speed, stator current, torque, stator flux and two capacitor voltages at no-load torque at rated-speed (1415 r/min) reversal condition for the RSFVC-based FS-PTC.

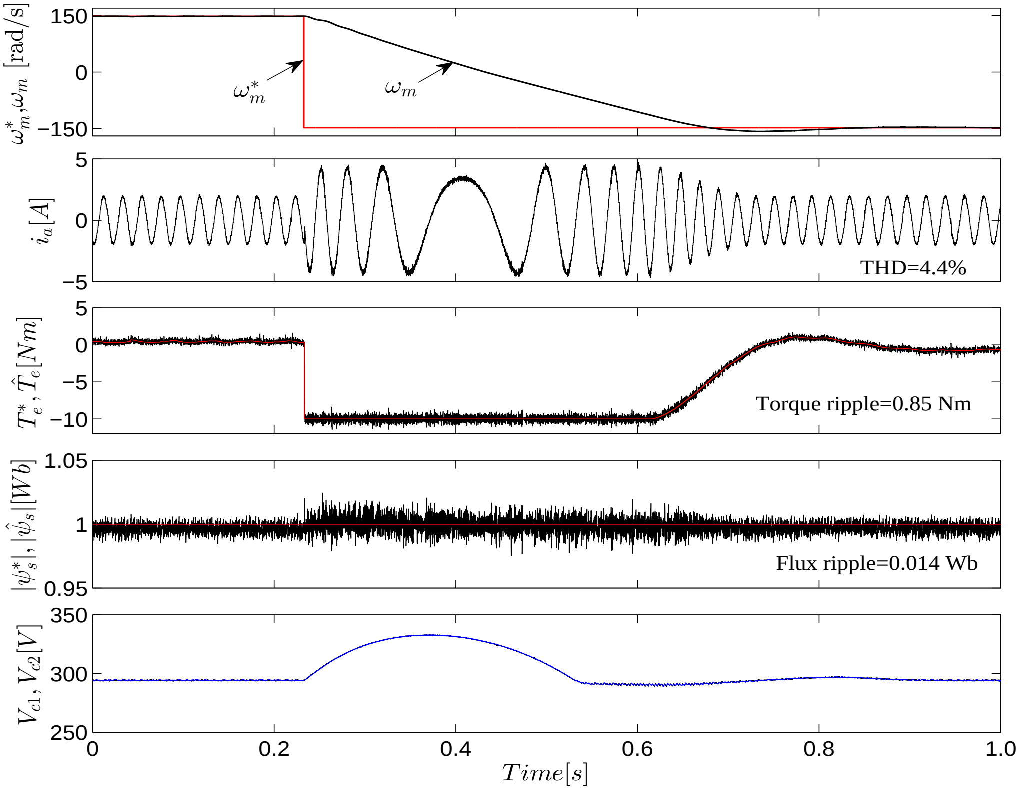

Figure 5.14: Experimental waveforms of speed, stator current, torque, stator flux and two capacitor voltages at no-load torque at rated-speed (1415 r/min) reversal condition for the compound FS-PTC.

5.6.4 Investigation of robustness against rated-load torque disturbance

The robustness of the control system against an external rated-load torque disturbance is tested, and is illustrated in Fig. 5.15. The load torque is suddenly changed from no-load to rated-load torque (7.4 Nm) as a disturbance on the fed machine. A small dip and a slight overshoot are apparent in the speed response due to the load torque disturbance, and the controller recovers the original speed within a short time (0.14 s). The stator current THD is reduced by 13.7%. This improvement is due to the increase of the power component of stator current. The torque ripple and flux ripple are slightly increased after the load is applied. The two capacitor voltages are balanced and, hence, the control system is unaffected by neutral-point voltage. During the load change, the stator flux remains constant at its rated value, which ensures decoupled control of torque

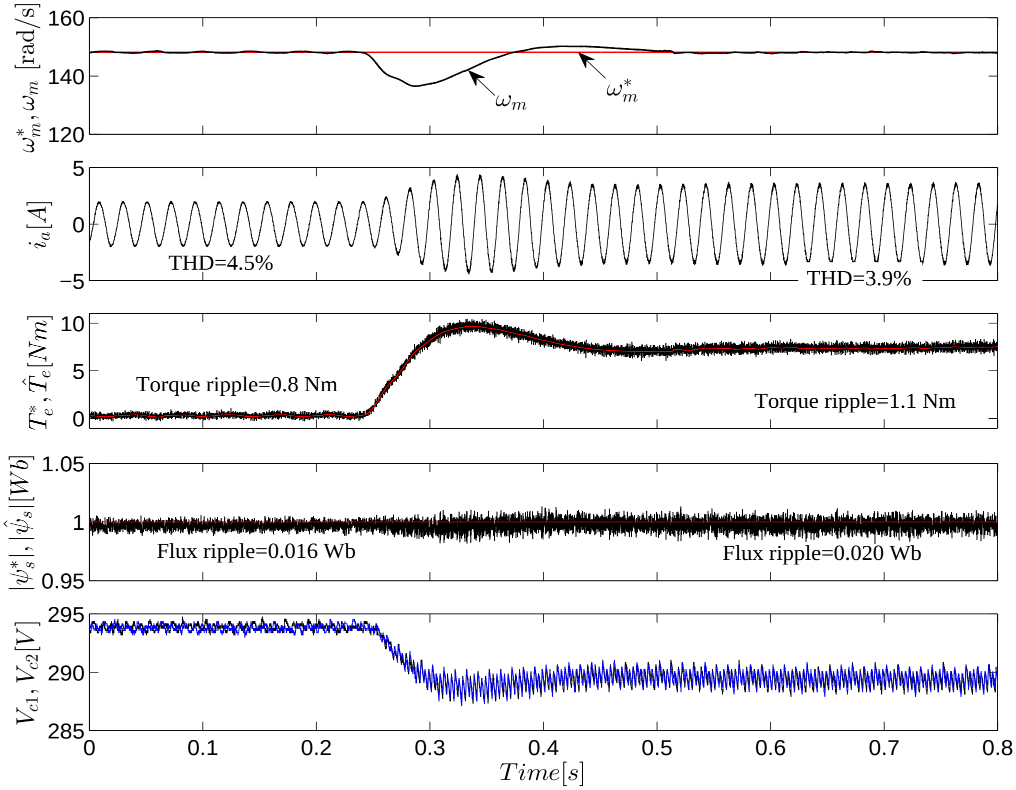

Figure 5.15: Experimental dynamic behaviour of the machine for the RSFVC-based FS-PTC at rated-speed under an external rated-load torque disturbance.

and flux. Similar behaviour is observed for the compound FS-PTC, as shown in Fig. 5.16. However, the speed recovery time after load disturbance is slightly longer—0.24 s, which is still acceptable.

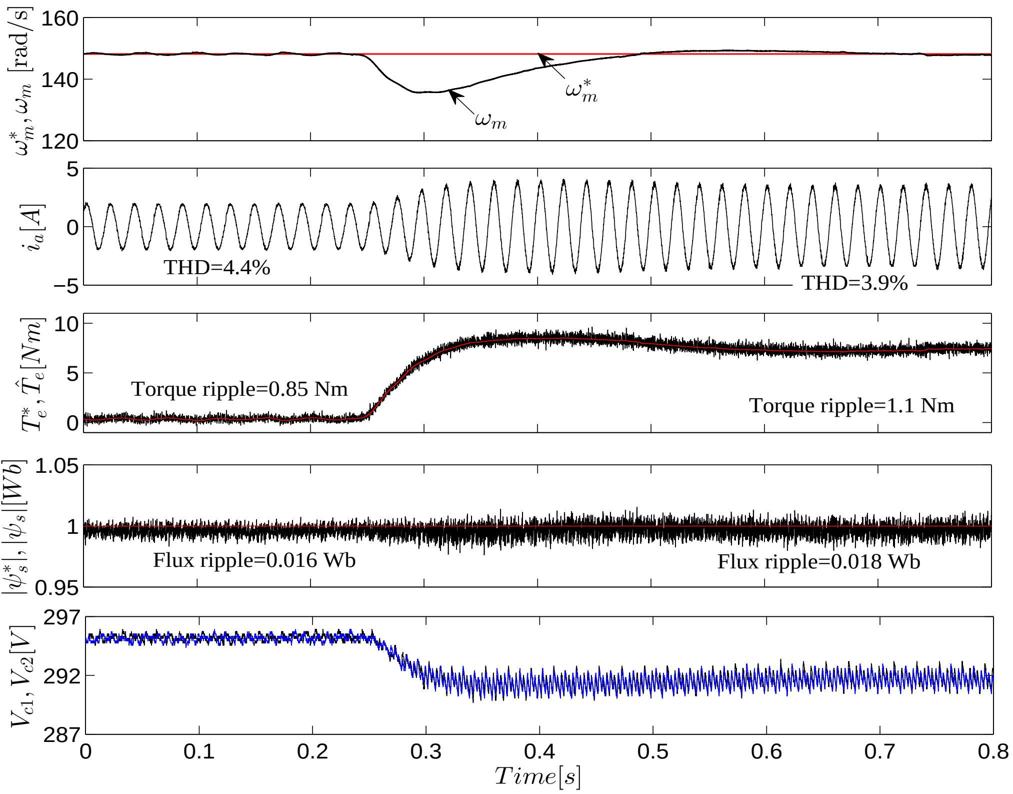

Figure 5.16: Experimental dynamic behaviour of the machine for the compound FS-PTC at rated-speed under an external rated-load torque disturbance.

5.6.5 Torque-transient characteristics

Figure 5.17(a) shows the step rated-torque-transient characteristics of the system. The step rated-torque (7.4 Nm) is achieved by changing the command speed from 100 r/min to 1000 r/min. During the transient, the controller selects the large and medium voltage vectors—in this case $\boldsymbol{v}_{20}$, $\boldsymbol{v}_{21}$, or $\boldsymbol{v}_{26}$. This yields a fast dynamic response, as shown in Fig. 5.17(a). The torque rise time for the RSFVC-based FS-PTC is 0.46 ms, whereas this is 0.5 ms for the conventional FS-PTC, as shown in Fig. 5.17(b). The difference in torque rise time is only 40 μs, which is less than a sampling period. Hence, the proposed simplified FS-PTC strategy retains the fast dynamic behaviour of the conventional FS-PTC strategy. From Fig. 5.17(c), it can be seen that the compound FS-PTC also retains the torque-transient behaviour of the conventional FS-PTC.

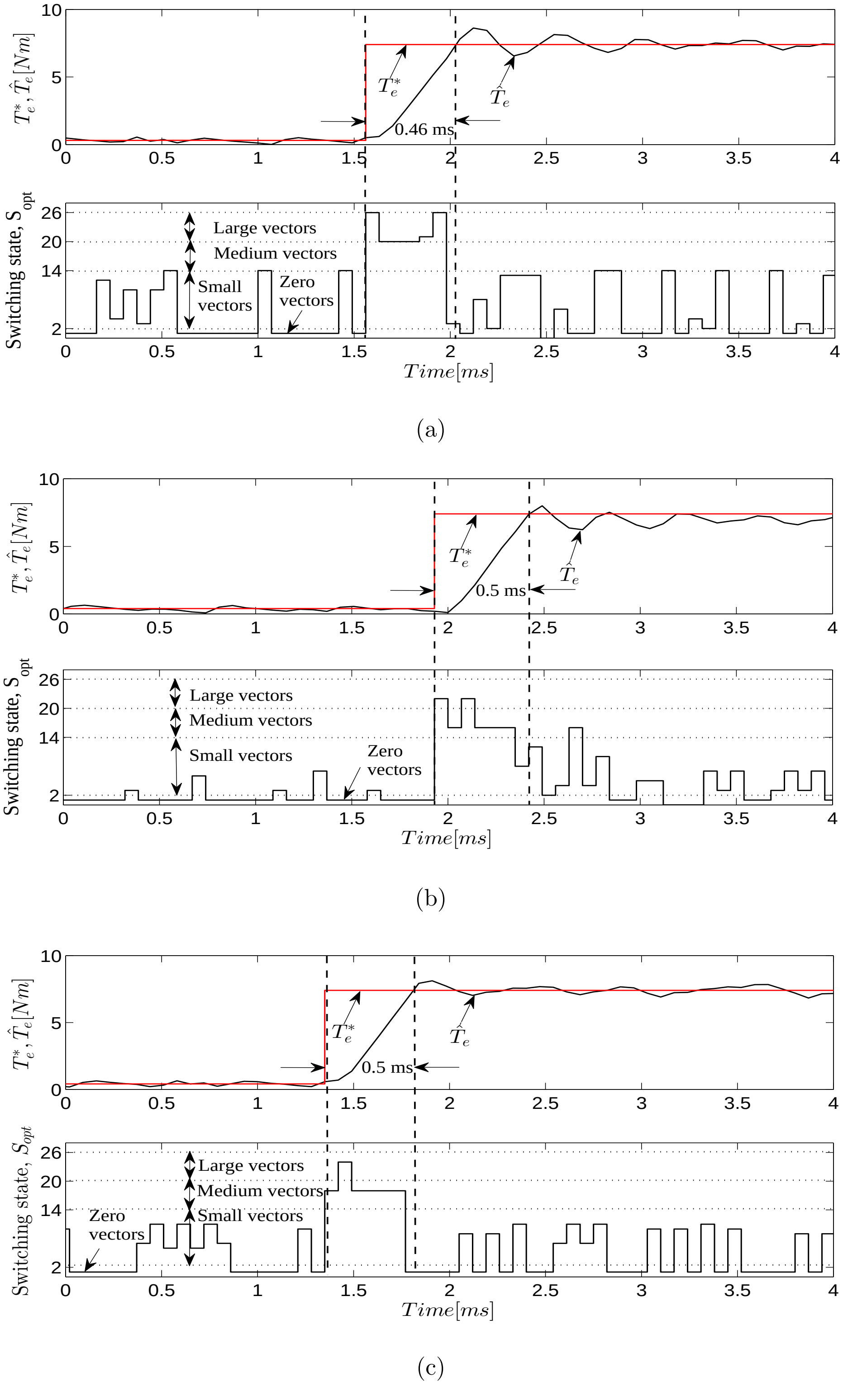

(a)

(b)

(c)

Figure 5.17: Experimental step rated-torque-transient characteristics showing the torque-transient and selected inverter switching states. (a) RSFVC-based FS-PTC, (b) conventional FS-PTC and (c) compound FS-PTC.

5.6.6 Investigation of average switching frequency

Figure 5.18(a) plots the average switching frequencies for the RSFVC-based FS-PTC over a wide speed range from 200 to 1400 r/min under different load torques from 0 to 7 Nm. The average switching frequency varies with the change of speed and load torque. However, the switching frequency variation for a particular speed at different load torques is very small (3% of the maximum average switching frequency which is 1.66 kHz at 1200 r/min), as can be seen from Fig. 5.18(b). The average switching frequencies for the proposed FS-PTC under different operating conditions are also compared with the conventional FS-PTC, as shown in Figs. 5.18(a) and 5.18(b). It can be seen that the average switching frequencies for the proposed and the conventional FS-PTC are very close. The absolute deviations in average switching frequencies are shown in Fig. 5.18(c); the maximum deviation is around 250 Hz. Fig. 5.18(b) shows that the variation ranges of average switching frequencies are 1.24–1.66 kHz and 1.28–1.78 kHz for the simplified and the conventional control strategies, respectively, in all operating conditions.

Figure 5.19(a) illustrates the average switching frequency behaviour of the compound FS-PTC in comparison with the conventional FS-PTC. It is seen that the average switching frequencies at low- and high-speed operations are similar, as it is evident in Fig. 5.19(b). At the speed range 600 to 1000 r/min, the average switching frequencies are slightly higher—maximum 600 Hz at 1000 r/min at 4 Nm load torque—for the compound FS-PTC than the conventional FS-PTC. As torque and flux performance is comparable, this slight increase in average switching frequency is acceptable.

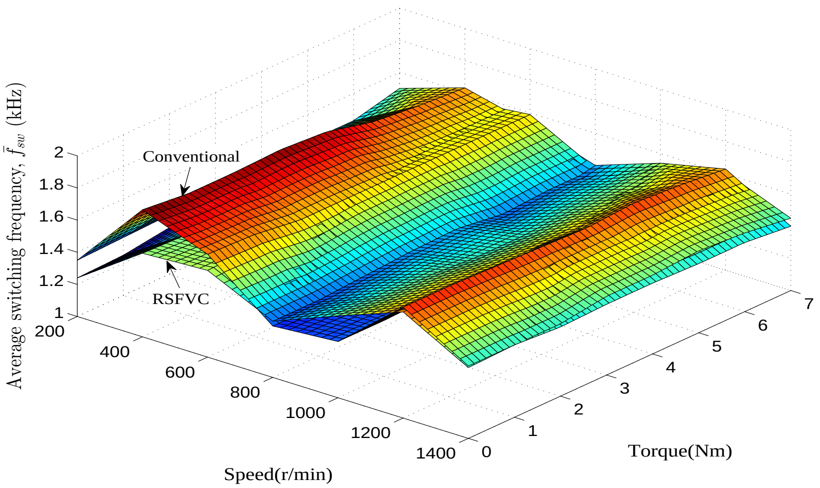

(a) Average switching frequencies $\bar{f}_{sw}$ from 200 to 1400 r/min and 0 to 7 Nm.

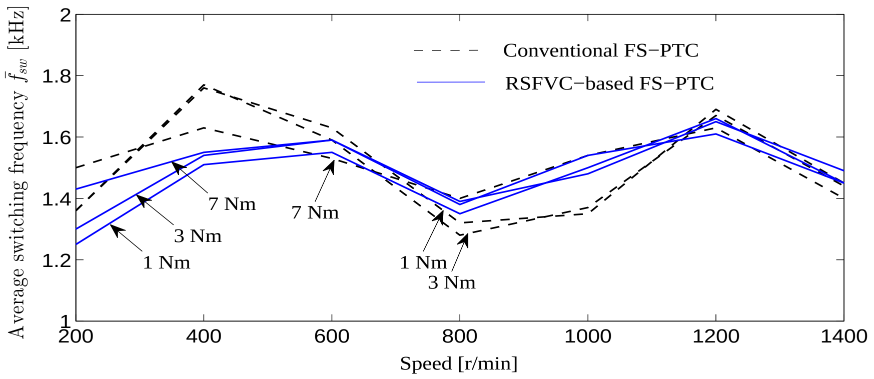

(b) $\bar{f}_{sw}$ vs. speed with torque as parameter.

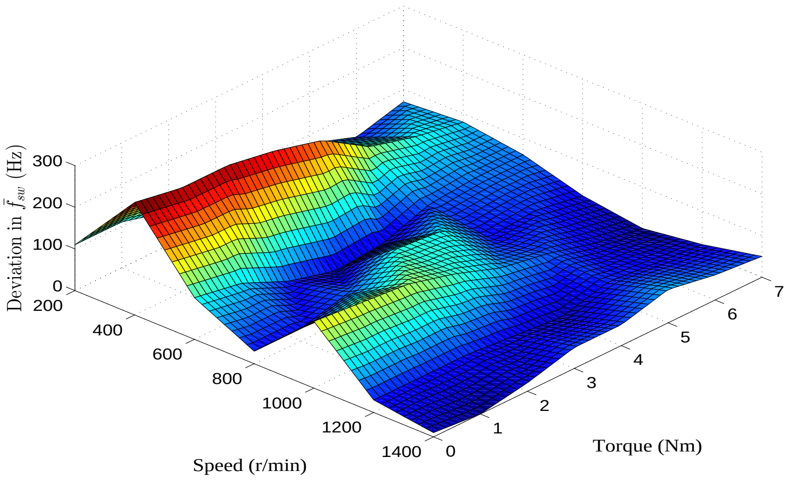

(c) Absolute differences of $\bar{f}_{sw}$ from 200 to 1400 r/min and 0 to 7 Nm.

Figure 5.18: Experimental investigation of the average switching frequencies $\bar{f}_{sw}$ for the proposed RSFVC-based FS-PTC in comparison with the conventional FS-PTC.

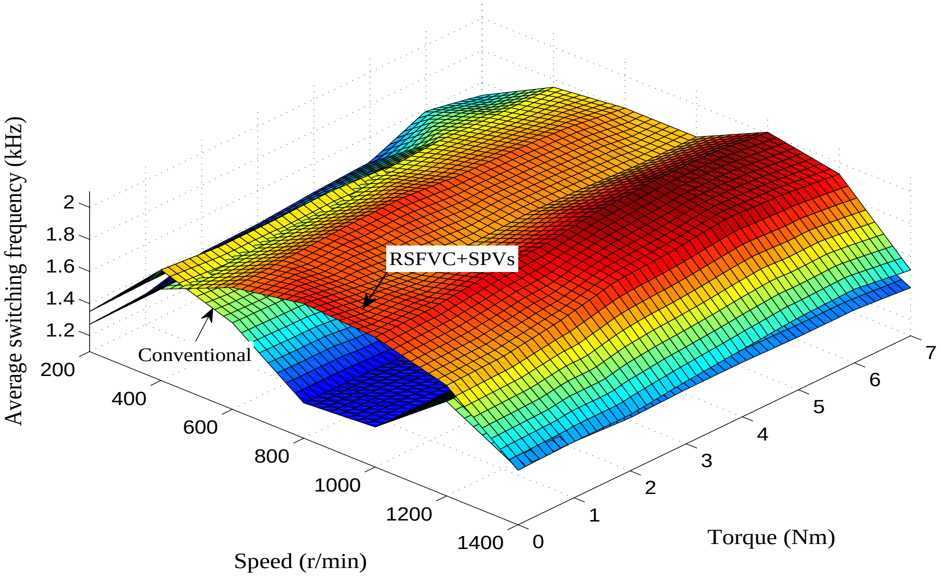

(a)

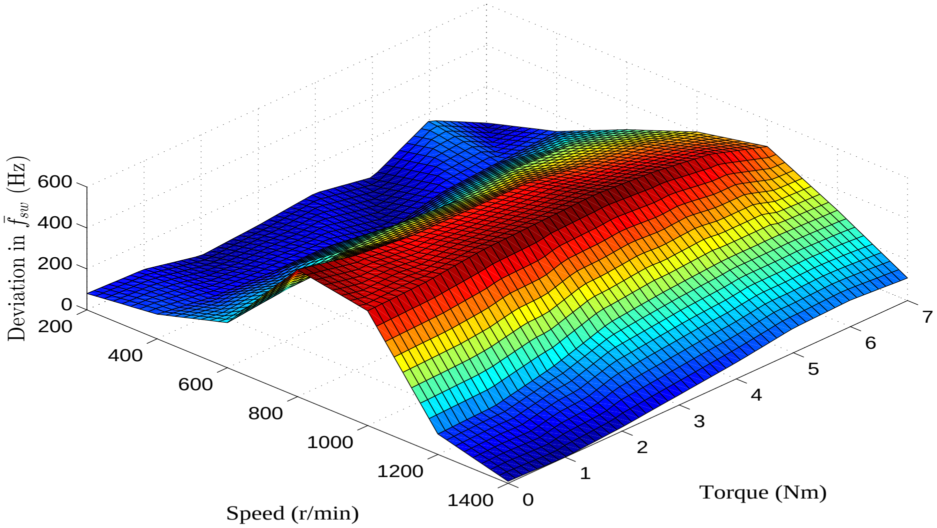

(b)

Figure 5.19: Experimental investigation of average switching frequencies $\bar{f}_{sw}$ from 200 to 1400 r/min and 0 to 7 Nm. (a) $\bar{f}_{sw}$ for the compound and conventional FS-PTC, and (b) absolute differences between the average switching frequencies.

5.7 Summary

This chapter has proposed a second simplified RSFVC-based FS-PTC for the IM drive fed by a 3L-NPC inverter. The simplified FS-PTC does not contain complex stator current and torque calculations inside the prediction loop. At the expense of a very small execution time—only 4.40 μs—the torque and stator flux amplitude references are converted to an equivalent stator flux reference vector. The overall computational efficiency is improved by 38% over the conventional FS-PTC algorithm. This is further increased to 49% by developing a compound FS-PTC, without affecting the system performance. Thus, the required processing power of the micro-controller is reduced. If the computational burden is not an issue for a particular micro-controller, the proposed RSFVC-based FS-PTC can be implemented with a higher sampling frequency than the conventional FS-PTC algorithm. When the sampling frequency is increased, the experimental results have shown that the performance is improved. Tuning effort on the weighting factor between the torque and flux errors is avoided by not predicting the torque inside the prediction loop. Experimental results verify that the RSFVC-based FS-PTC system is stable against parameters variation and dc-link voltage unbalance. The proposed controller yields torque and flux ripple, stator current THD, neutral-point voltage, torque and speed dynamics, and average switching frequency similar to those of the conventional FS-PTC strategy. In addition, the controller is robust against rated-load torque disturbance and yields an almost constant average switching frequency over a wide speed range; the maximum average switching frequency variation is 3% of the maximum average switching frequency at a particular speed.

Chapter 6

Simplified Sensorless FS-PTC of a 3L-NPC Inverter Fed IM Drive

6.1 Introduction

This chapter proposes a speed encoderless (or simply a sensorless) FS-PTC of IM supplied from a 3L-NPC inverter. For sensorless operation, PTC requires estimated speed and rotor/stator flux. This study estimates the rotor speed and flux using an EKF. Due to the complexity of EKF and the large number of available voltage vectors, the FS-PTC for a multi-level inverter-fed drive is computationally expensive. Consequently, the controller requires longer execution time that yields worse torque, flux and speed responses, especially at low-speed. To reduce the computational burden of the PTC algorithm, the proposed SPVs strategy is employed. A comparison between the SPVs- and RSFVC-based simplified FS-PTC strategies is presented, and selecting SPVs from the two proposed simplified approaches for sensorless operation is justified. Experimental results illustrate that the proposed sensorless strategy can estimate the speed accurately over a wide speed range, including the field-weakening region, while maintaining robustness and excellent torque and flux responses.

This chapter addresses the fourth objective of the thesis, and part of the contribution is published in [94, 117–119]. The chapter is organised as follows. A comparison between the SPVs- and RSFVC-based FS-PTC strategies is presented in Section 6.2. An EKF based sensorless FS-PTC is proposed in Section 6.3. In the same section, the SPVs strategy is applied to the sensorless FS-PTC to reduce the computational burden of the algorithm. Section 6.4 summarises the proposed control algorithm. The required computation time of the proposed algorithm is discussed in Section 6.5. Experimental outcomes are illustrated and discussed in Section 6.6.

6.2 Comparison between the SPVs- and RSFVC-based FS-PTC strategies

A detailed comparison between the SPVs- and the RSFVC-based FS-PTC strategies is presented in Table 6.1. Structurally, the SPVs-based FS-PTC strategy is simpler than the RSFVC-based FS-PTC strategy. This is because the RSFVC-based technique contains one additional PI controller and cascade connection. The main advantage of the RSFVC-based FS-PTC is that it does not require weighting factor tuning between the torque and flux errors in the cost function. However, this research shows that the SPVs-based FS-PTC (with the tuned weighting factor between torque and flux errors) yields a similar steady-state and transient performance to the RSFVC-based FS-PTC. This is detailed in Chapters 4 and 5. In the present comparative analysis, the steady-state performance is considered at 1000 r/min at rated-load torque (7.4 Nm). The required computational effort for both control strategies is similar.

We may recall that the main objective of this chapter is to analyse the sensorless FS-PTC performance of the 3L-NPC inverter fed IM drive. For a sensorless regenerative operation, a system may be unstable, especially at lower speeds [120]. Over-current may flow in the stator winding due to system instability. Hence, it is important to consider over-current protection in the controller design. Hardware based over-current protection can be implemented; however, the implementation cost and complexity will be increased. In PTC, the over-current can be controlled easily by predicting the stator current in the prediction loop (this was explained in Chapters 3 and 4). The RSFVC-based FS-PTC with the stator current prediction in the prediction loop will not be as computationally efficient. Apart from this, an effort has been made to retain the fundamental structure of

Table 6.1: Comparison between the SPVs- and the RSFVC-based FS-PTC strategies for the 3L-NPC inverter fed IM drive

Index	SPVs-based FS-PTC	RSFVC-based FS-PTC
Total number of PI controllers	One	Two
Additional cascade connections (compared to fundamental)	One (SPVs block)	Two (PI controller and RSFVC blocks)
Torque prediction	Direct	Indirect
Weighting factor λ_f tuning	required	not required
Predictive over-current protection	Possible	Not possible
Calculation time (μs)	36.90	36.82
Steady-state torque ripple (Nm)	0.90	0.95
Steady-state flux ripple (Wb)	0.020	0.018
Neutral-point voltage (V_{p-p})	≤ 1.4	< 1
THD for i_a (%)	3.5	3.5
Average switching frequency (kHz)	1.51	1.54
Torque rise time (ms)	0.5	0.46

the FS-PTC in the present sensorless analysis. Hence, the SPVs approach (instead of the RSFVC approach) is considered to ensure that the proposed sensorless control algorithm is computationally efficient.

6.3 Proposed SPVs-based sensorless FS-PTC

The FS-PTC strategy requires speed, stator current, stator flux and rotor flux information. The states that are not available for measurements, such as stator and rotor flux, are estimated using a suitable observer. In a sensorless operation, the rotor speed is also estimated. For the proposed speed sensorless drive, the rotor speed and flux are estimated

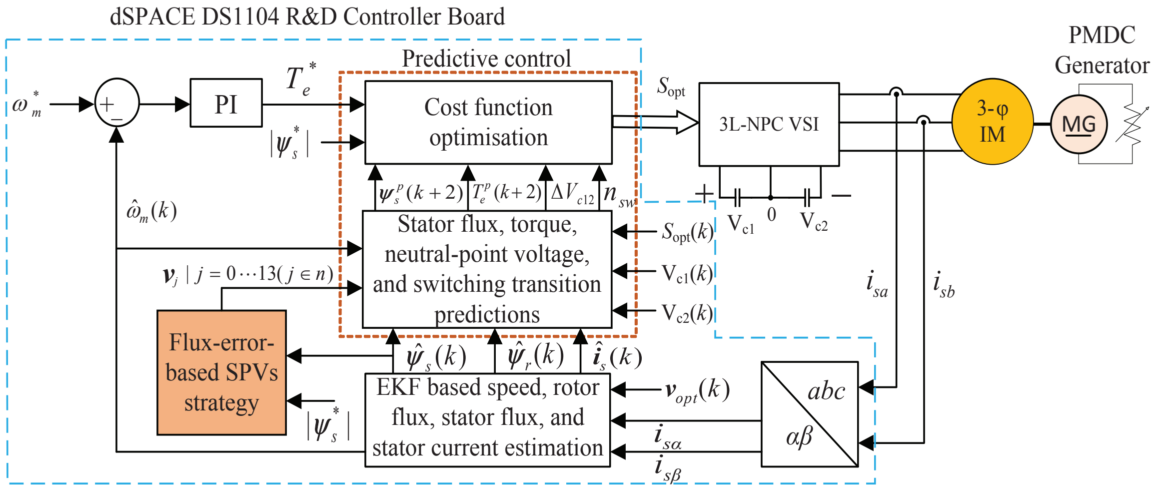

Figure 6.1: Proposed sensorless SPVs-based FS-PTC of IM drive fed by a 3L-NPC VSI.

using an EKF. The stator flux is then estimated from the estimated rotor flux using a simple relationship between them, see Eq. (3.2). Instead of the measured stator current, the estimated stator current is fed back into the predictive controller. The overall control structure is shown in Fig. 6.1. It consists of four stages: estimation, prediction vectors selection, predictions and optimisation. The steps are discussed in the following sections. The performance and required computational burden are analysed for the 3L-NPC VSI.

6.3.1 EKF for rotor speed and flux estimations

To obtain rotor speed and flux information, an extended rotor current model of the IM is employed in the EKF. The sixth-order nonlinear extended model of the IM, affected by system and measurement noises (for tuning of EKF), is given by [68, 94]:

$$\dot{x} = f(x, v) + w(t) \tag{6.1}$$

$$y = C_o x + u(t) \tag{6.2}$$

where $x = [i_{s\alpha} \; i_{s\beta} \; \psi_{r\alpha} \; \psi_{r\beta} \; \omega_m \; T_l]^T$,
$v = [v_{s\alpha} \; v_{s\beta}]^T$,

$$f(x,v) = \begin{pmatrix} -\left(\frac{R_s}{L_\sigma} + \frac{L_m^2 R_r}{L_\sigma L_r^2}\right) i_{s\alpha} + \frac{L_m R_r}{L_\sigma L_r^2}\psi_{r\alpha} + \frac{L_m \omega_e}{L_\sigma L_r}\psi_{r\beta} + \frac{v_{s\alpha}}{L_\sigma} \\ -\left(\frac{R_s}{L_\sigma} + \frac{L_m^2 R_r}{L_\sigma L_r^2}\right) i_{s\beta} - \frac{L_m \omega_e}{L_\sigma L_r}\psi_{r\alpha} + \frac{L_m R_r}{L_\sigma L_r^2}\psi_{r\beta} + \frac{v_{s\beta}}{L_\sigma} \\ \frac{L_m R_r}{L_r} i_{s\alpha} - \frac{R_r}{L_r}\psi_{r\alpha} - \omega_e \psi_{r\beta} \\ \frac{L_m R_r}{L_r} i_{s\beta} + \omega_e \psi_{r\alpha} - \frac{R_r}{L_r}\psi_{r\beta} \\ -\frac{3}{2}\frac{p}{J}\frac{L_m}{L_r}\psi_{r\beta} i_{s\alpha} + \frac{3}{2}\frac{p}{J}\frac{L_m}{L_r}\psi_{r\alpha} i_{s\beta} - \frac{T_l}{J} \\ 0 \end{pmatrix},$$

C_o is the model output matrix, $w(t)$ is the system/process noise and $u(t)$ is the measurement noise. The covariance matrices of $w(t)$ and $u(t)$ are Q and R, respectively. Apart from the estimated stator current in the controller, treating T_l as a state is useful for the low-speed estimation.

The output matrix C_o and the covariance matrices, Q and R, are given by

$$C_o = \begin{bmatrix} 1 & 0 & 0 & 0 & 0 & 0 \\ 0 & 1 & 0 & 0 & 0 & 0 \end{bmatrix} \tag{6.3}$$

$$Q = cov(w) = E\left\{ww^T\right\} \tag{6.4}$$

$$R = cov(u) = E\left\{uu^T\right\}. \tag{6.5}$$

The continuous model in Eqs. (6.1) and (6.2) is discretised for implementation of the EKF using the standard forward-Euler approximation—Eq. (2.11).

The recursive form of the EKF, including stochastic uncertainties, may be expressed by the following system of equations [70].

Prediction process:

$$\hat{x}[k|k-1] = \hat{x}[k-1|k-1] + f\left(\hat{x}[k-1|k-1], v[k]\right) T_s \tag{6.6}$$

$$P[k|k-1] = \frac{\partial f\left(x[k], v[k]\right)}{\partial x[k]} P[k|k] \frac{\partial f\left(x[k], v[k]\right)}{\partial x[k]}^T + Q \tag{6.7}$$

where $\hat{x}$ is the state estimate, P is the state estimate error covariance matrix and $\partial f / \partial x|_{\hat{x}[k], \hat{v}[k]}$ is the corresponding Jacobian matrix which involves linearisation of nonlinear state space model of the IM. For simplicity, all covariance matrices are assumed to be diagonal [70].

Kalman gain:

$$K[k] = P[k|k-1]C^T \left(CP[k|k-1]C^T + R\right)^{-1} \tag{6.8}$$

Innovation process:

$$\hat{x}[k|k] = \hat{x}[k|k-1] + K[k]\left(y[k] - C\hat{x}[k|k-1]\right) \tag{6.9}$$

$$P[k|k] = P[k|k-1] - K[k]CP[k|k-1] \tag{6.10}$$

The predictions in Eqs. (6.6) and (6.7) are updated with the present measurements by Eqs. (6.9) and (6.10) using the Kalman gain calculated in Eq. (6.8).

Equation (6.9) yields the desired estimated rotor speed $\hat{\omega}_m$, rotor flux $\hat{\boldsymbol{\psi}}_r$ and stator current $\hat{\boldsymbol{i}}_s$.

The stator flux is calculated using the relationship

$$\hat{\boldsymbol{\psi}}_s = \frac{L_m}{L_r}\hat{\boldsymbol{\psi}}_r + \sigma L_s \hat{\boldsymbol{i}}_s. \tag{6.11}$$

There is time delay between measurement and estimation. This delay degrades control performance, especially at lower speeds. Hence, the estimated current, instead of the measured current, is used in the stator flux estimation as well as in the prediction model to avoid this.

6.3.2 Selecting prediction vectors

The prediction vectors are selected based on the SPVs strategy. As the SPVs strategy has already been described in Chapter 4, it will not be repeated here. Between the two strategies (torque-error-based and flux-error-based), the stator-flux-error based one is selected in this study.

6.3.3 Prediction and optimisation

After the prediction vectors are selected, the control objectives—stator flux, torque, neutral-point voltage and number of switching transitions—are predicted. The outcomes of the observer—$\hat{\omega}_m$, $\hat{\boldsymbol{\psi}}_r$ and $\hat{\boldsymbol{i}}_s$, are employed in the model for the predictions.

The stator flux is predicted using the stator voltage model of the IM, as shown in Eq. (2.1). Using the estimated stator current, the expression in a discrete-time step is repeated here as follows:

$$\boldsymbol{\psi}_s^p(k+1) = \hat{\boldsymbol{\psi}}_s(k) + T_s\boldsymbol{v}_s(k) - T_sR_s\hat{\boldsymbol{i}}_s(k). \tag{6.12}$$

All predictions for other control objectives are similar, as detailed in Chapter 4. We may recall that the predicted variables are actuated by minimising a predefined cost function in order to determine an optimum voltage vector. Considering over-current protection, the cost function is as follows:

$$\begin{aligned} g = &\left|T_e^*(k+1) - T_e^p(k+1)\right| + \lambda_f\left|\,|\boldsymbol{\psi}_s^*| - |\boldsymbol{\psi}_s^p(k+1)|\,\right| \\ &+\lambda_{cv}\left|\Delta V_{c12}(k+1)\right| + \lambda_n n_{sw}(k+1) + I_m. \end{aligned} \tag{6.13}$$

Among the SPVs, the voltage vector that yields minimum g is selected as the voltage vector $\boldsymbol{v}_{opt}$, and is applied to the motor terminals via the inverter in the next sampling instant.

For the field-weakening operation, the reference torque T_e^* and the reference stator flux $\boldsymbol{\psi}_s^*$ in the cost function (6.13) are replaced by the new references of torque and flux as [94]:

$$\boldsymbol{\psi}_{s,new}^* = \frac{\omega_{m,base}}{\hat{\omega}_m} \cdot \boldsymbol{\psi}_s^* \tag{6.14}$$

$$T_{e,new}^* = \frac{\omega_{m,base}}{\hat{\omega}_m} \cdot T_e^* \tag{6.15}$$

where $\omega_{m,base}$ is the base speed of the fed machine.

The new reference of stator flux $\boldsymbol{\psi}_{s,new}^*$ is also used to calculate the flux-error $\delta\psi_s$ to select an appropriate pool of prediction vectors.

Hence, the new cost function to minimise under field-weakening is

$$\begin{aligned} g = &\left|T_{e,new}^*(k+1) - T_e^p(k+1)\right| + \lambda_f\left|\,\left|\boldsymbol{\psi}_{s,new}^*\right| - |\boldsymbol{\psi}_s^p(k+1)|\,\right| \\ &+\lambda_{cv}\left|\Delta V_{c12}(k+1)\right| + \lambda_n n_{sw}(k+1) + I_m. \end{aligned} \tag{6.16}$$

The delay compensation scheme [111] has been implemented to avoid one step delay caused by digital implementation.

6.4 Proposed sensorless control algorithm

The proposed sensorless FS-PTC procedure can be summarised by the following sequences.

Step 1) *Measurement*: Sampling $\boldsymbol{i}_s(k)$, $V_{c1}(k)$, $V_{c2}(k)$ and $\omega_m(k)$. The measured speed $\omega_m(k)$ is used only for comparison.

Step 2) *Apply*: Apply the optimum voltage vector $\boldsymbol{v}_{opt}(k)$.

Step 3) *Estimate*: Estimate the rotor speed $\hat{\omega}_m(k)$ and flux $\hat{\boldsymbol{\psi}}_r(k)$, and stator current $\hat{\boldsymbol{i}}_s(k)$ using the EKF. Also estimate the stator flux $\hat{\boldsymbol{\psi}}_s(k)$ using Eq. (6.11).

step 4) *Calculate*: Calculate the new reference of the stator flux and torque for the field-weakening operation using Eqs. (6.14) and (6.15), respectively, if required.

Step 5) *Select*: Select the prediction vectors using the SPVs strategy (see Subsection 4.5.1 in Chapter 4).

Step 6) *Predict and evaluate*: Predict the stator flux $\boldsymbol{\psi}_s^p(k+2)$, stator current $\boldsymbol{i}_s^p(k+2)$, torque $T_e^p(k+2)$, neutral-point voltage $\Delta V_{c12}(k+2)$ and number of switching transitions $n_{sw}(k+2)$ using Eqs. (6.12) (forwarding one step for instant $k+2$), (3.15), (3.16), (4.5) and (4.6), respectively. Also test the predicted current $\boldsymbol{i}_s^p(k+2)$ using Eq. (3.9) to avoid over-current in the stator winding. Then, evaluate the predicted variables by calculating the cost g using Eq. (6.13) (for normal operation) or (6.16) (for field-weakening operation). Perform this step for the selected 14 voltage vectors.

Step 7) *Optimise*: Select $\boldsymbol{v}_{opt}(k+2)$ that results minimum g in the cost function. Return to step 1).

6.5 Computational capacity requirements for the proposed control algorithm

The proposed control algorithm is coded in C and is implemented using dSPACE DS1104 R&D controller board with ControlDesk. The required maximum execution time is 91.87 μs, as shown in Table 6.2. Most of the execution time is spent on the estimations (rotor speed and flux) and predictions: 62% and 27%, respectively. However, the prediction time is comparatively short in relation to the control duration of 91.43 μs. If all the possible 27 voltage vectors of the inverter, instead of the proposed selected 14 voltage vectors, were used then the predictions stage would have been required 45.10 μs. Thus, the average predictions time is reduced by 46%, from 45.1 μs to 24.36 μs. However, the overall computational burden of the proposed sensorless PTC is reduced by 20%. For this reason, it is possible to execute the proposed sensorless control algorithm within 100 μs. Otherwise, the control algorithm would have been required around 120 μs. The average execution times for other stages of the proposed controller are insignificant compared with the estimations and predictions stages.

Table 6.2: Average execution time of the proposed SPVs-based sensorless FS-PTC algorithm

Index	Average execution times (μs)	
	SPVs	All vectors
Measurement	4.39	4.39
Switching	0.12	0.12
Voltage and current calculations	0.72	0.72
Estimations using EKF	56.60	56.60
Prediction vectors selection	1.28	0.00
Predictions	$\boxed{24.36}$	$\boxed{45.10}$
Optimisation	3.40	6.25
Switching frequency calculations	0.56	0.56
Total	91.43	113.74

6.6 Experimental results

The experimental results are obtained from the 3L-NPC inverter-fed sensorless FS-PTC drive. The controller parameters are given in Appendix A. The same experimental setup, as used in Chapters 4 and 5, is used. However, a dc-dc converter is used for loading the fed motor at low-speed. The sampling time of the controller is set to 100 μs.

The elements of the covariance matrices in EKF are tuned by extensive experimentation. The covariance matrices used are as follows.

$Q = diag\left([10^{-7}\ \ 10^{-7}\ \ 10^{-7}\ \ 10^{-7}\ \ 0.1\ \ 10^{-7}], 0\right)$

$R = diag\left([100\ \ 100], 0\right)$

The diagonal elements of initial state estimate error covariance matrix $P(0)$ are all equal to 10^{-9}. All initial values of state's $X(0)$ are assumed as 0. Using these tuned covariance matrices, the following investigations are carried out:

a) transient behaviour under rated-speed reversal;

b) steady-state behaviour;

c) low-speed behaviour with and without load torque;

d) robustness against an external rated-load torque disturbance;

e) step torque-transient characteristics;

f) rotor resistance sensitivity of the controller;

g) dynamic behaviour in the field-weakening region.

6.6.1 Transient behaviour under rated-speed reversal

The reverse speed operation of the proposed FS-PTC system at a rated-speed of 1415 r/min (148 rad/s) without load torque is performed, and the behaviour of the control system is illustrated in Fig. 6.2. From top to bottom, the curves are the three speeds, stator current, estimated torque, estimated stator flux and two dc-link capacitor voltages. The zoomed measured and estimated speed responses confirm that the estimated speed follows the actual speed accurately. Figure 6.2 shows that the stator flux is constant at

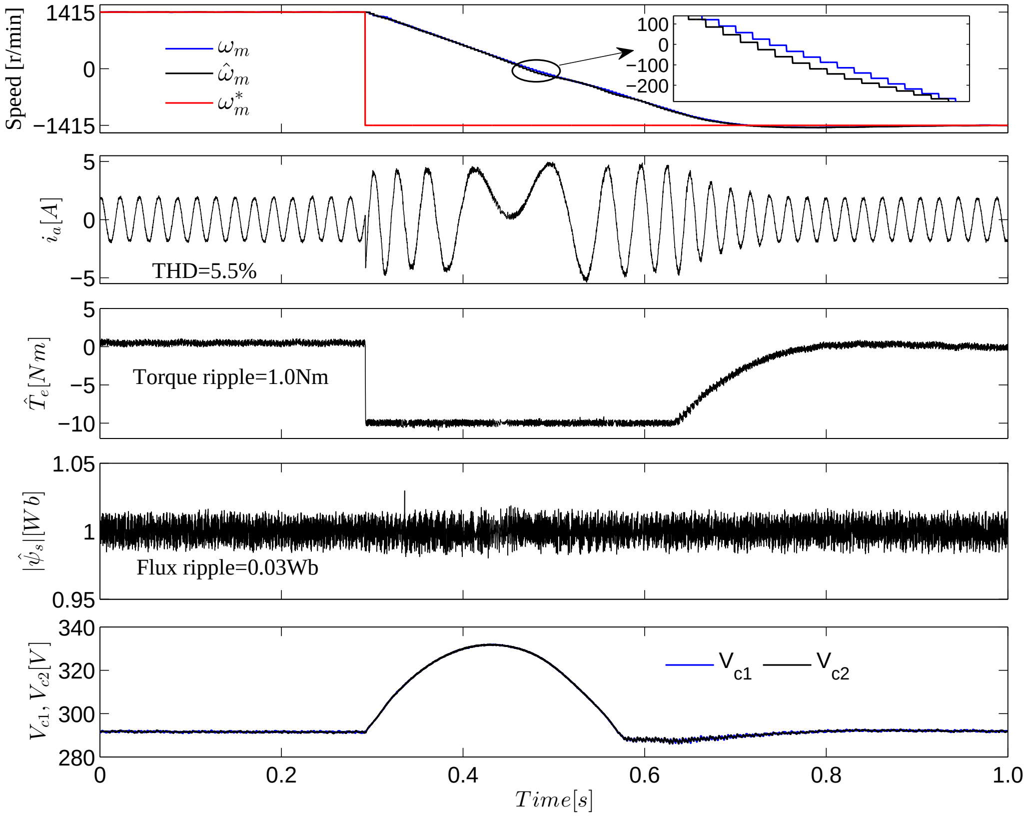

Figure 6.2: Experimental waveforms of speeds, stator current, estimated torque, estimated stator flux and two capacitor voltages under rated-speed (1415 r/min) reversal condition.

its nominal value of 1.0 Wb. The stator flux produces good sinusoidal stator current waveform. The THD of the stator current i_a at steady-state is 5.5%; THD is calculated with 10 cycles up to maximum 5 kHz (50% of the sampling frequency) using MATLAB. The performance in terms of torque and flux ripple is good; the torque ripple is 1.0 Nm and the flux ripple is 0.03 Wb. The capacitor voltages are balanced with very small fluctuations during the speed-transient. Hence, the neutral-point voltage is effectively controlled.

The speed estimation error is separately presented in Fig. 6.3. The speed error is calculated as $\Delta\omega_m = \hat{\omega}_m - \omega_m$; the symbol '$\wedge$' indicates the estimated value. To show a readable and clear error information, an average value of every 25 source data points is plotted. The mean value of $\Delta\omega_m$ at steady-state is 0.42% of the measured speed. It can be seen that the estimation errors during the transient and at zero crossing point are

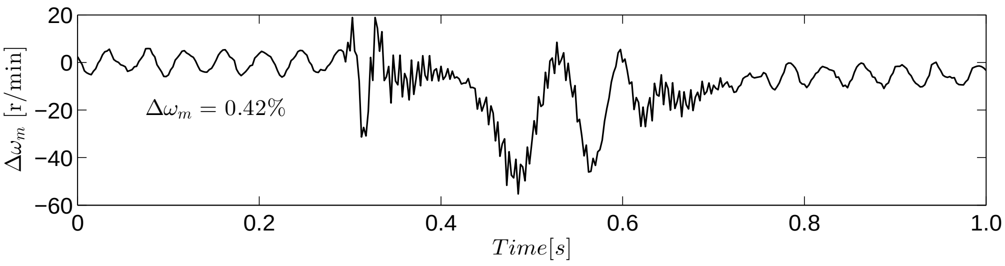

Figure 6.3: Experimental speed estimation error at rated-speed reversal.

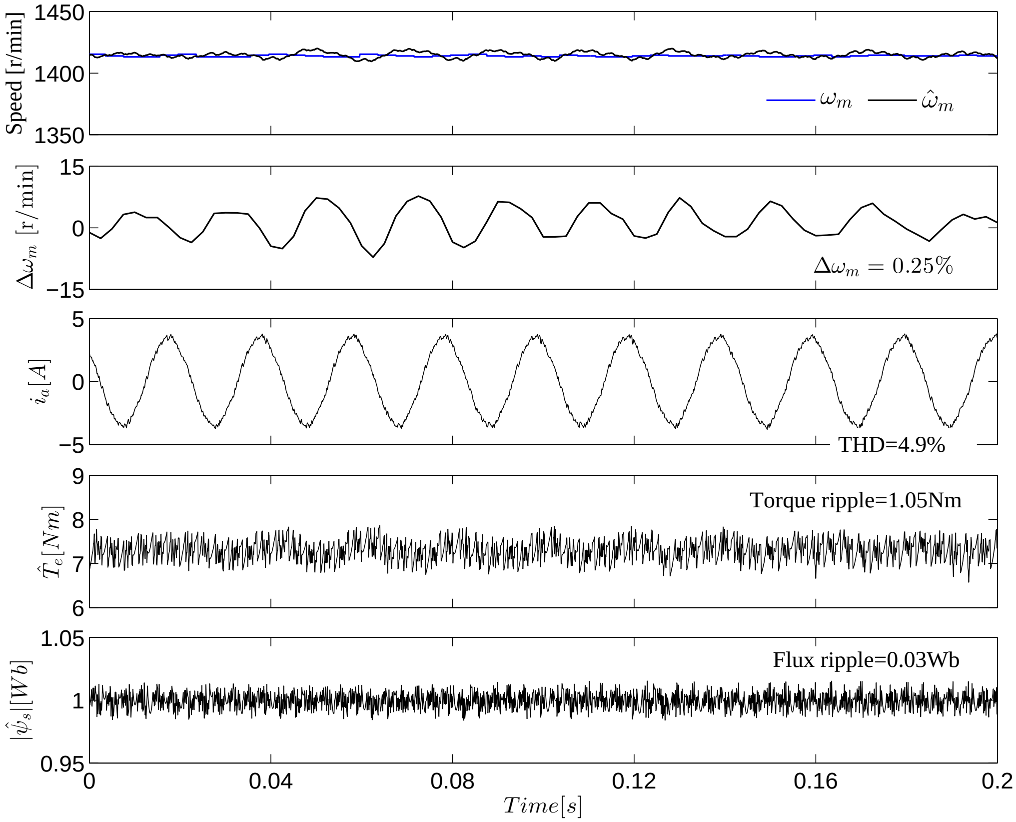

Figure 6.4: Experimental steady-state waveforms of speeds, speed error, stator current, estimated torque and estimated stator flux at rated-speed at rated-load torque.

acceptable.

6.6.2 Investigation of the steady-state behaviour

The steady-state tests are conducted at rated-speed at full-load torque, and the responses are illustrated in Fig. 6.4. The mean value of the steady-state speed estimation error is 0.25% of the measured speed. The controller yields good stator current waveform, torque

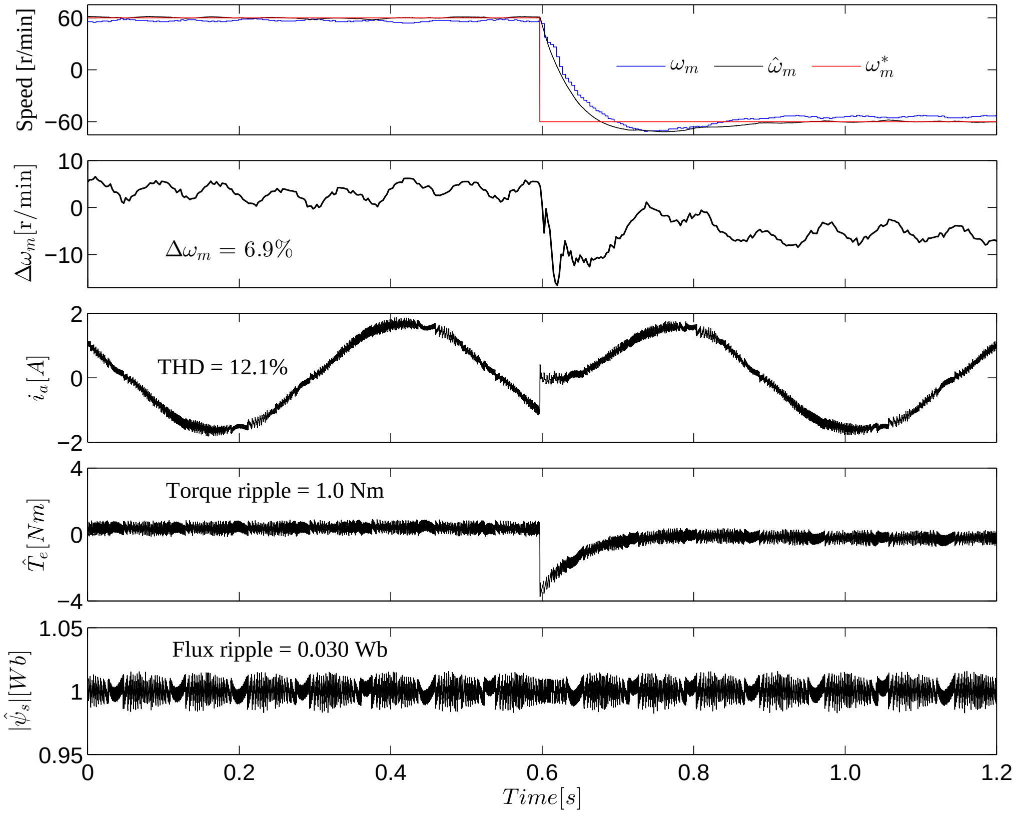

Figure 6.5: Experimental low-speed behaviour at ±60 r/min (±2Hz) at no-load torque.

and flux responses. At steady-state, the calculated stator current THD, torque ripple and flux ripple are 4.9%, 1.05 Nm and 0.03 Wb, respectively.

6.6.3 Low-speed behaviour with and without load torque

The low-speed dynamic behaviour of the machine is tested for ±60 r/min (±2 Hz) without load torque, and the responses are illustrated in Fig. 6.5. It can be seen that the estimated speed can track the actual speed accurately; the mean steady-state speed error is 6.9%. The speed error is higher (26% of the command speed) during the transient. This is because of the comparatively large current THD and variable switching frequency. However, the speed tracking accuracy, current THD, and torque and flux ripple are improved compared to the all voltage vectors based FS-PTC, as illustrated in Fig. 6.6. To convey the performance improvement in the proposed sensorless FS-PTC, the low-speed responses for the all voltage vectors based FS-PTC are illustrated using the sampling

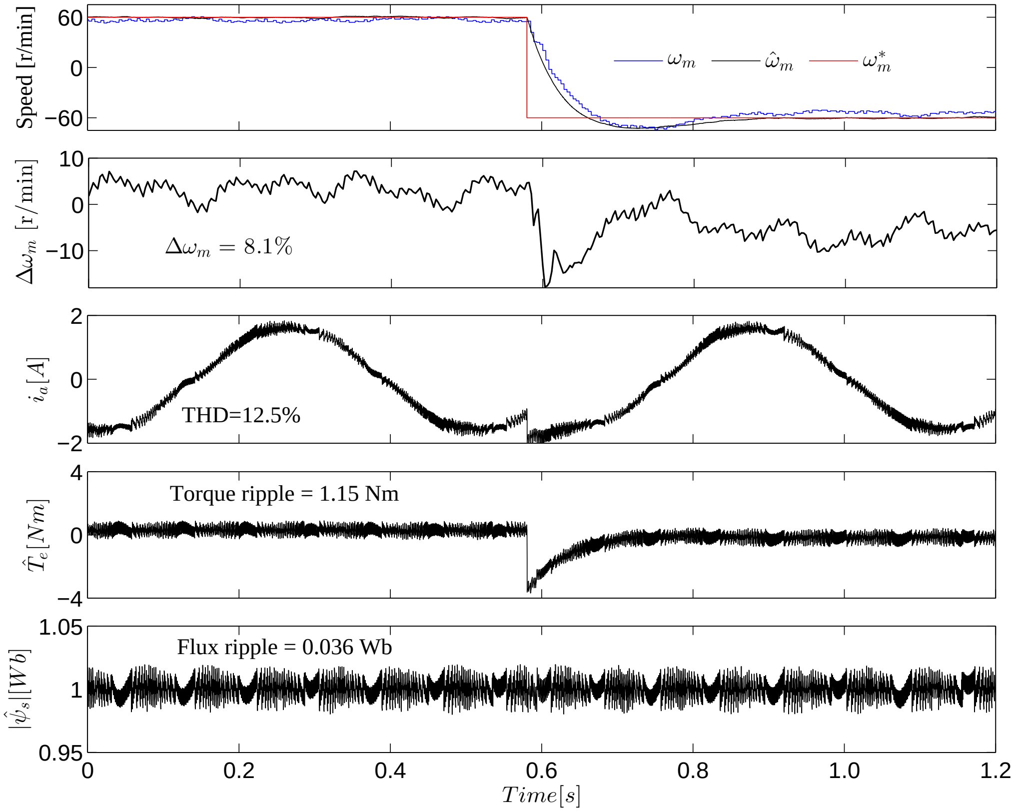

Figure 6.6: Experimental low-speed behaviour at ±60 r/min (±2Hz) for the all voltage vectors based FS-PTC at no-load torque using the sampling time of 120 μs.

time of 120 μs. To find an operating range of the system, the reference speed is reduced to 15 r/min (0.5 Hz) and full-load torque is applied; Fig. 6.7 shows the responses of the proposed control system. The mean steady-state speed error is 12.03%, and the system is stable. The stator current THD at the steady-state is 8.7%. Thus, the proposed sensorless drive functions well in the low-speed region. Figure 6.8 shows the low-speed (0.5 Hz) response for the all voltage vectors based FS-PTC. It can be seen that there is a large speed error (32.11%). In addition, the torque and flux ripple is increased. For the proposed FS-PTC, the torque ripple and the flux ripple are 1.0 Nm and 0.032 Wb, respectively; whereas, the ripples are 1.2 Nm and 0.040 Wb for the FS-PTC system using all the voltage vectors.

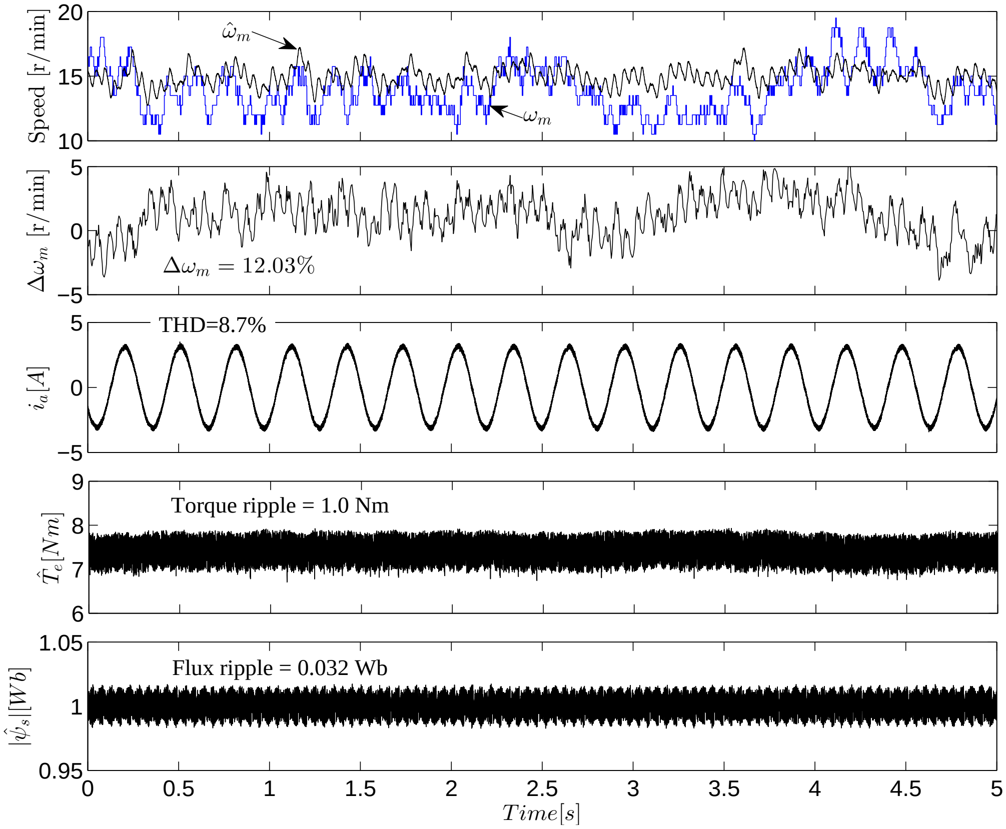

Figure 6.7: Experimental low-speed behaviour at 15 r/min (0.5 Hz) at full-load torque.

6.6.4 Investigation of robustness against rated-load torque disturbance

Figure 6.9 shows the robustness of the system against an external rated-load torque disturbance. The load is suddenly changed from no-load to rated-load torque (7.4 Nm) as a disturbance on the fed machine. The motor speed drops slightly, and the controller recovers within a short time (0.38 s). The speed estimation error is 0.4% of the measured speed, which is reduced to 0.25% after the load torque is applied. It is noted that the speed error is not significant during load transient at t =0.325 s. The THD of the stator current is reduced from 5.42% to 4.88% after the load torque is applied. The stator flux also remains constant at its rated value during load change, which confirms decoupled control of torque and flux.

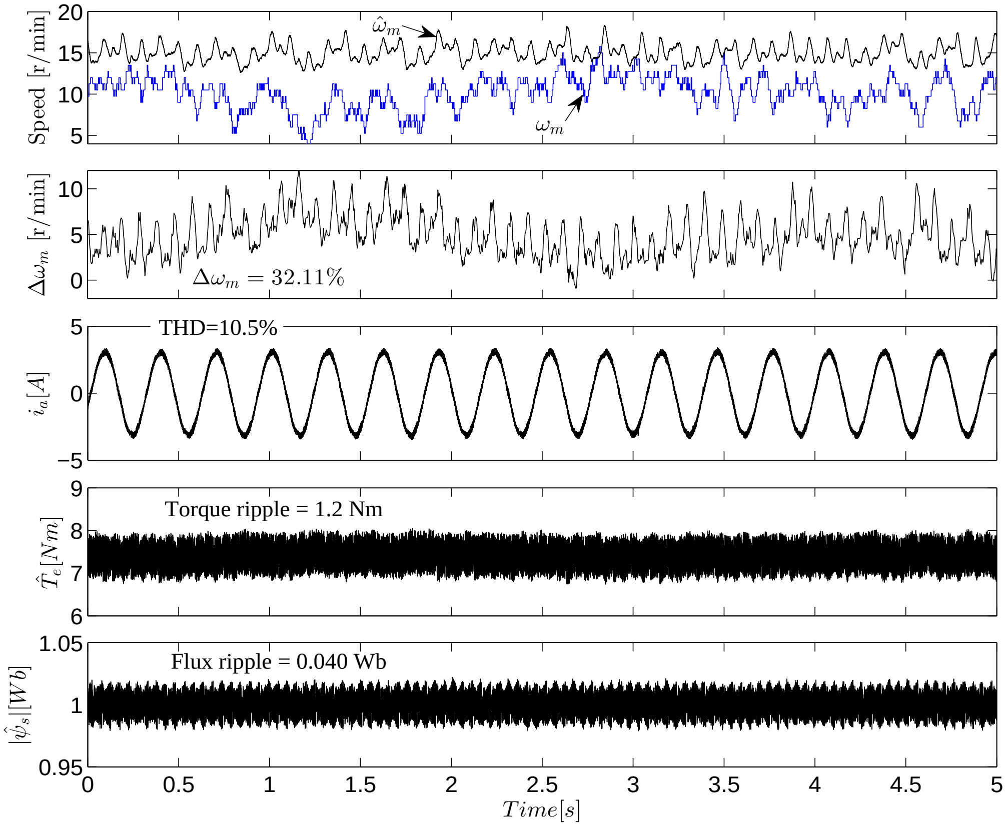

Figure 6.8: Experimental low-speed behaviour for the all voltage vectors based FS-PTC at 15 r/min (0.5 Hz) at full-load torque using the sampling time of 120 μs.

6.6.5 Torque-transient characteristics

Step torque-transient is investigated, and the results are presented in Fig. 6.10. Initially, the machine is started with 100 r/min, and a step speed of 1415 r/min is then commanded to achieve a step torque command. It can be seen that the controller alters active and zero vectors frequently in the steady-state condition. Whereas only active voltage vectors (long and medium) are selected during the transient. This yields fast dynamic torque response. The torque rise time of the proposed controller is 0.7 ms. It is noted that the torque rise time is 0.2 ms higher than the controller with speed sensor presented in the previous chapters. This is because the step torque here is 135% rated-torque (10 Nm), whereas it was equal to the rated-torque (7.4 Nm) in the previous cases.

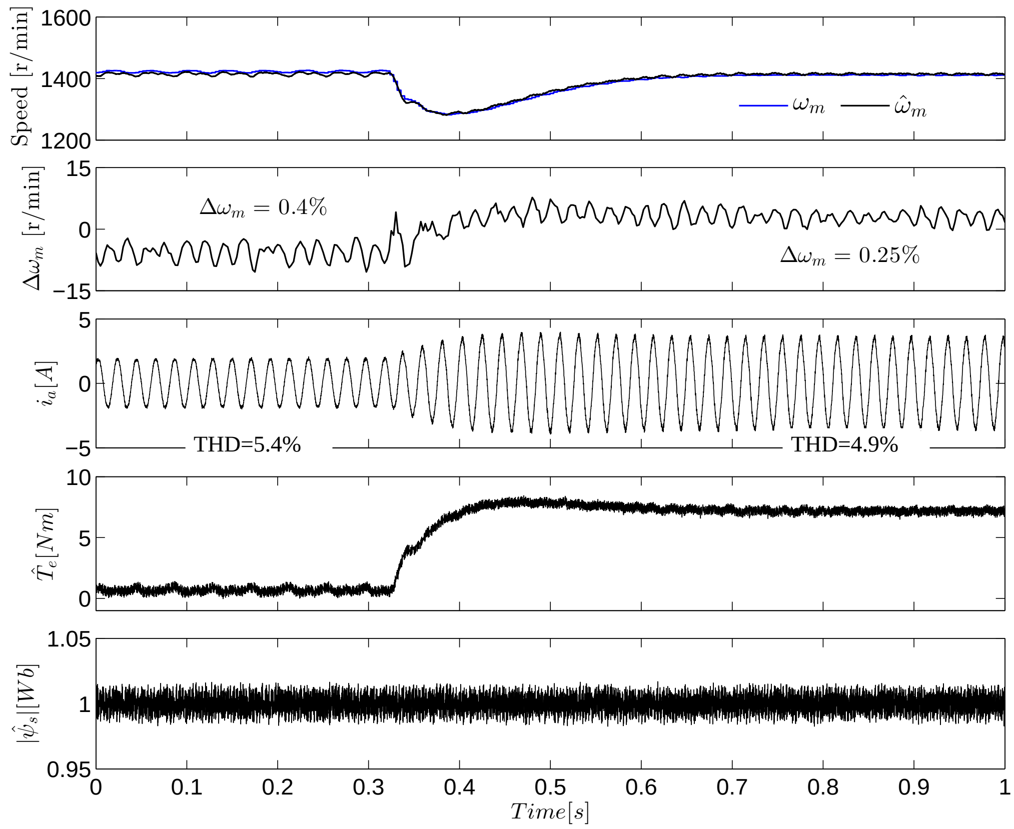

Figure 6.9: Experimental dynamic behaviour of the machine at rated-speed under an external rated-load torque disturbance.

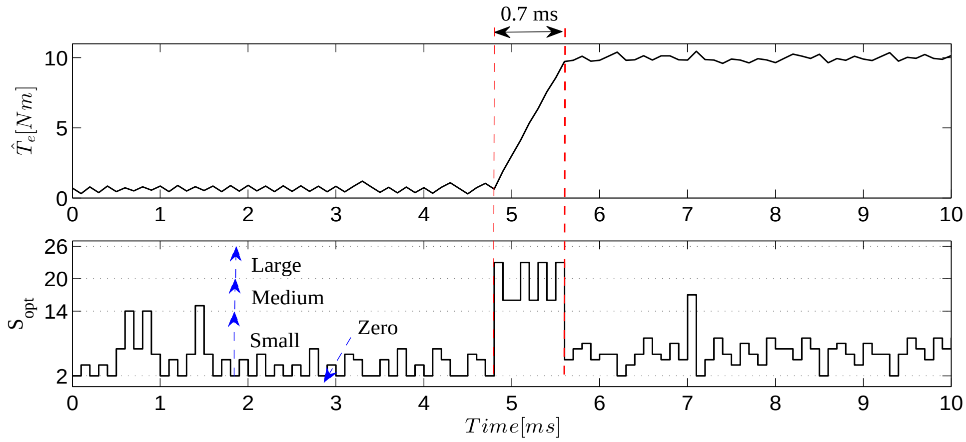

Figure 6.10: Experimental step torque response showing the selected inverter switching states S_{opt}.

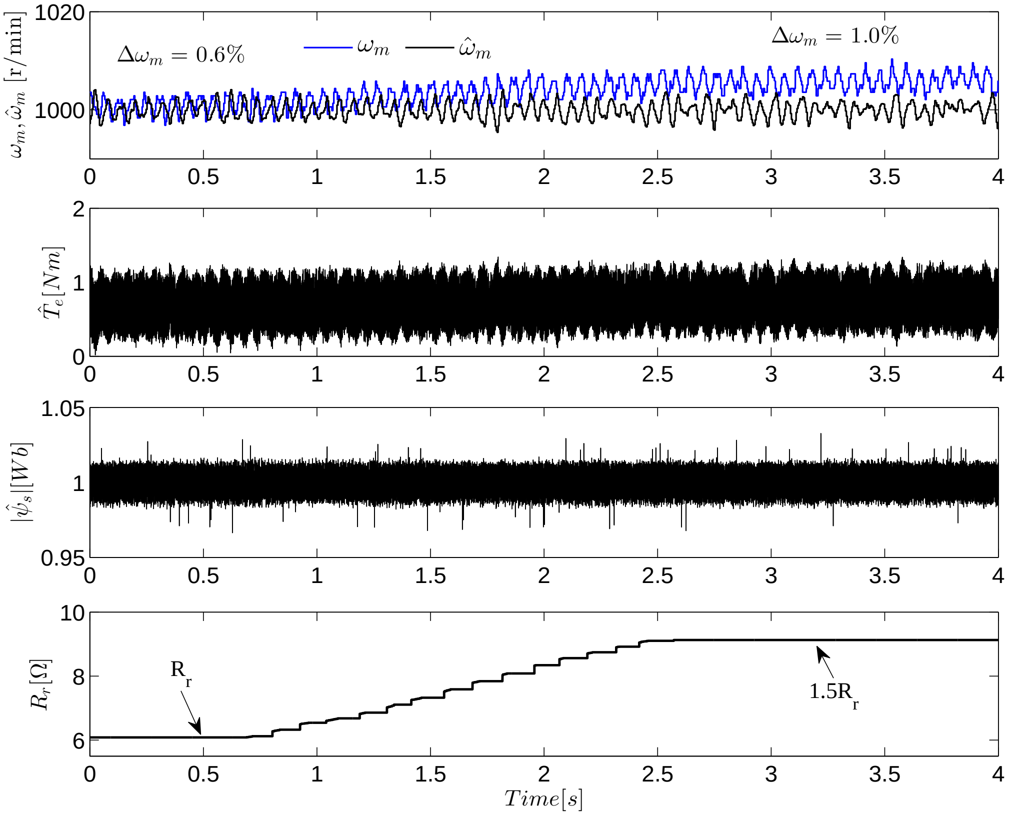

Figure 6.11: Experimental rotor resistance sensitivity at 1000 r/min without load torque.

6.6.6 Rotor resistance sensitivity of the controller

The resistance of the machine changes due to the change of temperature during motor operation. Accuracy of the rotor current model of IM is sensitive to rotor resistance variations, especially at high-speed. This is because the change of rotor resistance changes the rotor time constant. To investigate the rotor resistance sensitivity of the controller, the rotor resistance is increased gradually from 1 to 1.5 per unit. in the controller, and the responses are illustrated in Fig. 6.11. It can be seen that the speed error is increased slightly from 0.6% to 1.0%. However, the estimation error is still acceptable. Figure 6.11 also shows that the torque is increased slightly and the stator flux remains constant at its rated value. The system is stable without any online parameter estimation.

6.6.7 Dynamic behaviour in the field-weakening region

Finally, the behaviour of the proposed system in the field-weakening region is investigated. The tests are conducted without load torque; only inertia of the dc machine is connected to the fed motor. In order to maintain the speed limit (1800 r/min) of the dc machine, the dc-link voltage of the inverter is reduced to 300 V (which is 51% rated-voltage). Hence, the new base speed is about 716 r/min. The speed of the test setup is limited to 250% of the new base speed. The stator flux is also limited to the range of 33–100% rated stator flux to avoid very high-speed.

The machine is run up from 15 r/min to 1800 r/min (250% of the new base speed), and the behaviour of the system is illustrated in Fig. 6.12. The speed profile is divided into three different regions: region I (up to the base speed 716 r/min), region II (from 716 r/min to 1700 r/min) and region III (higher than 1700 r/min). In the region I, the torque is constant at its maximum value, so it is called constant torque region. In the region II, the torque command decreases as the speed increases to keep the delivered power constant, so it is called constant power region. In this region, the stator flux decreases proportionally with the increase of speed from the base speed to keep the back-emf constant. For this reason, the stator current is constant in the region II. The speed increases further and enters into the region III, where both torque and stator flux decrease, as the dc-link voltage is not sufficient to inject the required current. The regions II and III are called as field-weakening region. In all the three regions, the estimated speed matches with the real speed properly. The mean steady-state speed error is 0.6% of the measured speed, which is acceptable. The speed transitions, from one region to another, are seamless. The torque and stator flux can also track their command values accurately over the whole operating range. The dynamic torque vs. speed response of the machine corresponding to Fig. 6.12 is also plotted in Fig. 6.13 to show the field-weakening characteristic.

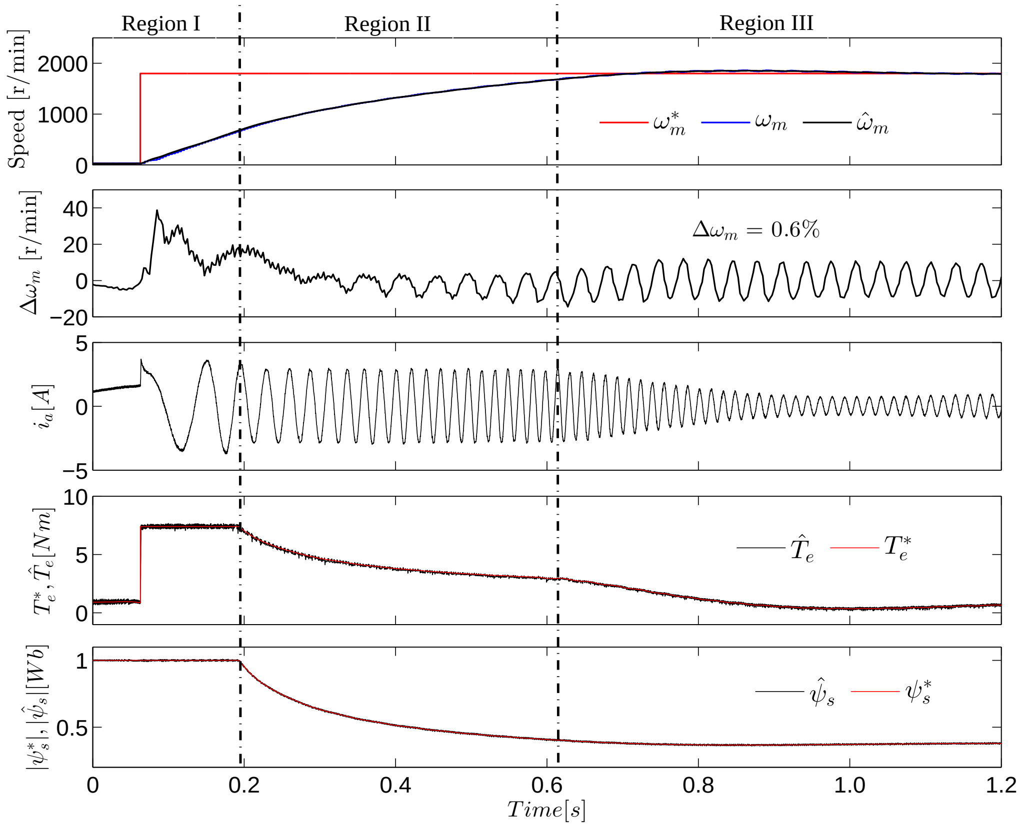

Figure 6.12: Experimental dynamic behaviour of the machine in the field-weakening region in step speed command.

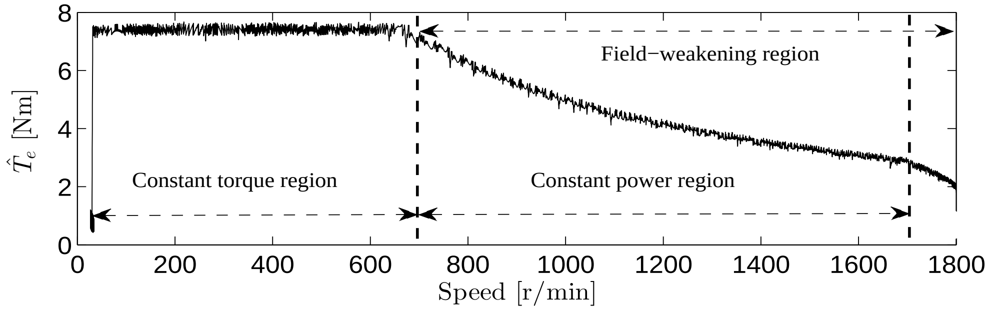

Figure 6.13: Experimental dynamic torque vs. speed response of the machine corresponding to Fig. 6.12 to show the field-weakening characteristic.

6.7 Summary

This chapter has proposed a simplified sensorless FS-PTC for IM supplied from a 3L-NPC inverter. The rotor speed and flux, and the stator current are estimated using an EKF. Only the rotor current model is employed for tuning the EKF. Using the SPVs strategy, the computational burden in the predictions step is reduced by 46%. However, the overall computational burden of the proposed sensorless PTC is reduced by 20%. This allows implementation of the proposed control algorithm with a low sampling time, which yields improved torque, flux and speed responses, especially at low-speed. The controller overcomes the neutral-point voltage problem of the inverter effectively. Experimental results illustrate that the proposed sensorless controller is capable of estimating the speed accurately from 15 r/min under full-load torque to a high-speed, including the field-weakening region. Good stator flux and torque responses are achieved under different operating conditions. The proposed controller is also robust against external rated-load disturbance and parameter variation.

Chapter 7

Conclusions and Future Prospects

The findings of this thesis can be summarised as follows:

1) Two simplified FS-PTC strategies based on SPVs and RSFVC in Chapters 3 and 5, respectively, have been proposed to reduce both the computational burden of the PTC algorithm and complexity when designing the cost function. It is found that the computational burden is reduced by up to 49%. Thus, the required processing power of the micro-controller is reduced significantly. The average switching frequency is reduced by 25% using the SPVs strategy for a 2L-VSI fed IM drive. It is also shown that designing a cost function for the proposed FS-PTC strategies is not as complex as the conventional FS-PTC strategy.

2) The performance of the FS-PTC with a 3L-NPC VSI has been investigated in Chapter 4. It is found that the average switching frequency is less, and its variation range over a wide speed range is also smaller, than the 2L-VSI fed IM drive. For a particular speed, the average switching frequency is almost constant at different load torques. Some other advantages are also apparent, such as low harmonic distortion in the stator current, and less torque and flux ripple. The neutral-point voltage inherited from the 3L-NPC inverter has been controlled effectively at around zero value. The computational burden of the proposed FS-PTC with the 3L-NPC inverter is reduced by 38% using the SPVs strategy.

3) Finally, a speed-sensorless simplified FS-PTC based on EKF has been demonstrated

in Chapter 6. The estimated current, instead of the measured current, has been proposed for the stator flux estimation and predictions to avoid the time delay between measurement and estimation. It is shown that the controller is capable of estimating the speed accurately from a very low-speed under full-load torque to a high-speed, including the field-weakening region. The computational burden of the proposed sensorless FS-PTC algorithm is reduced by 20% using the SPVs strategy, which yields improved torque, flux and speed responses, especially at low-speed.

All of the above findings have been experimentally verified. The analysis and verification are described fully in Chapters 3–6. The contributions are discussed further, along with possible future opportunities, below.

Chapter 3 has proposed a SPVs strategy for simplifying the FS-PTC. The simplified SPVs approach is applied to a 2L-VSI fed IM drive. The proposed controller only employed three voltage vectors, instead of the eight used in the conventional FS-PTC for prediction and optimisation. Thus the computational efficiency is improved. A reduction in the average switching frequency of each semiconductor switch is achieved by not considering the number of switching transitions in the cost function. This reduces the number of control objectives in the cost function. The reduced number of control objectives in the cost function makes the selection of weighting factors simpler than in the conventional method. These benefits are achieved without sacrificing the torque and flux performance.

These findings can assist future research in the following areas:

I) Incorporation of machine parameter estimation, dead-time compensation strategy, duty cycle control algorithm and more elaborate inverters—multi-level and matrix converters—within the FS-PTC IM drive strategy. Including these extra features would be possible due to the reduction in the computational burden proposed in this thesis.

II) Computationally efficient predictive control of other types of drives and converters. For example, the proposed simplified approach could be applied easily to a linear machine for nonlinear force (thrust) control, a permanent magnet synchronous machine (PMSM) for torque control and grid/PV connected converters for voltage/current/power control. For the linear machine, power-factor correction (PFC) can be easily combined with the duty cycle control.

III) A simplified DB PTC technique for motor drives with constant switching frequency. The predicted optimum voltage vector will be updated by a correction voltage to generate a reference voltage vector. The correction voltage will be produced based on DB torque and flux. In this case, the predicted optimal torque and flux will be used with the respective references. Finally, the reference voltage vector will be produced using SVM technique and applied to the motor terminals.

Chapter 4 has proposed the integration of the FS-PTC with a 3L-NPC VSI driven IM drive. It has been shown that a three-level inverter fed IM drive produces improved dynamic torque and flux responses, and stator current THD with the reduced average switching frequency, compared to the 2L-VSI fed IM drive. The variation range of average switching frequency in the whole operating range of the machine is also small, which is a hallmark of the proposed FS-PTC. For a particular speed, the average switching frequency is almost constant at different load torques. The inherent neutral-point voltage problem of a 3L-NPC inverter is handled easily by treating the neutral-point voltage as a variable to the cost function, and is maintained at around zero. The performance of the proposed controller has also been compared with the well established classical FOC and DTC strategies at the specific operation point. Experimental results show that the proposed FS-PTC yields better overall performance at a particular operating point. However, the computational burden of the proposed FS-PTC is much higher. To reduce the computational burden, the SPVs strategy is applied to the proposed 3L-NPC inverter fed IM drive. As a result, the computational burden of the proposed algorithm is significantly reduced without affecting the dynamic performance of the system. The proposed 3L-NPC VSI is of course expensive and is complex in structure when compared with a 2L-VSI. However, this study illustrates the effectiveness of the fundamental FS-PTC with a 3L-NPC VSI using today's commercially available DSP.

Chapter 5 has proposed a second simplified RSFVC-based FS-PTC for the IM drive supplied from the 3L-NPC inverter. Apart from the number of possible prediction vectors discussed in Chapters 3 and 4, the computational burden is evidently a consequence of the complex calculations in the prediction loop of the FS-PTC strategy. The proposed RSFVC-based FS-PTC does not contain complex stator current and torque calculations inside the prediction loop. Thus the controller demands less processing power. The required processing power for the RSFVC-based FS-PTC is further reduced by developing a compound FS-PTC strategy. This is the combination of the RSFVC- and SPVs-based FS-PTC strategies. The tuning effort on the weighting factor between torque and flux errors is also avoided as torque is now not predicted inside the prediction loop. Experimental results show that the proposed controller yields a similar performance to that achieved with the torque calculations in the prediction loop (discussed in Chapter 4). The proposed PTC structure contains one additional PI controller and simple block for the RSFVC. However, the stability test results and the torque-transient response confirm that the additional cascade connections have no negative effects on the dynamic performance of the system.

In future, the analysis proposed in Chapters 4 and 5 should facilitate FS-PTC use for medium- and high-voltage drive applications, where more inverter switching states may be available and a higher number of objectives need to be controlled. More specifically, the following projects are expected to benefit from the proposed FS-PTC strategies.

IV) A dual inverter fed open-end winding machine for fault tolerant operation, where 64 voltage vectors are available. The number of voltage vectors can be reduced using the proposed SPVs strategy. Zero common mode voltage and zero sequence current can be controlled by treating them as variables to the cost function.

V) A simplified FS-PTC for a multi-phase machine where additional objectives, such as common mode voltage and harmonic distortion in a particular plane, require control.

VI) A modified FS-PTC for SM driven by a 3L-NPC inverter, where the torque PI controller can be eliminated using the relation between torque and load angle; the torque is proportional to the load angle within a certain range.

VII) A simplified hybrid PTC, a combination of vector control and classical PTC, using the SPVs strategy. The vector control technique (inner current control loop) will be used to generate the reference voltage vector. The prediction vectors will be selected based on the position of the reference voltage vector. Finally, an optimum switching state will be selected based on prediction, as with the PTC. In this case, the computational burden is expected to be reduced significantly, especially in systems with multi-level converters and multi-phase machine drives in which the number of voltage vectors is expected to be large.

VIII) FS-PTC of high-power electrical drives fed by a three-level active neutral-point clamped (3L-ANPC) inverters under device failure conditions. Two types of device failure may be considered: open failure and short failure. In this project, balanced power loss distribution among the semiconductor devices in the inverter can be achieved by selecting proper zero switching states. In addition, the reliability of the system, compared to that of the 3L-NPC inverters, may be improved.

IX) A trade-off can be established between the system's performance and switching frequency using various control strategies (i.e., FOC, DTC and PTC). A graph of THD vs. switching frequency can be plotted to show how much higher a switching frequency would be required for FOC and DTC to achieve the same THD as with the PTC. Similarly, another graph of torque and flux ripple vs. switching frequency can also be plotted for the same torque and flux ripple as with the PTC.

Chapter 6 has proposed an EKF based simplified sensorless FS-PTC for IM supplied from the 3L-NPC inverter. The rotor speed and flux, and the stator current are estimated using the EKF. As both the predictive control and EKF require intensive calculations, the proposed sensorless strategy is computationally expensive. Using the proposed SPVs strategy, the computational burden of the predictive algorithm is reduced, enabling implementation of the proposed sensorless control algorithm with a short sampling time. As a result, the proposed controller yields improved torque, flux and speed responses, especially at low-speed. To avoid the time delay between measurement and estimation, the estimated current, instead of the measured current, has been proposed in the stator flux estimation, as well as in the predictions. Experimental results show that the controller is capable of estimating the speed accurately from a very low-speed under full-load torque to a high-speed, including the field-weakening region. Good stator flux and torque responses are achieved under different operating conditions. The proposed controller is also robust against external rated-load torque disturbance and parameter variation.

In future, this sensorless work can be extended for the followings.

X) Compensating the rotor resistance variations and a stability analysis of the proposed controller, to improve the system performance further.

XI) Designing a starting method from zero speed for the proposed sensorless FS-PTC. As both the initial rotation direction and speed is unknown, the motor may not start smoothly from zero speed. If the estimated speed is significantly lower than the actual speed, the sensorless drive may be unstable. Hence, it is useful to design an observer which will be used only for starting the machine. Once the estimated speed converges to the actual speed, the original sensorless controller will be activated.

XII) A comparative study of different model-based observers, such as MRAS, SMO and LO, for an sensorless FS-PTC strategy. This would determine the most appropriate observer. In FS-PTC, an appropriate observer is vital, as the predictions of control objectives are dependent on the estimated speed and flux. The errors in the estimated variables lead to incorrect selection of the voltage vectors, thus degrading the control performance. In the observer selection process, some parameters will be considered as the key factors. These could include the structural complexity of the overall system, the required computational effort, and the control performance. A reduction in the overall computational burden, as proposed in this thesis, will be more significant for less complex observers.

XIII) Simplified sensorless FS-PTC strategies are expected to be possible for linear machine and PMSM drives using the proposed SPVs strategy.

Finally, the experimental results presented in this thesis can be compared with simulation results to observe practical implementation effects. Simulation results may also help to provide insight into any unusual phenomena observed experimentally.

Bibliography

[1] H. W. Beaty and J. J. L. Kirtley, *Electric Motor Handbook.* McGraw-Hill, 1998.

[2] K. T. Chau, *Electric Vehicle Machines and Drives : Design, Analysis and Application.* Wiley, 2015.

[3] T. A. Lipo, *Vector control and dynamics of AC drives.* Oxford University Press, vol. 41, 1996.

[4] B. K. Bose, "Power electronics and motor drives recent progress and perspective," *IEEE Transactions on Industrial Electronics*, vol. 56, no. 2, pp. 581–588, Feb. 2009.

[5] ——, *Power Electronics and Motor Drives—Advances and Trends.* Burlington, MA: Academic, 2006.

[6] G. S. Buja and M. P. Kazmierkowski, "Direct torque control of PWM inverter-fed ac motors–a survey," *IEEE Transactions on Industrial Electronics*, vol. 51, no. 4, pp. 744–757, Aug. 2004.

[7] D. Casadei, F. Profumo, G. Serra, and A. Tani, "FOC and DTC: two viable schemes for induction motors torque control," *IEEE Transactions Power Electronics*, vol. 17, no. 5, pp. 779–787, Sep. 2002.

[8] I. Takahashi and T. Noguchi, "A new quick-response and high-efficiency control strategy of an induction motor," *IEEE Transactions on Industrial Applications*, vol. IA-22, no. 5, pp. 820–827, Sept. 1986.

[9] P. Vas, *Sensorless Vector and Direct Torque Control.* New York: Oxford Univ. Press, 1998.

[10] S.-K. Sul, *Control of Electric Machine Drive Systems.* Wiley-IEEE, 2011.

[11] M. Depenbrock, "Direct self-control (DSC) of inverter-fed induction machine," *IEEE Transactions on Power Electronics*, vol. 3, no. 4, pp. 420–429, Oct. 1988.

[12] K.-B. Lee, J.-H. Song, I. Choy, and J.-Y. Yoo, "Torque ripple reduction in DTC of induction motor driven by three-level inverter with low switching frequency," *IEEE Transactions on Power Electronics*, vol. 17, no. 2, pp. 255–264, Mar. 2002.

[13] C. Reza, M. Didarul Islam, and S. Mekhilef, "A review of reliable and energy efficient direct torque controlled induction motor drives," *Renewable and Sustainable Energy Reviews*, vol. 37, pp. 919–932, June 2014.

[14] C. E. Garcia, D. M. Prett, and M. Morari, "Model predictive control: theory and practice–a survey," *Automatica*, vol. 25, no. 3, pp. 335–348, May 1989.

[15] J. M. Maciejowski, *Predictive control with constraints.* Englewood Cliffs, NJ: Prentice Hall, 2002.

[16] E. F. Camacho and C. Bordons, *Model predictive control.* Springer, 2004.

[17] G. C. Goodwin, M. M. Seron, and J. A. D. Dona, *Constrained control and estimation–an optimization perspective.* Springer Verlag, 2005.

[18] J. Holtz and S. Stadtfeld, "Predictive controller for the stator current vector of AC machines fed from a switched voltage source," in *International Power Electronics Conference, IPEC, Tokyo*, 1983, pp. 1665–1675.

[19] J. H. Lee, "Model predictive control: Review of the three decades of development," *International Journal of Control, Automation, and Systems*, vol. 9, no. 3, pp. 415–424, Jun. 2011.

[20] S. Kouro, P. Cortes, R. Vargas, U. Ammann, and J. Rodriguez, "Model predictive control—a simple and powerful method to control power converters," *IEEE Transactions on Industrial Electronics*, vol. 56, no. 6, pp. 1826–1838, Jun. 2009.

[21] A. Linder and R. Kennel, "Model predictive control for electrical drives," in *Power Electronics Specialists Conference, 2005. PESC '05. IEEE 36th*, June 2005, pp. 1793–1799.

[22] P. Correa, M. Pacas, and J. Rodriguez, "Predictive torque control for inverter-fed induction machines," *IEEE Transactions on Industrial Electronics*, vol. 54, no. 2, pp. 1073–1079, April 2007.

[23] P. Cortes, M. P. Kazmierkowski, R. M. Kennel, D. Quevedo, and J. Rodriguez, "Predictive control in power electronics and drives," *IEEE Transactions on Industrial Electronics*, vol. 55, no. 12, pp. 4312–4324, Dec. 2008.

[24] P. Cortes, G. Ortiz, J. I. Yuz, J. Rodriguez, S. Vazquez, and L. G. Franquelo, "Model predictive control of an inverter with output LC filter for UPS applications," *IEEE Transactions on Industrial Electronics*, vol. 56, no. 6, pp. 1875–1883, June 2009.

[25] S. Bolognani, S. Bolognani, L. Peretti, and M. Zigliotto, "Design and implementation of model predictive control for electrical motor drives," *IEEE Transactions on Industrial Electronics*, vol. 56, no. 6, pp. 1925–1936, June 2009.

[26] A. Linder, R. Kanchan, R. Kennel, and P. Stolze, *Model-based predictive control of electric drives.* Germany:Cuvillier Verlag Gottingen, 2010.

[27] T. Geyer, "A comparison of control and modulation schemes for medium-voltage drives: Emerging predictive control concepts versus PWM-based schemes," *IEEE Transactions on Industry Applications*, vol. 47, no. 3, pp. 1380–1389, May 2011.

[28] J. Rodriguez and P. Cortes, *Predictive control of power converters and electrical drives.* Wiley, 2012.

[29] J. Rodriguez, M. P. Kazmierkowski, J. R. Espinoza, P. Zanchetta, H. Abu-Rub, H. A. Young, and C. A. Rojas, "State of the art of finite control set model predictive control in power electronics," *IEEE Transactions on Industrial Informatics*, vol. 9, no. 2, pp. 1003–1016, May 2013.

[30] S. Vazquez, J. I. Leon, L. G. Franquelo, J. Rodriguez, H. A. Young, A. Marquez, and P. Zanchetta, "Model predictive control: A review of its applications in power electronics," *IEEE Industrial Electronics Magazine*, vol. 8, no. 1, pp. 16–31, March 2014.

[31] S. Kouro, M. A. Perez, J. Rodriguez, A. M. Llor, and H. A. Young, "Model predictive control: MPC's role in the evolution of power electronics," *IEEE Industrial Electronics Magazine*, vol. 9, no. 4, pp. 8–21, Dec. 2015.

[32] M. Curkovic, K. Jezernik, and R. Horvat, "FPGA-based predictive sliding mode controller of a three-phase inverter," *IEEE Transactions on Industrial Electronics*, vol. 60, no. 2, pp. 637–644, Feb. 2013.

[33] C. Buccella, C. Cecati, and H. Latafat, "Digital control of power converters—a survey," *IEEE Transactions on Industrial Informatics*, vol. 8, no. 3, pp. 437–447, Aug. 2012.

[34] T. Atalik, M. Deniz, E. Koc, C. Gercek, B. Gultekin, M. Ermis, and I. Cadirci, "Multi-DSP and -FPGA-based fully digital control system for cascaded multilevel converters used in FACTS applications," *IEEE Transactions on Industrial Informatics*, vol. 8, no. 3, pp. 511–527, Aug. 2012.

[35] A. Sanchez, A. de Castro, and J. Garrido, "A comparison of simulation and hardware-in-the- loop alternatives for digital control of power converters," *IEEE Transactions on Industrial Informatics*, vol. 8, no. 3, pp. 491–500, Aug. 2012.

[36] E. Monmasson, L. Idkhajine, M. N. Cirstea, I. Bahri, A. Tisan, and M. W. Naouar, "FPGAs in industrial control applications," *IEEE Transactions on Industrial Informatics*, vol. 7, no. 2, pp. 224–243, May 2011.

[37] B. Alecsa, M. N. Cirstea, and A. Onea, "Simulink modeling and design of an efficient hardware-constrained FPGA-based PMSM speed controller," *IEEE Transactions on Industrial Informatics*, vol. 8, no. 3, pp. 554–562, Aug. 2012.

[38] M. W. Naouar, A. A. Naassani, E. Monmasson, and I. Slama-Belkhodja, "FPGA-based predictive current controllerfor synchronous machine speed drive," *IEEE Transactions on Power Electronics*, vol. 23, no. 4, pp. 2115–2126, July 2008.

[39] J. A. Riveros, F. Barrero, E. Levi, M. J. Duran, S. Toral, and M. Jones, "Variable-speed five-phase induction motor drive based on predictive torque control," *IEEE Transactions on Industrial Electronics*, vol. 60, no. 8, pp. 2957–2968, Aug. 2013.

[40] M. Preindl and S. Bolognani, “Model predictive direct torque control with finite control set for PMSM drive systems, part 1: Maximum torque per ampere operation,” *IEEE Transactions on Industrial Informatics*, vol. 9, no. 4, pp. 1912–1921, Nov. 2013.

[41] H. Miranda, P. Cortes, J. I. Yuz, and J. Rodriguez, “Predictive torque control of induction machines based on state-space models,” *IEEE Transactions on Industrial Electronics*, vol. 56, no. 6, pp. 1916–1924, June 2009.

[42] T. Geyer, G. Papafotiou, and M. Morari, “Model predictive direct torque control—part I: Concept, algorithm, and analysis,” *IEEE Transactions on Industrial Electronics*, vol. 56, no. 6, pp. 1894–1905, Jun. 2009.

[43] G. Papafotiou, J. Kley, K. G. Papadopoulos, P. Bohren, and M. Morari, “Model predictive direct torque control—part ii: Implementation and experimental evaluation,” *IEEE Transactions on Industrial Electronics*, vol. 56, no. 6, pp. 1906–1915, June 2009.

[44] M. Preindl and S. Bolognani, “Model predictive direct speed control with finite control set of PMSM drive systems,” *IEEE Transactions on Power Electronics*, vol. 28, no. 2, pp. 1007–1015, Feb. 2013.

[45] R. Kennel, J. Rodrguez, J. Espinoza, and M. Trincado, “High performance speed control methods for electrical machines: An assessment,” in *Industrial Technology (ICIT), 2010 IEEE International Conference on*, March 2010, pp. 1793–1799.

[46] J. Rodriguez, R. M. Kennel, J. R. Espinoza, M. Trincado, C. A. Silva, and C. A. Rojas, “High-performance control strategies for electrical drives: An experimental assessment,” *IEEE Transactions on Industrial Electronics*, vol. 59, no. 2, pp. 812–820, Feb. 2012.

[47] T. Geyer, “Computationally efficient model predictive direct torque control,” *IEEE Transactions on Power Electronics*, vol. 26, no. 10, pp. 2804–2816, Oct. 2011.

[48] Z. Ma, S. Saeidi, and R. Kennel, "FPGA implementation of model predictive control with constant switching frequency for PMSM drives," *IEEE Transactions on Industrial Informatics*, vol. 10, no. 4, pp. 2055–2063, Nov. 2014.

[49] C. A. Rojas, J. Rodriguez, F. Villarroel, J. R. Espinoza, C. A. Silva, and M. Trincado, "Predictive torque and flux control without weighting factors," *IEEE Transactions on Industrial Electronics*, vol. 60, no. 2, pp. 681–690, Feb. 2013.

[50] X. del Toro Garcia, A. Arias, M. G. Jayne, and P. A. Witting, "Direct torque control of induction motors utilizing three-level voltage source inverters," *IEEE Transactions on Industrial Electronics*, vol. 55, no. 2, pp. 956–958, Feb. 2008.

[51] J. Rodriguez, S. Bernet, P. K. Steimer, and I. E. Lizama, "A survey on neutral-point-clamped inverters," *IEEE Transactions on Industrial Electronics*, vol. 57, no. 7, pp. 2219–2230, July 2010.

[52] Y. Zhang, J. Zhu, Z. Zhao, W. Xu, and D. G. Dorrell, "An improved direct torque control for three-level inverter-fed induction motor sensorless drive," *IEEE Transactions on Power Electronics*, vol. 27, no. 3, pp. 1502–1513, March 2012.

[53] S. K. Hoseini, J. Adabi, and A. Sheikholeslami, "Predictive modulation schemes to reduce common-mode voltage in three-phase inverters-fed AC drive systems," *IET Power Electronics*, vol. 7, no. 4, pp. 840–849, April 2014.

[54] S. R. Pulikanti, M. S. A. Dahidah, and V. G. Agelidis, "Voltage balancing control of three-level active NPC converter using SHE-PWM," *IEEE Transactions on Power Delivery*, vol. 26, no. 1, pp. 258–267, Jan. 2011.

[55] N. Celanovic and D. Boroyevich, "A comprehensive study of neutral-point voltage balancing problem in three-level neutral-point-clamped voltage source PWM inverters," *IEEE Transactions on Power Electronics*, vol. 15, no. 2, pp. 242–249, Mar. 2000.

[56] R. Vargas, P. Cortes, U. Ammann, J. Rodriguez, and J. Pontt, "Predictive control of a three-phase neutral-point-clamped inverter," *IEEE Transactions on Industrial Electronics*, vol. 54, no. 5, pp. 2697–2705, Oct. 2007.

[57] S. Alepuz, S. Busquets-Monge, J. Bordonau, P. Cortes, and S. Kouro, "Control methods for low voltage ride-through compliance in grid-connected NPC converter based wind power systems using predictive control," in *Energy Conversion Congress and Exposition, 2009. ECCE 2009. IEEE*, Sept. 2009, pp. 363–369.

[58] E. Oyarbide, A. Martinez-Iturbe, S. Aurtenechea, M. A. Rodriguez-Vidal, and E. Laloya, "Exact predictive direct power control of three-level NPC converters for wind power applications," in *Power Electronics and Applications, 2009. EPE '09. 13th European Conference on*, Sept. 2009, pp. 1–9.

[59] J. D. Barros and J. F. Silva, "Optimal predictive control of three-phase NPC multilevel inverter: Comparison to robust sliding mode controller," in *Power Electronics Specialists Conference, 2007. PESC 2007. IEEE*, June 2007, pp. 2061–2067.

[60] ——, "Optimal predictive control of three-phase NPC multilevel converter for power quality applications," *IEEE Transactions on Industrial Electronics*, vol. 55, no. 10, pp. 3670–3681, Oct 2008.

[61] M. A. Perez, J. Rodriguez, E. J. Fuentes, and F. Kammerer, "Predictive control of AC-AC modular multilevel converters," *IEEE Transactions on Industrial Electronics*, vol. 59, no. 7, pp. 2832–2839, July 2012.

[62] A. A. de Melo Bento, P. K. P. Vieira, and E. R. C. da Silva, "Application of the one-cycle control technique to a three-phase three-level NPC rectifier," *IEEE Transactions on Industry Applications*, vol. 50, no. 2, pp. 1177–1184, March 2014.

[63] P. Stolze, F. Bauer, P. Landsmann, R. Kennel, and T. Mouton, "Predictive torque control of an induction machine fed by a neutral point clamped inverter," in *Workshop on Pred. Control of Elect. Drives and Power Electron.*, Oct. 2011, pp. 24–29.

[64] P. Stolze, P. Karamanakos, R. Kennel, S. Manias, and T. Mouton, "Variable switching point predictive torque control for the three-level neutral point clamped inverter," in *Eur. Power Electron. Conf.*, Sep. 2013, pp. 1–10.

[65] N. Al-Sheakh Ameen, A. A. Naassani, and R. M. Kennel, “Design of a digital system dedicated for electrical drive applications,” *J. EPE*, vol. 20, no. 4, pp. 37–44, Dec. 2010.

[66] C. Lascu, I. Boldea, and F. Blaabjerg, “Direct torque control of sensorless induction motor drives: a sliding-mode approach,” *IEEE Transactions on Industry Applications*, vol. 40, no. 2, pp. 582–590, March 2004.

[67] Y.-R. Kim, S.-K. Sul, and M.-H. Park, “Speed sensorless vector control of induction motor using extended Kalman filter,” *IEEE Transactions on Industry Applications*, vol. 30, no. 5, pp. 1225–1233, Sep. 1994.

[68] K. L. Shi, T. F. Chan, Y. K. Wong, and S. L. Ho, “Speed estimation of an induction motor drive using an optimized extended Kalman filter,” *IEEE Transactions on Industrial Electronics*, vol. 49, no. 1, pp. 124–133, Feb. 2002.

[69] F. Alonge, T. Cangemi, F. D’Ippolito, A. Fagiolini, and A. Sferlazza, “Convergence analysis of extended Kalman filter for sensorless control of induction motor,” *IEEE Transactions on Industrial Electronics*, vol. 62, no. 4, pp. 2341–2352, April 2015.

[70] S. Bolognani, L. Tubiana, and M. Zigliotto, “Extended Kalman filter tuning in sensorless PMSM drives,” *IEEE Transactions on Industrial Applications*, vol. 39, no. 6, pp. 1741–1747, Nov. 2003.

[71] A. N. Smith, S. M. Gadoue, and J. W. Finch, “Improved rotor flux estimation at low speeds for torque MRAS-based sensorless induction motor drives,” *IEEE Transactions on Energy Conversion*, vol. 31, no. 1, pp. 270–282, March 2016.

[72] T.-S. Kwon, M.-H. Shin, and D.-S. Hyun, “Speed sensorless stator flux-oriented control of induction motor in the field weakening region using luenberger observer,” *IEEE Transactions on Power Electronics*, vol. 20, no. 4, pp. 864–869, July 2005.

[73] M. Preindl and E. Schaltz, “Sensorless model predictive direct current control using novel second-order PLL observer for PMSM drive systems,” *IEEE Transactions on Industrial Electronics*, vol. 58, no. 9, pp. 4087–4095, Sept. 2011.

[74] J. Guzinski and H. Abu-Rub, “Speed sensorless induction motor drive with predictive current controller,” *IEEE Transactions on Industrial Electronics*, vol. 60, no. 2, pp. 699–709, Feb. 2013.

[75] F. Wang, X. Mei, H. Dai, S. Yu, and P. He, “Sensorless finite control set predictive current control for an induction machine,” in *2015 IEEE International Conference on Information and Automation*, Aug. 2015, pp. 3106–3111.

[76] S. Alireza Davari, D. A. Khaburi, F. Wang, and R. M. Kennel, “Using full order and reduced order observers for robust sensorless predictive torque control of induction motors,” *IEEE Transactions on Power Electronics*, vol. 27, no. 7, pp. 3424–3433, July 2012.

[77] F. Wang, Z. Chen, P. Stolze, J.-F. Stumper, J. Rodriguez, and R. Kennel, “Encoderless finite-state predictive torque control for induction machine with a compensated MRAS,” *IEEE Transactions on Industrial Informatics*, vol. 10, no. 2, pp. 1097–1106, May 2014.

[78] F. Wang, Z. Zhang, S. Alireza Davari, R. Fotouhi, D. Arab Khaburi, J. Rodriguez, and R. Kennel, “An encoderless predictive torque control for an induction machine with a revised prediction model and EFOSMO,” *IEEE Transactions on Industrial Electronics*, vol. 61, no. 12, pp. 6635–6644, Dec. 2014.

[79] T. Geyer and D. E. Quevedo, “Multistep finite control set model predictive control for power electronics,” *IEEE Transactions on Power Electronics*, vol. 29, no. 12, pp. 6836–6846, Dec. 2014.

[80] F. Wang, Z. Zhang, R. Kennel, and J. Rodriguez, “Model predictive torque control with an extended prediction horizon for electrical drive systems,” *International Journal of Control*, pp. 1–10, Aug. 2014.

[81] Z. Gong, P. Dai, X. Yuan, X. Wu, and G. Guo, “Design and experimental evaluation of fast model predictive control for modular multilevel converters,” *IEEE Transactions on Industrial Electronics*, early access early access,2015.

[82] C. Xia, T. Liu, T. Shi, and Z. Song, “A simplified finite-control-set model-predictive control for power converters,” *IEEE Transactions on Industrial Informatics*, vol. 10, no. 2, pp. 991–1002, May 2014.

[83] Y. Zhang and W. Xie, “Low complexity model predictive control—single vector-based approach,” *IEEE Transactions on Power Electronics*, vol. 29, no. 10, pp. 5532–5541, Oct. 2014.

[84] Y. Zhang and H. Lin, “Simplified model predictive current control method of voltage-source inverter,” in *Proc. of ICPE ECCE*, May 2011, pp. 1726–1733.

[85] P. Cortes, A. Wilson, S. Kouro, J. Rodriguez, and H. Abu-Rub, “Model predictive control of multilevel cascaded h-bridge inverters,” *IEEE Transactions on Industrial Electronics*, vol. 57, no. 8, pp. 2691–2699, Aug. 2010.

[86] A. Iqbal, H. Abu-Rub, S. K. M. Ahmed, P. Cortes, and J. Rodriguez, “Model predictive current control of a three-level five-phase NPC VSI using simplified computational approach,” in *Proc. of APEC*, Mar. 2014, pp. 2323–2330.

[87] Y. Zhang, W. Xie, Z. Li, and Y. Zhang, “Low-complexity model predictive power control: Double-vector-based approach,” *IEEE Transactions on Industrial Electronics*, vol. 61, no. 11, pp. 5871–5880, Nov. 2014.

[88] J. Hu, J. Zhu, G. Lei, G. Platt, and D. G. Dorrell, “Multi-objective model-predictive control for high-power converters,” *IEEE Transactions on Energy Conversion*, vol. 28, no. 3, pp. 652–663, Sept. 2013.

[89] T. J. Vyncke, S. Thielemans, and J. A. Melkebeek, “Finite-set model-based predictive control for flying-capacitor converters: Cost function design and efficient FPGA implementation,” *IEEE Transactions on Industrial Informatics*, vol. 9, no. 2, pp. 1113–1121, May 2013.

[90] Z. Zhang, H. Fang, and R. Kennel, “Novel ripple reduced direct model predictive control of three-level NPC active front end with reduced computational effort,” in *2015 IEEE International Symposium on Predictive Control of Electrical Drives and Power Electronics (PRECEDE)*, Oct. 2015, pp. 32–37.

[91] M. P. Akter, S. Mekhilef, N. M. L. Tan, and H. Akagi, "Modified model predictive control of a bidirectional AC-DC converter based on Lyapunov function for energy storage systems," *IEEE Transactions on Industrial Electronics*, vol. 63, no. 2, pp. 704–715, Feb. 2016.

[92] W. Xie, X. Wang, F. Wang, W. Xu, R. M. Kennel, D. Gerling, and R. D. Lorenz, "Finite-control-set model predictive torque control with a deadbeat solution for PMSM drives," *IEEE Transactions on Industrial Electronics*, vol. 62, no. 9, pp. 5402–5410, Sep. 2015.

[93] T. Geyer and D. E. Quevedo, "Performance of multistep finite control set model predictive control for power electronics," *IEEE Transactions on Power Electronics*, vol. 30, no. 3, pp. 1633–1644, March 2015.

[94] M. Habibullah and D.-C. Lu, "A speed-sensorless FS-PTC of induction motors using extended Kalman filters," *IEEE Transactions on Industrial Electronics*, vol. 62, no. 11, pp. 6765–6778, Nov. 2015.

[95] S. Alireza Davari, D. A. Khaburi, and R. Kennel, "An improved FCS-MPC algorithm for an induction motor with an imposed optimized weighting factor," *IEEE Transactions on Power Electronics*, vol. 27, no. 3, pp. 1540–1551, Mar. 2012.

[96] T. J. Vyncke, S. Thielemans, T. Dierickx, R. Dewitte, M. Jacxsens, and J. A. Melkebeek, "Design choices for the prediction and optimization stage of finite-set model based predictive control," in *Workshop on Predictive Control of Electrical Drives and Power Electronics (PRECEDE)*, Oct. 2011, pp. 47–54.

[97] M. B. Shadmand, R. S. Balog, and H. A. Rub, "Auto-tuning the cost function weight factors in a model predictive controller for a matrix converter VAR compensator," in *Energy Conversion Congress and Exposition (ECCE), 2015 IEEE*, Sept. 2015, pp. 3807–3814.

[98] P. Cortes, S. Kouro, B. La Rocca, R. Vargas, J. Rodriguez, J. I. Leon, S. Vazquez, and L. G. Franquelo, "Guidelines for weighting factors design in model predictive control of power converters and drives," in *Proc. of ICIT 2009*, Feb. 2009, pp. 1–7.

[99] R. Vargas, U. Ammann, B. Hudoffsky, J. Rodriguez, and P. Wheeler, "Predictive torque control of an induction machine fed by a matrix converter with reactive input power control," *IEEE Transactions on Power Electronics*, vol. 25, no. 6, pp. 1426–1438, Jun. 2010.

[100] P. Zanchetta, "Heuristic multi-objective optimization for cost function weights selection in finite states model predictive control," in *Workshop on Predictive Control of Electrical Drives and Power Electronics (PRECEDE)*, Oct. 2011, pp. 70–75.

[101] Y. Zhang and H. Yang, "Two-vector-based model predictive torque control without weighting factors for induction motor drives," *IEEE Transactions on Power Electronics*, vol. 31, no. 2, pp. 1381–1390, Feb. 2016.

[102] ——, "Model-predictive flux control of induction motor drives with switching instant optimization," *IEEE Transactions on Energy Conversion*, vol. 30, no. 3, pp. 1113–1122, Sep. 2015.

[103] F. Villarroel, J. R. Espinoza, C. A. Rojas, J. Rodriguez, M. Rivera, and D. Sbarbaro, "Multiobjective switching state selector for finite-states model predictive control based on fuzzy decision making in a matrix converter," *IEEE Transactions on Industrial Electronics*, vol. 60, no. 2, pp. 589–599, Feb. 2013.

[104] C. A. Rojas, S. Kouro, M. Perez, and F. Villarroel, "Multiobjective fuzzy predictive torque control of an induction machine fed by a 3L-NPC inverter," in *2015 IEEE International Symposium on Predictive Control of Electrical Drives and Power Electronics (PRECEDE)*, Oct. 2015, pp. 21–26.

[105] M. Yu, Y. Wang, and Y. Li, "A novel sorting-based multi-objective model predictive control for PMSG wind turbines," in *Industrial Electronics Society, IECON 2015 - 41st Annual Conference of the IEEE*, Nov. 2015, pp. 000 267–000 272.

[106] S. A. Davari, D. A. Khaburi, and R. Kennel, "Using a weighting factor table for FCS-MPC of induction motors with extended prediction horizon," in *IECON 2012 - 38th Annual Conference on IEEE Industrial Electronics Society*, Oct. 2012, pp. 2086–2091.

[107] D. Y. Ohm, “Dynamic model of induction motors for vector control,” *Drivetech, Inc., Blacksburg, Virginia*, pp. 1–10, 2001.

[108] J. Holtz, “The dynamic representation of ac drive systems by complex signal flow graphs,” in *Industrial Electronics, 1994. Symposium Proceedings, ISIE ’94., 1994 IEEE International Symposium on*, May 1994, pp. 1–6.

[109] M. Habibullah, D. D. C. Lu, D. Xiao, and M. F. Rahman, “A computationally efficient FS-PTC for im with minimum voltage vectors,” in *Proc. of IEEE Int. Conf. on Power Electron. and Drive Systems (PEDS)*, June 2015, pp. 992–997.

[110] M. Habibullah, D.-C. Lu, D. Xiao, and M. F. Rahman, “A simplified finite-state predictive direct torque control for induction motor drive,” *IEEE Transactions on Industrial Electronics*, vol. 63, no. 6, pp. 3964–3975, June 2016.

[111] P. Cortes, J. Rodriguez, C. Silva, and A. Flores, “Delay compensation in model predictive current control of a three-phase inverter,” *IEEE Transactions on Industrial Electronics*, vol. 59, no. 2, pp. 1323–1325, Feb. 2012.

[112] https://www.dspace.com/shared/support/faqpdf/faq292.pdf.

[113] M. Habibullah, D.-C. Lu, D. Xiao, and M. F. Rahman, “Finite state predictive torque control of induction motor supplied from a three-level NPC voltage source inverter,” *IEEE Transactions on Power Electronics*, vol. 32, no. 1, pp. 479–489, Jan. 2017.

[114] L. Gao, J. E. Fletcher, and L. Zheng, “Low-speed control improvements for a two-level five-phase inverter-fed induction machine using classic direct torque control,” *IEEE Transactions on Industrial Electronics*, vol. 58, no. 7, pp. 2744–2754, July 2011.

[115] J. Zhang and M. F. Rahman, “A direct-flux-vector-controlled induction generator with space-vector modulation for integrated starter alternator,” *IEEE Transactions on Industrial Electronics*, vol. 54, no. 5, pp. 2512–2520, Oct. 2007.

[116] L. Tang, L. Zhong, M. F. Rahman, and Y. Hu, “A novel direct torque controlled interior permanent magnet synchronous machine drive with low ripple in flux and torque and fixed switching frequency,” *IEEE Transactions on Power Electronics*, vol. 19, no. 2, pp. 346–354, Mar. 2004.

[117] M. Habibullah, D. D. C. Lu, D. Xiao, J. E. Fletcher, and M. F. Rahman, “Predictive torque control of induction motor sensorless drive fed by a 3L-NPC inverter,” *IEEE Transactions on Industrial Informatics*, early access, 2016.

[118] M. Habibullah and D. D. C. Lu, “An improved sensorless FS-PTC of induction motors using estimated stator currents,” in *2015 IEEE Symposium on Sensorless Control for Electrical Drives (SLED)*, June 2015, pp. 1–6.

[119] M. Habibullah and D. D.-C. Lu, “Encoderless FS-PTC for induction motor with extended kalman filter,” in *2014 Australasian Universities Power Engineering Conference (AUPEC)*, Sept. 2014, pp. 1–5.

[120] L. Harnefors and M. Hinkkanen, “Stabilization methods for sensorless induction motor drives—a survey,” *IEEE Journal of Emerging and Selected Topics in Power Electronics*, vol. 2, no. 2, pp. 132–142, June 2014.

Appendices

Appendix A

Parameters and specifications

Table A.1: The 415 V, 3-ϕ, 50 Hz IM parameters

$R_s = 6.03\ \Omega$	$\psi_{snom} = 1.0$ Wb
$R_r = 6.085\ \Omega$	$T_{nom} = 7.4$ Nm
$L_s = 0.5192$ H	$N_p = 2$
$L_r = 0.5192$ H	$J = 0.011787$ Kg.m^2
$L_m = 0.4893$ H	$\omega_m = 1415$ r/min

Table A.2: DC machine ratings

P = 1.1 kW
V = 180 V
$I_a = 6.9$ A
$\omega = 1800$ r/min

Table A.3: 2L-VSI specification

Maximum dc-link voltage	1200 V
Maximum current	50 A
Converter switches	IGBT

Table A.4: 3L-NPC VSI specification

Maximum dc-link voltage	900 V
dc-link capacitors	3300 μF/450 V× 2
Converter switches	SKM100GB123D
Gate units	SKYPER 32PRO

Table A.5: Controllers' parameters for the proposed FS-PTC drives

2L-VSI (Chapter 3)	3L-NPC VSI (Chapter 4)	RSFVC-based FS-PTC (Chapter 5)	Sensorless FS-PTC (Chapter 6)
$V_{dc} = 587V$ $T_s = 50\mu s$ $k_{p\omega} = 0.396$, $k_{i\omega} = 9.056$ $\lambda_f = 30$, λ_n=0.05 I_{max}=5.0 A	$V_{dc} = 587V$ $T_s = 70\mu s$ $k_{p\omega} = 0.3$, $k_{i\omega} = 3.0$ λ_f=25,18(for the SPVs) $\lambda_{cv} = 10^{-4}$, $\lambda_n = 10^{-6}$ I_{max}=5.0 A For the FOC strategy $k_{p\omega} = 0.2$, $k_{i\omega} = 10$ $k_{p-id} = 20$, $k_{i-id} = 10$ $k_{p-iq} = 50$, $k_{i-iq} = 10$ $i_{qref-max} = 3.537A$ $\lvert\psi_{rref}\rvert = 0.93Wb$	$V_{dc} = 587V$ $T_s = 70\mu s$ $k_{p\omega} = 0.3$, $k_{i\omega} = 5.0$ $k_{pT_e} = 200$, $k_{iT_e} = 50$ λ_f=25 (for the conventional FS-PTC) $\lambda_{cv} = 10^{-4}$, $\lambda_n = 10^{-6}$	$V_{dc} = 587V$ $T_s = 100\mu s$ $k_{p\omega} = 0.3$, $k_{i\omega} = 3.0$ λ_f=25 $\lambda_{cv} = 10^{-4}$, $\lambda_n = 10^{-6}$ I_{max}=5.0 A

Appendix B

Experimental setup

The experimental setup is shown in Fig. B.1(a). For the experiment with a 2L-VSI, the same setup is used replacing the 3L-NPC VSI with the 2L-VSI as shown in Fig. B.1(b). The setup mainly consists of a squirrel-cage IM specified in Table A.1, a 2L-VSI or 3L-NPC VSI and a DC machine. The specifications of the 2L-VSI and 3L-NPC VSI are given in Table A.3 and A.4, respectively. The inverters have internal high-current protection circuit, which has not been used in this study. A software based over-current protection is implemented by applying zero vector continuously if over-current flows in the stator winding. Some other hardware based protections exist, such as short circuit, over temperature and under voltage. A permanent magnet dc machine is coupled to the rotor shaft to analyse the loaded behaviour of the system; the DC machine rating is given in Table A.2. A rheostat is placed across the dc machine armature to change the load on the fed motor. However, for the sensorless operation, a dc-dc converter is employed for loading the motor at a low-speed. Two LEM voltage sensors 'LV 25-P' and two LEM current sensors 'LA 55-P' with proper circuit arrangements, as shown in Figs. B.2 and B.3, respectively, are used to measure the dc-link voltage and stator current. An incremental encoder of 5000 PPR is mounted on the motor shaft to measure the speed. The outer speed loop of the controller is sampled in every 2.5 ms to minimize the quantization error. A digital deadtime generator, as shown in Fig. B.4, is used to inject the required deadtime between two complementary switching signals; the deadtime used is 2.5 μs. These complementary switching signals are required to drive the complementary switches

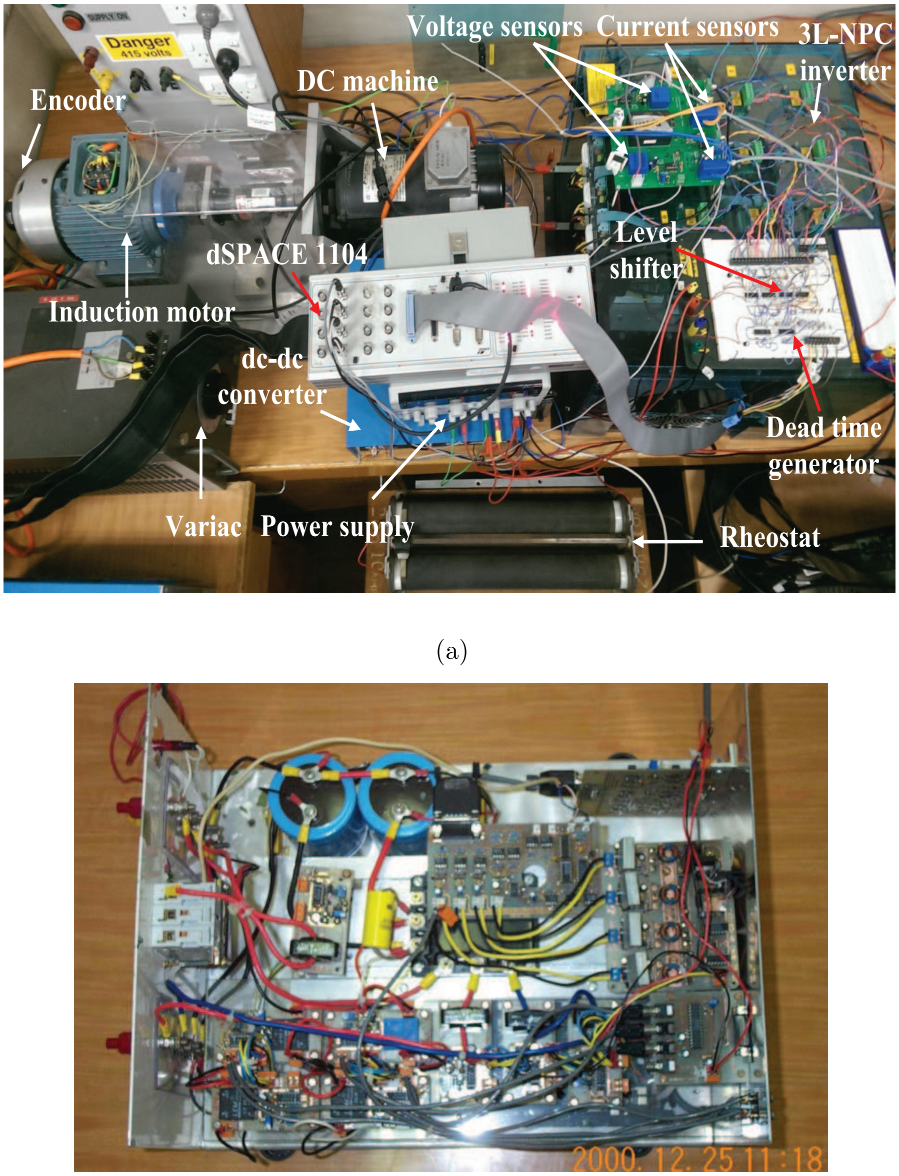

(a)

(b)

Figure B.1: (a) Experimental setup with the 3L-NPC VSI and (b) top view of the 2L-VSI.

in the inverter. The voltage level of the output of the deadtime generator is boosted from +5 to +15 V using the IC 'HEF4104'. This is done to ensure the adequate voltage level of the switching signals applied to the semiconductor switches.

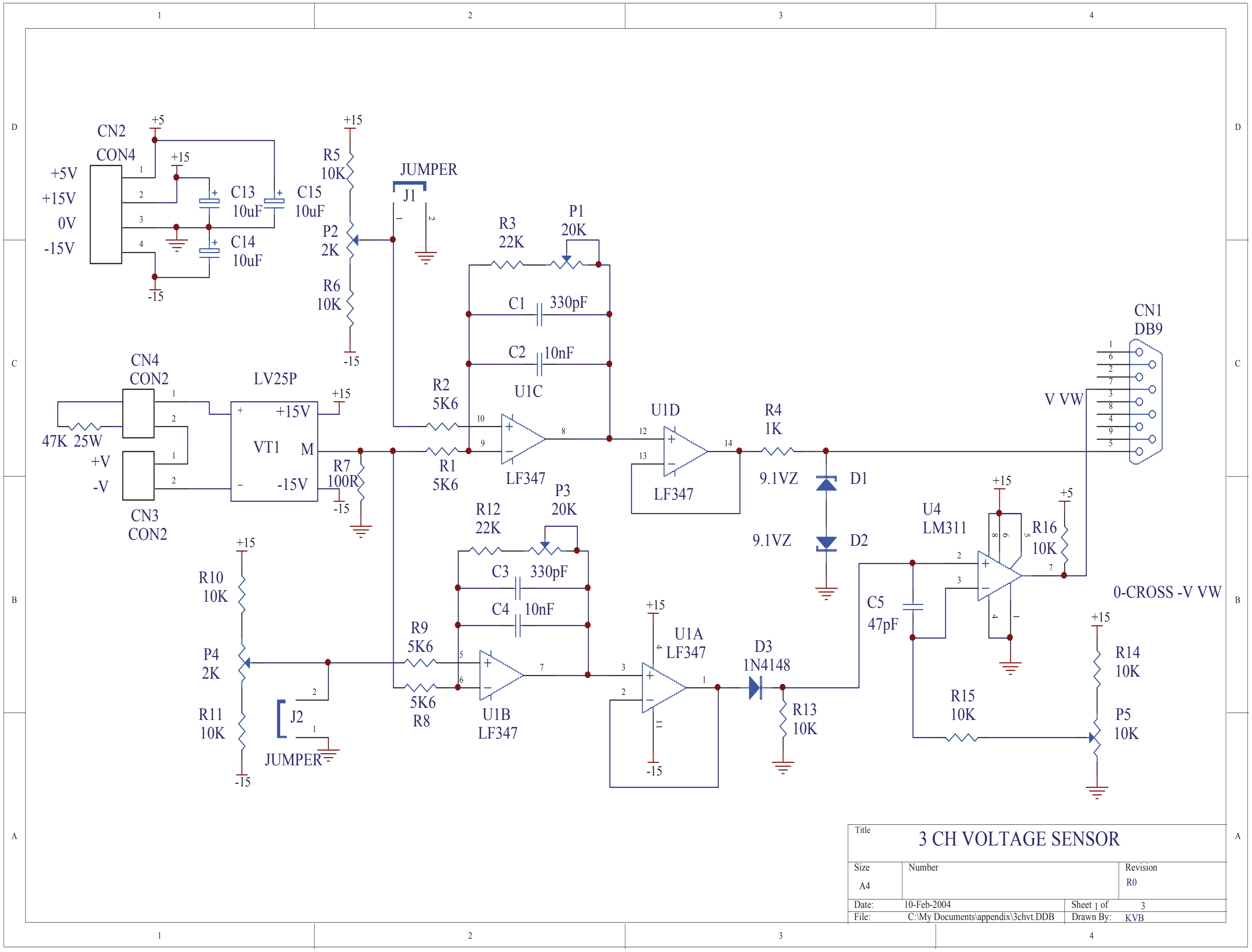

Figure B.2: Voltage sensor board

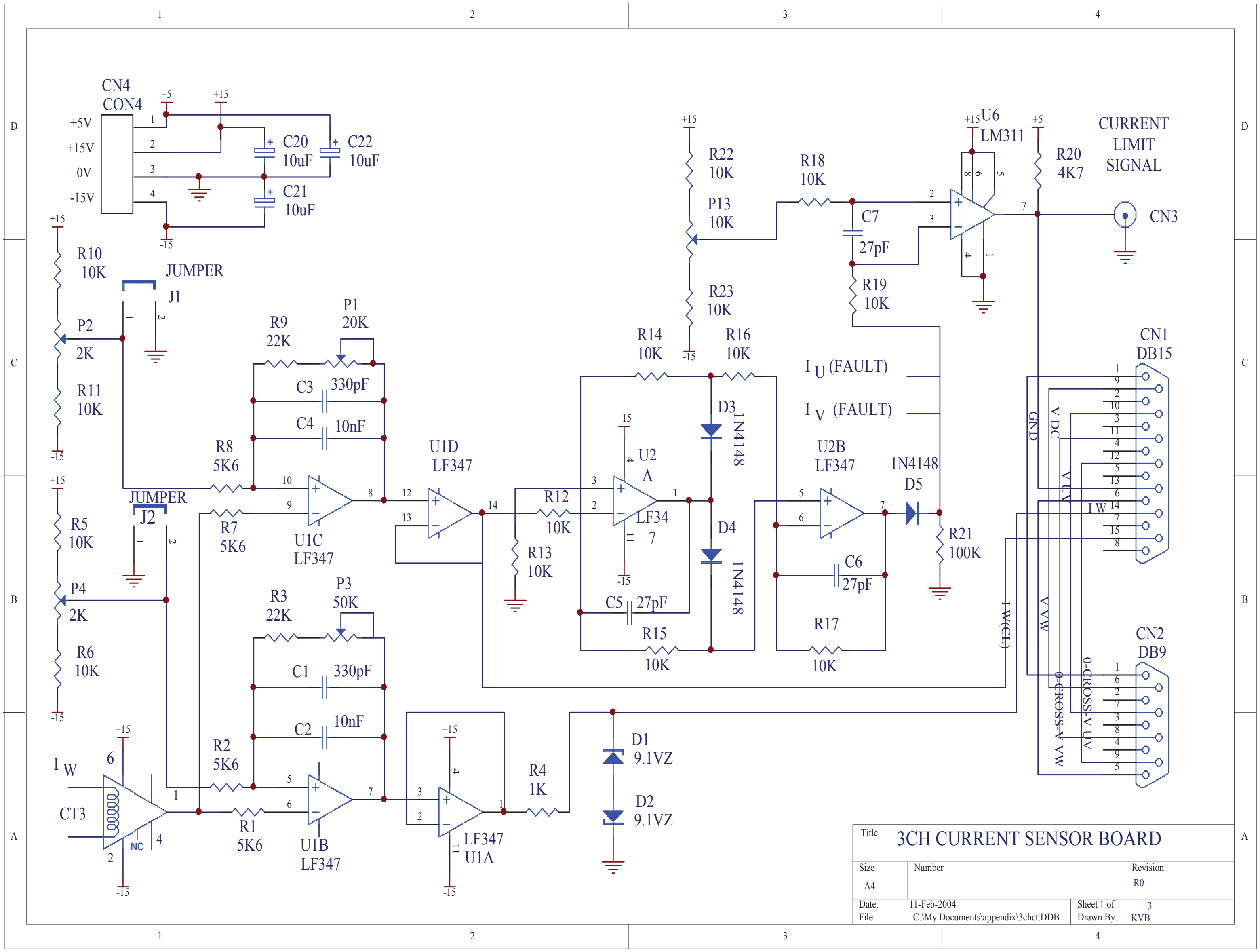

Figure B.3: Current sensor board

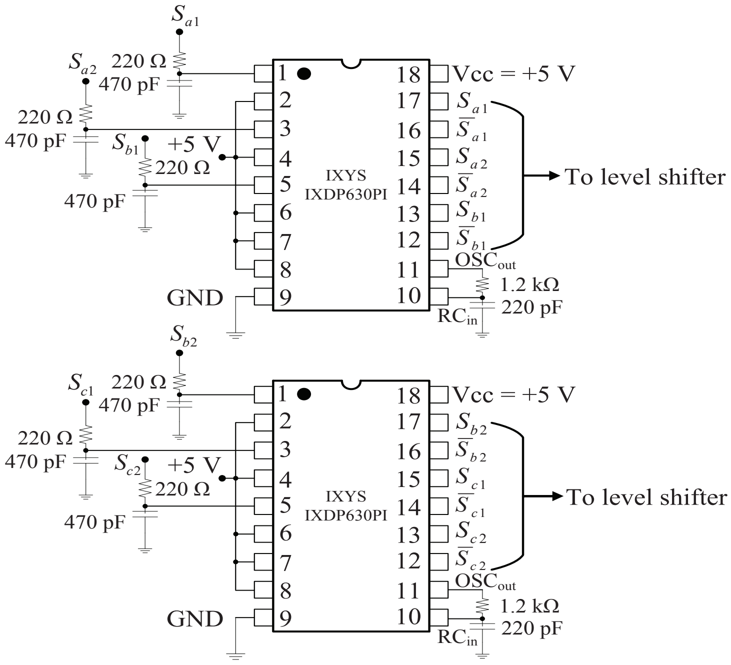

Figure B.4: Digital deadtime generator.

B.1 Modification in the gate circuits of the 3L-NPC VSI

The 3L-NPC VSI used in this thesis was an ANPC inverter; however, the generated switching signals by the controller are exactly same as used for a diode clamped inverter, as discussed in Chapter 2. Every phase of the inverter is constructed with the three gate units of 'SKYPER 32PRO', as shown in Fig. B.5(a). Each gate unit has two IGBT switches, which has internal cross over protection. Hence, two switches in a unit can not be turned *on* at the same time. Both the switches in a unit will be *off* if two logic one signals are applied simultaneously. When a logic zero is applied to both the clamping switches $\{S_{a3}, S_{a4}\}$, the inverter exactly acts as a diode clamped inverter, and this strategy is followed to connect the output poles to the positive and negative rails of the bus bar. As both the switches in gate unit 3 can not be turned *on* simultaneously, a logic one signal is applied to both clamping switches for the neutral-point connection. In this case, the load current can flow in either direction, as shown in Fig. B.5(b). A logic

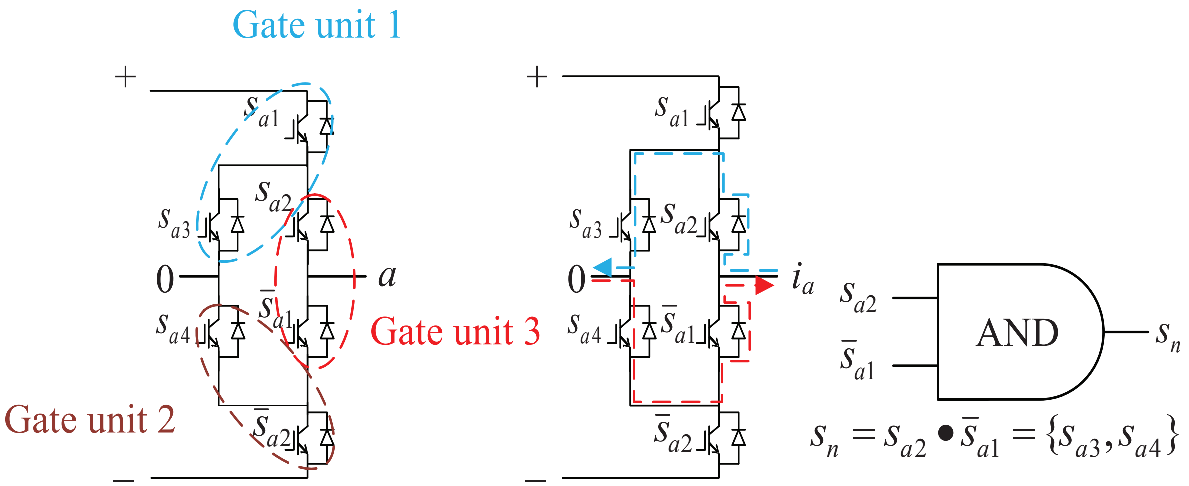

(a) (b) (c)

Figure B.5: Internal structure of the 3L-NPC inverter and its operating principle for the neutral-point connection for each phase. (a) Orientation of the gate units for phase a, (b) illustration of the neutral-point connection for positive and negative load currents $\pm i_a$ and (c) generation of the switching signals for the clamping switches.

AND gate 'HEF4081BP' is employed for each phase to generate the switching signals for the clamping switches, as shown in Fig. B.5(c). The switching signals of the gate unit 3 are used as the inputs to the AND gate. Hence, the clamping switches are turned *on* when only neutral-point connection is required. All the possible switching signals for each phase $x = \{a, b, c\}$ are shown in Table B.1. Note that only an external logic AND gate is employed to operate the ANPC inverter as a diode clamped inverter.

Table B.1: All the switching signals and corresponding outputs for each phase of the 3L-NPC inverter

Switching states					Output voltage
S_{x1}	S_{x2}	$\bar{S}_{x1}$	$\bar{S}_{x2}$	S_n	v_{x0}
1	1	0	0	0	$+V_{dc}/2$
0	1	1	0	1	0
0	0	1	1	0	$-V_{dc}/2$

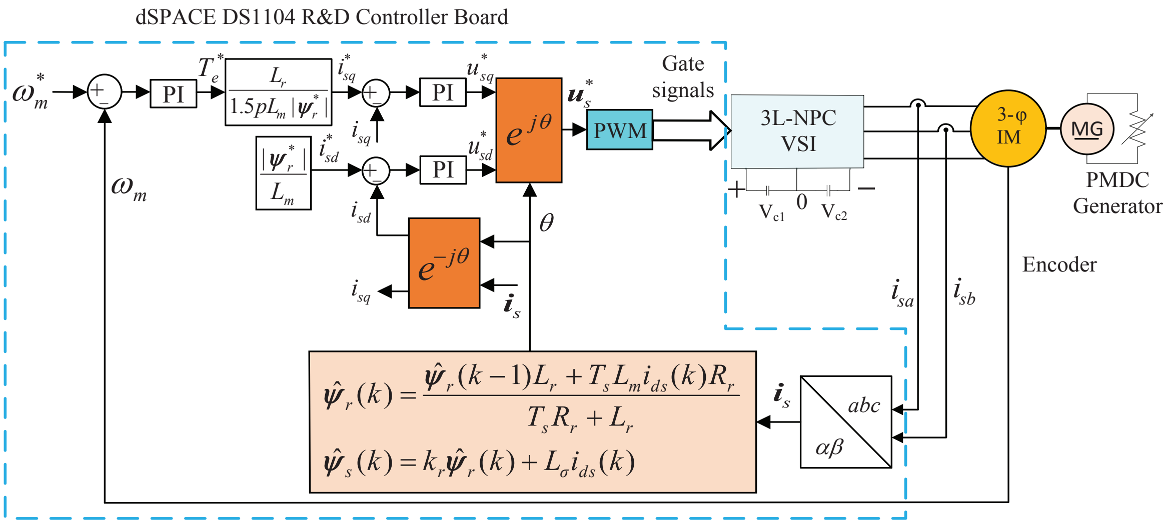

Figure B.6: FOC scheme used to compare its dynamic performance with the proposed FS-PTC.

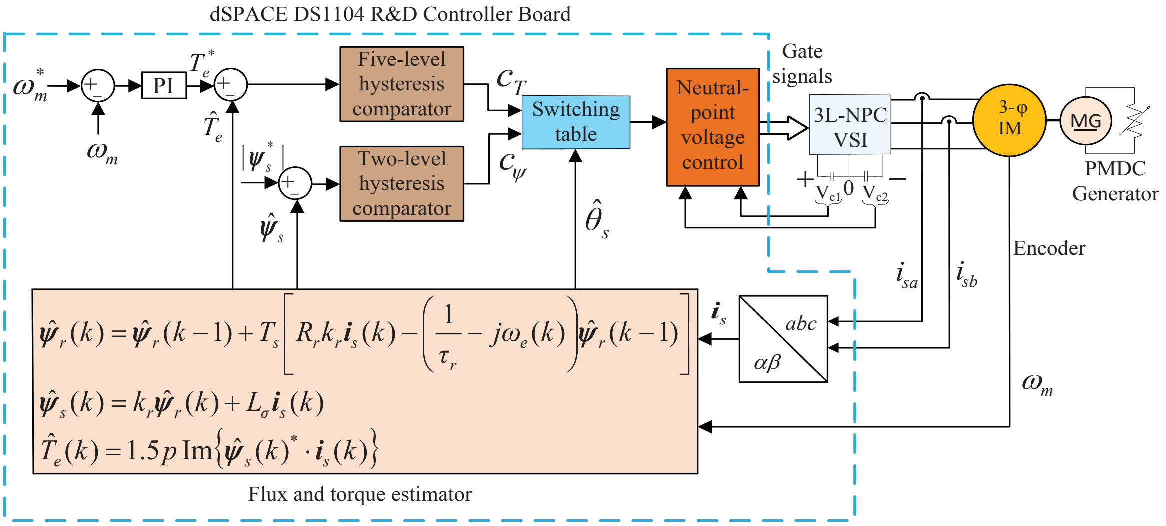

Figure B.7: DTC scheme used to compare its dynamic performance with the proposed FS-PTC.